

Design and Manufacturing of Modular Self-Compensating Hydrostatic Journal Bearings

by

Markku Sami Antero Kotilainen

S.M., Mechanical Engineering
Helsinki University of Technology, 1997

SUBMITTED TO THE DEPARTMENT OF MECHANICAL ENGINEERING
IN PARTIAL FULFILLMENT OF THE DEGREE OF

DOCTOR OF PHILOSOPHY

at the

MASSACHUSETTS INSTITUTE OF TECHNOLOGY

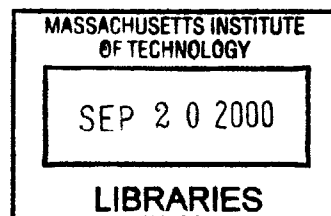
June 2000

© 2000 Massachusetts Institute of Technology
All rights reserved

Signature of Author
Department of Mechanical Engineering
June 2, 2000

Certified by
Alexander H. Slocum
Professor of Mechanical Engineering
Thesis Supervisor

Accepted by
Ain A. Sonin
Professor of Mechanical Engineering
Chairman, Committee for Graduate Students



ENG

1000
1000
1000
1000

1000

1000

1000

1000

1000
1000
1000
1000

Design and Manufacturing of Modular Self-Compensating Hydrostatic Journal Bearings

by

Markku Sami Antero Kotilainen

Submitted to the Department of Mechanical Engineering
on July 2, 2000 in Partial Fulfillment of the
Requirements for the Degree of Doctor of Philosophy in Mechanical Engineering
at the Massachusetts Institute of Technology

ABSTRACT

In order to carry a load, a multi recess hydrostatic bearing supplied with a single pressure source requires compensation devices. These devices are also known as restrictors and they allow the recess pressures to differ from each other. These devices, when properly selected and tuned, can deliver excellent bearing performance. However, these devices add to the complexity of the bearing and they are sensitive to manufacturing errors. These devices must often be tuned specifically for each bearing and are therefore expensive to install and maintain.

Self-regulating or self-compensating bearings do not need any external devices to achieve load-carrying capability and they do not add to the total degrees of freedom of the system. However, in many cases the proposed designs require multiple precision manufacturing steps such as EDM and grinding in addition to precision shrink fit.

In this work a self-compensating design, which eliminates all but one precision-manufacturing step, was manufactured and tested. Novel manufacturing methods for different sizes were introduced. The test results were compared with theoretical results and satisfactory agreement was achieved. The bearing sensitivity to manufacturing errors was analyzed computationally using statistical methods. These results were used to show that the introduced manufacturing methods are more cost effective than the applicable precision or semi precision manufacturing methods even when the performance variation is taken into account.

When hydrostatic journal bearing is rotated hydrodynamic effects are introduced. Often, these effects are ignored by assuming them to be insignificant. Two non-dimensional parameters were derived to estimate the significance of the hydrodynamic effects and limits to these parameters were searched numerically. Design theory, along with first order equations to estimate bearing performance was developed.

Thesis Supervisor:
Professor Alexander H. Slocum
Department of Mechanical Engineering

ACKNOWLEDGMENTS

First and foremost, I would like to thank my wife, Päivi. Who followed me here and unconditionally supported and loved me. No words or thank you can ever do justice to what you have done for me. Tämä on sinulle oma pikku sipulini.

I would like to thank my always inspirational advisor Prof. Alex Slocum, who's endless energy, amazing creativity, knowledge and wisdom are without parallel. It was great learning from you, I could not have had a better advisor. I would also like to thank the rest of my thesis committee, Professors David Trumper and Samir Nayfeh, who were always supportive and helpful.

I would also like to thank my dad for his support and advice.

I would also like to thank the following foundations for making this endeavour financially possible: Walter Ahlströmin säätiö, Jenny ja Antti Wihurin rahasto, Alfred Kordelinin säätiö, Thanks to Scandinavia foundation, Suomen Kulttuurirahasto and Suomen Akatemia.

Thankfully,

Sami Kotilainen
June 2. 2000
Cambridge, Massachusetts

Abstract	3
Acknowledgments	5
Nomenclature	19
Chapter 1. Introduction	21
1.1 Scope of the Thesis	21
1.2 Background	23
1.2.1 Bearing Technology	23
1.2.2 Hydrodynamic Bearings	24
1.2.3 Hydrostatic Bearings	25
Chapter 2. Surface Self-compensation	35
2.1 Surface Self-Compensating Hydrostatic Bearings	35
2.2 Why Bushing?	42
Chapter 3. Modeling	43
3.1 Lumped Parameter Modeling	43
3.1.1 Validity of the Geometric Assumption	44
3.1.2 Example Lumped Parameter Model	47
3.2 Finite Difference Modeling	50
3.2.1 Bearing Geometry Generation	53
3.2.2 Validity of the Finite Difference Solution	54
3.2.3 Turbulence Modeling	59
Chapter 4. Analytical Considerations	63
4.1 Static characteristics of a plain journal bearing	64
4.1.1 Infinitely long bearing	64
4.1.2 Short bearing	67
4.2 Dynamic coefficients of a plain journal bearing	69
4.2.1 Derivation of the dynamic coefficients	70
4.2.2 Infinitely Short Bearing	76
4.2.3 Infinitely Long Bearing	82
4.3 Fixed Restrictor Deep-Pocket Hydrostatic Bearing	88
4.4 Bearing Stability	90
4.5 Summary of the Analytical Analysis	93

Chapter 5. Design	95
5.1 General Considerations	95
5.2 Low (laminar) Speed	104
5.2.1 Summary of Laminar Design Issues	128
5.3 High Speed (Turbulent)	128
5.4 Adjustable Clearance and Shape	136
5.5 Summary of Design	142
Chapter 6. Manufacturing	145
6.1 Selecting a Manufacturing Method	145
6.2 Manufacturing of the 6" Prototype Bushing	148
6.2.1 Shrinkage and Dimensional Variation	150
6.2.2 Run-Test of Groove Width Measurement Data	153
6.2.3 Chi-Square () Test of Groove Width Measurement Data	154
6.3 Manufacturing of the 1.25" Prototype Bushing	157
6.3.1 Problems with 1.25" Prototype Manufacturing	158
6.3.2 Solutions to Manufacturing Problems	160
6.3.3 Shrinkage and Dimensional Variation	160
6.4 Sensitivity of the Bearing to Manufacturing Errors	162
6.4.1 Model	162
6.4.2 The Effect of Manufacturing Errors on Load Capacity	164
6.4.3 Cost vs. Quality Analysis	171
Chapter 7. Testing	179
7.1 Static Testing of the 6" Prototype	179
7.1.1 Test Set-up	180
7.1.2 Results	187
7.1.3 Conclusions	196
7.2 Dynamic Stiffness Testing of the 6" Prototype	197
7.2.1 Test Set-up	197
7.2.2 Results	198
7.3 Static Testing of the 1.25" Prototype	200
7.3.1 Test Set-up	200
7.3.2 Results	203
7.3.3 Conclusions	204
7.4 Error Motion Measurements	205

7.4.1	Testing Method	205
7.4.2	Test Set-up	207
7.4.3	Results	208
7.4.4	Conclusions	212
Chapter 8.	Applications	213
8.1	General	213
8.2	TurboTool	214
8.2.1	Preliminary Analysis of TurboTool Concept	215
8.3	Conceptual Very Small Machine Tool	221
8.3.1	Functional Requirements for Small 5-Axis Machine	221
8.3.2	Concept Selection	225
8.3.3	Concept Feasibility	225
8.4	Sealing	232
Chapter 9.	Conclusions and future work	237
References	241
Appendix A.	Automatic Geometry Generation	245
Appendix B.	Data analysis for error motion measurements	275
Appendix C.	Wobble Plate	281
Appendix D.	Finite element program to solve linearized dynamic response of the TurboTool	283
Appendix E.	Detailed drawings of the 6" bearing test stand	291

Figure 1.1	Simple hydrostatic bearing. Principle of operation and pressure diagrams	26
Figure 1.2	Hydrostatic double- or opposed pad bearing and pressure diagrams.	27
Figure 1.3	Hydrostatic bearing electric circuit analogy	27
Figure 1.4	Spool valve compensators	30
Figure 1.5	a) Diaphragm restrictor b) Diaphragm as a flow divider	31
Figure 1.6	Shallow recess hydrostatic bearing	32
Figure 2.1	Surface self-compensating linear bearing [Slocum, 1992].	36
Figure 2.2	Normalized load capacity and stiffness of self-compensating bearing. Normalized by fixed restrictor bearing.	38
Figure 2.3	Cross sectional and developed view of surface self-compensating journal bearing	39
Figure 2.4	Developed view of surface self-compensating bearing	39
Figure 2.5	Surface self-compensating journal bearing with deterministic compensators [Slocum, 1994]	40
Figure 2.6	Surface self-compensating bearing with cross drilled collectors and load pockets on shaft	41
Figure 2.7	Bearing design with all the geometry on the shaft surface	41
Figure 3.1	Circumferential flow over land in displaced journal bearing	44
Figure 3.2	Ratio between full solution and flat plate approximation in case of circumferential flow in a journal bearing	46
Figure 3.3	Ratio between full solution and flat plate approximation in case of axial flow in a journal bearing	47
Figure 3.4	Lumped parameter model	47
Figure 3.5	Equivalent circuit	48
Figure 3.6	Finite difference grid	51
Figure 3.7	a) Too coarse mesh results in wider than real grooves, b) Points close to groove edge result in better interpolation of real geometry	54
Figure 3.8	Groove depth test case	55
Figure 3.9	Bearing force as function of eccentricity ratio	58
Figure 3.10	Variation of the recirculation pressure gradient with groove depth	59
Figure 4.1	Co-ordinate system	66
Figure 4.2	Non-dimensional load for the different assumptions	68
Figure 4.3	Attitude angle for the different assumptions	69

Figure 4.4	Section showing bearing co-ordinate system	70
Figure 4.5	Intermediate bearing co-ordinate frame	72
Figure 4.6	Pressure given by Equation 4.41.	77
Figure 4.7	Change of basis	78
Figure 4.8	Stiffness coefficients for infinitely short bearing with Sommerfeld's conditions	79
Figure 4.9	Damping coefficients for infinitely short bearing with Sommerfeld's conditions	79
Figure 4.10	Stiffness coefficients for infinitely short bearing with Gumbel's conditions 81	
Figure 4.11	Damping coefficients for infinitely short bearing with Gumbel's conditions 82	
Figure 4.12	Pressure given by Equation 4.56.	83
Figure 4.13	Stiffness coefficients for long bearing with Sommerfeld's conditions	85
Figure 4.14	Damping coefficients for long bearing with Sommerfeld's conditions	85
Figure 4.15	Stiffness coefficients for long bearing with Gumbel's conditions	87
Figure 4.16	Damping coefficients for long bearing with Gumbel's conditions	87
Figure 4.17	Typical fixed restrictor hydrostatic bearing	89
Figure 5.1	Sensitivity of initial pressure ratio to manufacturing errors	102
Figure 5.2	Sensitivity to clearance errors.	103
Figure 5.3	Design parameter relation to bearing geometry	104
Figure 5.4	as function of resistance ratio	106
Figure 5.5	Removing central lands to improve high speed frictional characteristics	109
Figure 5.6	Normalized A^* for laminar flow	111
Figure 5.7	Normalized A^* for transitional flow	112
Figure 5.8	Normalized A^* for turbulent flow	112
Figure 5.9	Pressure formation in converging gap	113
Figure 5.10	Converging gap divided into sections	115
Figure 5.11	Ratio between uninterrupted and interrupted hydrodynamic force	116
Figure 5.12	Coordinate system for the 2.35" bearing results	119
Figure 5.13	Pressure distribution for the grooved and plain bearing with supply pressure ()	120

Figure 5.14	Pressure distribution for the grooved and plain bearing without supply pressure ()	121
Figure 5.15	Bearing force for different 2.35" bearing cases	121
Figure 5.16	Hydrodynamic force of the grooved bearing and the short bearing approximation divided by the	122
Figure 5.17	Pressure distribution for a bearing with high power ratio (38) ()	124
Figure 5.18	Pressure distribution for a bearing with high power ratio (25) () and central lands removed	125
Figure 5.19	Pressure distribution for a bearing with high power ratio (40) () and central lands removed	126
Figure 5.20	Simple step bearing	127
Figure 5.21	Pressure distribution for a high speed (100 000 rpm) bearing	130
Figure 5.22	Pressure distribution for laminar design at 100 000 rpm	132
Figure 5.23	Pressure distribution for SC5 design at 100 000 rpm	134
Figure 5.24	Pressure distribution for SC6 small recess design at 100 000 rpm.	135
Figure 5.25	Cylinder with internal and external pressure	138
Figure 6.1	Stereolithography negative of grooving geometry	149
Figure 6.2	A) Core-box, B) Sand core in the mold	150
Figure 6.3	A) Cast bushing, B) Groove detail	150
Figure 6.4	The measured and normal distributions for groove width data	156
Figure 6.5	A) 3D-Printed wax pattern, B) Investment cast part	157
Figure 6.6	Problems with printing deep grooves	159
Figure 6.7	Lumped parameter discretization.	163
Figure 6.8	Bearing force distribution with $ecc=0.1$, % of land width	165
Figure 6.9	Force angle distribution with $ecc=0.1$, % of the land widths	166
Figure 6.10	Bearing force distribution with $ecc=0.5$, % of land width	169
Figure 6.11	Bearing force distribution with $ecc=0.1$, % of groove width	170
Figure 6.12	Loss function concept	172
Figure 6.13	The derivation of expected cost	173
Figure 6.14	Normalized manufacturing cost as function of quantity	176
Figure 6.15	Normalized manufacturing cost as function of quantity	177
Figure 7.1	General view of the test setup	180
Figure 7.2	Bearing assembly and the location of the capacitance probes	182

Figure 7.3	Photograph of the test setup	183
Figure 7.4	Bearing assembly	185
Figure 7.5	Reaction forces on the shaft in the case that both bushings have the same geometry	186
Figure 7.6	Gap test. Pump turned off and on while measuring the displacement.	187
Figure 7.7	Uncorrected force-displacement curves at 250 psi measured with the 50k force transducer	188
Figure 7.8	3D Finite element model	190
Figure 7.9	Displacement of the test setup with 10 000N load	191
Figure 7.10	The simplified beam model	192
Figure 7.11	Beam model displacement	192
Figure 7.12	Corrected force-displacement curves at 250 psi with 50k force transducer. (Corr1=corrected results of the probe 1, Corr2=corrected results of the probe 3)	193
Figure 7.13	Corrected force-displacement curves at 250 psi supply pressure and the 5k force transducer. (Corr1=corrected results from probe 1, Corr3=corrected results from probe 3)	195
Figure 7.14	Impact and acceleration measurement points	197
Figure 7.15	The dynamic stiffness and phase traces for the points 1,2 and 5.	199
Figure 7.16	Simple single d.o.f system	199
Figure 7.17	General and side view of the test set-up. General view is rotated upside down for clarity.	201
Figure 7.18	Photograph of the test set-up	201
Figure 7.19	Bearing assembly	202
Figure 7.20	Force displacement results at 500 psi.	203
Figure 7.21	Two gauge method with offset spherical master	206
Figure 7.22	The error motion test set-up.	208
Figure 7.23	Error motion test set-up (2" ball)	208
Figure 7.24	Error motion trace for single revolution	209
Figure 7.25	Error motion for multiple revolutions	209
Figure 7.26	Asynchronous error motion	210
Figure 7.27	Noise level with pump on	211
Figure 7.28	Noise without the pump	212
Figure 8.1	Embodiment of a TurboTool concept	215

Figure 8.2	Finite element representation of the TurboTool	220
Figure 8.3	Transfer function for the tool tip displacement of the TurboTool	221
Figure 8.4	Typical gantry type arrangement of axis	223
Figure 8.5	Hexapod (Steward platform)	224
Figure 8.6	Linear-rotary concepts (actuators not shown)	225
Figure 8.7	Circular concept	225
Figure 8.8	Double yoke design	228
Figure 8.9	Finite element representation of the lower yoke	230
Figure 8.10	Transfer functions for the lower yoke	231
Figure 8.11	Slinger seal	233
Figure 8.12	Labyrinth seal	234
Figure 8.13	Clamped circular flat plate	235
Figure 8.14	Combination of slinger, lip and air barrier seal	236
Figure 8.15	Combined air barrier lip seal	236

TABLE 3.1	Reynold's numbers and entrance length for the test case	56
TABLE 3.2	Pm for different groove depths and diameters	56
TABLE 3.3	Initial pocket pressure ratios for the two models	57
TABLE 3.4	Dimensions for the two different test cases	61
TABLE 3.5	Comparison of flow rates for Case #1	61
TABLE 3.6	Comparison of flow rates for Case #2	62
TABLE 5.1	Non-dimensional parameters for different bearing geometries and types [Wasson, 1996]	98
TABLE 5.2	Flow regimes for different bearing regions	105
TABLE 5.3	Minimum film thickness for different bearing sizes and surface speeds . . 110	
TABLE 5.4	Maximum allowable surface pressures for different bearing materials	110
TABLE 5.5	Main dimensions of 2.35" bearing	118
TABLE 5.6	Summary of the computed results	119
TABLE 5.7	Comparison between finite difference computed and derived estimated val- ues	123
TABLE 5.8	Dimensions of 100 000 rpm bearing	130
TABLE 5.9	Summary of different high speed cases (100 000 rpm)	132
TABLE 5.10	Summary of the high speed designs (100 000 rpm)	136
TABLE 6.1	Possible bushing manufacturing methods	146
TABLE 6.2	Diameter Measurements of 6" Bushings	152
TABLE 6.3	Groove Width Measurement Statistics	153
TABLE 6.4	Chi-Square Test for Groove Width Measurement Data	156
TABLE 6.5	Measurement statistics of the first two sets of 3D-printed parts	161
TABLE 6.6	Measurement statistics of the sets III and IV of 3D-printed parts	161
TABLE 6.7	Summary of the results for % of the land widths case	166
TABLE 6.8	Summary of the results for % of the groove width case	167
TABLE 6.9	Summary of the results for % of the land widths case	167
TABLE 6.10	Summary of the results for % of the land widths case	167
TABLE 6.11	Summary of the results for % of the land widths case	168
TABLE 6.12	Summary of the results for % of the land widths case	169
TABLE 7.1	Specifications of the load cells	181

TABLE 7.2	Initial Stiffness at 250 psi	195
TABLE 7.3	Flow rate at 500 psi	196
TABLE 7.4	Initial stiffness of the 1.25" prototype	204
TABLE 7.5	Measured and predicted flow for the 1.25" bearing	204
TABLE 8.1	Bearing dimensions for TurboTool	217
TABLE 8.2	Bearing properties at equilibrium point under maximum machining force 218	
TABLE 8.3	Concept selection	226
TABLE 8.4	Geometric error gains	228
TABLE 8.5	Static stiffness of the double yoke concept	229
TABLE 8.6	First natural frequencies of the yokes	230

NOMENCLATURE

A	area [m ²]
A_i	Routh-Hurwitz coefficient
A^*	equivalent friction area
B, b	damping coefficient [Ns/m]
c	heat capacity []
C_f	friction factor
C	clearance [m]
D	diameter [m]
e	radial displacement [m]
E	Young's modulus [Pa]
f	frequency [Hz]
F, f	force [N]
f_r	friction factor
g	gravitational acceleration [m/s ²]
h	film thickness [m]
i	current [A]
I	second moment of inertia [m ⁴]
K, k	stiffness [N/m]
L	length [m]
M, m	mass [kg]
N	rotational speed [rev/min]
N_{Ta}	Taylor number
n	shear stress ratio, index
P, p	pressure [Pa], power [W]
Q	volumetric flow rate [m ³ /s]
R	radius [m]
R_i	flow resistance [Pa/m ³ /s]
Re	Reynolds number
S	Sommerfelds number
T	torque [Nm]
u, U	velocity [m/s], displacement [m]
V	volume [m ³]
W	load [N]
w	width [m]
δ	displacement (small) [m]
ε	strain, eccentricity
ζ	hydraulic resistance ratio
γ	angle between pocket and restrictor [rad]
λ	scale factor
μ	viscosity [Pa s], mean value

Π	power ratio
Ψ	pumping ratio
ρ	density [kg/m ³]
σ	stress [Pa]
ν	Poisson's ratio
τ	shear stress [Pa]
ϕ	attitude angle [rad]
ω	rotational speed [rad/s]
$(\dot{\quad})$	time derivative

Chapter 1

INTRODUCTION

This chapter includes an introduction to this thesis. It is also intended to serve as an short introduction to bearing technology in general and specifically to non-contact fluid film bearings.

1.1 Scope of the Thesis

The purpose of this research is to create a fundamental new machine element: a modular hydrostatic bushing. In this research, a design theory for conformable surface self-compensating hydrostatic bushing bearings is developed and then be to design and manufacture surface self-compensating hydrostatic bushing bearings. The design is divided into three distinct sections: low-speed design, high-speed design and conformability. Two different designs and sizes are manufactured and tested and compared to calculated values. Analytical, lumped parameter and finite difference approaches are used to model the bearing behavior. The validity of different models are discussed. Different manufacturing methods are compared by means of statistical model which models the effect of manufacturing errors on the bearing performance. A cost-function approach [Taguchi, 1989] is used to derive a single measure which is then used to compare the different methods. Different applications such as a very small machine tool, high speed milling spindle and linear-rotary axis are discussed.

This thesis will attempt to make the following fundamental contributions:

- Incorporate surface self-compensation technology into a bushing bearing

Surface self-compensating bearings offer great advantages over traditional hydrostatic bearings. They utilize surface geometry for metering the fluid flow (compensation), collecting the fluid and channeling the fluid to the opposite side of the bearing to a pocket region. This design does not use capillaries or diaphragms to achieve load compensation. Everything needed is included in the surface geometry of the bearing. This research will incorporate this technology into a cast or molded bushing bearing to create a versatile and robust hydrostatic bearing. [Slocum, 1992, Wasson, 1996].

- Find economically viable manufacturing methods for the bearing

Manufacturing the bushings is by no means a trivial task because of the fluid circuitry required by the self-compensation.

- Model the bearing performance in the presence of manufacturing and other errors

Different manufacturing methods have different natural variations associated with the accuracy they can produce. These manufacturing errors can be best described in statistical terms because of their inherent randomness. Monte-Carlo and cost function approach is used to derive a single numeric value which can be used to determine the total expected cost of the bearing. By using this measure to perform the comparison between different manufacturing methods, the comparison becomes more analytic.

- Design adjustable-gap hydrostatic bushing bearing

Self-compensation allows the bearing gap to be changed without changing the designed properties of the bearing. The possibility to adjust the bearing gap is attractive because it allows the adjusting of the flow rate and pumping power and also introduces a possibility to use larger manufacturing tolerances.

· Complement the design theory of surface self-compensated bushings by studying the effect of hydrostatics on journal bearing stability.

Hydrostatic bearing stability is investigated using computational methods at high speed. The possibility to use hydrostatics to enhance the stability of a journal bearing is researched. Different high speed designs are proposed. The shape of the bushing surface can also be designed to enhance the stability [Frene, 1990]. The possibility to conform the bushing to enhance stability will be discussed.

1.2 Background

This section discusses shortly different types of bearings and their applications. First a very general look into bearing technology is taken and then a little more detailed look is taken into fluid film bearings in general and more specific introduction to hydrostatic bearing follows.

1.2.1 Bearing Technology

Bearings are among the most important mechanical machine elements. Their main function is to guide motion and carry load. Other requirements are be speed-, acceleration-, range of motion, stiffness, damping, accuracy, friction, thermal requirements, environmental requirements, size, life time and cost. As broad as are the requirements is the selection from which a designer can select a device to fulfill them. Bearings can be categorized in many ways, the broadest maybe being the division into contact and non-contact bearings. Contact bearings can be further divided into sliding contact, rolling element and flexural bearings. Non-contact bearings include hydrostatic, hydrodynamic, aerostatic and magnetic bearings. All of the above mentioned general types include multiple sub-types or variations. Already it is obvious that the selection is enormous and very specific set of requirements must be formed to end up with an optimum type for a certain application. Comparison in general terms is not possible or fair, since the performance characteristics are so varied. The requirements of the specific application determines the weight of the

different desired qualities and only then the best possible solution for those weights can be found. For example, in machine tool spindles rolling element-, hydrodynamic-, air-, magnetic- and hydrostatic bearings are used. This example proves that even for fairly specific application, machine tool spindle, the choice is far from obvious. In this thesis some comparisons are made and it must be noted that comparison always refers to a certain subset of requirements and should not be generalized.

Next a bit more detailed look is taken into two types of non-contact bearings, namely the hydrodynamic and hydrostatic bearings.

1.2.2 Hydrodynamic Bearings

Hydrodynamic bearings form their load carrying capacity by the pressure rise in a converging oil film. This requires relative motion between the surfaces and the surfaces not being parallel. The reason why hydrodynamic bearings are introduced in this thesis is that the hydrodynamic effect also exists in hydrostatic bearings with varying magnitude and importance. Chapter 4 formulates analytical solutions to the hydrodynamic bearing to demonstrate and approximate its effect on hydrostatic bearing performance.

Hydrodynamic bearings are used as both thrust and journal bearings and in combination. There exists many variations and shapes such as partial arc, full arc, lobed, herring bone and tilting pad hydrodynamic bearings. Different geometrical features or pressurized oil supply can be implemented to make sure load carrying oil film exists everywhere.

Hydrodynamic bearings have many desirable properties. They are self-acting and do not need external sources to operate, they have long life when used properly, they are robust, have high stiffness, damping and load capacity. In some cases they have undesirable properties such as the relative motion required between the surfaces (stop and go applications), instability at high speeds (half frequency whirl), relatively large eccentricities required to achieve load capacity, high viscous drag at high speeds and high temperature rise due to that. Many of these features can be diminished or eliminated by using certain designs, for

example tilting pad bearings are stable (against whirl) at all operating speeds. Naturally there are trade offs between different desired properties and implemented design features. To learn more about hydrodynamic bearings the reader is referred to Chapter 4 or [Frene, 1990].

1.2.3 Hydrostatic Bearings

Hydrostatic bearings are non-contact bearings which use an external pressure source (pump) to create the load carrying capacity. They form the separating lubricant film as soon as the pump is turned on and therefore do not require relative motion between the separated surfaces. Hydrostatic bearings are characterized by infinite life (without catastrophic event), low friction (laminar speeds), zero static friction (no stick slip), high load capacity, stiffness and damping. Also the thermal characteristics are controllable to a certain degree by adjustment of flow rate and lubricant type. The main disadvantage compared to most other type bearings is the complicated (expensive) lubricant supply system. Also, at high speeds, the viscous drag can become relatively high.

Typical Applications of Hydrostatic Bearings

Typical applications for hydrostatic bearings are [Bassani, 1992, Slocum, 1992]

- Telescopes, radio telescopes, large radar antennas. For example the Mount Palomar telescope where hydrostatic bearings support 500 ton mass that makes a one revolution in a day
- Air preheaters for boilers in power plants
- Rotating mills for ores or slags
- Stamping presses
- Machine tool slides and spindles
- Hydrostatic steady rests for large lathes
- Vibration attenuators for measuring instruments
- Dynamometers

Principle of Operation

Figure 1.1 shows the operation of a simple hydrostatic bearing. As a pump is turned on, the pressure in the recess increases until lifting pressure is reached and oil film separates the members. Different loads W lead to different pressures in the recess and different film thicknesses h . In order for the bearing to sustain load in the reverse direction another pad

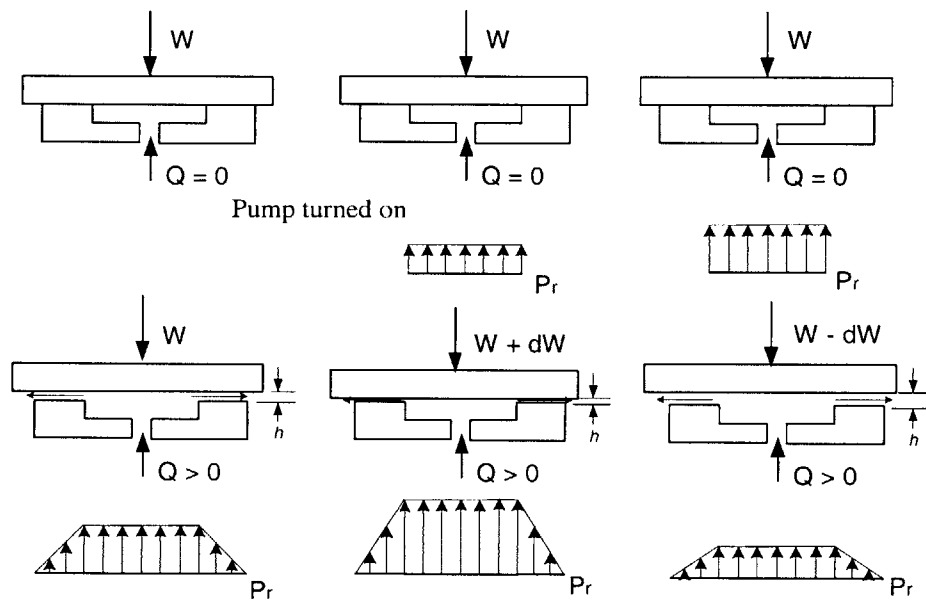


Figure 1.1 Simple hydrostatic bearing. Principle of operation and pressure diagrams

must be added on top as shown in Figure 1.2. Now the bearing is preloaded, since even for zero load the recess pressures are greater than zero. Now as load is applied the pressure increases on the opposite side of the load and equilibrium is achieved. When two or more recesses are used all the recesses must be supplied with their own pressure source, otherwise the recess pressures will always be equal and the bearing is unable to carry any load. This is, in most cases, inconvenient and expensive. Alternatively single pressure source (pump) can be used if each recess is fed through adequate compensating device, which usually is called flow restrictor. The simplest way to demonstrate the need for the compen-

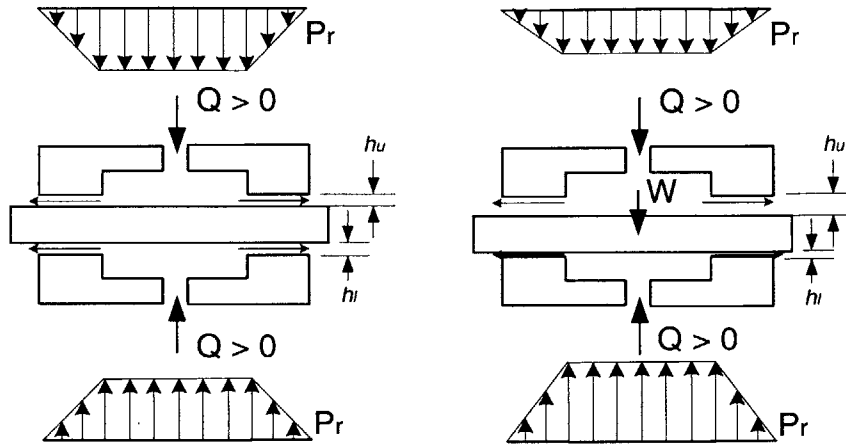


Figure 1.2 Hydrostatic double- or opposed pad bearing and pressure diagrams.

sating device is to use a electrical network analogy. The bearing system can be though of as a simple voltage divider as seen in Figure 1.3.

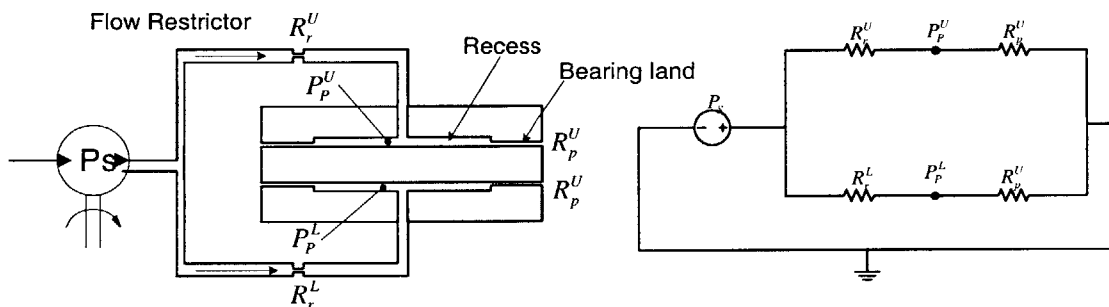


Figure 1.3 Hydrostatic bearing electric circuit analogy

The flow resistances are the pressure difference over that particular part of the bearing divided by the corresponding flow rate. These values can be, in most cases, calculated from fully developed, one dimensional Navier-Stokes equations. The derivation of formulas for these resistances is described in detail in Chapter 3. Here they are treated as given quantities in illustrative purposes. The recess pressures become

$$P_p^i = P_s \frac{R_p^i}{R_r^i + R_p^i} \quad (1.1)$$

where the subscript r refers to restrictor, p to recess (pocket) and the superscript i either to upper or lower recess. The pressure difference and therefore the load carrying force between the upper and lower recess becomes

$$\Delta P = P_s \left(\frac{R_p^l}{R_r^l + R_p^l} - \frac{R_p^u}{R_r^u + R_p^u} \right) \quad (1.2)$$

It is obvious from Equation 1.2 that if the restrictor resistance becomes zero the pressure difference becomes zero also and the bearing is unable to carry any load; thus each bearing recess need its own compensating device or restrictor.

Compensating Devices

Compensating devices can be divided into fixed and variable resistance devices. Constant resistance devices include flat edge pins and capillary tubes. Flat edge pins are devices where a standard round pin is ground to have one flat surface. When this device is pressed into a hole it creates small enough opening to create necessary resistance to the flow. Both of these devices operate in the laminar flow regime and therefore the opening is small compared to the length of the device. The resistance is a function of the device geometry only and is independent of the bearing geometry or supply pressure. The bearing performance is very sensitive to the dimensions of these devices and therefore they must be manufactured with great care. Capillary tubes are difficult to manufacture accurately enough and therefore the resistance must be adjusted by adjusting the length of the capillary tubes. This can be done in a separate test rig or preferably in the actual bearing itself by measuring the bearing pocket pressures and adjusting the capillaries to achieve desired recess pressure [Slocum, 1992]. This can be a tedious process and makes the bearing relatively expensive. Also with these devices the careful filtering of the fluid is necessary due

to the small openings. If one of the capillaries or pins is clogged this will severely impact the bearing performance and in most cases lead to complete failure.

Another compensating device is the orifice restrictor. An orifice is a hole with a sharp edge with a diameter to length ratio that is much larger than in a case of a capillary. The flow resistance is based on the turbulence introduced by the restrictor. In this case the resistance is no longer independent of the recess pressure. The flow rate of these devices changes as a square root of the pressure difference across it. The use of orifices instead of laminar fixed resistance compensating devices yields better stiffness performance but the fluid temperature control becomes more important. This is due to the fact that the recess resistance is a function of the viscosity, but the orifice resistance is not. Therefore if the viscosity varies from the design value so does the load capacity. In fact, if the lubricant temperature is not controlled, but is allowed to grow, will eventually lead to bearing failure. As the temperature increases the load capacity becomes lower causing the film thickness to decrease which introduces more friction, which in turn increases the temperature again. Also the analysis becomes more complicated since the orifice resistance is a function of recess pressure. Turbulence introduced by the orifices also introduces noise and can lead to erosion. [Slocum, 1992, Kurtin, 1993, Bassani, 1992]

Another class of compensating devices are the variable resistance restrictors. With these devices very high stiffness can be obtained, even infinite for a certain load ranges, if properly designed. All of these devices are based on the same principle, which is to increase the flow into the recess where the pressure is increasing therefore increasing the pressure faster and creating equilibrium conditions with less displacement. This results in a higher stiffness. These devices include elastic restrictors, spool-controlled restrictors, diaphragms, constant flow valves, infinite stiffness valves and electronic compensators.

An elastic capillary is a capillary tube that is able expand as the recess pressure increases i.e. capillary made out of low modulus material such as rubber. Another type of elastic restrictor is a ring type restrictor which expands to allow higher flow into pocket where

the pressure is higher. An example of this type of restrictor is described in [Miyasaki, 1974]

Two different variations of a spool valve are shown in Figure 1.4. Device consists of spool which is balanced by a spring and recess pressure. The resistance depends on the length x . As the recess pressure varies the length x varies thus changing the resistance. By making the piston or the spool tapered the change in resistance as x is varies can be made larger thus enhancing the performance.

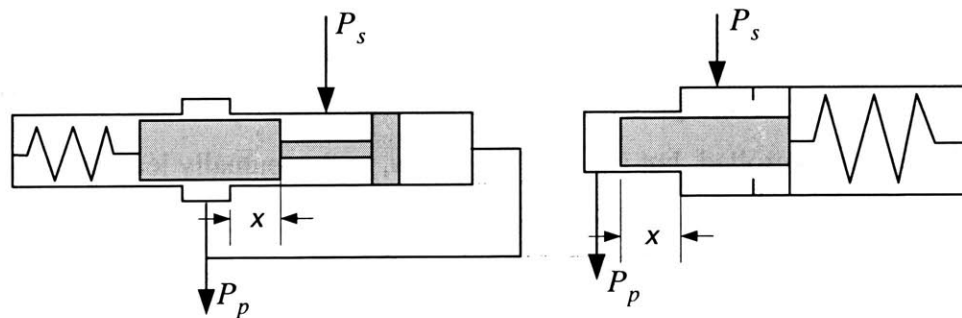


Figure 1.4 Spool valve compensators

A diaphragm restrictor is shown in Figure 1.5. The fluid flow is restricted by means of elastic diaphragm. The preload can be adjusted by means of adjustable spring. In this case the device can be tuned in such way that the flow rate becomes almost proportional to recess pressure. This bearing will work as a infinite stiffness bearing for a certain range of load conditions. Part b) in Figure 1.5 shows a diaphragm used as a flow divider. Flow dividers can be used when fluid is supplied for two opposing pads. Also spool valves can be used as flow dividers.

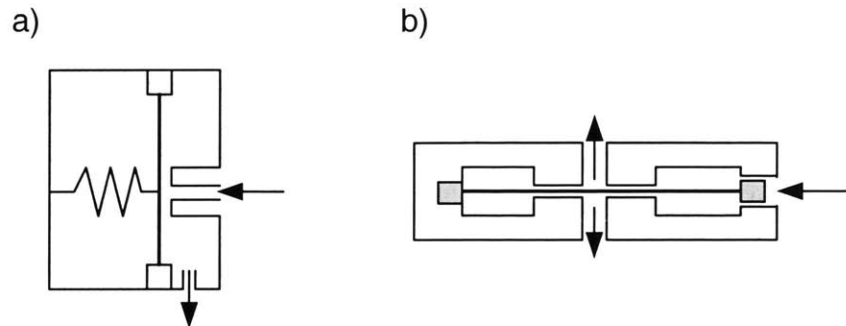


Figure 1.5 a) Diaphragm restrictor b) Diaphragm as a flow divider

Constant flow valves are devices that are able to produce a constant flow. Spool valves in Figure 1.4 can deliver constant flow if properly tuned. To enhance the performance a reference restrictor, such as orifice, can be added downstream. Bearings with constant flow devices are prone to pressure saturation i.e., they do not work if the difference between the recess pressure and the supply pressure becomes too small.

All above mentioned devices operate by means of the recess pressure. This could also be done by means of servo-controlled valves. A displacement probe would measure the displacement of the bearing and a control system would operate the valves accordingly. This system would greatly add to the complexity of the system and has the potential to become unstable unless careful modeling and design is performed.

All of the variable resistance compensating devices add to the complexity of the system and add to the degrees of freedom in the system. All external restrictor devices must be tuned to a certain bearing geometry and are sensitive to manufacturing errors. Many of them also have very small opening which can cause clogging problems unless the fluid is filtered carefully. Hydrostatic bearings which eliminate totally or partially these problems are inherently compensated bearings and self-compensated bearings. More thorough discussion of the typical problems encountered with the external restrictor bearings can be found in Chapter 5.

Inherently compensated bearings are based on principle that the pressure variation in a recess due to load is due to a particular recess shape or the presence of an elastic element, such as a layer of elastomer or a flexible plate. The recess shape utilized is either shallow recess or tapered recess. If the recess depth is initially of the same order as the clearance, the pressure drop in the recess is no longer insignificant. As the load is applied and the clearance reduced the recess clearance becomes less significant and more of the pressure drop happens across the lands thus increasing the load. Figure 1.6 shows the schematic operation of a shallow recess bearing. These bearings are very difficult to manufacture because of the difficulty of making a very shallow recess. In order to overcome this manufacturing problem, bearings made out of elastomers have been proposed [Dowson, 1967]. This bearing consists of an elastomer layer attached to a rigid frame. Since pressure is higher in the middle of the pad and varies toward the edge the elastic material forms a recess. Also some inherent compensating bearings have been proposed that simple integrate either diaphragm or spool valve type behavior into the bearing structure itself [Brzeski, 1979, Tully, 1977].

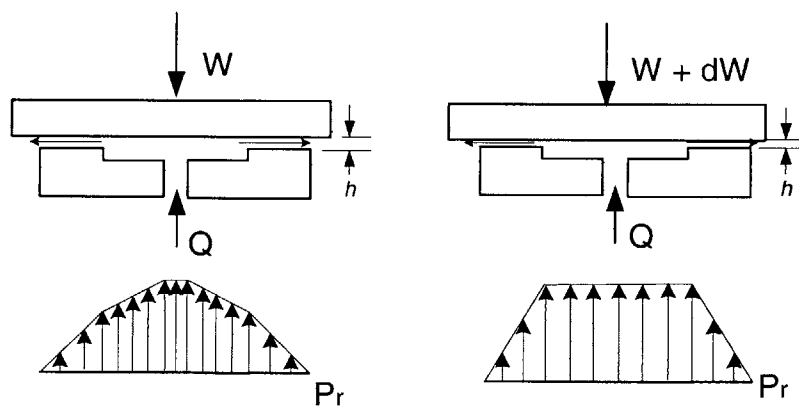


Figure 1.6 Shallow recess hydrostatic bearing

Also reference bearings can be used to adjust the restrictor resistance into a main load carrying bearing. Simplified form of this idea lead us to self-compensated or surface self-

compensated bearings. In these bearings the bearing clearance is used to provide the compensation. This type of bearing is discussed in more detail in Chapter 2.

Chapter 2

SURFACE SELF-COMPENSATION

In this chapter the basic principle of surface self-compensation is explained and several proposed designs are shown.

2.1 Surface Self-Compensating Hydrostatic Bearings

The idea of surface self-compensation is very simple. In most general form the bearing is surface self-compensating if the bearing surface itself is used to provide the necessary hydraulic resistance. By this definition the shallow recess bearings in the last section could be included, but this section is about slightly different designs.

In surface self-compensating bearings, the fluid is first supplied to a compensation pocket and after it flows over compensation pocket lands it is collected and supplied to the opposite side of the bearing into load bearing pocket from where it again flows over lands into atmosphere. The first pocket acts as a compensator, where resistance is not fixed but changes as the supported structure is displaced. Figure 2.1 illustrates the principle of operation.

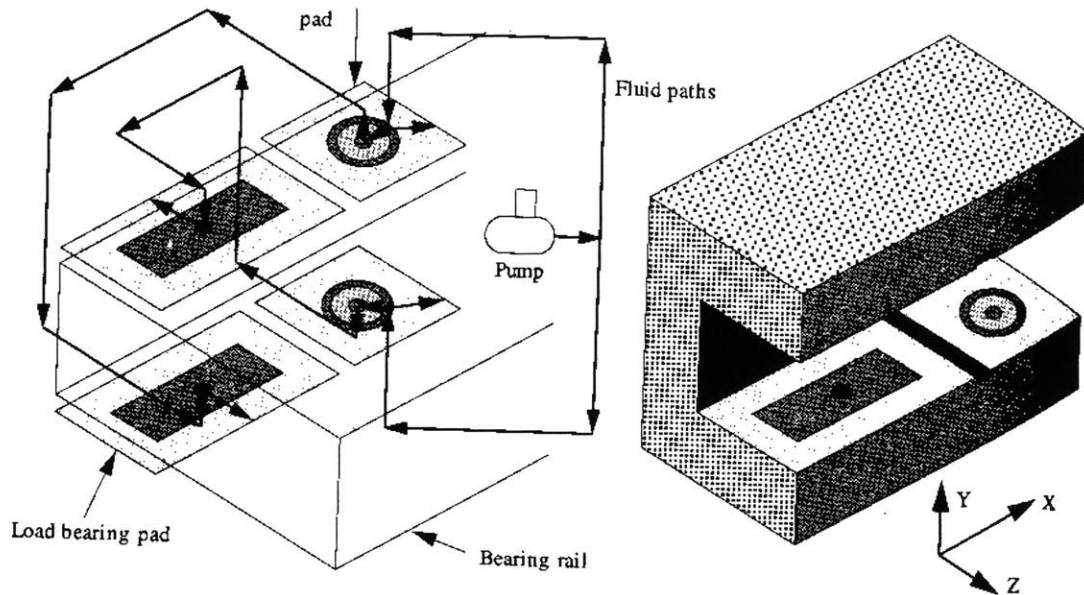


Figure 2.1 Surface self-compensating linear bearing [Slocum, 1992].

The compensator resistance is not constant in this case but varies favorably to enhance the bearing operation. If the supported structure in Figure 2.1 is displaced downwards, the clearance on the upper side increases, causing more fluid to flow through upper compensation pocket (hydraulic resistance decreases). At the same time the clearance on the opposite side decreases causing the hydraulic resistance out of the pocket to increase. The opposite will happen to the other compensator-load recess pair. This will cause the pressure difference to increase more rapidly, resulting in greater stiffness. The major advantage of this type of compensation is the avoidance of matching the restrictor resistances to pocket resistances (they are a function of the same dimension) and the decreased risk of clogging. The clogging risk is decreased because no very small area openings (capillaries) are eliminated. This idea of cross feeding was first introduced in patents by [Hoffer 1948; Gerard 1950 Geary, 1962]. The principle of surface self-compensation is best illustrated by Equation 1.2. When the supported structure is given a displacement δ Equation 1.2 for self-compensated bearings becomes

$$\Delta P = P_s \left(\frac{1}{\zeta \frac{(h-\delta)^3}{(h+\delta)^3} + 1} - \frac{1}{\zeta \frac{(h+\delta)^3}{(h-\delta)^3} + 1} \right) \quad (2.1)$$

where ζ is the initial resistance ratio of the compensator and the pocket. The load capacity is the product of ΔP and the effective area of the bearing pads. The stiffness is obtained by differentiating Equation 2.1 with respect to δ . The stiffness becomes

$$K = A_{eff} \frac{\partial}{\partial \delta} (\Delta P) = P_s A_{eff} \left[\frac{1}{\left[\zeta \frac{(h-\delta)^3}{(h+\delta)^3} + 1 \right]^2} \left\{ 3\zeta \frac{(h-\delta)^2}{(h+\delta)^3} + 3\zeta \frac{(h-\delta)^3}{(h+\delta)^4} \right\} + \dots \right. \\ \left. \frac{1}{\left[\zeta \frac{(h+\delta)^3}{(h-\delta)^3} + 1 \right]^2} \left\{ 3\zeta \frac{(h+\delta)^2}{(h-\delta)^3} + 3\zeta \frac{(h+\delta)^3}{(h-\delta)^4} \right\} \right] \quad (2.2)$$

For a fixed laminar restrictor, the pressure difference and the stiffness become

$$\Delta P_{fixed} = P_s \left(\frac{1}{\zeta \frac{(h-\delta)^3}{h^3} + 1} - \frac{1}{\zeta \frac{(h+\delta)^3}{h^3} + 1} \right) \quad (2.3)$$

$$K_{fixed} = P_s A_{eff} \left[\frac{3}{\left[\zeta \frac{(h-\delta)^3}{h^3} + 1 \right]^2} \zeta \frac{(h-\delta)^2}{h^3} + \frac{3}{\left[\zeta \frac{(h+\delta)^3}{h^3} + 1 \right]^2} \zeta \frac{(h+\delta)^2}{h^3} \right] \quad (2.4)$$

Figure 2.2 shows the load capacity and stiffness as a function of eccentricity δ/h , normalized by the load capacity and the stiffness of a laminar fixed restrictor bearing. The dotted line represents the normalized quantities with $\zeta = 1$ and the solid line $\zeta = 1$ for fixed restrictor and $\zeta = 4$ for self-compensating bearing.

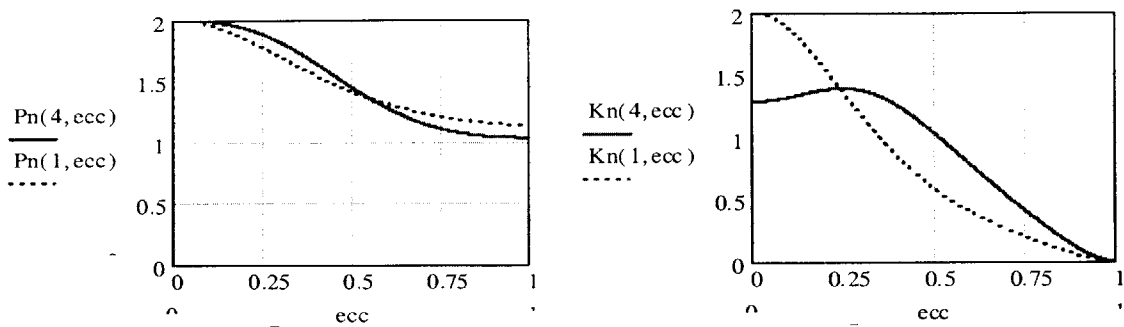


Figure 2.2 Normalized load capacity and stiffness of self-compensating bearing. Normalized by fixed restrictor bearing.

It is clear that the load capacity of a self-compensating bearing is always higher than with a fixed restrictor. The initial stiffness of a self-compensating bearing is twice that of fixed restrictor bearing. As the eccentricity becomes larger the stiffness of a self-compensating bearing drops off more rapidly than that of the fixed restrictor and at higher eccentricities becomes less than that of fixed restrictor. This can be partly effected by adjusting the initial resistance ratio. This has no significant effect in practice because hydrostatic bearings are designed to operate at small eccentricities most of the time. However, this should be taken into account when the bearing is designed. This analysis was for a ideal opposed pad bearing. More detailed look into how a general bearing can be analyzed is presented in Chapter 3.

This self-compensating technology can also be applied to hydrostatic journal bearings. Figure 2.3 shows a cross sectional and developed view of a three pocket surface self-compensating journal bearing [Geary, 1962].

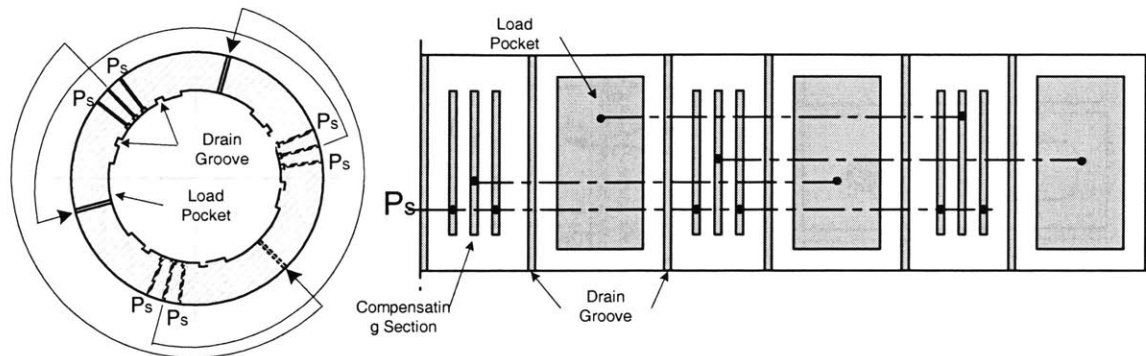


Figure 2.3 Cross sectional and developed view of surface self-compensating journal bearing

Another version of the bearing in Figure 2.3 is shown in Figure 2.4 [Stansfield, 1970]. It is advantageous to minimize the size of the compensating pockets and maximize load carrying pockets. The design of Figure 2.4 is more difficult to design and analyze due to the arrangement of the supply and collecting pockets. The middle section of compensating pocket is at supply pressure and the collecting groove surrounding it is dependent on the eccentricity (location of the shaft). The pressure at the collecting groove then determines the leakage flow out into the drainage grooves. A more deterministic bearing is one where the pressure source surrounds the collecting groove [Slocum 2, 1992]. In this case the outer groove is always at supply pressure and the leakage flow is easier to determine. The journal bearing version of this is shown in Figure 2.5 [Slocum, 1994].

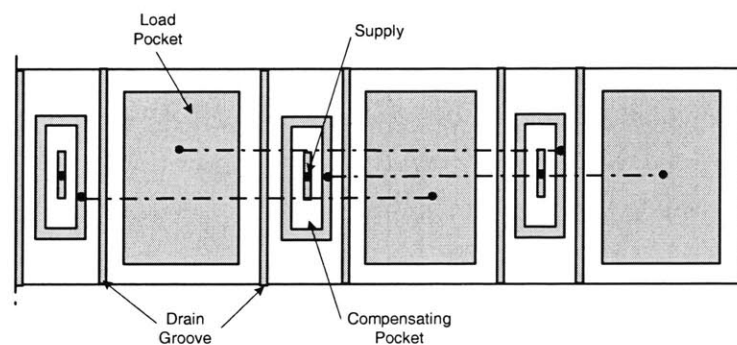


Figure 2.4 Developed view of surface self-compensating bearing

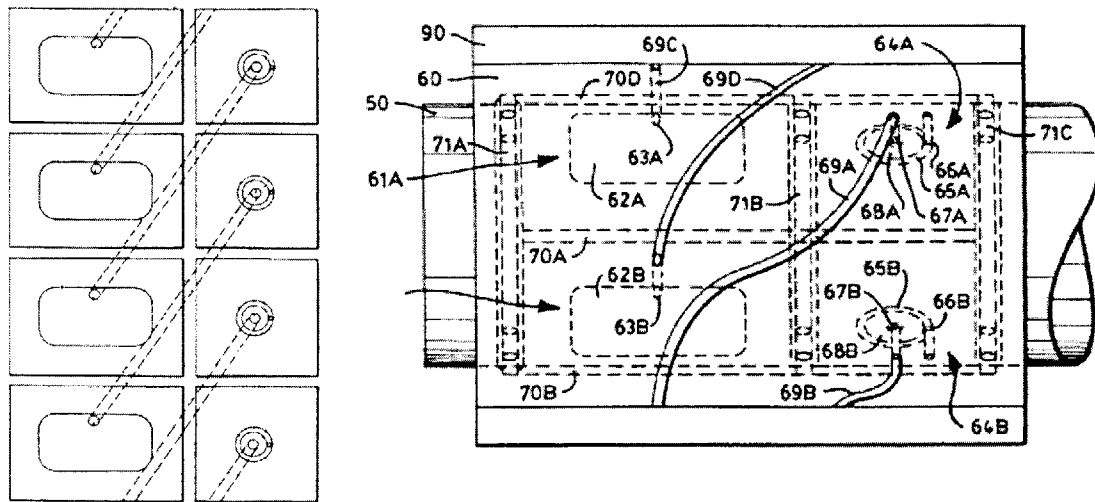


Figure 2.5 Surface self-compensating journal bearing with deterministic compensators [Slocum, 1994]

In this version the compensator pocket is removed to the side from the load carrying pockets. This is advantageous since the diameter of the bearing is, in most cases, more critical than the length of the bearing.

In [Wasson, 1997, Wasson, 1996] surface self-compensating bearings were introduced that had all the necessary geometry integrated into the shaft. This offers few advantages over the previous designs with geometry in the bushings. First, it makes the precision shrink fit unnecessary and second it can make the manufacturing slightly easier and more cost efficient because standard milling tools can be used. Also, in case of cluster spindles, it allows the shafts to be placed closer together by eliminating the need for bushings. Figure 2.6 shows a design where the collector pockets are connected to load pockets by cross drilling through the shaft.

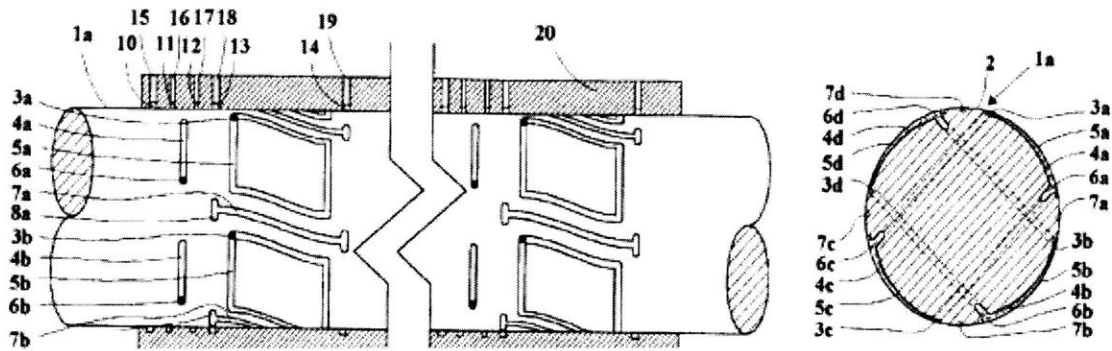


Figure 2.6 Surface self-compensating bearing with cross drilled collectors and load pockets on shaft

An alternative design that has all the fluid circuitry machined on the surface of the shaft including the connecting passages is shown in Figure 2.7. This will introduce more leakage flows, but as is shown in later sections, very good performance can still be achieved. The bearing design manufactured in this work is very close to that in Figure 2.7 except that the geometry is on bushing surface. The reasons to have the geometry on bushing surface are explained in next section.

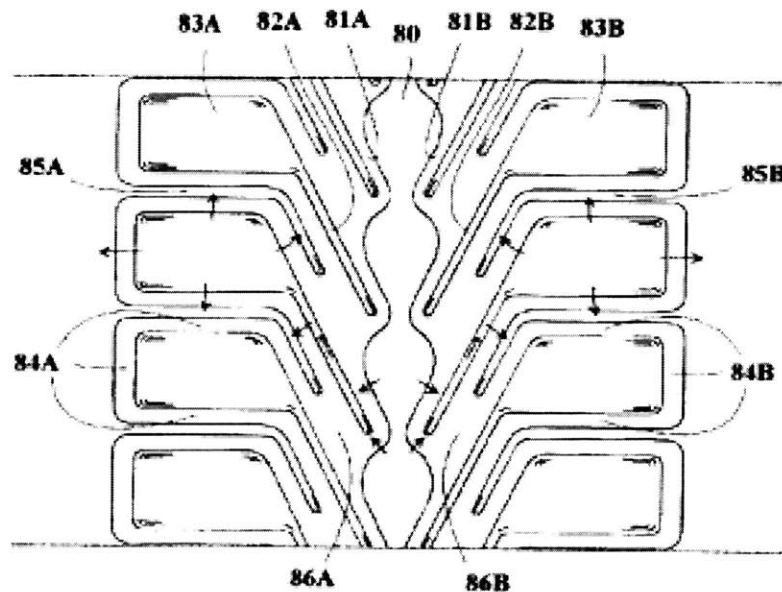


Figure 2.7 Bearing design with all the geometry on the shaft surface

2.2 Why Bushing?

Having the bearing geometry on bushing surface is advantageous in most cases. The advantages are that the bushing can be made out of good bearing material such as bronze and a standard hardened ground steel shaft can be used without any special manufacturing operations. Manufacturing bushings with geometry on the internal surface only is challenge, which is solved in this work. This makes them more cost effective and interchangeable than the shaft design. Also the balancing becomes an issue when multiple features are machined on the rotating member. A bushing also offers more versatility in terms of linear motion. Having the bearing geometry on the rotary member makes the pressure field unsteady even for fixed journal position due to the local variation of film thickness due to rotation. This can have significant effect at larger eccentricities [Zirkelback, 1998]. This makes the resultant force and force coefficients periodic. In short, the advantages of a bushing are the following:

- More cost effective (with mfg. methods introduced in this work)
- More easily replaceable
- More modular
- Better material pairs (unless plain bushing is used with grooved shaft)
- Linear motion capability
- Steady pressure field

Chapter 3

MODELING

In this chapter two different numerical ways of modeling hydrostatic bearings are described. First, a lumped parameter model based on laminar flow between flat plates is described. Then a finite difference solution method for the Reynold's equation is described briefly and its application to certain features of hydrostatic bearings are discussed. The limitations of both methods are also discussed. Results from both methods are compared.

3.1 Lumped Parameter Modeling

In the lumped parameter method the bearing is divided into regions where the flow can be approximated by one dimensional fully developed laminar flow between two plates. If the aforementioned conditions are met and gravity is ignored the Navier-Stokes equation for the flow reduces to [Fay, 1994]

$$\mu \frac{d^2 u}{dy^2} = \frac{dp}{dx} \quad (3.1)$$

By integrating twice and taking into account the non-slip boundary conditions, $u(0) = u(h) = 0$, the velocity becomes

$$u = \frac{1}{2\mu} \left(\frac{dp}{dx} \right) y(h-y) \quad (3.2)$$

By integrating the velocity over the clearance h and multiplying by the width the flow rate is obtained

$$Q = w \frac{h^3}{12\mu} \left(\frac{dp}{dx} \right) \quad (3.3)$$

By integrating the pressure gradient over the length the hydraulic resistance becomes

$$R = \frac{\Delta p}{Q} = \frac{12\mu L}{h^3 w} \quad (3.4)$$

3.1.1 Validity of the Geometric Assumption

In a general case the assumption of flow between parallel plates is not valid, for example in the case of a journal bearing with non zero eccentricity the surfaces are at an angle. First, the hydraulic resistance for a circumferential flow over land is derived and compared to that of Equation 3.4 and then the same is done for axial flow Figure 3.1 describes schematically the situation and the coordinates.

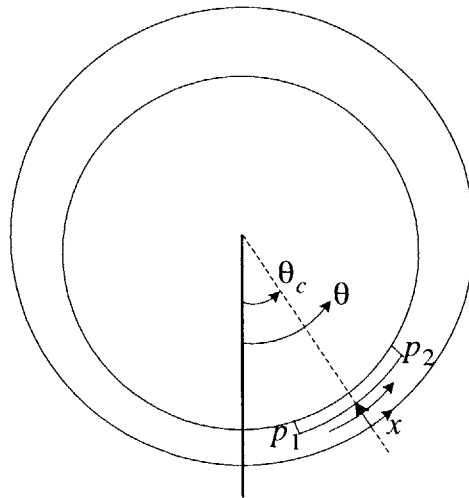


Figure 3.1 Circumferential flow over land in displaced journal bearing

The clearance as function of eccentricity and the location θ_c is

$$h = C \left(1 - \varepsilon \cos \left(\theta_c + \frac{x}{D} \right) \right) \quad (3.5)$$

Where C is the original clearance. By inserting this into Equation 3.3 the pressure gradient becomes

$$\frac{dp}{dx} = -\frac{12\mu Q}{w} \frac{1}{C^3 \left[1 - \varepsilon \cos \left(\theta_c + \frac{x}{D} \right) \right]^3} \quad (3.6)$$

By introducing co-ordinate $\xi = \frac{x}{L}$ the hydraulic resistance becomes

$$R_c = \frac{12\mu L}{wC^3} \int_{-\frac{1}{2}}^{\frac{1}{2}} \frac{1}{\left[1 - \varepsilon \cos \left(\theta_c + \frac{L}{D} \xi \right) \right]^3} d\xi \quad (3.7)$$

Closed form solution to this integral is long and tedious to find. Figure 3.2 shows the hydraulic resistance of Equation 3.7 divided by the nominal resistance of Equation 3.4, evaluated numerically, as function of eccentricity for L/D ratio of 0.1, which is realistic in most cases. Note that this L/D ratio is not the same as the bearing L/D ratio. It can be noted that even for relatively high eccentricity ratios the difference in hydraulic resistance is very small.

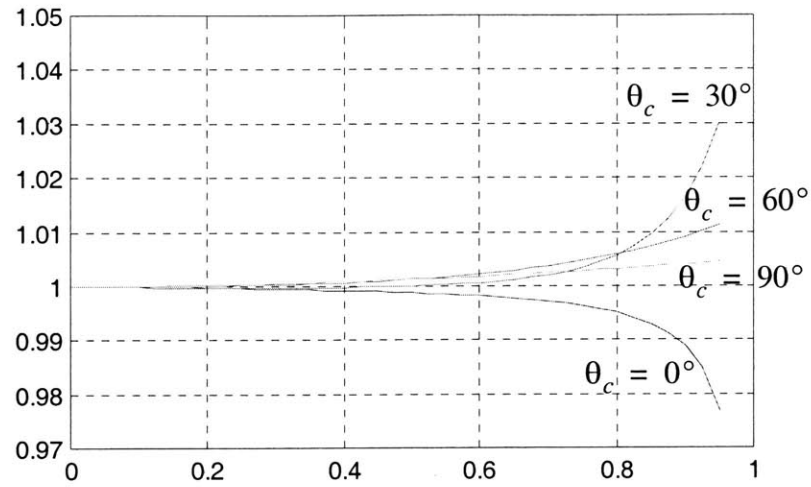


Figure 3.2 Ratio between full solution and flat plate approximation in case of circumferential flow in a journal bearing

In case of a axial flow the pressure gradient is constant and the hydraulic resistance becomes

$$R_a = \frac{12\mu L}{wC^3} \frac{1}{\int_{-\frac{1}{2}}^{\frac{1}{2}} \left[1 - \varepsilon \cos\left(\theta_c + \frac{w}{D}\xi\right) \right]^3 d\xi} \quad (3.8)$$

Figure 3.3 shows the hydraulic resistance of Equation 3.8 divided by the nominal resistance of Equation 3.4, evaluated numerically, as function of eccentricity for L/D ratio of 0.1, which is realistic in most cases. It can be noted that again, even for relatively high eccentricity ratios the difference in hydraulic resistance is very small. It can be concluded that geometric assumption of flow between flat parallel plates is valid for most cases.

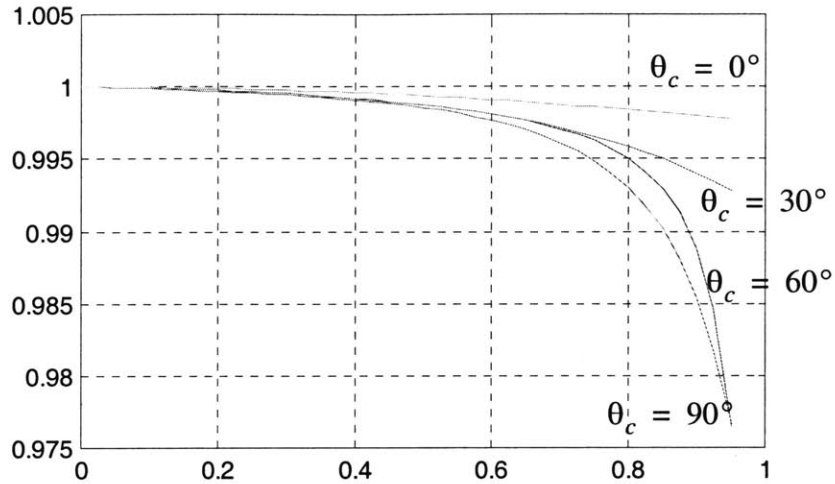


Figure 3.3 Ratio between full solution and flat plate approximation in case of axial flow in a journal bearing

3.1.2 Example Lumped Parameter Model

Here an example of lumped parameter model implementation for a bearing is presented.

The relation of the lumped parameter model to the real geometry is shown in Figure 3.4.

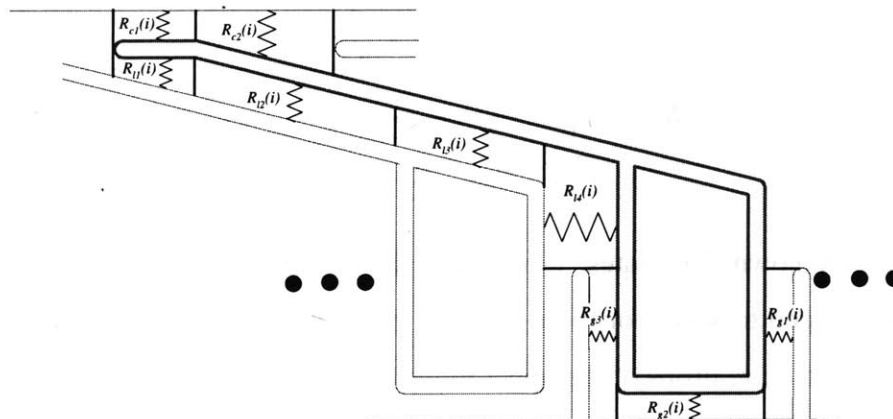


Figure 3.4 Lumped parameter model

The resistor symbols represent the hydraulic resistance of the particular flow path it is placed on. The equivalent resistance network is shown in Figure 3.5.

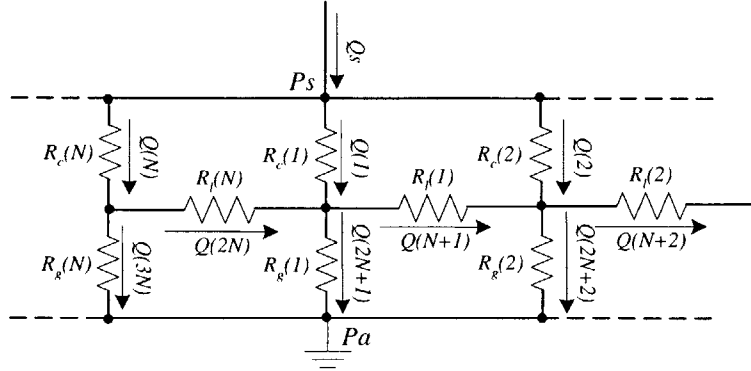


Figure 3.5 Equivalent circuit

The resistances R_c , R_l and R_g of Figure 3.5 are the equivalents of the multiple parallel resistances

$$R_c = \frac{1}{\frac{1}{R_{c1}} + \frac{1}{R_{c2}}} \quad (3.9)$$

$$R_l = \frac{1}{\frac{1}{R_{l1}} + \frac{1}{R_{l2}} + \frac{1}{R_{l3}} + \frac{1}{R_{l4}}}$$

$$R_g = \frac{1}{\frac{1}{R_{g1}} + \frac{1}{R_{g2}} + \frac{1}{R_{g3}}}$$

There are $3N$ unknown flow rates, where N is the number of pockets in a bearing. $3N$ equations are needed to solve for these $3N$ flow rates. First, N equations are obtained by setting the total pressure drops of the upper loops to zero.

$$R_c(i)Q(i) + R_lQ(N+i) - R_c(i+1)Q(i+1) = 0 \quad i=1,2,\dots,N \quad (3.10)$$

The second set of N equations are obtained by setting the flow rates into each central node to zero (Kirshoff's law)

$$Q(i) + Q(N + i - 1) - Q(2N + i) - Q(N + i) = 0 \quad i=1,2,\dots,N \quad (3.11)$$

The third set of equations is obtained setting the pressure drop across the compensators and pocket land equal to the difference between the supply and atmospheric pressure.

$$R_c(i)Q(i) + R_g(i)Q(2N + i) = P_s - P_a \quad i=1,2,\dots,N \quad (3.12)$$

By simultaneously solving the Equations 3.10, 3.11 and 3.12 the unknown flow rates are obtained. Once the flow rates are obtained the pocket pressures are

$$P(i) = P_s - R_c(i)Q(i) \quad i=1,2,\dots,N \quad (3.13)$$

Once the pressures are known the effective or average pressure on each land can be calculated. This average pressure times the area of each land is the force on each land. These forces can then be divided into components according to whichever co-ordinate system is chosen and then summed to obtain the resulting bearing force. The algorithm for solving the bearing force is the following

- input bearing geometry and displacement
- calculate the hydraulic resistances for each land patch according to Equation 3.4
- Form the system of equations to solve for flow rates (Equations 3.10-3.12)
- Solve for the flow rates
- Calculate the pocket pressures according to Equation 3.13
- Form the pressure field in the bearing
- Integrate the pressure field to obtain bearing force

3.2 Finite Difference Modeling

The Reynolds equation is the governing equation for fluid flow in thin gaps. The generalized form of Reynolds equation in x, z coordinate (y is in the direction of film thickness) is [Pinkus, 1961]

$$\frac{\partial}{\partial x} \left(\frac{\rho h^3 \partial p}{\mu \partial \theta} \right) + \frac{\partial}{\partial z} \left(\frac{\rho h^3 \partial p}{\mu \partial z} \right) = 6(U_1 - U_2) \frac{d}{dx} (\rho h) + 12\rho V_0 \quad (3.14)$$

where U_1 and U_2 are the velocities of the surfaces and V_0 is the velocity at which they approach each other. In most cases the other surface is stationary and in a case of steady loading with incompressible lubricant Equation 3.14 reduces to

$$\frac{\partial}{\partial x} \left(\frac{h^3 \partial p}{\mu \partial x} \right) + \frac{\partial}{\partial z} \left(\frac{h^3 \partial p}{\mu \partial z} \right) = 6U \frac{dh}{dx} \quad (3.15)$$

This can be divided into finite differences

$$\begin{aligned} \frac{\partial}{\partial x} \left(h^3 \frac{\partial p}{\partial x} \right) &= \frac{h^3_{i,j+\frac{1}{2}} \left(\frac{P_{i,j+1} - P_{i,j}}{\Delta x} \right) - h^3_{i,j-\frac{1}{2}} \left(\frac{P_{i,j} - P_{i,j-1}}{\Delta x} \right)}{\Delta x} \\ \frac{\partial}{\partial z} \left(h^3 \frac{\partial p}{\partial z} \right) &= \frac{h^3_{i+\frac{1}{2},j} \left(\frac{P_{i+1,j} - P_{i,j}}{\Delta z} \right) - h^3_{i-\frac{1}{2},j} \left(\frac{P_{i,j} - P_{i-1,j}}{\Delta z} \right)}{\Delta z} \\ \frac{dh}{dx} &= \frac{h_{i,j+\frac{1}{2}} - h_{i,j-\frac{1}{2}}}{\Delta x} \end{aligned} \quad (3.16)$$

A schematic grid is shown in Figure 3.6.

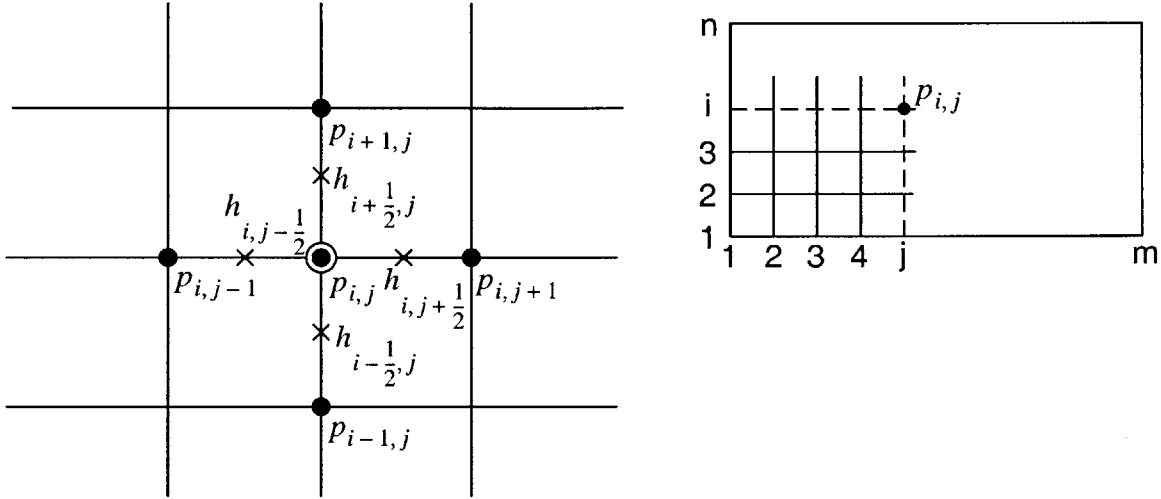


Figure 3.6 Finite difference grid

The clearance can be computed between the pressure points by interpolating between the clearances at the pressure points. Substituting Equations 3.16 into Equation 3.15 and solving for $p_{i,j}$ the following equation is obtained

$$p_{i,j} = a_0 + a_1 p_{i+1,j} + a_2 p_{i-1,j} + a_3 p_{i,j+1} + a_4 p_{i,j-1} \quad (3.17)$$

where a_0, a_1, a_2, a_3, a_4 are given constants for each point and are

$$a_0 = 6\mu U \frac{\left(h_{i,j-\frac{1}{2}} - h_{i,j+\frac{1}{2}} \right)}{\Delta x b} \quad (3.18)$$

$$a_1 = \frac{h_{i+\frac{1}{2},j}^3}{\Delta z^2 b}, \quad a_2 = \frac{h_{i-\frac{1}{2},j}^3}{\Delta z^2 b}$$

$$a_3 = \frac{h_{i,j+\frac{1}{2}}^3}{\Delta x^2 b}, \quad a_4 = \frac{h_{i,j-\frac{1}{2}}^3}{\Delta x^2 b}$$

$$b = \frac{h_{i+\frac{1}{2},j}^3 + h_{i-\frac{1}{2},j}^3}{\Delta x^2} + \frac{h_{i,j+\frac{1}{2}}^3 + h_{i,j-\frac{1}{2}}^3}{\Delta z^2}$$

The pressure at each point is a function of the above stated constants and the four surrounding pressures. For n times m mesh of points this leads to nm simultaneous equations, which can be solved iteratively by mathematical relaxation methods or by Gauss-Seidel iteration, or by using matrix methods (for example as presented in [Lund, 1978]).

If the iterative process is used, a criteria for stopping the iteration must be determined. [Pinkus, 1961] suggest the following criteria: iteration can be stopped when

$$\frac{\sum_{i=1}^m \sum_{j=1}^n |(p_{i,j})^k - (p_{i,j})^{k-1}|}{\sum_{j=1}^m \sum_{i=1}^n (p_{i,j})^k} < A \quad (3.19)$$

where k is the number of iterations performed and it is recommended that A is on the order of 0.0005. Other criteria could also be used such as determining the largest allowable individual change in pressure point by point. After the pressure field is calculated it is integrated to obtain load. The pressure field due to V can be obtained similarly, but in this case Equation 3.14 must be used instead of Equation 3.15.

In order to obtain the dynamic coefficients or the stiffness and damping coefficients either a perturbation method or numerical integration can be used. In numerical integration a small displacement and velocity is given about the equilibrium point and the resulting changes in force are calculated. The force obtained is then divided by the given small displacement or velocity to obtain the stiffness and damping coefficients. In the perturbation method the pressure of Equation 3.14 is given the following first order perturbation

$$p = p_0 + p_x \Delta x + p_y \Delta y + p_x \dot{\Delta x} + p_y \dot{\Delta y} \quad (3.20)$$

which results in the following system of equations in a case of journal bearing [Lund, 1978]

$$\left[\frac{1}{R^2} \frac{\partial}{\partial \theta} \left(\frac{h^3}{\mu} \frac{\partial}{\partial \theta} \right) + \frac{\partial}{\partial z} \left(\frac{h^3}{\mu} \frac{\partial}{\partial z} \right) \right] \begin{bmatrix} p_0 \\ p_x \\ p_y \\ p_x \\ p_y \end{bmatrix} = \begin{bmatrix} 6\omega \frac{\partial h}{\partial \theta} \\ -6\omega \left(\sin \theta + 3 \frac{\cos \theta \partial h}{h \partial \theta} \right) - \frac{h_0^3}{4\mu R^2} \frac{\partial p_0}{\partial \theta} \frac{\partial}{\partial \theta} \left(\frac{\cos \theta}{h_0} \right) \\ -6\omega \left(\cos \theta + 3 \frac{\sin \theta \partial h}{h \partial \theta} \right) - \frac{h_0^3}{4\mu R^2} \frac{\partial p_0}{\partial \theta} \frac{\partial}{\partial \theta} \left(\frac{\sin \theta}{h_0} \right) \\ \cos \theta \\ \sin \theta \end{bmatrix} \quad (3.21)$$

Once the all the pressures are solved they can be integrated to obtain the stiffness and damping coefficients.

3.2.1 Bearing Geometry Generation

In order to efficiently analyze a multitude of bearings and to use finite difference solutions as a design tool a convenient way to generate the bearing geometry was needed. A MATLAB script was written which generates the bearing geometry and then writes it to a file. This .m file is shown in Appendix B.

In order to model bearings where flow occurs also outside the bearing i.e. bearing where the flow between pockets and restrictors is directed outside the bearing bore (back groove designs) a special technique is needed. A approximate model can be done by assigning each recess (both the load and the restrictor recess) a pump and capillary restrictor. Then by calculating the resistance of the restrictor recess, a equivalent capillary restrictor can be assigned to each load carrying recess. Each restrictor recess is assigned a large capillary which has negligible resistance. Then a solution is calculated and the pressures in each load carrying recess is obtained and then assigned to the respective restrictor recess. This way a approximate and fairly accurate approximation can be obtained. Only major drawback is that the numerical differentiation scheme to obtain stiffness is not any longer reliable. The MATLAB script which creates geometry and input files for this case are shown in appendix B.

3.2.2 Validity of the Finite Difference Solution

Solution to basic Reynolds equation is very well known and good agreement between experimental and calculated solutions have been obtained. The solution becomes less accurate when turbulence and deep grooves are introduced in the solution domain. In this section the effect of deep grooves and turbulence is determined and conclusions are drawn on the validity of the solutions with certain parameters.

Maximum Groove Depth Test

When the solution domain (the bearing) has grooves in its geometry, a few things have to be taken into account. First, if the clearance is interpolated between the clearance in the pressure points the location of pressure points can become very important. Figure 3.7 illustrates this point. If the grid is not dense enough and the pressure point is located at the groove edge, the interpolation will lead to grooves that appear too wide. This effect can be minimized by using denser mesh and by locating points close to the groove edge as seen in Figure 3.7 b)..

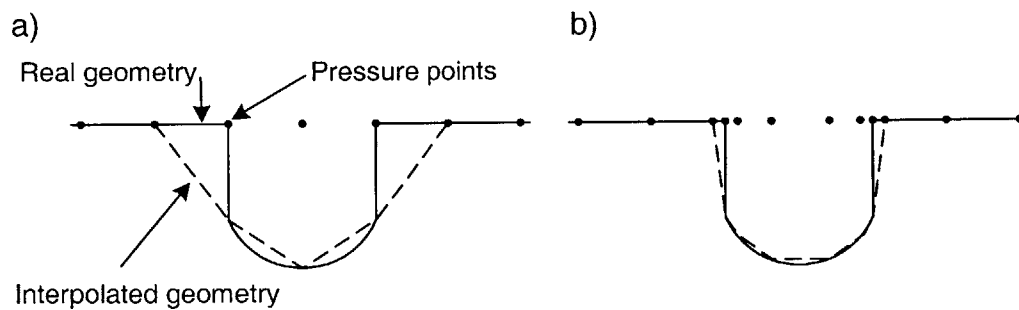


Figure 3.7 a) Too coarse mesh results in wider than real grooves, b) Points close to groove edge result in better interpolation of real geometry

Another issue with the grooves is their depth. The bearing which is to be modeled has multiple surface grooves whose depth are 10-30 times the clearance. Since the equation and its finite difference approximation has terms proportional to h^3 , it is possible that the solution will yield erroneous results if the ratio between the clearance and groove depth is too large (as will be seen later a ratios of 10-15 can still yield relatively good results). Also the assumptions made in deriving the Reynolds equation includes the assumption of small lubricant film thickness. To test these effects, a simple model, seen in Figure 3.8, is constructed.

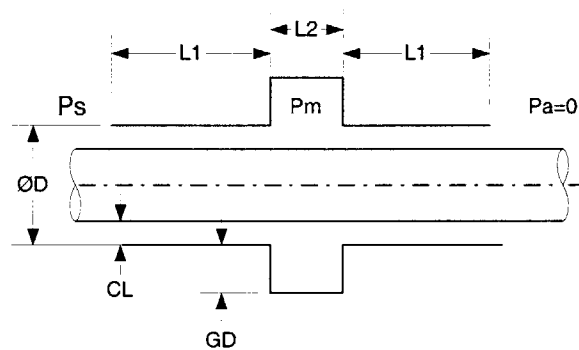


Figure 3.8 Groove depth test case

For the fully developed laminar case the pressure drop in the large gap can be ignored. For the plane Poiseuille flow between two flat plates (the curvature is very large compared to the clearance and can be ignored) the flow rate is [Fay, 1994]

$$Q = \pi D \frac{h^3}{12\mu L} \Delta P \quad (3.22)$$

By equating the flow into the large gap and out of the gap the pressure in the middle portion becomes

$$P_M = \frac{1}{2} P_S \quad (3.23)$$

To justify the assumption of fully developed laminar flow Table 3.1 summarizes the Reynolds numbers and entrance length [Shah, 1978] of the three test cases.

TABLE 3.1 Reynold's numbers and entrance length for the test case

D (mm)	$Re = \frac{\rho Vh}{\mu}$	$L_e = 0.011DRe$ (μm)
10	0.13	14.3
30	0.39	128.7
63.5	0.83	579.8

The entrance length for the largest diameter case is about 5% of the length of the annulus. It can be concluded that the fully developed laminar flow is a valid approximation for this case.

Table 3.2 shows the calculated pressures in the mid section of the model for different groove depths and diameters. The clearance value used in this test is 25 μm , which is a typical value for a hydrostatic bearing

TABLE 3.2 P_m for different groove depths and diameters

GD/CL	P_m/P_s ($D=10$ mm)	P_m/P_s ($D=30$ mm)	P_m/P_s ($D=63.5$ mm)
5	0.493	0.495	0.495
10	0.47	0.47	0.47
15	0.40	0.42	0.43
20	0.38	0.34	0.37
30	0.24	0.28	0.28

The groove depth should not exceed 15 times the clearance in any case and should preferably be about 10 times the clearance, otherwise the pressure drop across the bearing lands becomes too large. Shallower than actual grooves introduce other types of errors, namely too shallow grooves may result in significant pressure drop in them and also the pressure gradient due to fluid recirculation becomes large. Therefore it is desirable to have the computational groove depth as large as possible but not exceeding 15 times the clearance. Obviously if the real bearing groove depth is shallower than that then the real value should

be used. To further illustrate the point, the lumped parameter model results are compared with finite difference model for stationary bearing.

The first measure to compare between the two models is the initial pocket pressure ratio (Table 3.3) i.e. the pressure in the pocket region with $\varepsilon = 0$ and zero speed (this comparison is entirely for zero operating speed) divided by the supply pressure. The reason for the slight difference is the too large pressure drop across axial lands and that the lumped parameter model is not exact either.

TABLE 3.3 Initial pocket pressure ratios for the two models

	Lumped parameter model	Finite difference model	Difference
P_i/P_s	0.36	0.32	11%

In Figure 3.9, the bearing load for both the lumped parameter and finite difference models are plotted against the eccentricity ratio. The reason the load is a less for the finite difference model is the one discussed earlier i.e., the pressure drop across lands is too large. Also the lumped parameter model might be a little too idealized and therefore yields too large values. The agreement is therefore entirely satisfactory.

Next, the effect of groove depth to recirculation pressure gradient is investigated. In [Wasson, 1994, Wasson, 1996] a formulation for the pressure gradient due to recirculation in the grooves was developed. The following system of equations can be solved for friction factor C_f and shear stress ratio n .

$$\ln\left(Re_p \sqrt{\frac{C_f}{2}}\right) = \frac{-n^3 + 3n^2 + n + 1}{2n^2} + \kappa \frac{(1 - 2n^2)}{6nC_c} - \kappa C - \ln(n) \quad (3.24)$$

$$\sqrt{\frac{2}{C_f}} = C(1 - n) + \frac{1 - n}{\kappa} \ln\left(Re_p \sqrt{\frac{C_f}{2}}\right) - \frac{n}{\kappa} \ln(n) + \frac{(n^2 + 1)(1 - n)}{n\kappa} + \frac{1 - n^2}{2C_c} \quad (3.25)$$

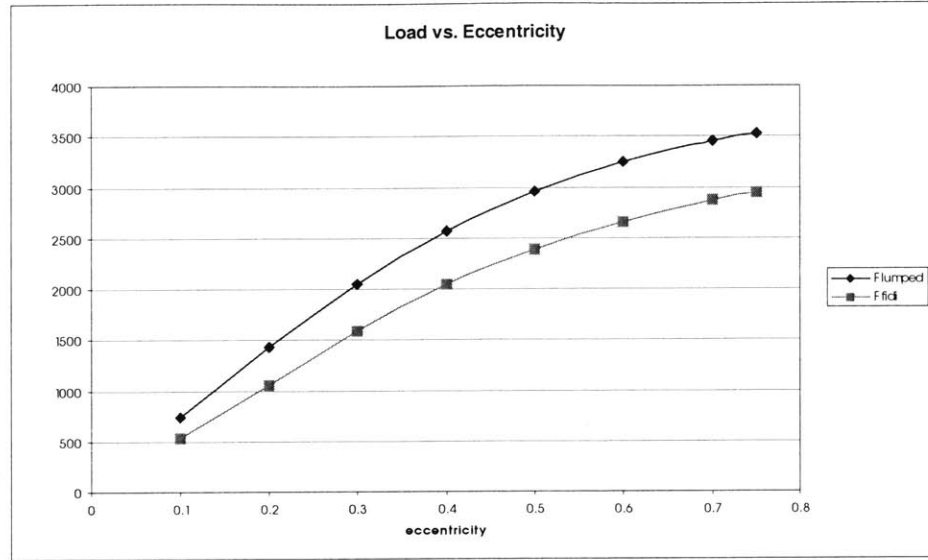


Figure 3.9 Bearing force as function of eccentricity ratio

where κ is von Karmann's constant ($=0.42$), Re_p is the Reynolds number in the groove or pocket, C is log-law constant ($=5.43$) and C_c is a constant that was empirically determined to be equal to -0.17 in [Wasson, 1994]. These friction factors are derived for smooth surfaces. For a turbulent pipe flow the significant differences in friction factors start to occur when surface roughness to pipe diameter ratio is about 0.01 and Reynolds number approximately 100000 [Fay, 1994]. These conditions are rarely met in bearings. Some possible situations and possible effects are discussed in design and future work sections. By substituting C_f and n into following equations the fully developed turbulent pressure gradient can be found.

$$\left(\frac{dp}{dx}\right)_f = \rho \cdot \frac{u_t^2}{h_p} (n^2 + 1); \quad n = \frac{u_b}{u_t}; \quad u_t = \sqrt{\frac{\tau_t}{\rho}}; \quad u_b = \sqrt{\frac{\tau_b}{\rho}} \quad (3.26)$$

To account for the effect of the fluid turning at the leading and trailing edge of the pocket, the following relation may be used [Wasson, 1994, Wasson, 1996].

$$\frac{dp}{dx} = \left(\frac{dp}{dx}\right)_f \left\{ 1 + \ln \left[1 + 2.71 Re_p^{-0.134} \left(\frac{h_p}{L_p} \right)^{3.51} Re_p^{-0.131} \right] \right\} \quad (3.27)$$

In Figure 3.10 the variation in recirculation pressure gradient as a function of groove depth for a typical bearing is plotted. It can be concluded that for deep grooves the value of the pressure gradient does not change significantly after about 10 times the clearance. Also for narrow grooves the pressure rise or drop is insignificant. I

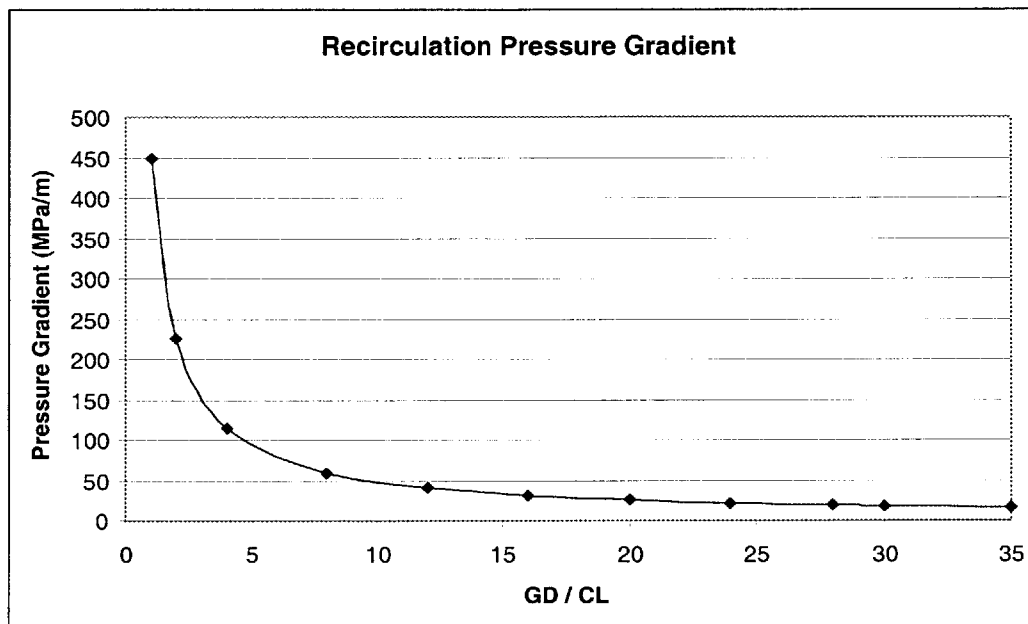


Figure 3.10 Variation of the recirculation pressure gradient with groove depth

As a conclusion the grooves should have maximum depth of 10-15 times the clearance. This can introduce slight errors in the results, but as long as this is realized the results can still be used.

3.2.3 Turbulence Modeling

Turbulence is an inherently chaotic phenomenon and can only be modeled in a statistical or approximate sense. In lubrication problem, this is usually done by so-called friction factors. These friction factors are a function of the local Reynolds number and they are used to modify the Reynolds equation. The derivation of these friction factors is beyond the

scope of this thesis, but the validity of the assumptions made by the primary finite difference code used in this work is of interest. The friction factors used are based on [Constantinescu, 1968, Elrod, 1967]. These friction factors approach the experimentally obtained factor asymptotically for high and low Reynolds number. Agreement in the transitional Reynold's number (1000-10000) is fairly poor, specially in a case of a Poiseuille (pressure driven) flow [Elrod, 1967]. Fortunately, turbulent Poiseuille flow is not typically encountered in bearings, but it is still of interest to know how accurately the turbulent flow can be predicted. To investigate this, the results calculated by the finite difference code are compared to analytical solutions based on bulk flow friction factors developed in [Hirs, 1973]. The bulk flow friction factors have better accuracy in transitional flow.

The mean velocities can be found by solving the following system of equations.

$$\frac{-h^2 \partial P}{\mu U \partial x} \left(\frac{\mu}{\rho U h} \right)^{1+m_0} = \frac{1}{2} n_0 \left\{ U_x (U_x^2 + U_y^2)^{\frac{1+m_0}{2}} + (U_x - 1) [(U_x - 1)^2 + U_y^2]^{\frac{1+m_0}{2}} \right\} \quad (3.28)$$

$$\frac{-h^2 \partial P}{\mu U \partial y} \left(\frac{\mu}{\rho U h} \right)^{1+m_0} = \frac{1}{2} n_0 \left\{ U_y (U_x^2 + U_y^2)^{\frac{1+m_0}{2}} + U_y [(U_x - 1)^2 + U_y^2]^{\frac{1+m_0}{2}} \right\} \quad (3.29)$$

where $U_x = \frac{u_x}{U}$, $U_y = \frac{u_y}{U}$ are the normalized (by surface speed U) mean velocities. For the case of $e = 0$ (shaft is centered in the bore) the $\frac{\partial P}{\partial x} = 0$ and the left hand side of the Equation 3.28 becomes zero. The equations can be further simplified by noticing that the x-direction velocity profile is skew symmetric and therefore the mean velocity $U_x = 0.5$. The constants $m_0 = -0.25$ and $n_0 = 0.066$ are for smooth surfaces with Reynold's numbers smaller than 10^6 [Hirs, 1973].

The test model for this case is a simple centered annulus with pressure difference between two sides.

Table 3.4 gives the dimensions for the two different cases.

TABLE 3.4 Dimensions for the two different test cases

Dimension	Case #1	Case #2
D	76.2 (mm)	76.2 (mm)
h	0.0762 (mm)	0.02 (mm)
ΔP	$2.78 \cdot 10^6$	$2.78 \cdot 10^6$
μ	0.000398	0.000398
ρ	977	977
L	24.6 (mm)	24.6 (mm)
$Re_{\Delta P} @ 0 \text{ rpm}$	6400	465

In Case #1 the flow due to the pressure gradient is turbulent or in the transitional region. In Case #2 the axial flow is laminar.

In Table 3.5 comparison between the analytical calculations based on Equations 3.28 and 3.29 and the finite difference calculations are made for Case #1.

TABLE 3.5 Comparison of flow rates for Case #1

rpm	Analytical /4/	Finite Difference /3/	Difference	Re_{axial}	Re_{circum}
0	37.7 l/min	150 l/min	298%	6400	0
15 000	32.6 l/min	40.4 l/min	24%	5500	11200
30 000	23.9 l/min	25.2 l/min	5.4%	4000	22400

The error decreases as the Reynolds number increases as can be expected. The extremely large error for the 0 rpm case shows that the program does not take into account the turbulence generated by the pressure gradient and the 150 l/min flow rate corresponds to the laminar case. It is also to be expected that the flow rates calculated by the program are higher since the two Reynold's numbers are of the same order of magnitude and the other gets ignored by the program.

In Table 3.6 comparison between the analytical calculations based on Equations 3.28 and 3.29 and the finite difference calculations are made for Case #2.

TABLE 3.6 Comparison of flow rates for Case #2

rpm	Analytical /4/	Finite Difference /3/	Difference	Re_{axial}	Re_{circum}
0	2.72 l/min	2.72 l/min	0%	465	0
10 000	2.63 l/min	1.82 l/min	31%	440	1960
20 000	1.66 l/min	1.34 l/min	19%	280	3920
30 000	1.23 l/min	1.05 l/min	15%	207	5880
100 000	0.502 l/min	0.500 l/min	0.4%	84	19580

Again the results get better as the speed is increased. This time the flow calculated by the finite difference program is lower than the flow calculated analytically.

This test case shows that the results obtained in the transitional region are not very accurate and must be interpreted with care. It also shows that the program ignores any turbulent effects created by pressure driven flow and therefore if such conditions exist results obtained can be very erroneous. Fortunately this is not usually the case. It must be noted that the analytical solution is also just an approximation; the transitional flow is very difficult to predict accurately.

In conclusion, the finite difference code used can predict the bearing performance with satisfactory accuracy. Care must be taken when the results are interpreted, especially in the transitional flow region. To check some results when the bearings are designed, also other finite difference based code was also used, which used the bulk flow friction factors. This code was very slow and has numerical stability problems, so it was not utilized more than just to check some results in the transitional flow region. More about this is discussed in the high speed design section.

Chapter 4

ANALYTICAL CONSIDERATIONS

In this chapter the static and dynamic characteristics of a plain journal bearing and restrictor compensated hydrostatic bearings are analyzed. First, an analytical approach is used to approximately determine the characteristics of a plain journal bearing. This is necessary to see how accurately surface self-compensating bearings hydrodynamic characteristics can be approximated with plain bearing theory. It can be assumed that the plain journal bearing represents the upper bound of damping achieved by surface compensated bearings. Similarly, the deep pocket hydrostatic bearings can be thought to represent the lower bound. In addition, the approximate magnitude of the hydrodynamic effect can be determined from the static analytical solution. These results can be later used as design aids to help guide the initial bearing design under given conditions or given requirements. Also, the criteria for bearing stability will be derived with certain assumptions. A numerical (finite difference) approach is then used, in Chapter 5, to determine the characteristics of a particular design. Conclusions are drawn regarding the validity of the analytical solutions and the extent they can be used as design aids of the bearings. These results are derived in non-dimensional form so that they are as general as possible.

4.1 Static characteristics of a plain journal bearing

The load capacity and the attitude angle (the angle between the load and line of centers) describe the static characteristics of a fluid film bearing. To assess these quantities the Reynolds equation (Equation 4.1) must be solved.

$$\frac{1}{R^2} \frac{\partial}{\partial \theta} \left(\frac{h^3}{\mu} \frac{\partial p}{\partial \theta} \right) + \frac{\partial}{\partial z} \left(\frac{h^3}{\mu} \frac{\partial p}{\partial z} \right) = 6\omega \frac{dh}{d\theta} \quad (4.1)$$

Equation 4.1 is in θ, z coordinate system and R is the radius of the bore and ω the rotational speed. The more general form of the equation is shown in previous chapter. This equation has closed form analytical solutions in only a few simple cases. Sommerfeld solved this equation by neglecting axial flow, which is same as to assume an infinitely long bearing. The other solution is to assume the opposite, namely assuming infinitely short bearing by neglecting the circumferential term. This solution is not satisfactory analytically, but is shown to correspond well to the physical situation [Frene, 1990].

4.1.1 Infinitely long bearing

When L/D is large, the axial flow can be neglected and the Reynolds equation simplifies into:

$$\frac{1}{R^2} \frac{\partial}{\partial \theta} \left(\frac{h^3}{\mu} \frac{\partial p}{\partial \theta} \right) = 6\omega \frac{dh}{d\theta} \quad (4.2)$$

In practice this is a satisfactory assumptions if $L/D > 4$ [Frene, 1990]. The first solution to this equation was presented by Sommerfeld; it is very well known and will be presented here only in broad detail.

Sommerfeld's solution

Assuming that the bearing fluid is supplied via an infinitely narrow axial groove at abscissa ($\theta = 0$), the boundary conditions become

$$p(0) = p(2\pi) = P_a \quad (4.3)$$

This is called the Sommerfeld's boundary conditions. The film thickness is defined by

$$h = C(1 + \varepsilon \cos \theta) \quad (4.4)$$

The first integration of Equation 4.2 gives

$$\frac{dp}{d\theta} = 6\mu R^2 \omega \left(\frac{h - h^*}{h^3} \right) \quad (4.5)$$

where the h^* is the film thickness at the point where the pressure gradient is zero. The next integral becomes

$$p = 6\mu\omega \left(\frac{R}{C} \right)^2 \left[\int \frac{1}{(1 - \varepsilon \cos \theta)^2} d\theta - \frac{h^*}{C} \int \frac{1}{(1 - \varepsilon \cos \theta)^3} d\theta \right] + \chi \quad (4.6)$$

where χ is a constant of integration.

These integrals were later tabulated in [Booker, 1965], but Sommerfeld solved them by performing the following change of variables

$$1 + \varepsilon \cos \theta = \frac{1 - \varepsilon^2}{1 - \varepsilon \cos \psi} \quad (4.7)$$

In order to calculate the load carrying capacity and the attitude angle, the resulting pressure distribution must be integrated over the journal. This is most conveniently done in perpendicular co-ordinate system where one direction is in the direction of line of centers (Figure 4.1).

The equilibrium equations become

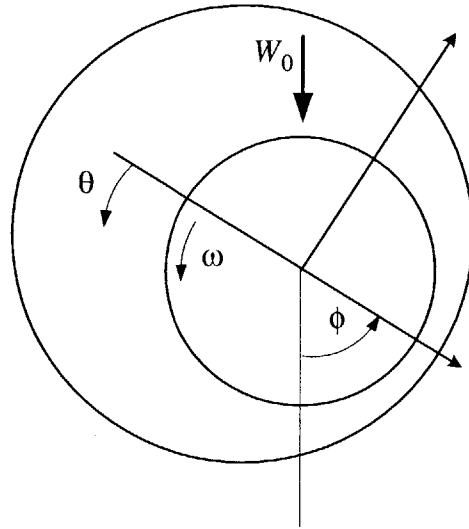


Figure 4.1 Co-ordinate system

$$\begin{aligned}
 W \cos \phi + L \int_0^{2\pi} p \cos \theta R d\theta &= 0 \\
 -W \sin \phi + L \int_0^{2\pi} p \sin \theta R d\theta &= 0
 \end{aligned} \tag{4.8}$$

from where the load and the attitude angle can be obtained.

$$\begin{aligned}
 W &= 12\mu\omega R^3 \frac{L}{C^2} \frac{\varepsilon\pi}{(2 + \varepsilon^2)(1 - \varepsilon^2)^{1/2}} \\
 \phi &= \frac{\pi}{2}
 \end{aligned} \tag{4.9}$$

The attitude angle is constant and perpendicular to the load. This leads to an unstable bearing, which is discussed in more detail later.

In this solution the pressure distribution was integrated over the entire extent of the journal. This is not always satisfactory since the pressure distribution yielded by Sommerfeld's solution has large negative pressures unless the bearing is very lightly loaded or

supplied with high pressure. Gumbel proposed a solution where these negative pressures are disregarded.

Gumbel's solution

In the case of long journal bearing the following load capacity and attitude angle are obtained

$$W = \frac{6\mu\omega RL}{(2 + \varepsilon^2)(1 - \varepsilon^2)} \left(\frac{R}{C}\right)^2 \varepsilon [4\varepsilon^2 + \pi^2(1 - \varepsilon^2)]^{1/2} \quad (4.10)$$

$$\phi = \operatorname{atan}\left(\frac{\pi\sqrt{1 - \varepsilon^2}}{2\varepsilon}\right)$$

More complicated solutions to this can also be found; for example, the Reynolds solution. To find out more about these the reader is referred to [Frene, 1990]. These more complicated solutions are unnecessary in this case since this formulation is only to represent the limiting case and the more accurate solutions to the specific case of surface self-compensated bearing is achieved numerically.

4.1.2 Short bearing

If the ratio L/D is small, the circumferential pressure gradient can be neglected compared to axial pressure gradient and the Reynolds equation reduces to

$$\frac{\partial}{\partial z} \left(\frac{h^3 \partial p}{\mu \partial z} \right) = 6\omega \frac{dh}{d\theta} \quad (4.11)$$

This assumption is valid if $L/D = \frac{1}{8}$, but it is used for ratios up to 0.5 [Frene, 1990]. This has proven to be a physically very good approximation. Hence worth, the integration is straightforward and the pressure field becomes

$$p(\theta, z) = -\frac{3\mu}{h^3} \left(\frac{L^2}{4} - z^2 \right) \omega \frac{\partial h}{\partial \theta} = \frac{-3\mu\omega}{C^2} \left(z^2 - \frac{L^2}{4} \right) \frac{\varepsilon \sin \theta}{(1 + \varepsilon \cos \theta)^3}. \quad (4.12)$$

This is symmetrical about π and therefore the Sommerfeld integration over the entire journal does not make sense (the load becomes zero), so Gumbel's condition must be used. The load and the attitude angle becomes

$$W = \mu LR \omega \left(\frac{L}{D}\right)^2 \left(\frac{R}{C}\right)^2 \frac{\varepsilon}{(1 - \varepsilon^2)^2} [16\varepsilon^2 + \pi^2(1 - \varepsilon^2)]^{1/2} \quad (4.13)$$

$$\phi = \text{atan}\left(\frac{\pi\sqrt{1 - \varepsilon^2}}{4\varepsilon}\right)$$

Figure 4.2 shows the non-dimensional load as a function eccentricity for all the presented cases and Figure 4.3 shows the attitude angle for all the presented cases.

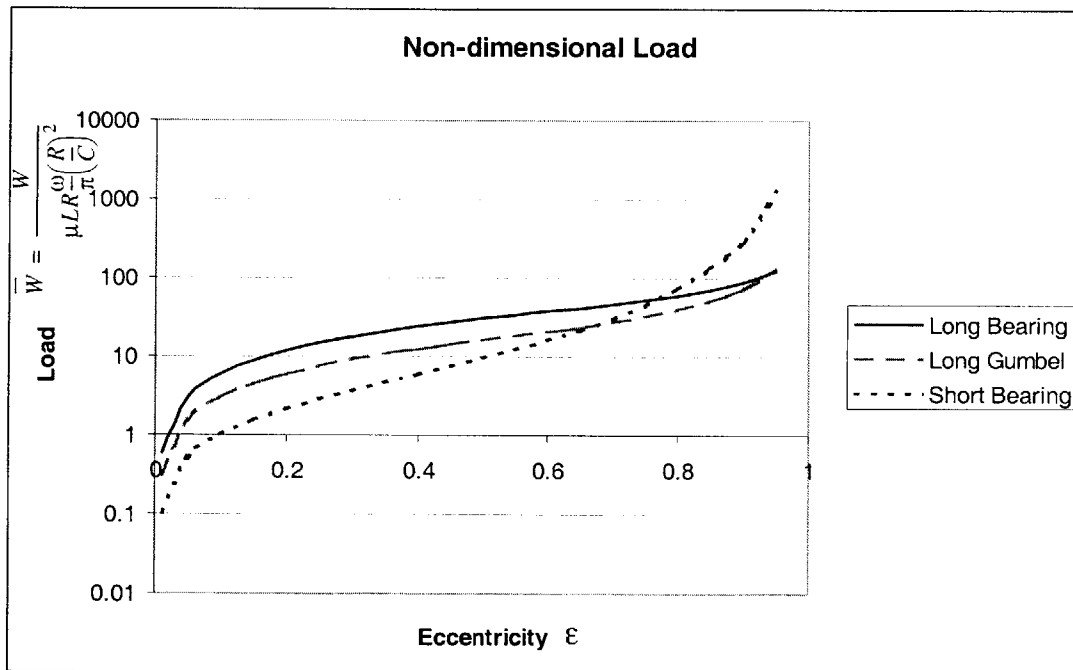


Figure 4.2 Non-dimensional load for the different assumptions

It should be noted that the loads should not be compared between the short and the long bearing, since they represent different geometries. The short bearing non-dimensional load

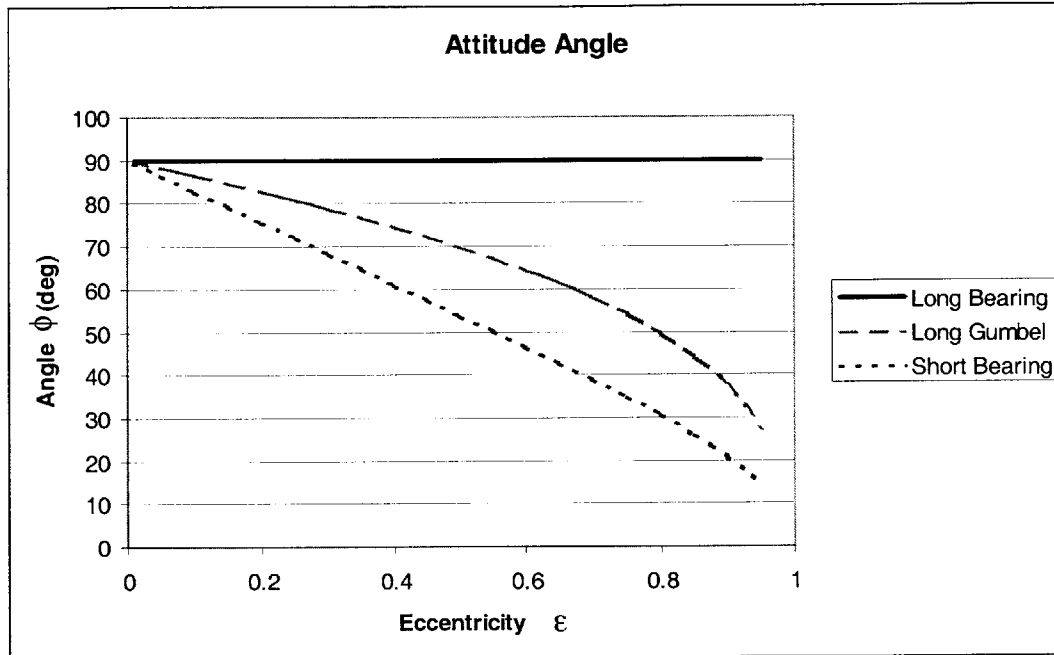


Figure 4.3 Attitude angle for the different assumptions

should be multiplied by $\left(\frac{L}{D}\right)^2$ to obtain the actual load in addition to the non-dimensionalization factor to obtain the actual (dimensional) load.

The long bearing has always an attitude angle of 90° , meaning the load and the displacement are at right angles with respect to each other. For the other cases the angle varies between 90° and 20° depending on the eccentricity. This attitude angle information can be later used in designing the hydrostatic circuit so that this angle can be compensated for. The most stable bearings usually have attitude angle close to 0° .

4.2 Dynamic coefficients of a plain journal bearing

The dynamic coefficients characterizing bearing behavior are derived from the dynamic form of Reynold's equation (Equation 4.14) with the following assumptions:

- Rigid rotor
- Small displacements about the static equilibrium (linear theory)

Linear theory is not able to predict the behavior of the rotor once it is unstable, but it is able to predict the critical speed or mass at which the system becomes unstable. Assumption of the rigid rotor makes the analysis simpler and allows for the comparison of different bearings in more general form. When designing a real system with a specific bearing it is, of course, important to take all the critical variables into account to achieve better design.

4.2.1 Derivation of the dynamic coefficients

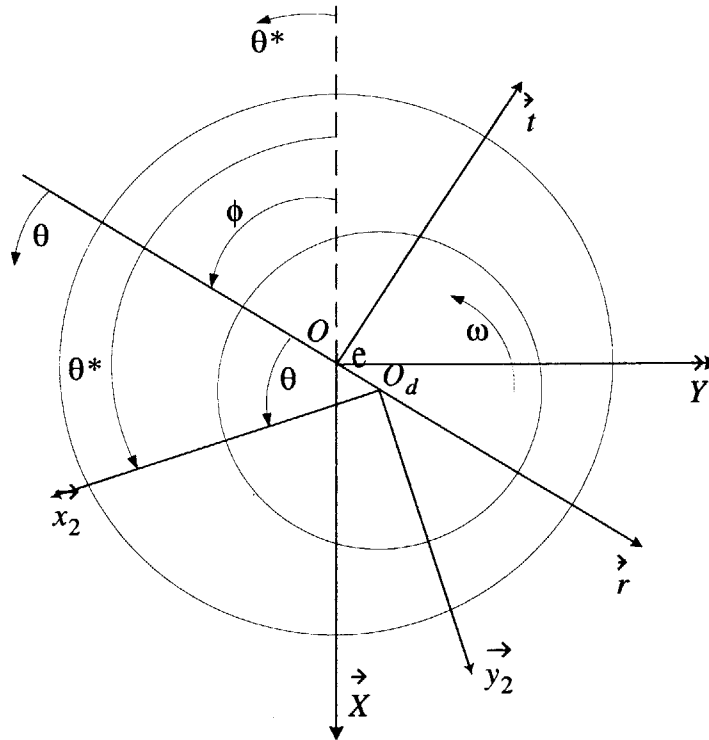


Figure 4.4 Section showing bearing co-ordinate system

The dynamic form of the Reynold's equation is

$$\frac{1}{R^2} \frac{\partial}{\partial \theta^*} \left(\frac{h^3 \partial p}{\mu \partial \theta^*} \right) + \frac{\partial}{\partial z} \left(\frac{h^3 \partial p}{\mu \partial z} \right) = 6 \left(\omega \frac{dh}{d\theta^*} + 2\dot{X} \cos \theta^* + 2\dot{Y} \sin \theta^* \right) \quad (4.14)$$

With the change of variables (see Figure 4.4)

$$X = e \cos \phi, Y = e \sin \phi, \theta^* = \theta + \phi \quad (4.15)$$

the Equation 4.14 becomes

$$\frac{1}{R^2} \frac{\partial}{\partial \theta} \left(\frac{h^3 \partial p}{\mu \partial \theta} \right) + \frac{\partial}{\partial z} \left(\frac{h^3 \partial p}{\mu \partial z} \right) = 6 \left((\omega - 2\dot{\phi}) \frac{dh}{d\theta} + 2\dot{e} \cos \theta \right) \quad (4.16)$$

With small displacements x, y around the point of equilibrium and velocities \dot{x}, \dot{y} the forces acting on the rotor can be written

$$F_x(x_0 + x, y_0 + y, \dot{x}, \dot{y}) = F_x(x_0, y_0, 0, 0) + x \cdot \left(\frac{\partial F_x}{\partial x} \right)_0 + y \cdot \left(\frac{\partial F_x}{\partial y} \right)_0 + \dot{x} \cdot \left(\frac{\partial F_x}{\partial \dot{x}} \right)_0 + \dot{y} \cdot \left(\frac{\partial F_x}{\partial \dot{y}} \right)_0 + \dots \quad (4.17)$$

$$F_y(x_0 + x, y_0 + y, \dot{x}, \dot{y}) = F_y(x_0, y_0, 0, 0) + x \cdot \left(\frac{\partial F_y}{\partial x} \right)_0 + y \cdot \left(\frac{\partial F_y}{\partial y} \right)_0 + \dot{x} \cdot \left(\frac{\partial F_y}{\partial \dot{x}} \right)_0 + \dot{y} \cdot \left(\frac{\partial F_y}{\partial \dot{y}} \right)_0 + \dots \quad (4.18)$$

By taking only the first order terms this can be written as

$$\begin{Bmatrix} f_x \\ f_y \end{Bmatrix} = -[k_{ij}] \begin{Bmatrix} x \\ y \end{Bmatrix} - [b_{ij}] \begin{Bmatrix} \dot{x} \\ \dot{y} \end{Bmatrix} \quad (4.19)$$

where f_x and f_y are the additional forces due to the displacements and velocities x, y, \dot{x}, \dot{y} i.e.

$$\begin{Bmatrix} f_x \\ f_y \end{Bmatrix} = \begin{Bmatrix} F_x(x_0 + x, y_0 + y, \dot{x}, \dot{y}) - F_x(x_0, y_0, 0, 0) \\ F_y(x_0 + x, y_0 + y, \dot{x}, \dot{y}) - F_y(x_0, y_0, 0, 0) \end{Bmatrix} \quad (4.20)$$

The dynamic coefficients, namely the stiffness and damping coefficients, in general form are

$$k_{ij} = - \left(\frac{\partial F_i}{\partial x_j} \right)_{Od} ; \quad b_{ij} = - \left(\frac{\partial F_i}{\partial \dot{x}_j} \right)_{Od} \quad (4.21)$$

The first of the indices shows the direction of the force and the second that of displacement (or velocity). The existence of cross coupling terms means that the force and the displacement (velocity) are not co-linear. To actually calculate these eight dynamic coefficients it is advantageous to choose an intermediate co-ordinate frame shown in Figure 4.5.

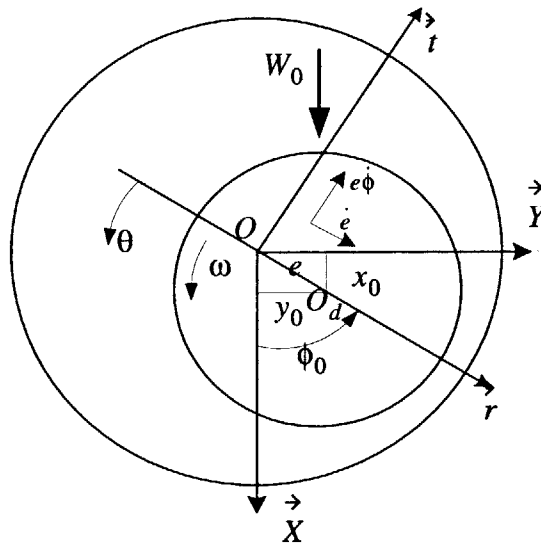


Figure 4.5 Intermediate bearing co-ordinate frame

With respect to the intermediate frame the position of the shaft center is

$$\overrightarrow{OO_d} = e\vec{r} \quad (4.22)$$

and the velocity is given by

$$\vec{V}(O_d) = \dot{e}\vec{r} + e\dot{\phi}\vec{t} \quad (4.23)$$

The best way to derive the dynamic coefficients, is to first write down the dynamic form of the Reynold's equation (Equation 4.14) with the following dimensionless variables:

$$Z = \frac{z}{L}, H = \frac{h}{C} = 1 + \varepsilon \cos(\theta), \varepsilon = \frac{e}{C}, P = \frac{P}{\mu\omega\left(\frac{R}{C}\right)^2\left(1 - 2\frac{\dot{\phi}}{\omega}\right)} \quad (4.24)$$

The Equation 4.14 becomes

$$\frac{\partial}{\partial\theta}\left(\frac{H^3\partial P}{12\partial\theta}\right) + \left(\frac{R}{L}\right)^2 \frac{\partial}{\partial Z}\left(\frac{H^3\partial P}{12\partial Z}\right) = \frac{1dH}{2d\theta} + \frac{\dot{\varepsilon}/\omega}{1 - 2(\dot{\phi}/\omega)} \cos\theta \quad (4.25)$$

This equation cannot be integrated directly to get pressure and the forces acting on the rotor (in the fluid film). For the rest of the analytical derivation it is assumed that a solution does exist. However, the components of the hydrodynamic forces are

$$\begin{Bmatrix} F_r \\ F_t \end{Bmatrix} = \mu LR \left(\frac{R}{C}\right)^2 \omega \left(1 - 2\frac{\dot{\phi}}{\omega}\right) \int_{-L/2}^{L/2} \int_{\theta_1}^{\theta_2} P \begin{Bmatrix} \cos\theta \\ \sin\theta \end{Bmatrix} d\theta dZ \quad (4.26)$$

The limits of integration are the beginning and the end of the active fluid film. What is considered to be active film depends on the assumptions made (boundary conditions) and the way negative pressures are handled. This will be discussed in more detail when analytical and numerical boundary conditions are presented. These limits depend on the position of the journal center and its velocity; thus

$$\begin{Bmatrix} F_r \\ F_t \end{Bmatrix} = \mu LR \left(\frac{R}{C}\right)^2 \omega \left(1 - 2\frac{\dot{\phi}}{\omega}\right) \begin{Bmatrix} \tilde{F}_r(\varepsilon, \phi, \dot{\varepsilon}/\omega, \dot{\phi}/\omega) \\ \tilde{F}_t(\varepsilon, \phi, \dot{\varepsilon}/\omega, \dot{\phi}/\omega) \end{Bmatrix}. \quad (4.27)$$

By taking into account Equation 4.20 and then developing the resulting equation into a first order Taylor series, the following equation is obtained for the additional forces due to the small displacements and velocities

$$\begin{Bmatrix} f_r \\ f_t \end{Bmatrix} = \mu LR \left(\frac{R}{C}\right)^2 \omega \left[\Delta\varepsilon \frac{\partial}{\partial\varepsilon} + \Delta\phi \frac{\partial}{\partial\phi} + \frac{\dot{\varepsilon}}{\omega} \frac{\partial}{\partial(\dot{\varepsilon}/\omega)} + \left(\frac{\dot{\phi}}{\varepsilon} \frac{\partial}{\partial(\dot{\phi}/\omega)}\right) \right] \begin{Bmatrix} \tilde{F}_r \\ \tilde{F}_t \end{Bmatrix} \Bigg|_{\substack{\varepsilon = \varepsilon_0, \phi = \phi_0 \\ \dot{\varepsilon} = \dot{\phi} = 0}} \quad (4.28)$$

$$- 2\mu LR \left(\frac{R}{C}\right)^2 \dot{\phi} \begin{Bmatrix} \tilde{F}_r \\ \tilde{F}_t \end{Bmatrix} \Bigg|_{\substack{\varepsilon = \varepsilon_0, \phi = \phi_0 \\ \dot{\varepsilon} = \dot{\phi} = 0}}$$

In the case of small perturbations the limits of integration will not change and the Equation 4.25 becomes linear in P and is a function of the parameter $\frac{\dot{\varepsilon}/\omega}{1-2(\dot{\phi}/\omega)}$ and can be solved by superposition method. Also the last terms in the first parenthesis vanish:

$$\left(\frac{\partial \tilde{F}_r}{\partial \dot{\phi}/\omega} \right)_{\dot{\varepsilon}=0} = \left(\frac{\partial \tilde{F}_t}{\partial \dot{\phi}/\omega} \right)_{\dot{\varepsilon}=0} = 0 \quad (4.29)$$

Equation 4.28 becomes

$$\begin{aligned} \begin{Bmatrix} f_r \\ f_t \end{Bmatrix} &= \mu LR \left(\frac{R}{C} \right)^2 \omega \left[\Delta \varepsilon \frac{\partial}{\partial \varepsilon} + \Delta \phi \frac{\partial}{\partial \phi} + \frac{\dot{\varepsilon}}{\omega} \frac{\partial}{\partial (\dot{\varepsilon}/\omega)} \right] \begin{Bmatrix} \tilde{F}_r \\ \tilde{F}_t \end{Bmatrix}_{\substack{\varepsilon = \varepsilon_0, \phi = \phi_0 \\ \dot{\varepsilon} = \dot{\phi} = 0}} \\ &- 2\mu LR \left(\frac{R}{C} \right)^2 \dot{\phi} \begin{Bmatrix} \tilde{F}_r \\ \tilde{F}_t \end{Bmatrix}_{\substack{\varepsilon = \varepsilon_0, \phi = \phi_0 \\ \dot{\varepsilon} = \dot{\phi} = 0}} \end{aligned} \quad (4.30)$$

from where the dynamic coefficients can be determined. Stiffness coefficients become:

$$\begin{aligned} k_{rr} &= -\mu LR \left(\frac{R}{C} \right)^2 \frac{\omega}{C} \left(\frac{\partial \tilde{F}_r}{\partial \varepsilon} \right)_0; \quad k_{rt} = -\mu LR \left(\frac{R}{C} \right)^2 \frac{\omega}{C} \left(\frac{\partial \tilde{F}_r}{\partial \phi} \right)_0 \\ k_{tr} &= -\mu LR \left(\frac{R}{C} \right)^2 \frac{\omega}{C} \left(\frac{\partial \tilde{F}_t}{\partial \varepsilon} \right)_0; \quad k_{tt} = -\mu LR \left(\frac{R}{C} \right)^2 \frac{\omega}{C} \left(\frac{\partial \tilde{F}_t}{\partial \phi} \right)_0 \end{aligned} \quad (4.31)$$

and the damping coefficients become

$$\begin{aligned} b_{rr} &= -\mu LR \left(\frac{R}{C} \right)^2 \frac{1}{C} \left(\frac{\partial \tilde{F}_r}{\partial \left(\frac{\dot{\varepsilon}}{\omega} \right)} \right)_0; \quad b_{rt} = -2 \left(\mu LR \left(\frac{R}{C} \right)^2 \frac{1}{C \varepsilon_0} \right) \tilde{F}_{r0} \\ b_{tr} &= -\mu LR \left(\frac{R}{C} \right)^2 \frac{1}{C} \left(\frac{\partial \tilde{F}_t}{\partial \left(\frac{\dot{\varepsilon}}{\omega} \right)} \right)_0; \quad b_{tt} = 2 \left(\mu LR \left(\frac{R}{C} \right)^2 \frac{1}{C \varepsilon_0} \right) \tilde{F}_{t0} \end{aligned} \quad (4.32)$$

In dimensionless form, the coefficients may be written as

$$K_{ij} = \frac{C}{W_0} k_{ij}; \quad B_{ij} = C \frac{\omega}{W_0} b_{ij} \quad (4.33)$$

with W_0 being the external load. The simplest form of the dynamic so-efficient can be found in terms of the Sommerfeld number S

$$S = \frac{\mu \omega R L}{\pi W} \left(\frac{R}{C} \right)^2 \quad (4.34)$$

and the partial derivatives

$$K_{rr} = -\pi S \left(\frac{\partial \tilde{F}_r}{\partial \varepsilon} \right)_0; \quad K_{rt} = -\frac{\pi S}{\varepsilon_0} \left(\frac{\partial \tilde{F}_r}{\partial \varepsilon} \right)_0 \quad (4.35)$$

$$K_{tr} = -\pi S \left(\frac{\partial \tilde{F}_t}{\partial \varepsilon} \right)_0; \quad K_{tt} = -\frac{\pi S}{\varepsilon_0} \left(\frac{\partial \tilde{F}_t}{\partial \varepsilon} \right)_0$$

$$B_{rr} = -\pi S \left(\frac{\partial \tilde{F}_r}{\partial \dot{\varepsilon} / \omega} \right)_0; \quad B_{rt} = -\frac{2 \cos \phi_0}{\varepsilon_0} \quad (4.36)$$

$$B_{tr} = -\pi S \left(\frac{\partial \tilde{F}_t}{\partial \dot{\varepsilon} / \omega} \right)_0; \quad B_{tt} = \frac{2 \sin \phi_0}{\varepsilon_0}$$

In addition it can be shown [Frene, 1990] that the approximation of constant limits of integration will lead to

$$B_{rt} = B_{tr} \quad (4.37)$$

The dimensionless stiffness and damping coefficient are function of the equilibrium position only and in addition the damping tensor is symmetric.

These coefficients will be solved for two elementary cases, namely the infinitely short and long bearing in next section. These coefficients also depend on the boundary conditions. Other than the elementary cases these coefficients must be solved numerically.

4.2.2 Infinitely Short Bearing

In an infinitely short bearing the circumferential pressure gradient becomes negligible compared to the axial pressure gradient.

$$\frac{1}{R} \frac{\partial p}{\partial \theta} \ll \frac{\partial p}{\partial z} \Rightarrow \frac{L}{R} \ll 1 \quad (4.38)$$

The equation 4.25 is reduced to

$$\frac{\partial}{\partial z} \left(\frac{h^3}{\mu} \frac{\partial p}{\partial z} \right) = 6 \left[(\omega - 2\dot{\phi}) \frac{\partial h}{\partial \theta} + 2\dot{e} \cos \theta \right]. \quad (4.39)$$

Equation 4.39 integrated with

$$p(0) = p(L) = 0; \quad h(\theta) = C(1 + \epsilon \cos \theta) \quad (4.40)$$

becomes

$$p(\theta, z) = -\frac{3\mu}{h^3} \left(\frac{L^2}{4} - z^2 \right) \left[(\omega - 2\dot{\phi}) \frac{\partial h}{\partial \theta} + 2\dot{e} \cos \theta \right] \quad (4.41)$$

No boundary condition can be imposed in the circumferential direction (no feed or drainage grooves). Equation 4.41 can be integrated with either Sommerfeld's or Gumbel's boundary conditions. These conditions are not always satisfactory from a physical point of view, but in certain situations can produce satisfactory agreement with experimental results [Frene, 1990]. Figure 4.6 shows the pressure distribution in a typical case (pressure is normalized with maximum pressure).

Sommerfeld's Condition

Sommerfeld's boundary condition assumes a full oil film and allows large negative pressures. This is the simplest case, since the integration is performed over the full extent of the journal.

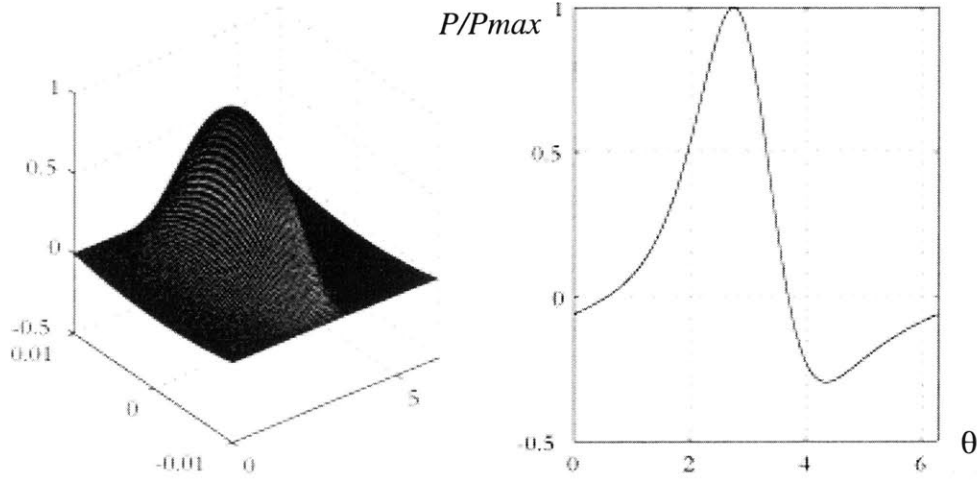


Figure 4.6 Pressure given by Equation 4.41.

The component forces can be found by performing the integration of Equation 4.26 with $\theta_1 = 0$, $\theta_2 = 2\pi$ and $|\varepsilon| \leq 1$. The forces become

$$F_r = \frac{-L^2\pi\dot{\varepsilon}}{R^2\omega\left(1 - \frac{2\dot{\phi}}{\omega}\right)} \left(\frac{1 + 2\varepsilon^2}{(1 - \varepsilon^2)^{5/2}} \right) \quad (4.42)$$

$$F_t = \frac{L^2\pi\varepsilon}{2R^2} \frac{1}{(1 - \varepsilon)^{3/2}}$$

from where (see the load capacity case)

$$S = \left(\frac{R}{L}\right)^2 \frac{2(1 - \varepsilon^2)^{5/2}}{\pi^2\varepsilon}; \quad \phi_0 = \frac{\pi}{2} \quad (4.43)$$

Now the dynamic coefficients can be written

$$K_{rr} = 0; \quad K_{rt} = \frac{1}{\varepsilon}; \quad K_{tr} = -\frac{1 + 2\varepsilon^2}{\varepsilon(1 - \varepsilon^2)}; \quad K_{tt} = 0 \quad (4.44)$$

$$B_{rr} = -\frac{2(1 + 2\varepsilon^2)}{\varepsilon(1 - \varepsilon^2)}; \quad B_{rt} = B_{tr} = 0; \quad B_{tt} = \frac{2}{\varepsilon}$$

these coefficients can be transformed into a more convenient x - y coordinate system by the normal coordinate change procedure, namely

$$[A]_{xy} = [Q]^T [A]_{rt} [Q] \quad (4.45)$$

where

$$[Q] = \begin{bmatrix} \cos\phi & \sin\phi \\ -\sin\phi & \cos\phi \end{bmatrix} \quad (4.46)$$

is the rotation matrix.

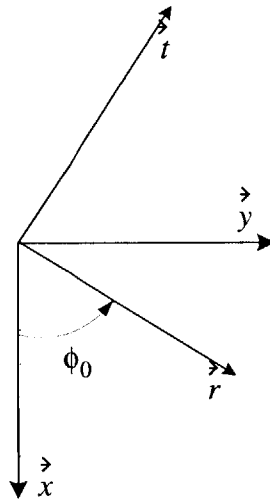


Figure 4.7 Change of basis

Figure 4.8 shows the non-dimensional stiffness coefficients for this case and Figure 4.9 the non-dimensional damping coefficients. All other coefficients are zero.

Gumbel's Condition

Gumbel's condition ignores the negative pressures by integrating only over the positive part of the pressure field (see Figure 4.6). The limits of integration become

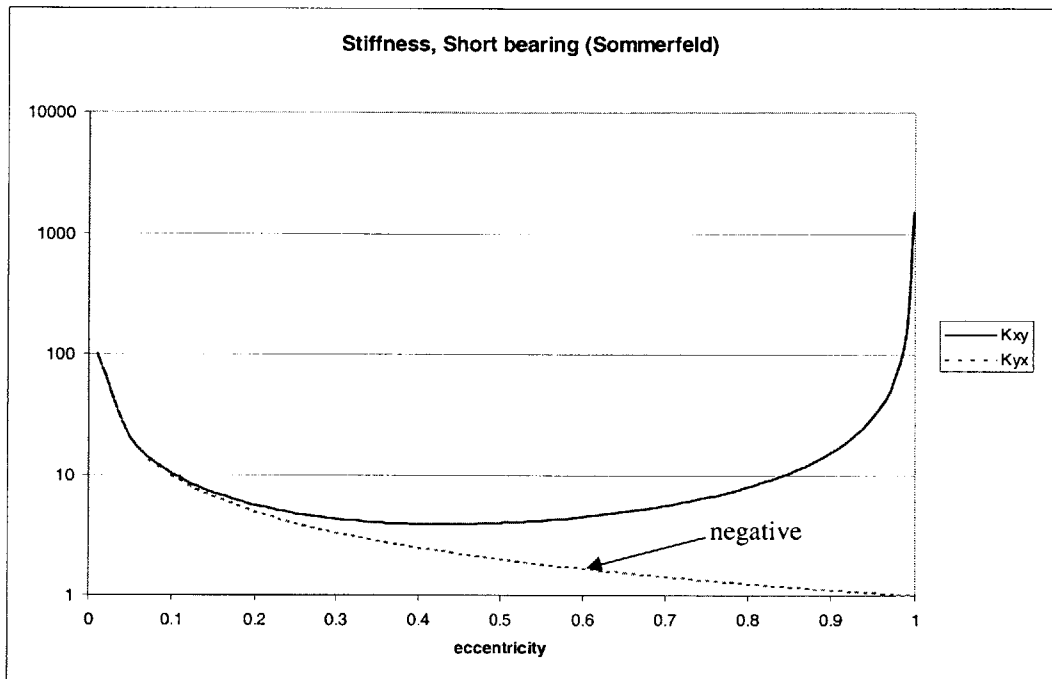


Figure 4.8 Stiffness coefficients for infinitely short bearing with Sommerfeld's conditions

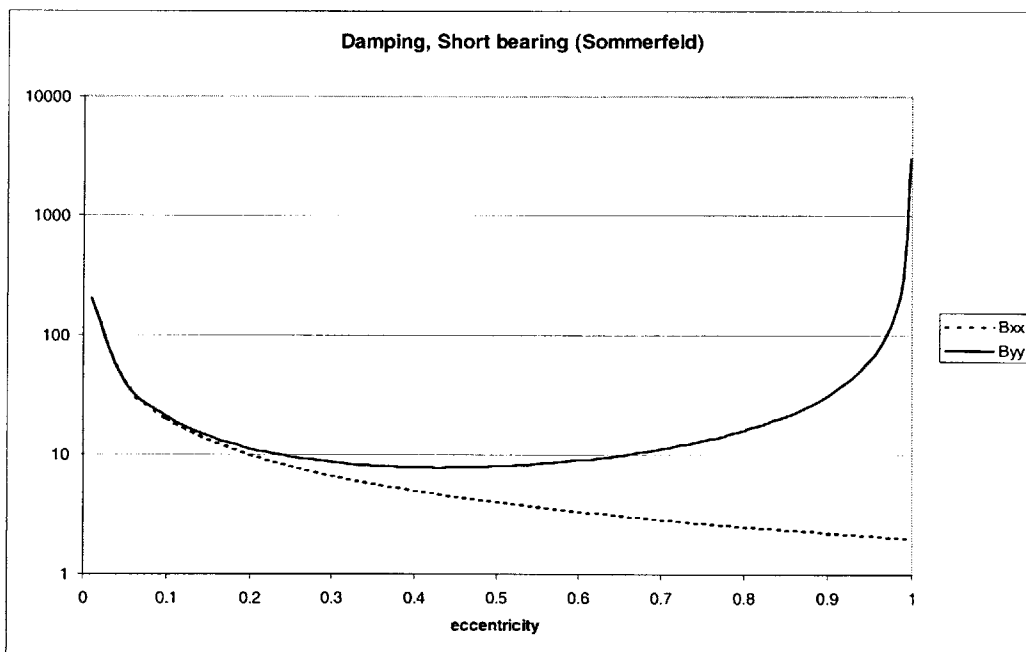


Figure 4.9 Damping coefficients for infinitely short bearing with Sommerfeld's conditions

$$\theta_1 = \text{atan}\left(\frac{2\dot{e}}{(\omega - 2\dot{\phi})C\varepsilon}\right); \quad \theta_2 = \theta_1 + \pi \quad (4.47)$$

and the component forces are

$$F_r = \frac{L^2}{2(1 - \varepsilon^2)R^2\omega\left(1 - 2\frac{\dot{\phi}}{\omega}\right)} \left[\frac{\pi\dot{e}(1 + 2\varepsilon^2)}{\sqrt{(1 - \varepsilon^2)}} + 2\varepsilon^2(\omega - 2\dot{\phi}) \right] \quad (4.48)$$

$$F_t = \frac{L^2}{2(1 - \varepsilon^2)R^2\omega\left(1 - 2\frac{\dot{\phi}}{\omega}\right)} \varepsilon \left[4\dot{e} + \frac{\pi}{2}(\omega - 2\dot{\phi})\sqrt{(1 - \varepsilon^2)} \right]$$

The Sommerfeld's number and the attitude angle are

$$S = \left(\frac{D}{L}\right)^2 \frac{(1 - \varepsilon^2)^2}{\pi\varepsilon[16\varepsilon^2 + \pi^2(1 - \varepsilon^2)]^{1/2}} \quad (4.49)$$

$$\phi_0 = \text{atan}\left(\frac{\pi\sqrt{(1 - \varepsilon^2)}}{4\varepsilon}\right)$$

Dynamic coefficient for this case are:

$$K_{rr} = \frac{8(1 + \varepsilon^2)}{(1 - \varepsilon^2)}\Psi(\varepsilon); \quad K_{rt} = \frac{\pi}{\varepsilon}\sqrt{(1 - \varepsilon^2)}\Psi(\varepsilon) \quad (4.50)$$

$$K_{tr} = \frac{-\pi(1 + \varepsilon^2)}{\varepsilon\sqrt{(1 - \varepsilon^2)}}\Psi(\varepsilon); \quad K_{tt} = 4\Psi(\varepsilon)$$

$$B_{rr} = \frac{-2\pi(1 + \varepsilon^2)}{\varepsilon\sqrt{(1 - \varepsilon^2)}}\Psi(\varepsilon); \quad B_{rt} = -8\Psi(\varepsilon) \quad (4.51)$$

$$B_{tr} = -8\Psi(\varepsilon); \quad B_{tt} = \frac{\pi}{\varepsilon}\sqrt{(1 - \varepsilon^2)}\Psi(\varepsilon)$$

where

$$\Psi(\varepsilon) = \frac{1}{\sqrt{16\varepsilon^2 + \pi^2(1 - \varepsilon^2)}} \quad (4.52)$$

Figure 4.10 shows the non-dimensional stiffness coefficients for this case (Gumbel's conditions) and Figure 4.11 the non-dimensional damping coefficients.

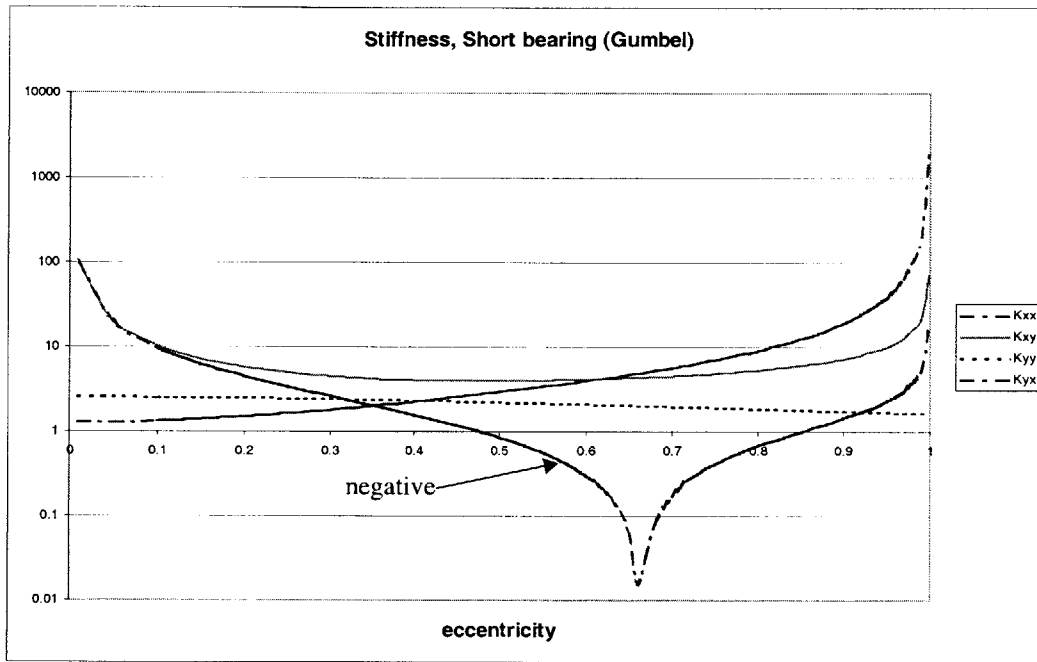


Figure 4.10 Stiffness coefficients for infinitely short bearing with Gumbel's conditions

For both cases it is good to derive the initial damping coefficient. By initial it is meant that eccentricity is zero. This is done in dimensional form, so that these formulas can later be used more conveniently. The initial stiffness is most easily obtained by letting the eccentricity go to zero in the computed force and then differentiating with respect to squeeze velocity \dot{e} .

$$B_{initial} = \frac{\partial(f_r)_{\epsilon \rightarrow 0}}{\partial \dot{e}} \tag{4.53}$$

In the case of the short bearing the initial stiffness for the two different conditions become

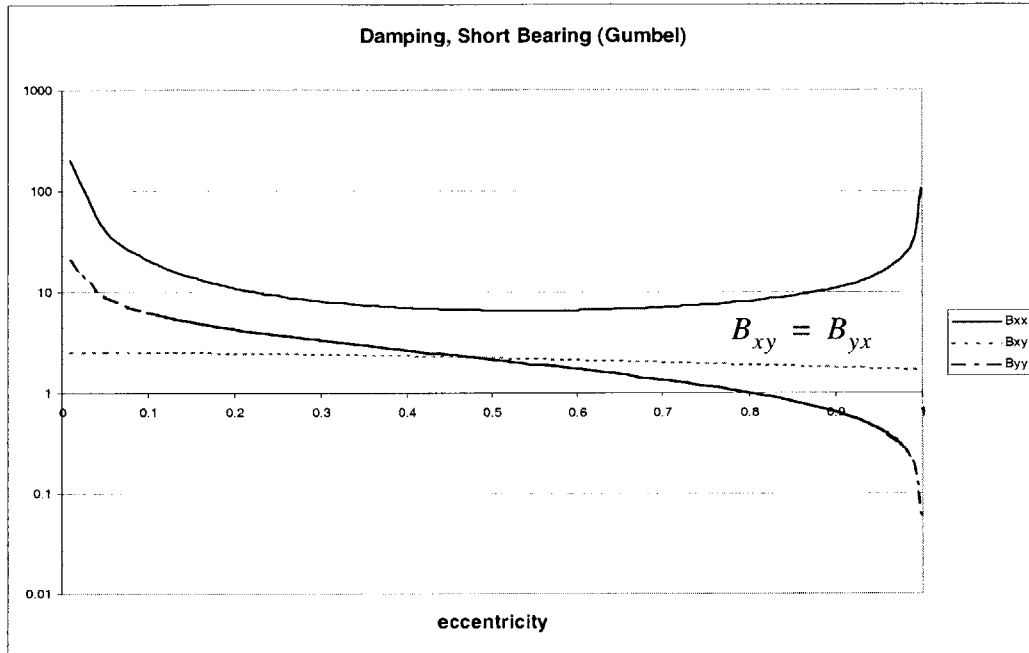


Figure 4.11 Damping coefficients for infinitely short bearing with Gumbel's conditions

$$\text{Sommerfeld: } B = \frac{\mu RL^3 \pi}{C^3} \quad (4.54)$$

$$\text{Gumbel: } B = \frac{\mu RL^3 \pi}{2C^3}$$

These give rather large values and the damping goes down significantly as the eccentricity is introduced.

4.2.3 Infinitely Long Bearing

In the approximation of an infinitely long bearing the axial flow is neglected. The criteria is inverse of the Equation 4.38. The dimensionless Reynolds equation becomes

$$\frac{1}{R^2} \frac{\partial}{\partial \theta} \left(\frac{h^3}{\mu} \frac{\partial p}{\partial \theta} \right) = 6 \left[(\omega - 2\dot{\phi}) \frac{\partial h}{\partial \theta} + 2\dot{e} \cos \theta \right] \quad (4.55)$$

The integration of Equation 4.55 is cumbersome. Either the Sommerfeld's coordinate change must be used or the tables of integrations from [Booker, 1965, Frene, 1990]. The film pressure is given by:

$$p(\theta) = 6\mu \left(\frac{R}{C}\right)^2 \left\{ \frac{(\omega - 2\dot{\phi})(2 + \varepsilon \cos\theta)\varepsilon \sin\theta}{(2 + \varepsilon^2)(1 + \varepsilon \cos\theta)^2} + \frac{\dot{\varepsilon}}{\varepsilon} \left[\frac{1}{(1 + \varepsilon \cos\theta)^2} - \frac{1}{(1 + \varepsilon)^2} \right] \right\} \quad (4.56)$$

Equation 4.56 is plotted with typical numbers in Figure 4.12. The pressure rise due to the

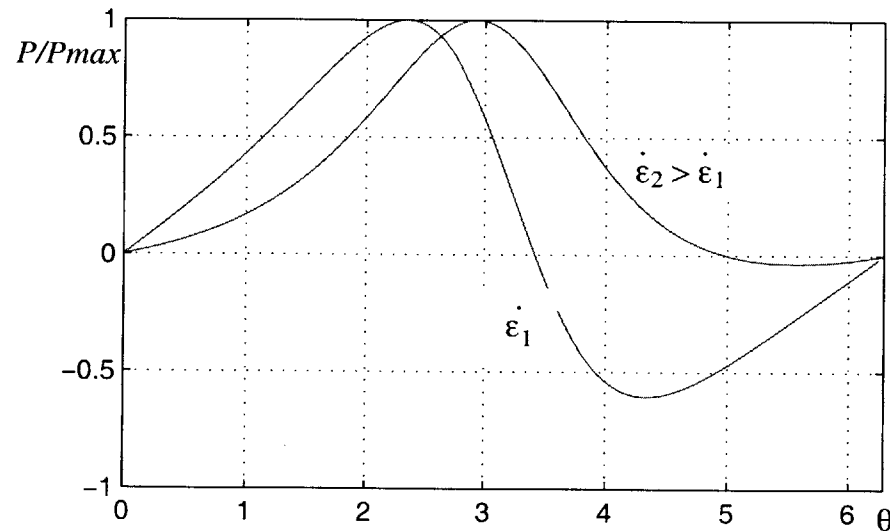


Figure 4.12 Pressure given by Equation 4.56.

squeeze effect is shown in the figure with the upper curve representing higher squeeze velocity. This will be again solved for the case of complete oil film and the for the case ignoring the negative pressures.

Sommerfeld's Condition

Again integrating from over the entire extent of the bearing the following results are obtained:

$$F_r = -12 \frac{\pi \dot{\epsilon}}{(1 - \epsilon^2)^{3/2} (\omega - 2\dot{\phi})} \quad (4.57)$$

$$F_t = 12 \frac{\pi \epsilon}{(2 + \epsilon^2)(1 - \epsilon^2)^{1/2}}$$

$$\phi_0 = \frac{\pi}{2}$$

$$S = \frac{(2 + \epsilon^2)(1 - \epsilon)^{1/2}}{12\pi^2 \epsilon}$$

and the stiffness coefficients become

$$K_{rr} = 0; \quad K_{rt} = \frac{1}{\epsilon} \quad (4.58)$$

$$K_{tr} = -\frac{2\epsilon^4 - \epsilon^2 + 2}{\epsilon(2 + \epsilon^2)(1 - \epsilon^2)}; \quad K_{tt} = 0$$

and the damping coefficients:

$$B_{rr} = \frac{2 + \epsilon^2}{\epsilon(1 - \epsilon^2)}; \quad B_{rt} = 0 \quad (4.59)$$

$$B_{tr} = 0; \quad B_{tt} = \frac{2}{\epsilon}$$

The non-dimensional coefficients are plotted in Figure 4.13 and Figure 4.14.

Gumbel's Conditions

Again ignoring the negative pressures and integrating over only the positive portion of the pressure distribution the following results are obtained:

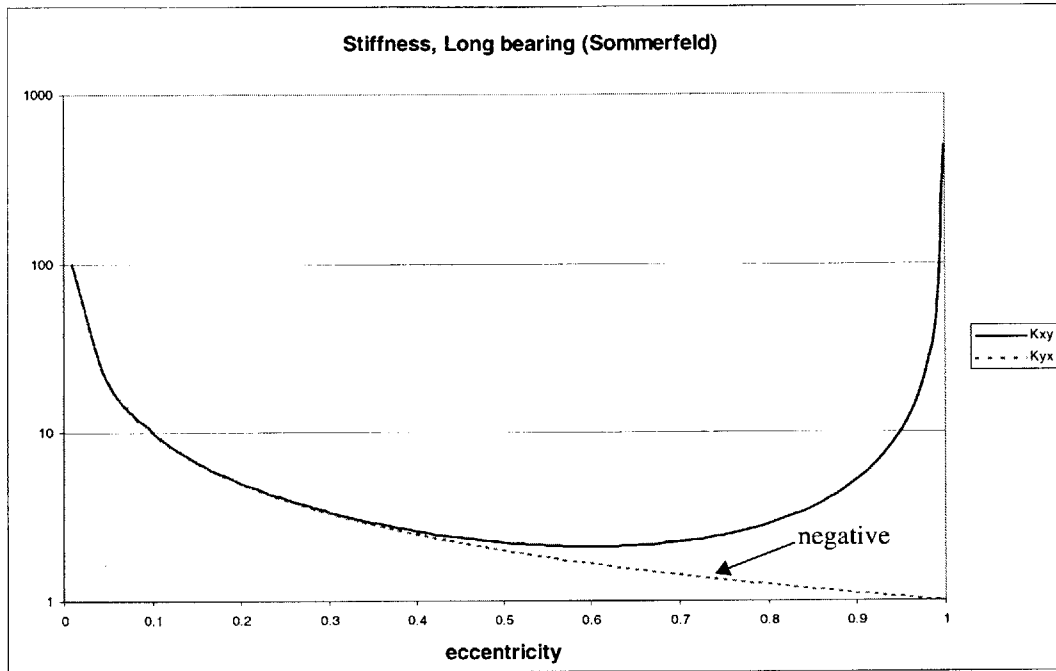


Figure 4.13 Stiffness coefficients for long bearing with Sommerfeld's conditions

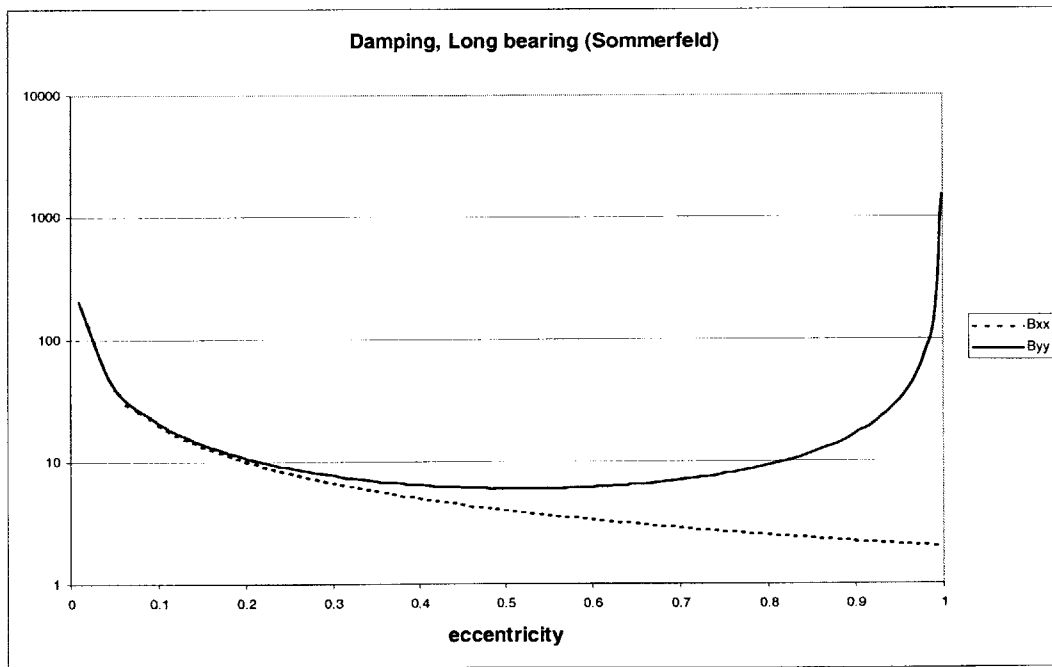


Figure 4.14 Damping coefficients for long bearing with Sommerfeld's conditions

$$\begin{aligned}
F_r &= \frac{-12}{(\omega - 2\dot{\phi})} \left\{ \frac{\varepsilon^2(\omega - 2\dot{\phi})}{(2 + \varepsilon^2)(1 - \varepsilon^2)} + \frac{\dot{\varepsilon}}{(1 - \varepsilon^2)^{3/2}} \left[\frac{\pi}{2} - \frac{8}{\pi(2 + \varepsilon^2)} \right] \right\} \\
F_t &= \frac{-12}{(\omega - 2\dot{\phi})} \left\{ \frac{\pi\varepsilon(\omega - 2\dot{\phi})}{(2 + \varepsilon^2)(1 - \varepsilon^2)^{1/2}} + \frac{2\varepsilon\dot{\varepsilon}}{(2 + \varepsilon^2)(1 - \varepsilon^2)} \right\} \\
\phi_0 &= \text{atan} \left(\frac{\pi\sqrt{1 - \varepsilon^2}}{2\varepsilon} \right) \\
S &= \frac{(2 + \varepsilon^2)(1 - \varepsilon^2)^{3/2}}{6\pi\varepsilon} \Omega(\varepsilon)
\end{aligned} \tag{4.60}$$

The stiffness coefficients become:

$$\begin{aligned}
K_{rr} &= \frac{4(2 + \varepsilon^4)}{(2 + \varepsilon^2)(1 - \varepsilon^2)^{1/2}} \Omega(\varepsilon); \quad K_{rt} = \frac{\pi^2(1 - \varepsilon^2)}{\varepsilon} \\
K_{tr} &= -\frac{2\varepsilon^4 + \varepsilon^2 - 2}{\varepsilon(2 + \varepsilon^2)} \Omega(\varepsilon); \quad K_{tt} = 2(1 - \varepsilon^2)^{1/2} \Omega(\varepsilon)
\end{aligned} \tag{4.61}$$

and the damping:

$$\begin{aligned}
B_{rr} &= \frac{\pi(2 + \varepsilon^2)}{\varepsilon(1 - \varepsilon^2)}; \quad B_{rt} = -4(1 - \varepsilon^2)\Omega(\varepsilon) \\
B_{tr} &= -4(1 - \varepsilon^2)\Omega(\varepsilon); \quad B_{tt} = \frac{2\pi(1 - \varepsilon^2)}{\varepsilon} \Omega(\varepsilon)
\end{aligned} \tag{4.62}$$

where

$$\Omega(\varepsilon) = \frac{1}{\sqrt{(1 - \varepsilon^2)[\pi^2 - \varepsilon^2(\pi^2 - 4)]}}. \tag{4.63}$$

These plotted in Figure 4.15 and Figure 4.16.

In the case of the long bearing the initial damping coefficient can be obtained the same way as in the case of the short bearing. They become

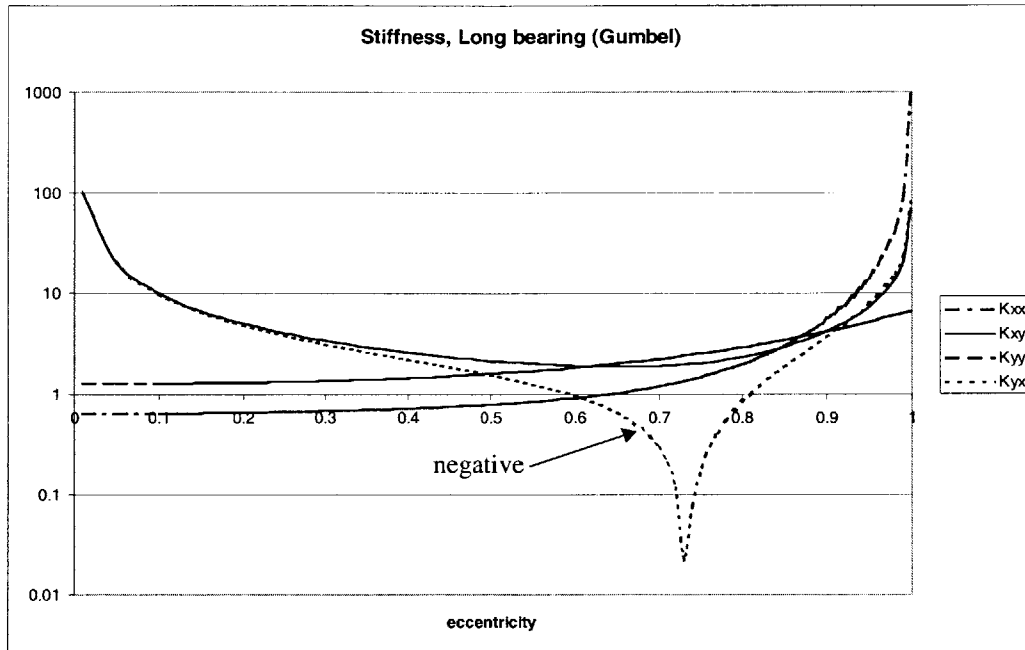


Figure 4.15 Stiffness coefficients for long bearing with Gumbel's conditions

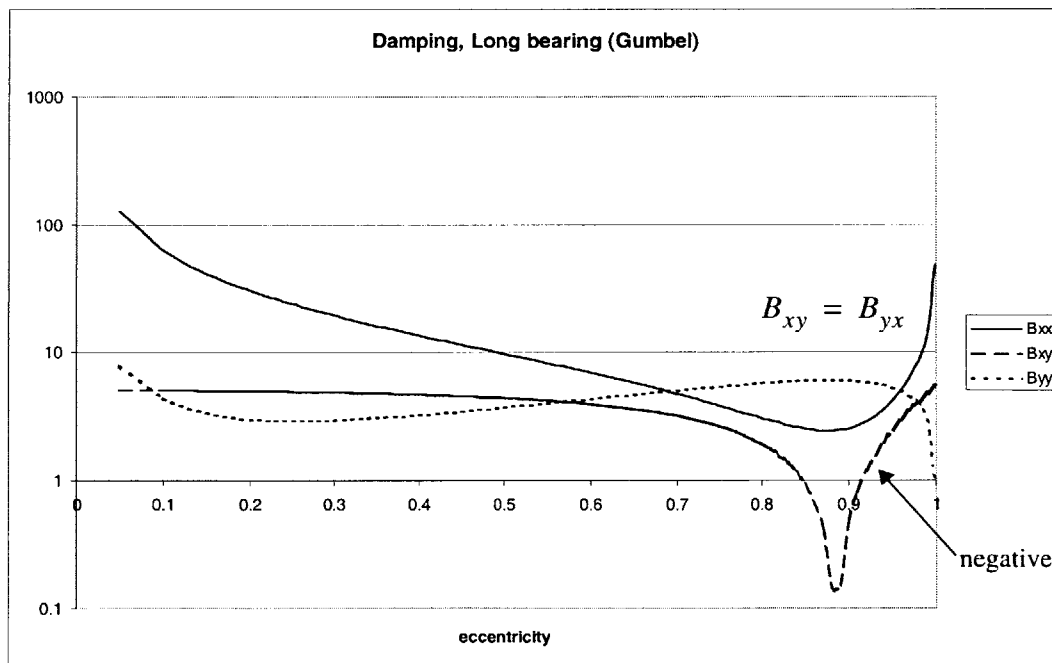


Figure 4.16 Damping coefficients for long bearing with Gumbel's conditions

$$\text{Sommerfeld: } B = \frac{12\mu R^3 L \pi}{C^3} \quad (4.64)$$

$$\text{Gumbel: } B = \frac{12\mu R^3 L \pi \left(\frac{\pi}{2} - \frac{4}{\pi}\right)}{C^3} \approx 0.3 \cdot \frac{12\mu R^3 L \pi}{C^3}$$

4.3 Fixed Restrictor Deep-Pocket Hydrostatic Bearing

Fixed restrictor (capillary or orifice) is the most commonly used hydrostatic bearing. Here it is used as a baseline and it represents the lower bound for damping properties. The static modeling of the bearing is fairly simple and can be done with the methods introduced in the modeling section. The most convenient way to predict the stiffness is to use the methods introduced in the modeling section to obtain the force-displacement relation and then use numerical differentiation to get the stiffness. There exist analytical solutions to these relations, see for example [Bassani, 1992, Frene, 1990]. These relations will not be presented here since it is only desired to find an approximate relation for the damping.

The bearing for which the damping is calculated is represented in Figure 4.17. The following assumptions are made:

- Laminar flow
- Centered shaft
- Translation speed is co-linear with x-axis
- Linear theory

Translational speed induces an pressure change in recess, which in turn induces a load. The damping coefficients are:

$$B_{xx} = -\frac{\Delta W_x}{\dot{e}}, B_{yx} = -\frac{\Delta W_y}{\dot{e}} \quad (4.65)$$

From mass conservation it follows that the flow into the recess equals the flow out to the atmosphere from the pocket plus the flow between the recesses minus the volume change

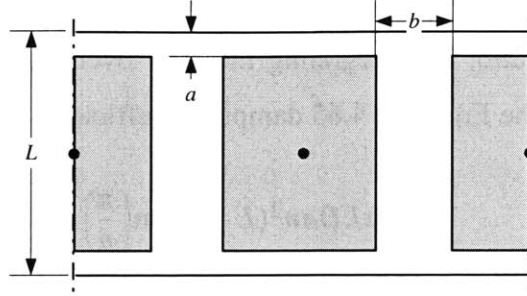


Figure 4.17 Typical fixed restrictor hydrostatic bearing

$$\frac{R_c}{\mu}(P_s - P_i) = \frac{\pi RC^3}{12\mu an} \left[4P_i + (2P_i - P_{i+1} - P_{i-1}) \frac{na(L-a)}{\pi bR} \right] - \frac{\partial V}{\partial t} \quad (4.66)$$

Let the recess pressure be $P_i = P_a + \Delta P_i$, where the ΔP_i is the pressure change due to the velocity \dot{e} . Substituting P_i into Equation 4.66 and noticing that at the centered position $R_c(P_s - P_a) = \frac{\pi RC^3}{12an} 4P_a$ the equation becomes

$$R_c \Delta P_i = \frac{\pi RC^3}{12an} \left[4\Delta P_i + (2\Delta P_i - \Delta P_{i+1} - \Delta P_{i-1}) \frac{na(L-a)}{\pi bR} \right] - \mu L D \dot{e} \sin\left(\frac{\pi}{n}\right) \cos\left(\frac{2\pi}{n}(i-1)\right) \quad (4.67)$$

The pressure change in a recess is only function of its location around the bearing. It follows that

$$\Delta P_i \cos\left(\frac{2\pi}{n}i\right) = \Delta P_{i+1} \cos\left(\frac{2\pi}{n}(i-1)\right) \quad (4.68)$$

Now the Equation 4.67 can be solved for P_i which becomes

$$\Delta P_i = \frac{6\dot{e}\mu L a n \sin\left(\frac{\pi}{n}\right) \cos\left(\frac{2\pi}{n}(i-1)\right)}{\pi C^3 \left(1 + \zeta + 2 \frac{a(L-a)}{\pi bR} \sin\left(\frac{\pi}{n}\right)^2 \right)} \quad (4.69)$$

where

$$\zeta = R_c \left(\frac{\pi R C^3}{12 a n} \right)^{-1} \quad (4.70)$$

which is the resistance ratio. By integrating the ΔP_i over the bearing area the ΔW is obtained and then using the Equation 4.65 damping coefficients are obtained.

$$B_{xx} = B_{yy} = \frac{3\mu L D a n^2 (L - a) \sin\left(\frac{\pi}{n}\right)^2}{\pi C^3 \left(1 + \zeta + 2 \frac{a(L - a)}{\pi b R} \sin\left(\frac{\pi}{n}\right)^2 \right)} \quad (4.71)$$

$$B_{xy} = B_{yx} = 0$$

Although these damping coefficients were obtained assuming centered shaft position it has been shown numerically that for small eccentricity ratios $\varepsilon < 0.4$ these results do not change [Frene, 1990].

4.4 Bearing Stability

Usually in the case of fluid film bearings the bearing stability is defined in terms of critical mass above which the bearing becomes unstable. This critical mass is defined to be the mass of the perfectly rigid rotor. This analysis is based entirely on linear analysis, but a theorem by Liapounov [Frene, 1990] states that if a linearized system is stable then the non-linear system is also stable to small perturbations. Therefore the stability of a operating point can be assessed by linear analysis. The assumption of a perfectly rigid rotor can be justified by stating that this makes the comparison of different bearings easier. Naturally, if a specific rotor-bearing system is considered the compliance of the rotor must be taken into account.

The linearized equations of motion at a certain operating point are

$$M \begin{Bmatrix} \ddot{x} \\ \ddot{y} \end{Bmatrix} + [b_{ij}] \begin{Bmatrix} \dot{x} \\ \dot{y} \end{Bmatrix} + [k_{ij}] \begin{Bmatrix} x \\ y \end{Bmatrix} = \{0\} \quad (4.72)$$

Again, for the sake of generality, the Equation 4.72 is non-dimensionalized with

$$\begin{aligned} \bar{M} &= \frac{MC\omega^2}{W}, K_{ij} = \frac{k_{ij}C}{W}, B_{ij} = \frac{b_{ij}C\omega}{W}, X = \frac{x}{C}, Y = \frac{y}{C} \\ \dot{X} &= \frac{\dot{x}}{C\omega}, \dot{Y} = \frac{\dot{y}}{C\omega}, \ddot{X} = \frac{\ddot{x}}{C\omega^2}, \ddot{Y} = \frac{\ddot{y}}{C\omega^2} \end{aligned} \quad (4.73)$$

Solution of the form:

$$X = \tilde{X}e^{\lambda\omega t} \text{ where } \lambda = c + id \quad (4.74)$$

leads to the following system of equations

$$\begin{bmatrix} \bar{M}\lambda^2 + B_{xx}\lambda + K_{xx} & B_{xy}\lambda + K_{xy} \\ B_{yx}\lambda + K_{xy} & \bar{M}\lambda^2 + B_{yy}\lambda + K_{yy} \end{bmatrix} \begin{Bmatrix} \tilde{X} \\ \tilde{Y} \end{Bmatrix} = \{0\} \quad (4.75)$$

This system has a solution if the characteristic polynomial is zero. The characteristic polynomial becomes

$$f(\lambda) = A_0\lambda^4 + A_1\lambda^3 + A_2\lambda^2 + A_3\lambda + A_4 \quad (4.76)$$

Where

$$\begin{aligned} A_0 &= \bar{M}^2, A_1 = \bar{M} \cdot tr(B_{ij}), A_2 = \bar{M} \cdot tr(K_{ij}) + det(B_{ij}) \\ A_3 &= B_{xx}K_{yy} + B_{yy}K_{xx} - B_{xy}K_{yx} - B_{yx}K_{xy}, A_4 = det(K_{ij}) \end{aligned} \quad (4.77)$$

The system will be dynamically stable if all the real parts of the roots of the complex polynomial f are negative [Den Hartog, 1985]. The Routh-Hurwitz criterion states that all roots

of f have negative real parts if, and only if, the following inequalities are satisfied [Den Hartog, 1985, Frene, 1990]:

$$A_0 \Delta_1 > 0, \Delta_2 > 0, \Delta_3 > 0, \Delta_4 > 0 \quad (4.78)$$

where Δ_i represents the Hurwitz determinant of i :th order

$$\Delta_i = \begin{vmatrix} A_1 & A_3 & A_5 & A_7 & \dots \\ A_0 & A_2 & A_4 & A_6 & \dots \\ 0 & A_1 & A_3 & A_5 & \dots \\ 0 & A_0 & A_2 & A_4 & \dots \\ \dots & \dots & \dots & \dots & A_i \end{vmatrix} \quad (4.79)$$

In this case the A_0 is always positive (mass squared) and therefore the conditions 4.78 can be written as

$$\Delta_i > 0, i = 1, 2, 3, 4 \quad (4.80)$$

These inequalities lead to the following conditions for stability

$$\begin{aligned} \Delta_1 > 0 &\Rightarrow A_1 > 0 \\ \Delta_2 > 0 &\Rightarrow A_1 A_2 - A_0 A_3 > 0 \\ \Delta_3 > 0 &\Rightarrow A_1 A_2 A_3 - A_1^2 A_4 - A_0 A_3^2 > 0 \\ \Delta_4 > 0 &\Rightarrow A_4 (A_1 A_2 A_3 - A_1^2 A_4 - A_0 A_3^2) > 0 \end{aligned} \quad (4.81)$$

These relations can also be written as [Den Hartog, 1985]

$$\begin{aligned} A_i > 0, i = 1, 2, 3, 4 \\ A_1 A_2 A_3 - A_1^2 A_4 - A_0 A_3^2 > 0 \end{aligned} \quad (4.82)$$

The lower inequality represents the upper threshold for the mass [Frene, 1990]. The critical mass in terms of stiffness and damping becomes

$$\bar{M} < \frac{A_3 \cdot \text{tr}(B_{ij}) \cdot \det(B_{ij})}{[\text{tr}(B_{ij})]^2 \cdot \det(K_{ij}) + A_3^2 - A_3 \cdot \text{tr}(B_{ij}) \cdot \text{tr}(K_{ij})} \quad (4.83)$$

and in terms of the individual coefficients

$$\begin{aligned} \bar{M}_c &= \frac{K_s}{\gamma^2}, \text{ where} & (4.84) \\ K_s &= \frac{K_{xx}B_{yy} + K_{yy}B_{xx} - K_{xy}B_{yx} - K_{yx}B_{xy}}{B_{xx} + B_{yy}} \\ \gamma^2 &= \frac{(K_{xx} - K_s)(K_{yy} - K_s) - K_{xy}K_{yx}}{B_{xx}B_{yy} - B_{xy}B_{yx}} \end{aligned}$$

There are three different zones for the bearing operation. 1) The mass is smaller than the critical mass. In this case the operation is stable. 2) The mass is equal to critical mass. In this case the equilibrium is marginal and the shaft centre describes a closed orbit. The whirl exists. 3) The mass is greater than the critical mass and the equilibrium is unstable. In order to calculate the shaft motion, in this case, non-linear analysis is required.

4.5 Summary of the Analytical Analysis

Analytical solutions to Reynolds equations in the limiting cases were obtained along with the damping solution of a deep pocket hydrostatic bearing. These solutions can be used to obtain initial estimates for damping when designing a new hydrostatic or hybrid bearing. It also yields estimates of the hydrodynamic load and load angle which can be used in estimating the hydrodynamic effect on the hydrostatic bearing. These estimates represent the absolute maximum possible hydrodynamic effect and in typical case are much larger than the actual hydrodynamic effect. This is discussed in detail in the design section. Also, simple expressions for initial damping were derived.

The key results are summarized in the following paragraph.

Initial damping for the case of short bearing

$$\begin{aligned} \text{Sommerfeld: } B &= \frac{\mu RL^3 \pi}{C^3} & (4.85) \\ \text{Gumbel: } B &= \frac{\mu RL^3 \pi}{2C^3} \end{aligned}$$

Initial damping for the case of long bearing

$$\text{Sommerfeld: } B = \frac{12\mu R^3 L \pi}{C^3} \quad (4.86)$$

$$\text{Gumbel: } B = \frac{12\mu R^3 L \pi}{C^3} \left(\frac{\pi}{2} - \frac{4}{\pi} \right) \approx 0.3 \cdot \frac{12\mu R^3 L \pi}{C^3}$$

Damping at small eccentricities for the case of deep pocket fixed restrictor hydrostatic bearing

$$B = \frac{3\mu L D a n^2 (L - a) \sin\left(\frac{\pi}{n}\right)^2}{\pi C^3 \left(1 + \zeta + 2 \frac{a(L - a)}{\pi b R} \sin\left(\frac{\pi}{n}\right)^2 \right)} \quad (4.87)$$

The approximate hydrodynamic load and load angle is presented in Figure 4.2 and Figure 4.3 respectively.

Chapter 5

DESIGN

In this chapter the fundamental steps required to design a hydrostatic bearing are discussed. First the criteria why a surface self-compensating bearing might be advantageous over traditional design are discussed and then different possibilities to achieve surface self-compensation are introduced. Then a single design is chosen and its performance is evaluated. High speed designs are then presented. Also, a possibility to adjust the bearing clearance shape for certain applications is discussed.

5.1 General Considerations

In the introduction chapter the properties of self-compensating bearings compared to those of fixed compensation were briefly discussed. In this section a comparison between capillary compensated bearing and self-compensated bearing is made. The reason why capillary compensation was chosen to justify the self-compensation is that it operates in laminar flow regime as does the self-compensating bearing. The variable restrictor devices are not considered, because they severely add to the complexity of the bearing system and can not be justified in general use where simplicity is desired.

When designing a bearing system or specifically a hydrostatic bearing following functional requirements must be considered:

- Load capacity

- Stiffness
- Power losses (due to shear and pump)
- Reliability/Robustness
- Cost (installing and maintenance)

In [Wasson, 1996] a number of different designs, both self-compensating and fixed (laminar) restrictor, were characterized. The following non-dimensionalized variables are used to compare the different designs. Load carrying efficiency is defined as

$$\tilde{F} = \frac{F}{P_s LD} \quad (5.1)$$

This is simply the bearing force divided by the cross sectional area multiplied by the supply pressure. This is a function of the bearing eccentricity. In order to get a single number what to compare the load capacity will be defined as the load carrying efficiency at 0.75 eccentricity. The specific stiffness is defined as

$$\tilde{K} = \frac{\tilde{F}}{\epsilon} \quad (5.2)$$

This also is a function of eccentricity. Here the specific stiffness is defines as a initial specific stiffness, meaning it is calculated at zero eccentricity. The specific flow rate is defined as

$$\tilde{Q} = \frac{Q}{\left(\frac{P_s \pi D C^3}{12 \mu L}\right)} \quad (5.3)$$

which is the ratio between the flow through the bearing and the flow through a annulus with same diameter and clearance as the bearing has. This measure indicates the pumping power consumed by the bearing. The specific stiffness or load capacity also acts as an approximate measure for the shear power loss, since shear loss is proportional to bearing surface area and both measures are normalized by the cross sectional area. This works because the bearing has to be designed for a certain load capacity or stiffness and then cer-

tain shear power is obtained depending on the viscosity and the operational speed. It must be noted that the actual shear power is proportional to the surface area, not the cross sectional area of the bearing. Table 5.1 summarizes the aforementioned non-dimensional parameters for different bearing geometries [Wasson, 1996]. These bearings all had L/D ratio of one with $L=80\text{mm}$. Each bearing was optimized for initial stiffness which, in many cases, is the critical characteristic.

Bearings FR1 and FR2 are fixed laminar restrictor bearings and bearings SC1 through SC8 are surface self-compensating bearings where the fluid circuitry is outside the bearing or machined and cross-drilled in shaft. Bearing SC9 is basically the shallow recess bearing discussed in the introductory section and the SC10 is a self-compensating bearing with all the surface geometry internal to bearing, that is on the internal surface of the journal. The gray areas represent areas of larger clearance (grooves).

It can be immediately noted that the shallow recess (groove compensation) design SC9 is not comparable in terms of these performance parameters. However, if the bearing fluid is compressible e.g. air, this design eliminates most stability problems associated with compressibility and it is therefore used in air spindle applications. The second thing to note is that the specific flow rate varies by a factor of 6 depending on the design. The flow rate indicates the pumping power, but also the bearings ability to carry heat away from the bearing. Therefore high flow rate is not necessarily an undesirable feature. The specific stiffness of self-compensating designs is generally better than that of the fixed restrictor ones. The initial stiffness is not better by factor of two, unlike in the Figure 2.2 on page 38, due to the leakage flows in a real bearing. The load carrying efficiency of the fixed restrictor bearings are generally better than in the case of self-compensating bearings. This is due to the fact that more of the total bearing area is carrying load. Any of the designs represented in Table 5.1 could be the best design for a certain application. However, in general terms, since the stiffness is usually more critical than load capacity and the difference in load carrying efficiency is not very large, the self-compensating designs can be said to have slightly better performance.

TABLE 5.1 Non-dimensional parameters for different bearing geometries and types [Wasson, 1996]

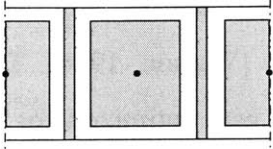
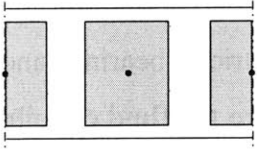
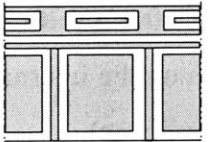
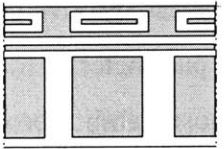
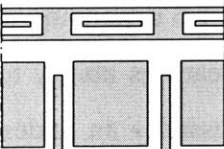
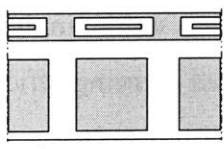
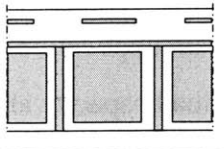
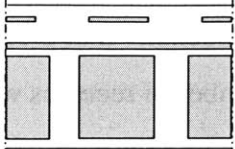
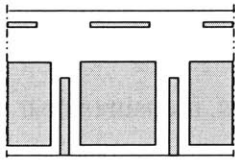
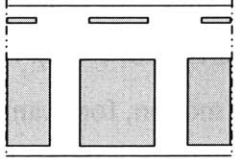
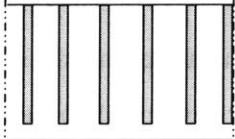
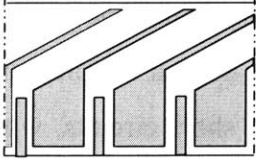
Bearing		\tilde{K}	\tilde{F}	\tilde{Q}
FR1		0.856	0.542	57.4
FR2		0.915	0.562	12.1
SC1		1	0.469	50.5
SC2		1.29	0.54	27.7
SC3		1.16	0.487	26.6
SC4		1.01	0.425	7.3
SC5		0.729	0.323	20.2

TABLE 5.1 Non-dimensional parameters for different bearing geometries and types [Wasson, 1996]

Bearing		\tilde{K}	\tilde{F}	\tilde{Q}
SC6		0.934	0.392	13.6
SC7		1.03	0.453	15.6
SC8		1.03	0.45	8.1
SC9		0.274	0.182	9.6
SC10		1.02 (0.723)	0.337	9.8

Here it must be noted that with design SC10, the angle between the beginning of the groove and the pocket is not 180° . This results to the displacement and the applied force not being parallel, but at 45° angle. This makes the \tilde{K} appear larger than it is in general case. In a situation where only the direction of the load is the critical direction the value in Table 5.1 is valid. In general situation this value would be 0.723. Similar capability can be obtained with self-compensating designs SC1-SC8. This additional design parameter

becomes important when hydrodynamic effects and stability are considered. This is described in more detail in next sections.

The complexity of the system is considered next. In many journal bearing applications the bearing has 6 or more recesses to ensure homogeneity that is same load and stiffness characteristics in all directions. In the past the number of recesses was limited by the complexity of supply system and manufacturing costs and therefore 4 recess bearings are widely encountered. In the self-compensating system the number of recesses is limited only by the land widths and manufacturing cost, the supply system is same for all number off recesses. Six is still a good number of recesses, it ensures near optimal performance [Wasson, 1996] and might be advantageous from the error motion point of view. It is suggested that if the number of recesses is an even multiple of the number of error lobes in the journal the radial error motion are diminished [Stansfield, 1970]. Also there is evidence that a great number of recesses diminishes the error motion, for example in [Sihler, 1998] reduction of error from part accuracy to bearing error motion by factor of 25 was obtained for a 10" diameter rotary table. However, a rotary table had 20 recesses which is not practical in most cases for journal bearings, unless air is used the design SC9. Self-compensating bearings SC1-SC8 all have the fluid circuitry external to bearing. The most convenient way to accomplish this is to connect the compensator pocket to the load pocket by having a groove on the outside surface of the bearing. This requires a precision shrink fit that is fairly strong. It has to be accurate and strong so that the pressurized fluid can not flow to the neighboring grooves thus creating fluid short circuits, which seriously degrade the bearing performance. Bearing SC10 does not require this feature since the fluid circuitry is on the internal surface. This is also very simple design, although manufacturing it can be difficult, specially in a case of bushing. The manufacturing issue is discussed in detail in Chapter 6. This thesis solves the manufacturing issue and the design SC10 becomes very attractive.

The smallest opening in the self-compensating designs is at least two orders of magnitude larger in area than in the capillary compensated bearings. This makes the clogging prob-

lems practically non-existent. The SC10 design is again the most attractive since all the grooves are exposed to the fluid shearing induced by the shaft rotation which makes the clogging even less probable.

The final thing to consider when comparing self-compensating designs to fixed restrictor design is the sensitivity to manufacturing errors in the bearing clearance and in the capillary diameter. These errors are the reason for the expensive and tedious tuning that is necessary for capillary compensated bearings. As mentioned in the introductory section the bearing performance is a function of initial resistance ratio, meaning the ratio between the inlet capillary resistance to the pocket resistance. Equation 5.4 describes the resistance ratio normalized by the intended resistance ratio as function of relative manufacturing errors (error/nominal).

$$\zeta_{ratio} = \frac{\hat{\zeta}}{\zeta} = \frac{(1 + \hat{e}_h)^3}{(1 + \hat{e}_c)^4} \quad (5.4)$$

where \hat{e}_h is the relative error in bearing clearance and \hat{e}_c in capillary radius. This is plotted in Figure 5.1 with the relative errors ranging from -10% to 10% of nominal values. It is obvious from the figure that tuning is necessary, because the initial pressure ratio varies between 0.5 and 2. For self-compensating bearing this parameter is always equal to 1, which means that in the presence of constant manufacturing error the initial pressure ratio is always equal to the designed value.

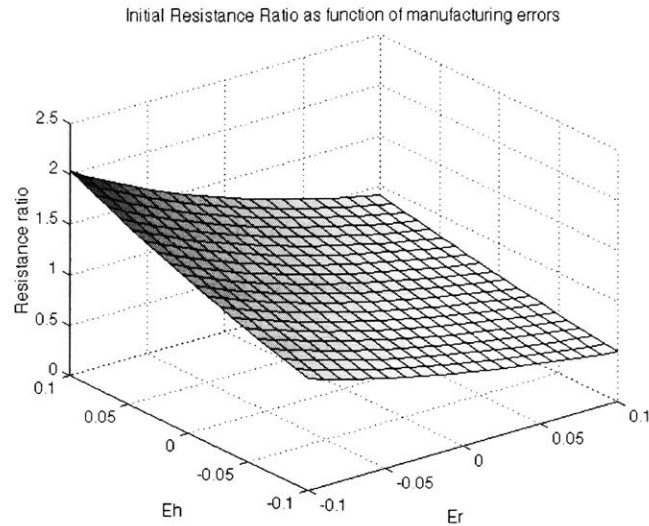


Figure 5.1 Sensitivity of initial pressure ratio to manufacturing errors

To demonstrate the effect of errors in bearing clearance to the initial stiffness of the bearing the stiffness with manufacturing errors normalized by the stiffness without the manufacturing errors are as follows. For capillary compensated bearing

$$\frac{\hat{K}}{K} = \frac{4(\hat{e}_h + 1)^2}{[(\hat{e}_h + 1)^3 + 1]^2} \quad (5.5)$$

and for self-compensating bearing

$$\frac{\hat{K}}{K} = \frac{1}{1 + \hat{e}_h} \quad (5.6)$$

This parameter is plotted as a function of the normalized clearance error in Figure 5.2. This assumes the initial resistance ratio of one, if any errors in clearance would not exist. The capillary compensated bearing is slightly more sensitive to small errors but if large errors exists then the self-compensated bearing becomes clearly superior.

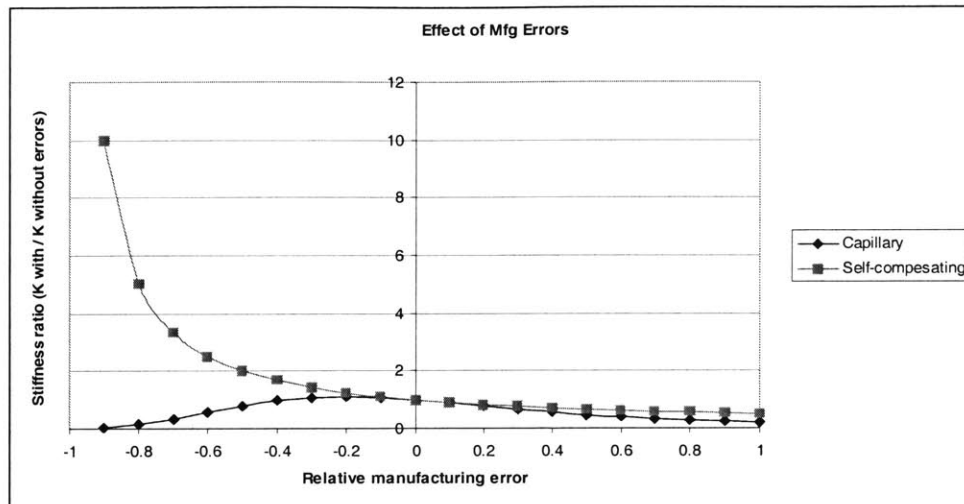


Figure 5.2 Sensitivity to clearance errors.

In summary the surface self-compensating bearings have generally:

- higher stiffness
- less complexity (parts)
- lower probability of clogging
- higher tolerance against manufacturing errors
- lower ultimate load capacity

Results of this comparison determine that in many cases the self-compensating design is superior to fixed restrictor design.

In order to decide between the self-compensating designs more specific goals for the design has to be set. In this work, simplicity, robustness and cost effectiveness are the main goals along with adequate performance. Of these goals the robustness and cost become the critical parameters, because simplicity is achieved when the need for the external compensating devices is eliminated. The most robust of the designs is SC10 because it eliminates the need for the precision shrink fit thus eliminating the possibility of unwanted fluid shorts. Also the grooves are exposed to the fluid shearing to keep them from clogging. Also the design can be manufactured very economically by using manufacturing methods described in Chapter 6. Also this design can be manufactured relatively

easily by machining it to the shaft and was proven to work well that way [Wasson, 1996]. For these reasons the design SC10 was chosen to be manufactured as test bearings in this thesis. The design aspects of this bearing are discussed in the next two sections.

5.2 Low (laminar) Speed

First the main design parameters of the SC10 design are introduced. The most general first order design parameters are the diameter, length, clearance, supply pressure and fluid properties of the bearing. These are the same for any hydrostatic bearing. The second order design parameters are the resistance ratio ζ (inlet/outlet resistance) which determines the stiffness and load carrying behavior as a function of eccentricity. A specific parameter for self-compensating journal bearing is the angular position of the load carrying pocket with respect to compensator (γ in Figure 5.3). This can be utilized to introduce cross-coupled stiffness terms, which in general are bad for stability but can be used to offset the cross-coupling terms introduced by the hydrodynamic effects. This can also be used to make the bearing appear stiffer in a certain direction as explained in previous section. How these bearing design parameters are related to the bearing geometry, in this particular design is shown in Figure 5.3.

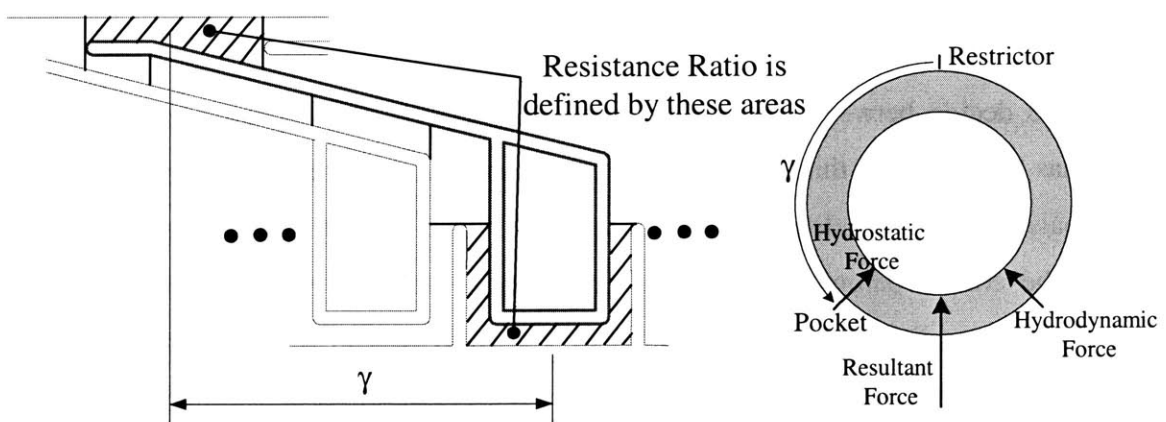


Figure 5.3 Design parameter relation to bearing geometry

Laminar speed designs will address a wide variety of operating conditions, which can be divided into three different groups. First the operating speed in which both the land and groove areas are laminar. Second the operating speed in which the lands are laminar but the grooves transitional. Third the operating speed in which the groove areas are turbulent but the lands are still laminar. The operating conditions where the land flow turns transitional and turbulent are discussed in the next section. The criteria in Table 5.2 can be used to determine if the land and the groove flow are laminar, transitional or turbulent.

TABLE 5.2 Flow regimes for different bearing regions

Bearing Region	Laminar	Transitional	Turbulent
Land	$Re < 1600$	$1600 < Re < 2400$	$Re > 2400$
Groove	$Re < 1000$	$1000 < Re < 2000$	$Re > 2000$

Where the Reynolds number is defined as

$$Re = \frac{\rho V h_i}{\mu} \quad (5.7)$$

where i refers to the land or groove depth.

It is very difficult to define a general design procedure or rules that would be valid in every situation. However, the following procedure is proposed for the initial sizing of the bearing. This procedure can be generalized to most design situations. First it is assumed that the main functional requirement is to be able to carry a given load and/or have a certain stiffness. To first order following equations can be used

$$F = \tilde{F} P_s L D \quad (5.8)$$

where \tilde{F} is typical constant for this type of bearing. Typically value $\tilde{F} \cong \frac{1}{3}$ can be used. The stiffness is

$$K = \tilde{K} \frac{P_s L D}{h} \quad (5.9)$$

where $\tilde{K} \cong 0.7$ for a bearing which is optimized for stiffness (initial pressure ratio of approximately 0.5). If only single sensitive direction exists value $\tilde{K} \cong 1$ may be used. The dependence as a function of resistance ratio is shown in

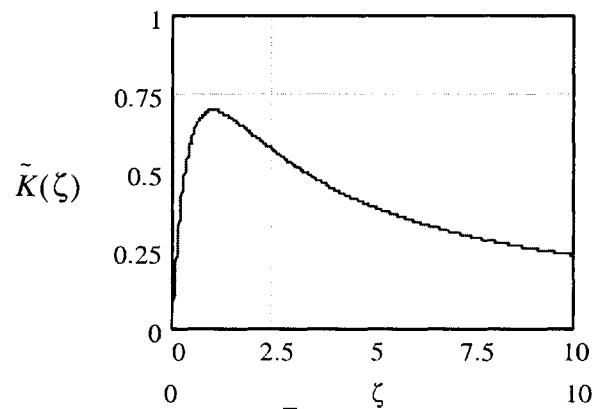


Figure 5.4 \tilde{K} as function of resistance ratio

The flow rate is approximately

$$Q = \tilde{Q} P_s \frac{\pi D h^3}{12 \mu L} \quad (5.10)$$

where $\tilde{Q} \cong 10$. Next the power consumed by the bearing is estimated. The power consists of the power used to shear the fluid within the bearing and the power consumed by pumping the fluid into bearing. Also power is consumed when the fluid is accelerated in the bearing due to the rotation, but this momentum torque can be neglected in most cases [Bassani, 1992]. It can become notable in very high speed cases and will be discussed in the next section when turbulent design are explored. A first order estimate for the shear power is that of shearing between two concentric rotating cylinders with fluid film separating them:

$$P_{\tau} = \frac{1}{4}\mu\pi\frac{LD^3\omega^2}{h} \quad (5.11)$$

The pumping power is

$$P_p = P_s Q \quad (5.12)$$

These provide enough relations to set up the design problem. The shear power estimate is very crude and should only be used for very rough calculations. It works best when the bearing rotates very slowly. In order to estimate the power consumption more accurately, the bearing is divided into two regions, the lands and the grooves. The shearing power consumed by the land areas is derived directly from equation 5.11 and is

$$P_{\tau_{land}} = \frac{1}{4}\mu\frac{\omega^2 D^2}{h} A_{land} \quad (5.13)$$

where A_{land} is the total area of land regions. This relation holds for speeds where the land flow is laminar. The flow in the grooves and recesses can be modeled as cavity flow if the recess depth is at least 10 times the clearance. In cavity flow the fluid circulates within the recess and therefore the velocity gradient, which determines the shear, is no longer linear. Also, the flow becomes turbulent even at relatively slow operating speeds due to the higher clearance. In order to conveniently characterize such flow conditions friction factors are used. These friction factors are non-dimensional parameters and are defined as

$$f_r = \frac{\tau}{\frac{1}{2}\rho V^2} \quad (5.14)$$

where V is the surface speed of the moving member. The power consumed by the recess areas becomes

$$P_{\tau_{recess}} = f_r \frac{1}{2}\rho V^3 A_{recess} \quad (5.15)$$

Here the power will be defined as

$$P_{\tau_{recess}} = \frac{f_r^* \frac{1}{2} \rho V^3 A_{recess}}{Re_p} = \frac{1}{8} f_r^* \mu \frac{\omega^2 D^2}{h_r} A_{recess} \quad (5.16)$$

The total friction power becomes

$$P_{\tau_{tot}} = P_{\tau_{recess}} + P_{\tau_{land}} = \frac{1}{4} \mu \frac{\omega^2 D^2}{h} \left(A_{land} + \frac{1}{2} \frac{h}{h_r} f_r^* A_{recess} \right) \quad (5.17)$$

where the friction factor is [Wasson, 1996]

$$0 < Re_p < 1000 \quad f_r^* = 8 \left\{ 1 + 2.76 \left(\frac{h_p}{L_p} \right) \left[1 + 0.00135 Re_p^{1.09} \left(\frac{h_p}{L_p} \right)^{-0.21} \right] \right\} \quad (5.18)$$

$$1000 < Re_p < 2000 \quad f_r^* = 0.0088 Re_p \left\{ 1 + \ln \left[1 + 2.71 Re_p^{-0.134} \left(\frac{h_p}{L_p} \right)^{3.51 Re_p^{-0.131}} \right] \right\}$$

$$Re_p > 2000 \quad f_r^* = 0.047 Re_p^{0.774} \left\{ 1 + \ln \left[1 + 2.71 Re_p^{-0.134} \left(\frac{h_p}{L_p} \right)^{3.51 Re_p^{-0.131}} \right] \right\}$$

where the $\frac{h_p}{L_p}$ is the depth to length ratio of the grooves. To simplify expressions the equation can be written as

$$P_{\tau_{tot}} = \frac{1}{4} \mu \frac{\omega^2 D^2}{h} A^* \quad (5.19)$$

where A^* is a equivalent friction area. The total power loss is the sum of friction and pumping power

$$P_{tot} = P_{\tau_{tot}} + P_p = (1 + \Pi) P_s^2 \frac{\tilde{Q} \pi D h^3}{12 \mu L} \quad (5.20)$$

where Π is the power ratio (friction power/pumping power).

$$\Pi = \frac{P_{\tau_{tot}}}{P_p} = \frac{3 \mu^2 \omega^2 D L A^*}{P_s^2 \tilde{Q} \pi h^4} \Rightarrow \mu = \frac{P_s h^2}{\omega} \sqrt{\frac{\tilde{Q} \Pi}{3 D L A^*}} \quad (5.21)$$

By substituting μ into equation 5.20 the total power becomes

$$P_{tot} = \frac{(1 + \Pi)}{\sqrt{\Pi}} P_s D h \omega \pi \sqrt{\frac{D \tilde{Q} A^*}{48L}} \quad (5.22)$$

Equation 5.22 is minimized with power ratio equal to 1. This cannot always be obtained and higher power ratios are regularly encountered. In general, higher the speed higher the power ratio. Another important factor when minimizing power is A^* . This is dependent on the recess areas and depths. When the operating speed becomes high it is advantageous to minimize the recess area. This can be done by removing the central land area of the main recess as shown in Figure 5.5. This also improves the damping characteristics of the bearing.

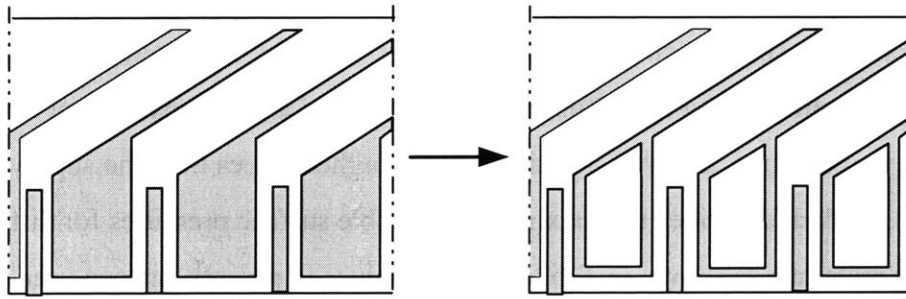


Figure 5.5 Removing central lands to improve high speed frictional characteristics

Now the design problem can be stated the following way:

$$\min(P_{tot}) \text{ w.r.t } L, D, P_s, \mu, h \quad (5.23)$$

subject to constraints

$$F \geq F_s, K \geq K_s, \frac{L}{D} \geq 1, h \geq h_{min} \quad (5.24)$$

In general the clearance should be minimized, but it is subject to practical constraints, namely the accuracy it can be manufactured economically. There also exists standards for the minimum oil film thickness in hydrodynamic bearings and these minimum thicknesses

can also be applied to hydrostatic bearings. Table 5.3 presents these minimum film thicknesses in μm as they are in DIN 31652 standard [Kivioja, 1996].

TABLE 5.3 Minimum film thickness for different bearing sizes and surface speeds

Diameter (mm)	Surface Speed V (m/s)				
	< 1	$1 < V \leq 3$	$3 < V \leq 10$	$10 < V \leq 30$	>30
24...63	3	4	5	7	10
63...160	4	5	7	9	12
160...400	6	7	9	11	14
400...1000	8	9	11	13	16
1000...2500	10	12	14	16	18

Also when selecting the pumping power, practical considerations must be taken into account such as reasonable cost pumps and safety. Also the maximum surface pressure allowed by different bearing materials must be considered and it must be kept in mind that the bearing pressure can, in some situations, reach higher values than the supply pressure. DIN 31652 standard describes the maximum allowable surface pressures for different typical bearing materials as shown in Table 5.4. The values in parenthesis can be used with very small surface speeds and other special cases [Kivioja, 1996].

TABLE 5.4 Maximum allowable surface pressures for different bearing materials

Bearing Material	Maximum Surface Pressure (MPa)
Pb- and Sn alloys	5 (15)
CuPb-alloys	7 (20)
CuSn-alloys	7 (25)
AlSn-alloys	7 (18)
AlZn-alloys	7 (20)

Once the minimization is done the temperature rise of the oil should be checked. This can be done by [Bassani, 1992]

$$\Delta T = \frac{P_{tot}}{Q\rho c} = \frac{P_s}{\rho c}(1 + \Pi) \quad (5.25)$$

For most mineral oils $\rho c \approx 1.6 \cdot 10^6 \text{ J/m}^3 \text{ }^\circ\text{C}$. In order to use the equation 5.22 values for the effective shear area A^* are needed. In Figure 5.6-Figure 5.8 normalized values for A^* are plotted with the bearing diameter as a parameter for a typical bearing. These values can be generalized for the most cases for the bearings with the central pocket lands. The values are normalized by the total bearing surface area πLD .

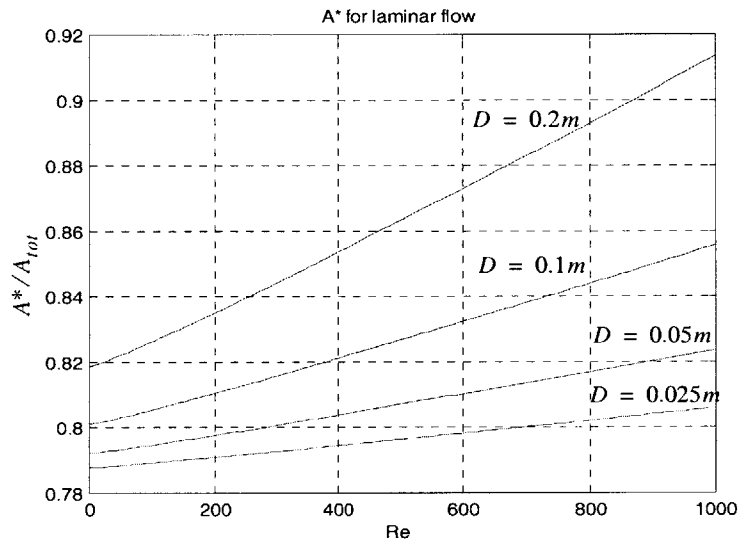


Figure 5.6 Normalized A^* for laminar flow

In this case the recess depth to clearance ratio was 30 with clearance of $25\mu\text{m}$. The Reynolds number figures refer to are the recess Reynolds number. The values of friction factors (and therefore the A^*) do not change discontinuously between the different flow regions in physical world, like they do in Figure 5.6-Figure 5.8. Therefore, if the Reynolds number is close to transition the values obtained can be inaccurate and should be used with care. However, these factors yield good results, as will be seen in the end of this section.

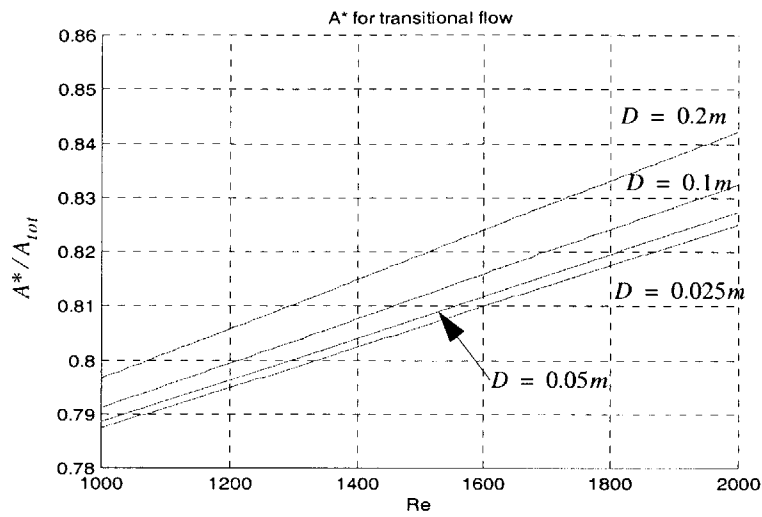


Figure 5.7 Normalized A^* for transitional flow

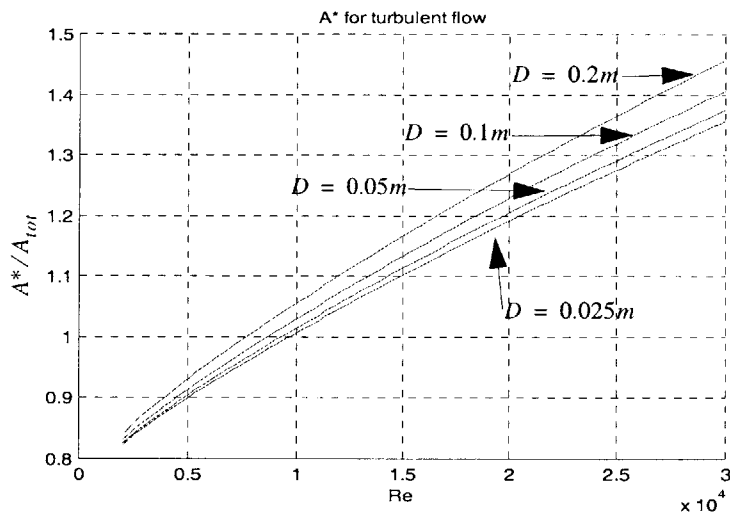


Figure 5.8 Normalized A^* for turbulent flow

For the above discussion a smooth bearing surfaces were assumed. This assumption is valid when estimating the friction power because the friction factors do not vary very much with Reynolds numbers remaining less than 30000. In addition, only the flow in the grooves is turbulent and the relative area of the grooves is small compared to land area. Also the lands areas are smooth.

As the land area with lower clearance is increased (as in Figure 5.5) the hydrodynamic effects can become important. The basics of hydrodynamic pressure formation were introduced in Chapter 4 for different boundary conditions and approximations. Here the validity of those approximations as applied to grooves surface self-compensating bearing are considered.

In this type of bearing, the surface is interrupted with grooves which lessens the hydrodynamic pressure formation. In order to evaluate when the hydrodynamic force starts to have an effect the following analysis is performed. The force analysis is simplified to first order case assuming that the bearing can be modeled approximately by Couette flow between two converging plates. The force of that simplified case is then compared to similar case in which the plates are interrupted by grooves in which the pressure is known ($=0$). Figure 5.9 shows schematically the situation. This ratio can then be used together with force analysis from Chapter 4 to estimate the effect of hydrodynamic pressure formation.

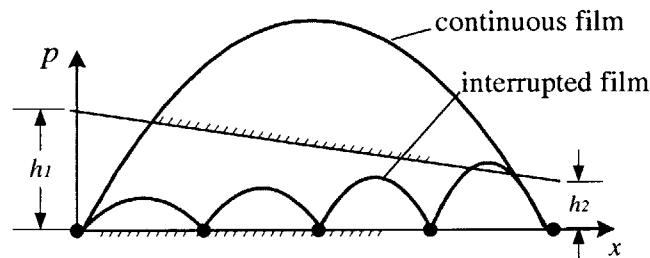


Figure 5.9 Pressure formation in converging gap

The Navier-Stokes equation simplifies in this case to

$$\frac{\partial^2 u}{\partial y^2} = \frac{1}{\mu} \frac{dp}{dx} \quad (5.26)$$

$$+ u(0) = -U, u(h) = 0$$

This is integrated to obtain velocity

$$u(y) = \frac{1}{2\mu} \frac{dp}{dx} (y^2 - hy) + U \left(\frac{y}{h} - 1 \right) \quad (5.27)$$

This then integrated over the gap and solved for the pressure gradient

$$Q = \int_0^h u(y) dy \Rightarrow \frac{dp}{dx} = -\frac{12\mu}{h^3} \left(Q + \frac{1}{2}Uh \right) \quad (5.28)$$

By using a chain rule

$$\frac{dp}{dx} = \frac{dp}{dh} \frac{dh}{dx} = \frac{dp}{dh} \cdot \frac{h_2 - h_1}{L} \quad (5.29)$$

By substituting 5.29 into 5.28 and separating variables and integrating with boundary conditions $p(0) = p(L) = 0$ the flow rate is obtained

$$Q = \frac{h_1 h_2}{h_1 + h_2} U \quad (5.30)$$

By substituting 5.30 back into 5.28 and integrating from 0 to x the following relation for the pressure is obtained

$$p(x) = \frac{6\mu UL}{h^2(h_2^2 - h_1^2)} (h - h_1)(h - h_2) \quad (5.31)$$

By integrating once more the resultant force is obtained

$$F = \int_0^L p dx = \frac{6\mu UL^2}{h_1^2(k-1)} \left(\ln k - 2 \frac{(k-1)}{k+1} \right) \quad (5.32)$$

$$k = \frac{h_2}{h_1}$$

Now the force is derived for the same case except that the plate is divided in to n sections as shown in Figure 5.10.

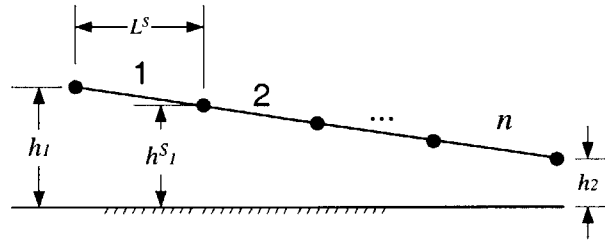


Figure 5.10 Converging gap divided into sections

The h_1 for each segment is

$$h_1^S = h_1 \left(k - i \frac{(k-1)}{n} \right) \quad (5.33)$$

The length of each segment is

$$L^S = \frac{L}{n} \quad (5.34)$$

The ratio k becomes

$$k^S = \frac{k - \frac{(i-1)(k-1)}{n}}{k - \frac{i(k-1)}{n}} \quad (5.35)$$

where i is the index of each segment starting from h_2 . The total resultant force for this case becomes

$$F^S = \sum_{i=1}^n \frac{6\mu UL^2}{n^2 (k^S - 1) h_1^2 \left(k^S - i \frac{(k^S - 1)}{n} \right)^2} \left\{ \ln(k^S) - 2 \frac{(k^S - 1)}{k^S + 1} \right\} \quad (5.36)$$

Now the ratio between the forces is

$$F_{ratio} = \frac{F}{F^S} = \sum_{i=1}^n \frac{n^2(k^S - 1) \left(k^S - i \frac{(k^S - 1)}{n} \right)^2 \left(\ln k - 2 \frac{(k-1)}{k+1} \right)}{(k-1) \left(\ln(k^S) - 2 \frac{(k^S - 1)}{k^S + 1} \right)} \quad (5.37)$$

This is function of only k and n . This is plotted for different values of n as a function of k in Figure 5.11.

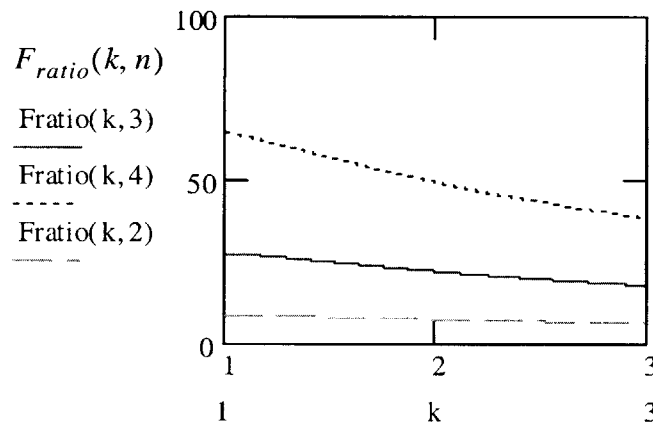


Figure 5.11 Ratio between uninterrupted and interrupted hydrodynamic force

Typically this should be evaluated with $k=2$ and $n = \#pockets/2$. The k value corresponds approximately to an eccentricity of 0.5 which can be considered as maximum eccentricity for most cases. The value of n comes from the cast that the hydrodynamic pressure formation zone is interrupted approximately that many times. For a 6 pocket bearing the $F_{ratio} = 22$ is obtained. Now this value should be used to divide the hydrodynamic force derived in Chapter 4 in order to obtain an estimate of the hydrodynamic effect. This yields

$$W = \frac{\mu LR\omega}{F_{ratio}} \left(\frac{L}{D}\right)^2 \left(\frac{R}{C}\right)^2 \frac{\varepsilon}{(1-\varepsilon^2)^2} [16\varepsilon^2 + \pi^2(1-\varepsilon^2)]^{1/2} \quad (5.38)$$

$$\Rightarrow W \cong (0.14 \cdot \mu LR\omega) \left(\frac{L}{D}\right)^2 \left(\frac{R}{C}\right)^2$$

when $\varepsilon = 0.5$

Now it is of interest to find a limiting value for operating speed or viscosity when the hydrodynamic effect becomes significant. Usually the viscosity is the free design variable since the operating speed is fixed in most cases. The easiest way to do this is to substitute values into equation 5.38 and compare the values obtained to the hydrostatic force values. This problem is not well posed since the hydrostatic force can be altered by altering the supply pressure. By setting the power ratio to a certain value, a closed form solution to the hydrodynamic force can be obtained. Values for power ratio, which have yielded good results in the past vary between 0.5-4 [Bassani, 1992]. By substituting the viscosity from equation 5.21 into equation 5.38 the following formula for the hydrodynamic force as a function of power ratio is obtained

$$W = \frac{0.14}{8} P_s L^2 \sqrt{\frac{\tilde{Q}\Pi}{3\pi A^{**}}} \quad (5.39)$$

where A^{**} is the $A^*/(\pi LD)$ for which a value can be obtained from Figure 5.6-Figure 5.8. This relation shows that the hydrodynamic effect is proportional to square root of the power ratio. As an example, an upper limit for the power ratio ($\Pi = 4$) is chosen [Bassani, 1992]. The ratio between hydrodynamic and hydrostatic forces for bearing with typical geometry ($L/D = 1$) becomes

$$\frac{W}{F_{static}} = 0.0175 \frac{1}{\tilde{F}} \sqrt{\frac{\tilde{Q}\Pi}{3\pi A^{**}}} < 0.2 \quad (5.40)$$

This suggests that the hydrodynamic force will not exceed 20% of the hydrostatic force in any case for eccentricity of 0.5 unless the power ratio becomes very large. In [Bassani,

1992] it is suggested that the power ratio should be <3 . To test the statement of equation 5.40, two example cases are evaluated and described next. First a case where the power ratio is close to 0.5 and then a case where the power ratio has an extreme value of >30 . The latter case is used just to make the hydrodynamic force significant.

In order to evaluate the effect that the hydrodynamic pressure formation has on the bearing performance, a 2.35" bearing is analyzed. The main dimensions of this bearing are summarized in Table 5.5.

TABLE 5.5 Main dimensions of 2.35" bearing

Dimension	Value
D	59.7 mm
L	55.8 mm
h	0.0305 mm
P_s	3.5 MPa
μ	0.0011 Pa s
ρ	995 kg/m ³
N	10 000 rpm

First it is analyzed for static conditions (0 rpm) and then with rotational speed of 10 000 rpm which corresponds to $Re = 850$ at zero eccentricity in the clearance and $Re = 12750$ in the grooves. By comparing these results the effect of the hydrodynamic pressure formation can be determined. Bearing was also analyzed without supply pressure in order to obtain a pure hydrodynamic pressure distribution. The coordinate system used is shown in Figure 5.12.

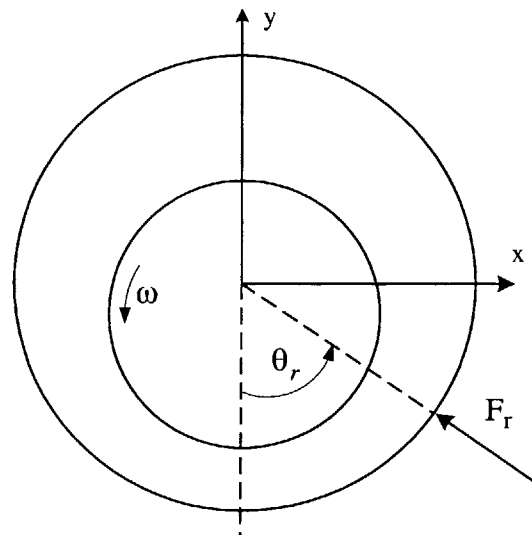


Figure 5.12 Coordinate system for the 2.35" bearing results

The results for the different cases are summarized in Table 5.6.

TABLE 5.6 Summary of the computed results

Eccentricity	Only hydrostatic 0 rpm, $P_s=3.5$ MPa		Hydrostatic and hydrodynamic 10 000 rpm, $P_s=3.5$ MPa		Only hydrodynamic 10 000 rpm, $P_s=0$ MPa	
	F_r (N)	θ_r	F_r (N)	θ_r	F_r (N)	θ_r
0.1	710	44	650	40	18	-110
0.3	1920	46	1750	42	100	-85
0.5	2850	47	2570	42	200	-73
0.7	3420	47	3040	38	415	-53
0.9	3700	48	5060	12	3360	-18

The difference in force between rotating and non-rotating cases is very small as expected. Even at relatively large eccentricity of 0.7 the difference is only about 10%. This can be expected since the power ratio is low. In Figure 5.13 the bearing pressure distribution is shown for rotating and non-rotating case with eccentricity of 0.5. As can be seen there is hardly any evidence of hydrodynamic pressure formation. Also it must be noted that the

hydrostatic pressure is slightly less than in real situation due to the numerical problems having grooves as deep as they are in real manufactured bearings. This was discussed in more detail in modeling section.

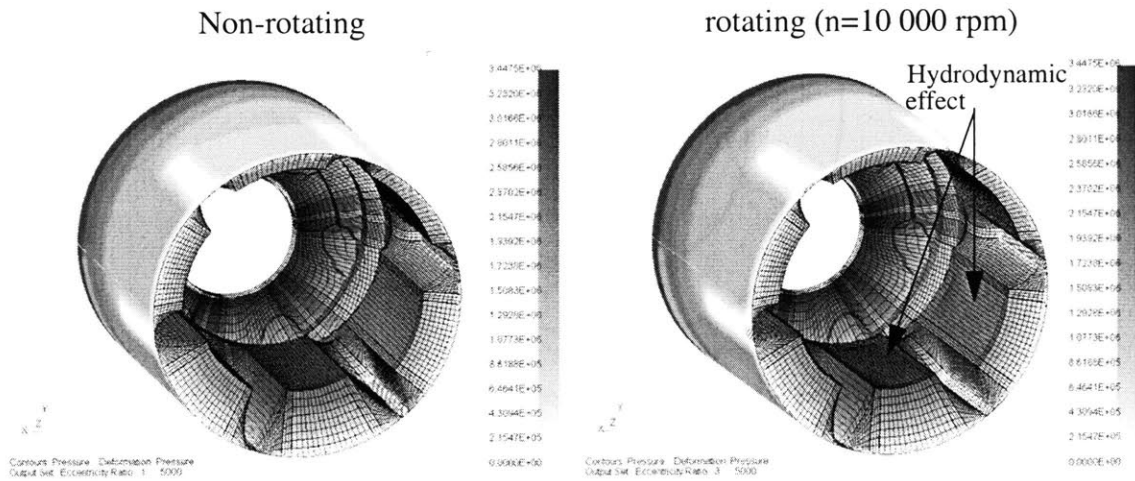


Figure 5.13 Pressure distribution for the grooved and plain bearing with supply pressure ($\epsilon = 0.5$)

In order to get better idea of the purely hydrodynamic effect and to illustrate that the grooves interrupt the pressure formation, the bearing was analyzed without supply pressure. In Figure 5.14 the pressure distribution of the self-compensating bearing without the supply pressure and plain bearing are shown at 0.5 eccentricity. The highest pressure of the plain bearing is an order of magnitude greater than in the case of the grooved bearing (note the different scales for the pressure in Figure 5.14). In Figure 5.15 the force versus the eccentricity is plotted for the hydrostatic, plain hydrodynamic, hydrostatic without supply pressure and the short bearing approximation from Chapter 4. The short bearing approximation is able to predict the plain bearing force fairly well at low to medium eccentricities. Graph also shows how insignificant the pure hydrodynamic effect is for the grooved bearing, which is consistent with the F_{ratio} derived earlier. In Figure 5.16 the force given by the short bearing approximation is divided by the F_{ratio} and compared with the finite difference results. Furthermore, at low eccentricities, the hydrostatic bearing load is higher than for the plain journal bearing, which shows why hydrostatic bearing

is advantageous in precision applications. It should also be mentioned that the plain bearing is unstable at very low eccentricities (<0.01).

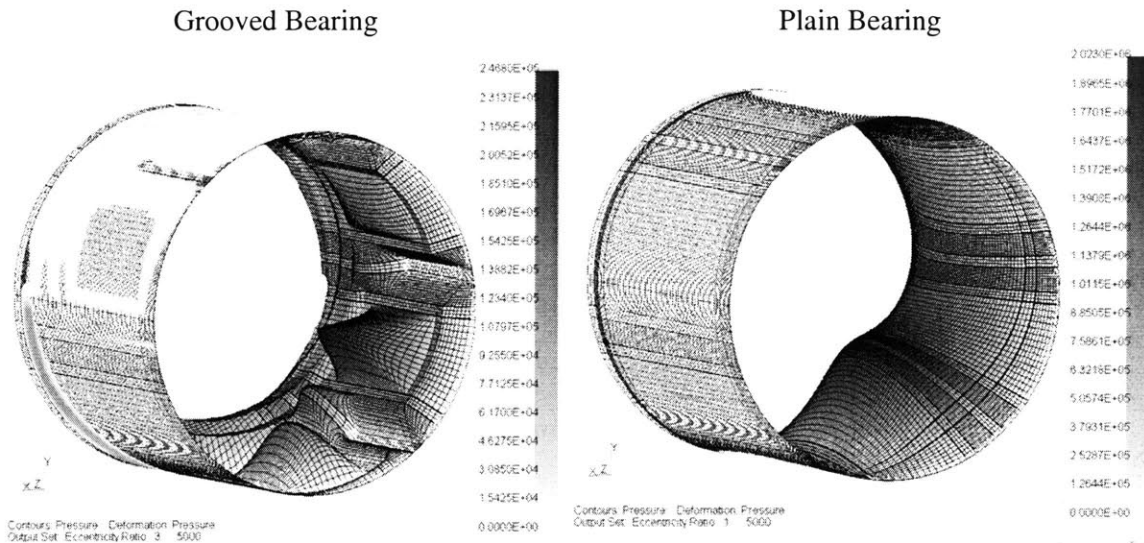


Figure 5.14 Pressure distribution for the grooved and plain bearing without supply pressure ($\epsilon = 0.5$)

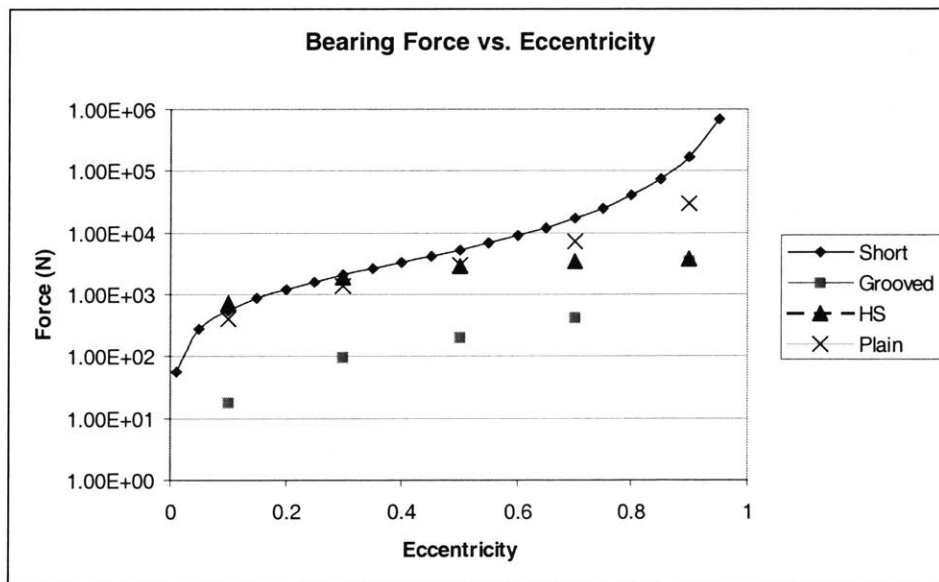


Figure 5.15 Bearing force for different 2.35" bearing cases

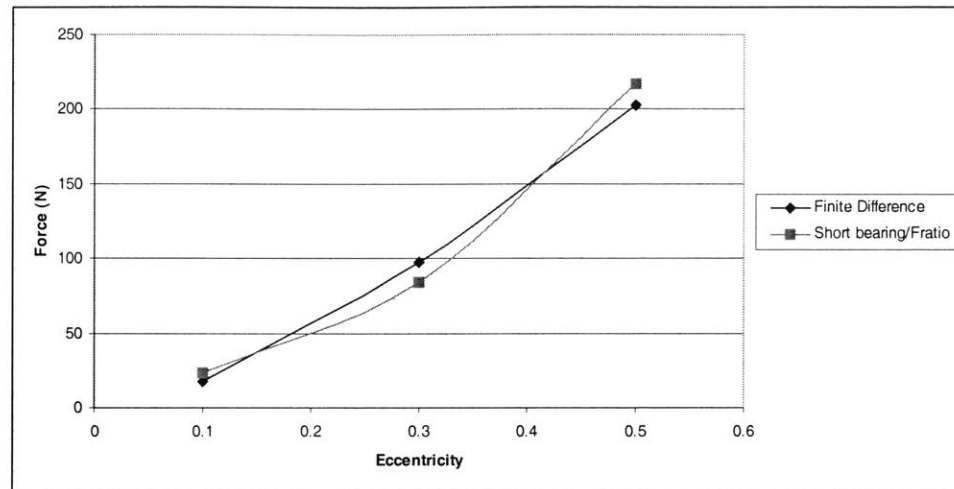


Figure 5.16 Hydrodynamic force of the grooved bearing and the short bearing approximation divided by the F_{ratio}

Only at very large eccentricities (~ 0.9) does the hydrodynamic effect become important. Surprisingly the force of the non-rotating bearing is larger than in the rotating case for most eccentricities. This is due to two effects; first the fluid is pumped back towards the restrictors when bearing is rotating. This acts as extra restrictor hydraulic resistance, which lowers the load and stiffness. In other words it makes the ζ larger than intended. Another effect is the pressure rise in the restrictors due to this effect. The groove end acts as a step bearing creating a pressure step, which can be considerable at high speeds. However, this effect is almost symmetric and therefore does not contribute to load when integrated over the journal. This effect will be discussed in more detail in the next section. Here the stiffness and load capacity loss are mainly due to the added hydraulic resistance due to rotation.

For this case the hydrodynamic effect was very small as expected. In Table 5.7 the finite difference results are compared to the results from the first order approximations derived in this section for the bearing modeled above. The differences are very small and by taking into account that the load and stiffness calculated by finite difference are slightly smaller than real, for reasons explained in modeling section, the errors are reduced even further.

The only significant difference is in the W . This is partly due to fact that the power ratio used to calculate W is calculated at zero eccentricity and the hydrodynamic force is estimated at 0.5 eccentricity. However, this does not matter since the intention is to determine only if the hydrodynamic force is significant.

TABLE 5.7 Comparison between finite difference computed and derived estimated values

Property	1st order estimate	Finite Difference	Difference
$K_{\varepsilon = 0}$	264 $N/(\mu m)$	233 $N/(\mu m)$	13%
$F_{\varepsilon = 0.75}$	3830 N	3500 N	9%
Q	14.9 l/min	16.7 l/min	11%
P_p	860 W	960 W	10%
$P_{\tau_{tot}}$	406 W	403 W	1%
Π	0.47	0.42	11%
W	130 N	200 N	35%

Next a bearing with a power ratio of approximately 38 is presented. This power ratio is very high and should be avoided, if possible. The power ratio is increased by increasing the viscosity to 0.012 $Pa \cdot s$. It is presented here to illustrate what type effects the hydrodynamic pressure formation has. Figure 5.17 shows the pressure distribution for this case. Now the typical hydrodynamic pressure formation is clearly evident. Also it should be noticed that the hydrodynamic effect severely reduces the hydrostatic pressure in the diverging part of the bearing. This is very detrimental to the bearing behavior and can lead to instability by introducing large cross coupling stiffness terms. Here the pressure build up along the grooves is also evident which further reduces the bearing performance.

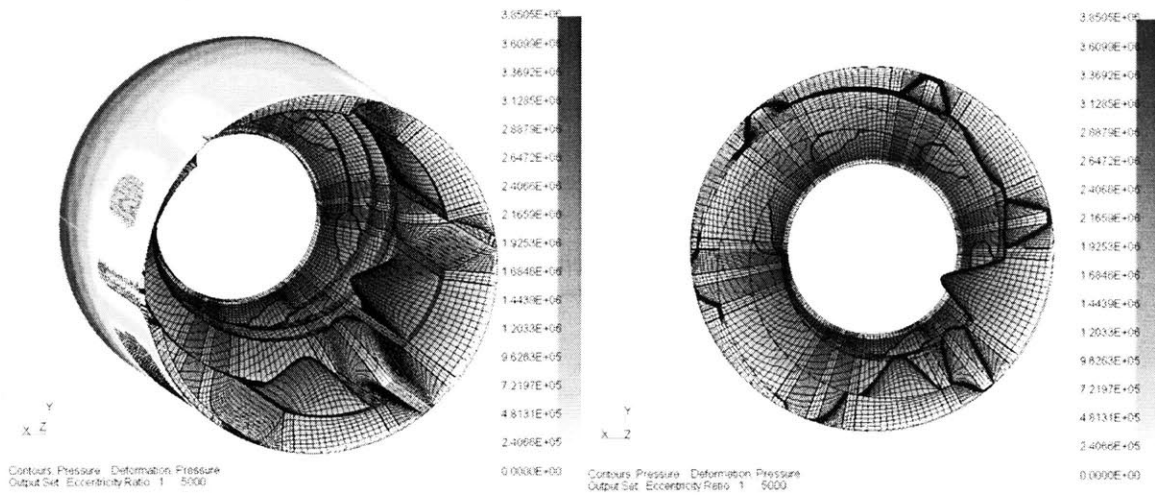


Figure 5.17 Pressure distribution for a bearing with high power ratio (38) ($\epsilon = 0.5$)

In this case the bearing power ratio can be reduced by removing the central land regions in the pocket, because even the groove flow is laminar. Removing the central lands and therefore making the pockets deep will reduce the power ratio to about 25. Figure 5.18 shows the pressure distribution for this case. It is clear that the typical hydrodynamic pressure distribution is removed and more even pressure distribution is obtained and the bearing is more stable. However, the pressure build up along the grooves is still evident. It can be concluded that for higher power ratios the possibility of the hydrodynamic pressure formation should be minimized by removing the bearing lands. Depending on the Reynolds number in the grooves, the friction can either go down (laminar) or up (turbulent) therefore changing the power ratio.

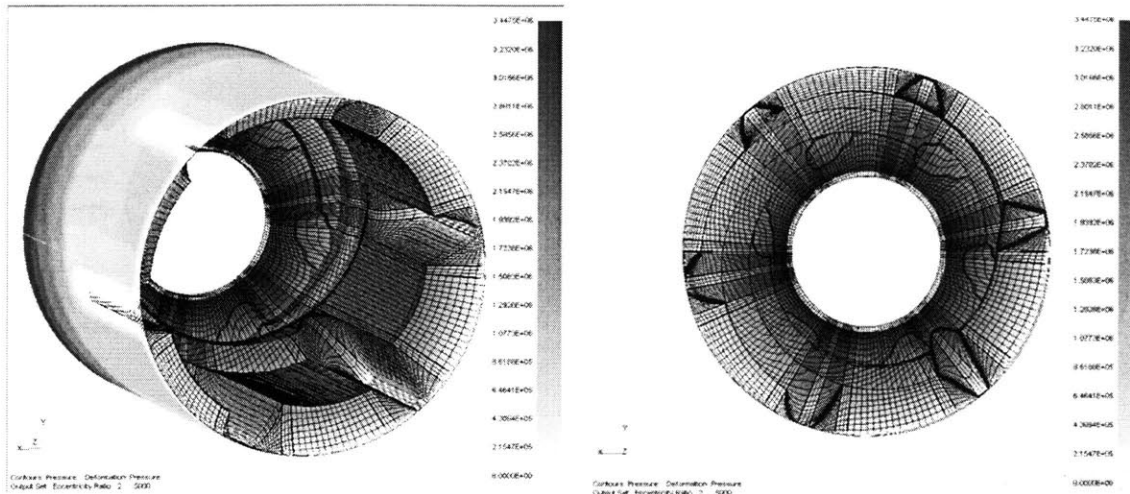


Figure 5.18 Pressure distribution for a bearing with high power ratio (25) ($\epsilon = 0.5$) and central lands removed

In order to test the hypothesis that higher power ratio alone determines if the bearing works, the viscosity for the bearing with lands removed is increased to obtain higher power ratio. Viscosity is increased to $0.019 \text{ Pa}\cdot\text{s}$ and the power ratio becomes approximately 40. Figure 5.19 shows the pressure distribution in this case. Again the hydrodynamic pressure formation is absent, but the pressure build up in the grooves is very high. In fact, the pressure goes to zero for the converging section of the bearing and the restrictor pressure for one of the grooves becomes higher than the supply pressure thus reversing the flow on that part. The zero pressure zones should be avoided, because the oil film will break down, dirt can be sucked into bearing and instability can occur. It is concluded that the bearing behavior is undesirable for higher power ratios, but the power ratio alone can not determine if the bearing will work or not due to the pressure build up effect in the grooves. Removing the central lands allows higher power ratios but care should be taken to analyze every situation if the power ratio exceeds a value of 4.

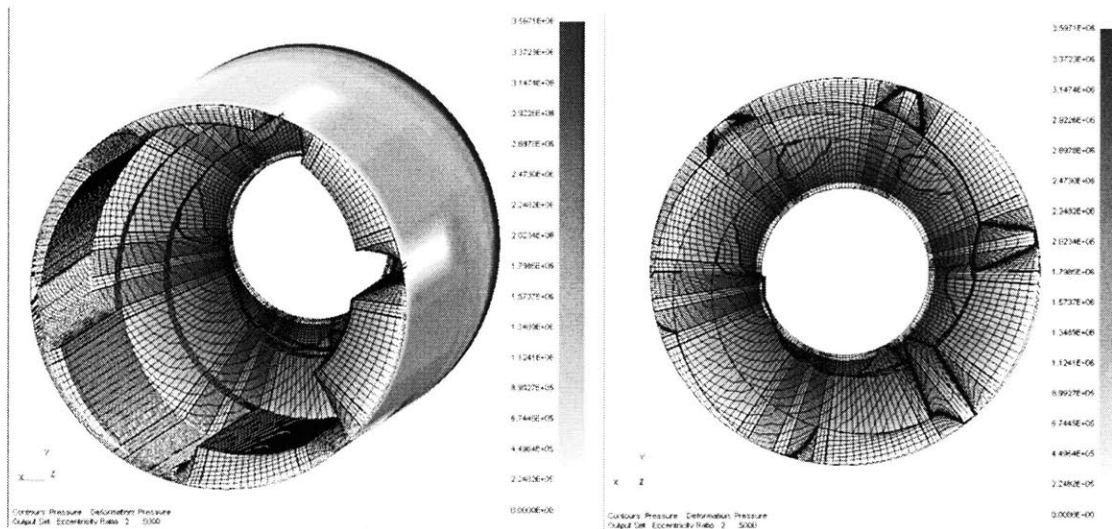


Figure 5.19 Pressure distribution for a bearing with high power ratio (40) ($\epsilon = 0.5$) and central lands removed

As mentioned earlier, the pressure build up along the grooves is a separate effect from hydrodynamic pressure formation and therefore the power ratio can not be successfully used to determine if this effect will be detrimental to bearing behavior. Here a separate non-dimensional variable is derived, which can be used to determine if the pressure rise in the grooves is significant. The surface groove can be thought as a simple step bearing shown in Figure 5.20. It must be noted that here the intention is only to derive a non-dimensional variable, not solve for exact pressure distribution in the groove and therefore such gross simplifications are justified.

Similarly as in the case of flow between converging plates a pressure distribution can be derived for the case in Figure 5.20. The pressure becomes [Pinkus, 1961]

$$p(x) = \frac{6\mu U}{h_1^2} \left[1 - \frac{h_2(L_1 h_2^2 + L_2 h_1^2)}{L_1 h_2^3 + L_2 h_1^3} \right] x, \text{ for part } L_1 \quad (5.41)$$

$$p(x) = \frac{6\mu U}{h_2^2} \left[\frac{h_1(L_1 h_2^2 + L_2 h_1^2)}{L_1 h_2^3 + L_2 h_1^3} - 1 \right] x, \text{ for part } L_2$$

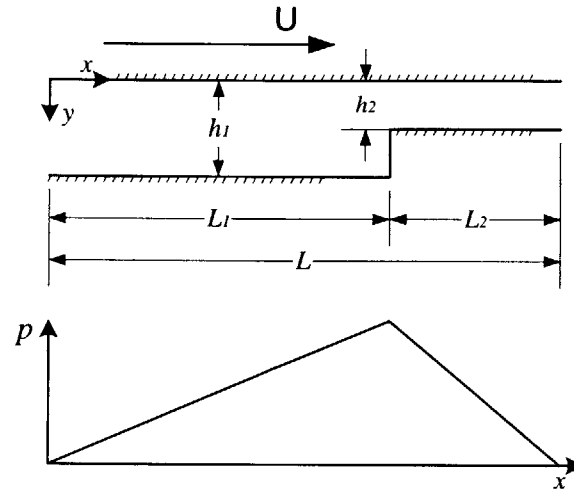


Figure 5.20 Simple step bearing

Here the analysis can be limited to the first equation only, which represents the pressure build up in the groove. This can also be written in form

$$p(x) = \frac{6\mu U}{h_1^2} \left[\frac{1 + \frac{L_1}{L_2} \left(\frac{h_1}{h_2}\right)^2}{1 + \frac{L_1}{L_2} \left(\frac{h_1}{h_2}\right)^3} \right] x \quad (5.42)$$

The coordinate x represents the groove length which is some fraction of the bearing circumference. Also the groove depth is some multiple of clearance. Now equation 5.42 can be written as

$$p = \frac{6\mu U}{h_1^2} \left[\frac{1 + \frac{L_1}{L_2} \left(\frac{h_1}{h_2}\right)^2}{1 + \frac{L_1}{L_2} \left(\frac{h_1}{h_2}\right)^3} \right] aD = \frac{\mu U D}{h^2} \zeta \quad (5.43)$$

where ζ is a number which is a function of geometry only and does not change greatly for different bearing sizes and can therefore be discarded. What is of real interest is the relation of the pressure build up in the groove to the supply pressure of the bearing. Therefore

the result of the equation 5.43 is non-dimensionalized with the supply pressure P_s . The following non-dimensional parameter called pumping ratio is obtained

$$\psi = \frac{\mu UD}{h^2 P_s} = \frac{\mu \omega D^2}{2h^2 P_s} \quad (5.44)$$

By varying this parameter it was determined that pumping ratios less than 6 yielded acceptable results with certain safety margin and pumping ratios greater than 10 are very unlikely to work. In between 6-10 care should be taken and each design should be analyzed. For example the pressure distribution of Figure 5.19 is 11.3. The pumping ratio in a case presented in Figure 5.18 has pumping ratio of 7. It can be noted that the pressure build up noticeable but not yet detrimental.

5.2.1 Summary of Laminar Design Issues

In this section formulas for estimating bearing performance were derived and compared to numerical results obtained with finite difference computations. These initial estimate formulas can be used to estimate the bearing behavior fairly accurately. Parameters called power ratio and pumping ratio were introduced and used to analyze the bearing behavior. Namely, the effect of hydrodynamic pressure formation and pressure build up in the grooves respectively. It was concluded, that at normal [Bassani, 1992] power ratios ($\Pi < 4$) the hydrodynamic effects are very small and can safely be ignored. Most situations fall into this category. For power ratios between 10 and 20 the bearing can work with lands removed and for power ratios over 25 the bearing should not be used. For power ratios 6-10 the bearing design should be analyzed carefully.

5.3 High Speed (Turbulent)

As the operating speed increases, at some point the flow on the bearing lands becomes turbulent. Usually the viscosity has to be decreased as the operating speed is increased to lower the shear power consumption. This results to earlier transition to turbulent flow. In general, turbulence should be avoided if possible. The shear friction increases more rap-

idly once turbulence is introduced and the bearing behavior is more difficult to predict accurately.

When the flow on the lands turns turbulent can be determined by Taylor number. It is defined as

$$N_{Ta} = Re \sqrt{\frac{h}{R}} \quad (5.45)$$

The flow between two concentric cylinders is laminar when $N_{Ta} < 41$, transitional when $41 < N_{Ta} < 63$ and turbulent when $N_{Ta} > 63$. For typical hydrostatic clearance-radius ratios the first transition occurs at Reynolds numbers above 1000 and the second transition around 2000. For small clearance-radius ratios the friction factors are [El Telbany, 1982]

$$0 < Re < 1600 \quad f_l = \frac{2}{Re} \quad (5.46)$$

$$1600 < Re_p < 2400 \quad f_l = 0.00125$$

$$Re_p > 2400 \quad f_l = \frac{1}{2} \left[\frac{0.182}{\log\left(\frac{Re}{4}\right)} \right]^2$$

These factors can be used in equation 5.17 to estimate the bearing power consumption. When bearing is designed to operate in turbulent conditions it is natural to try to see if the same design that worked very well under laminar conditions would work in turbulent flow regime. A relatively small diameter (25 mm) and very high speed bearing (100 000 rpm) will serve as an evaluation bearing for the high speed turbulent design. Major bearing parameters are shown in Table 5.8

TABLE 5.8 Dimensions of 100 000 rpm bearing

Dimension	Value
D	25 mm
L	25 mm
h	19 μ m
P_s	7 MPa
μ	0.0009 Pa s
ρ	995 kg/m ³
N	100 000 rpm

The Reynolds number for this bearing is approximately 2750 in land regions at concentric position. The pressure distribution is shown in Figure 5.21

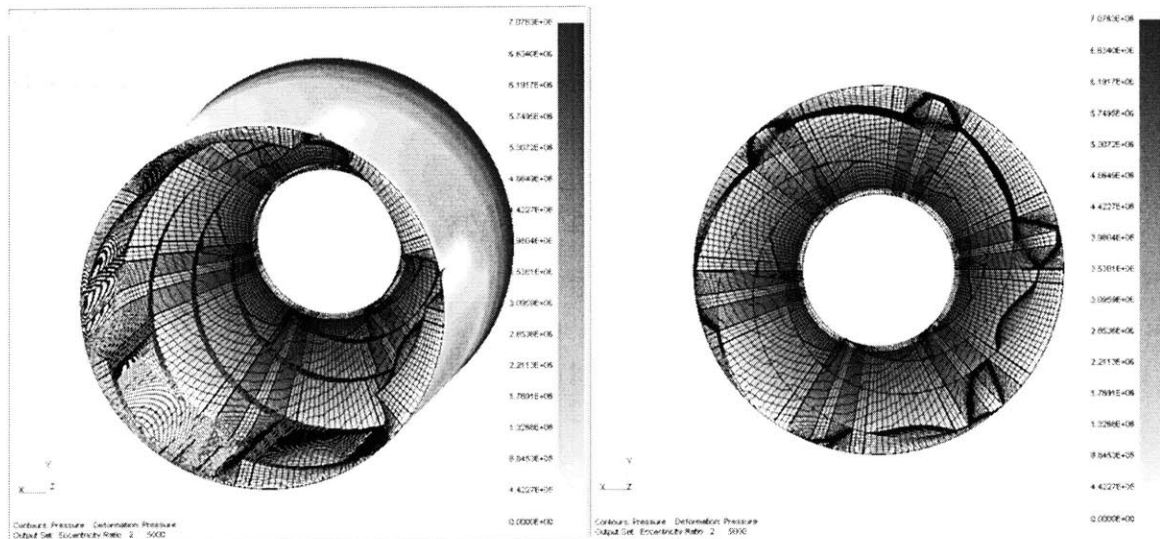


Figure 5.21 Pressure distribution for a high speed (100 000 rpm) bearing $\varepsilon = 0.5$

There is evidence of hydrodynamic pressure formation, but the most detrimental thing is the very large pressure rise in the grooves which causes the pressure to become zero in two of the pockets in the diverging section. This bearing is unstable and contains zero pressure zones. Removing the central lands does not help the situation significantly. Zero pressure zones can be removed by increasing the initial pocket pressure by increasing the pocket

outlet hydraulic resistance. However, these measures are not sufficient in this case and the bearing can not be made to operate with the parameters described in Table 5.8. The previously described pumping ratio can not be applied to turbulent land flow because the wall friction significantly increases as the flow turns turbulent. This causes the pressure rise to become very large in the grooves for almost any situation. Therefore the use of this type of bearing with turbulent land flow is not recommended. Another option, which is attractive in this case since the Reynolds number is relatively close to the laminar region is to try to move the land flow into the laminar flow regime. This can be done by decreasing the clearance and increasing the viscosity. The surface velocity is approximately 130 m/s and from Table 5.3 the minimum allowable film thickness is 10 μm . The clearance should allow for eccentricity without minimum film thickness constraint being violated. In this case the bearing is to operated at low eccentricities, so 15 μm clearance is selected. This allows for 0.3 eccentricity without violating the minimum film thickness constraint. In order to make the land flow laminar a minimum viscosity of 0.002 is needed. Here a viscosity of 0.0025 is selected. Figure 5.22 shows the pressure distribution for this case. Pressure field is calculated at eccentricity of 0.5 in order it to be comparable to the previous case.

The pressure distribution is more even and the hydrodynamic effect is significant as can be expected since the power ratio is very large $\Pi = 70$. The pumping ratio $\psi = 5$ is in safe region. By removing the bearing lands the hydrodynamic effect can be minimized making the bearing more stable, but at the same time load capacity, stiffness and damping are decreased. The summary of the results for the laminar 100 000 rpm bearing is represented for the central land, removed central land, and turbulent design case. Only the laminar cases work in this situation and between them there is a trade of between stability and load capacity and stiffness. It should be noted that these results are for a single bearing. In most applications bearings are used in pairs.

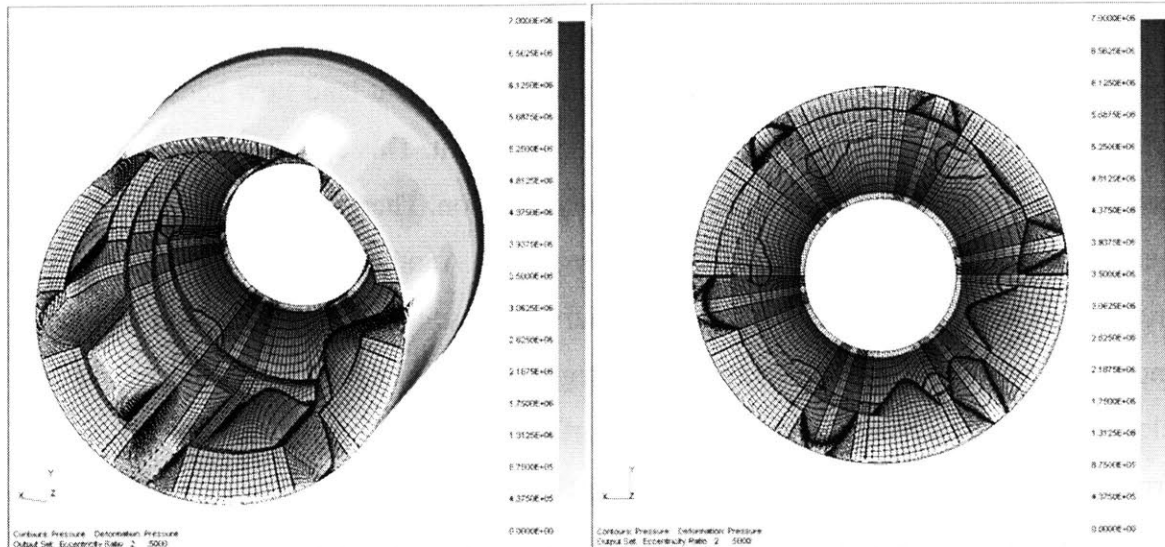


Figure 5.22 Pressure distribution for laminar design at 100 000 rpm $\epsilon = 0.5$

TABLE 5.9 Summary of different high speed cases (100 000 rpm)

Measure	w/o Central Lands	Central Lands	Turbulent
Force (N), $\epsilon = 0.1$	120	150	155
Force Angle ($^{\circ}$)	-41	-51	-110
Pumping Power (W)	90	90	410
Shear Power (W)	5400	5760	6650
Stiffness (N/m)	$\begin{bmatrix} 5.5 & 5.6 \\ -4.7 & 5.6 \end{bmatrix} \cdot 10^7$	$\begin{bmatrix} 6.6 & 10 \\ -9.4 & 8.4 \end{bmatrix} \cdot 10^7$	$\begin{bmatrix} -0.2 & 8 \\ -7.9 & 0.1 \end{bmatrix} \cdot 10^7$
Damping (Ns/m)	$\begin{bmatrix} 2.3 & 0 \\ 0 & 2.3 \end{bmatrix} \cdot 10^4$	$\begin{bmatrix} 2.9 & 0 \\ 0 & 2.9 \end{bmatrix} \cdot 10^4$	$\begin{bmatrix} 1.5 & 0 \\ 0 & 1.5 \end{bmatrix} \cdot 10^4$
Critical Mass (kg)	10.9	6.9	Unstable

In the case described above, it was possible to make the flow on the lands laminar, if this is not practical it is suggested that these exposed groove bearings should not be used. Therefore other designs are suggested. These design are to be used in turbulent land flow which

is very rare and special situation and therefore it can be accepted that the simplicity of the previously described design is lost to obtain acceptable behavior. Since the grooves that connect the restrictors to pockets on the surface are the root of the problem, the most natural solution is to remove them. If the grooves are removed, the compensation has to be either achieved by external devices such as orifices or capillaries or the connecting of the restrictor pockets to load pockets has to be achieved some other way. This can be done by machining the grooves on the external surface and drilling through the bearing body to connect to the pockets. This bearing is then precision shrink fitted into a bore.

Before it was concluded that the grooves should be removed, a number of different grooved designs were tried. Designs included: higher initial pressure ratio, removed central lands, reversed rotational direction and different combinations of these. These design changes failed to yield acceptable performance.

Self-compensation was chosen as the compensation method in order to keep the bearing monolithic without external restricting devices. The first bearing analyzed is the bearing SC5 in Table 5.1. This type of bearing is close to a traditional hydrostatic bearing with deep pockets and small land area. Bearing flow rate is relatively high which is desirable at very high speeds for cooling purposes. Bearing dimensions are the same as in Table 5.8. The pressure distribution is shown in Figure 5.23.

The recirculation pressure gradient is evident in this case causing the trailing edge of each pocket to have higher pressure. This bearing works well at high speeds and is stable. Only drawback is higher shear power due to the relatively large deep recesses. Results are summarized in Table 5.10.

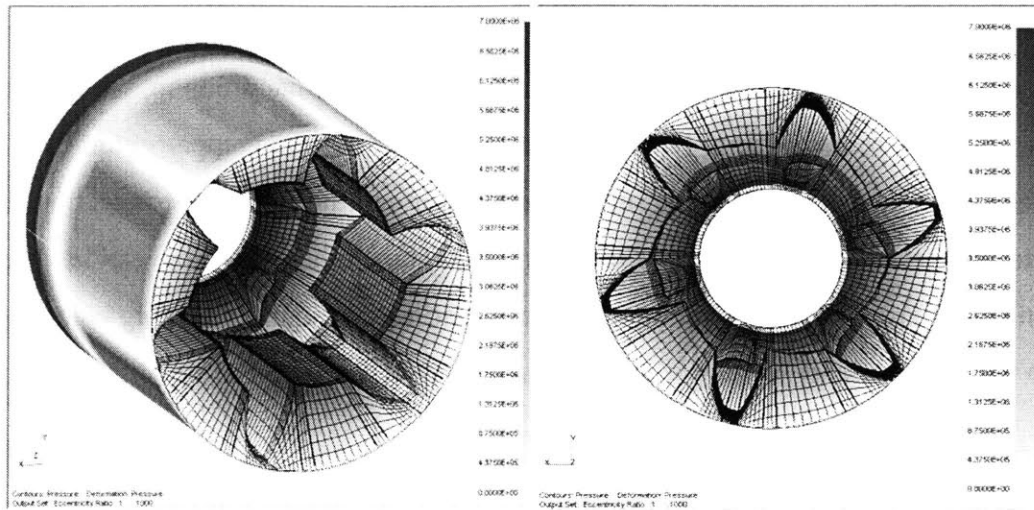


Figure 5.23 Pressure distribution for SC5 design at 100 000 rpm $\epsilon = 0.1$

In order to minimize shear power the pockets can be made smaller in size. This will result in a smaller hydrostatic forces, but depending on the specifications it can still be used. By removing grooves in between the pockets the shear power and flow rate can be reduced further (design SC6 in Table 5.1). This also has an effect on hydrodynamic pressure formation which becomes more significant which is evident from the increased load capacity. No visual evidence of this formation can not be seen in pressure distribution.

As can be seen from the Table 5.10 the large recess bearing has the highest shear power and the small recess the smallest. The small recess bearing without the drainage grooves has the highest load capacity due to the largest hydrodynamic effect and larger high pressure areas. The typical hydrodynamic pressure distribution is not clearly evident only by looking at the pressure distribution as can be seen from Figure 5.24, but can be noticed by observing the pressure in between the recesses. The trade off is in stability. The cross-coupling stiffness terms are clearly larger in the case of the small recess bearing which is evident from the large load angle. Unfortunately, due to the special technique (see modeling section) used to model these type of bearings where the oil film is non-continuous but contains fluid paths outside the bearing bore reliable stiffness numbers were not obtained. Therefore stability could not be calculated. By using engineering judgement it can be

stated that the large pocket design is most likely to be most stable and the small recess without drainage grooves the least stable. Although the small recess bearing has the highest damping. Also the initial recess pressure rises more for the small pocket designs than for the large pocket design.

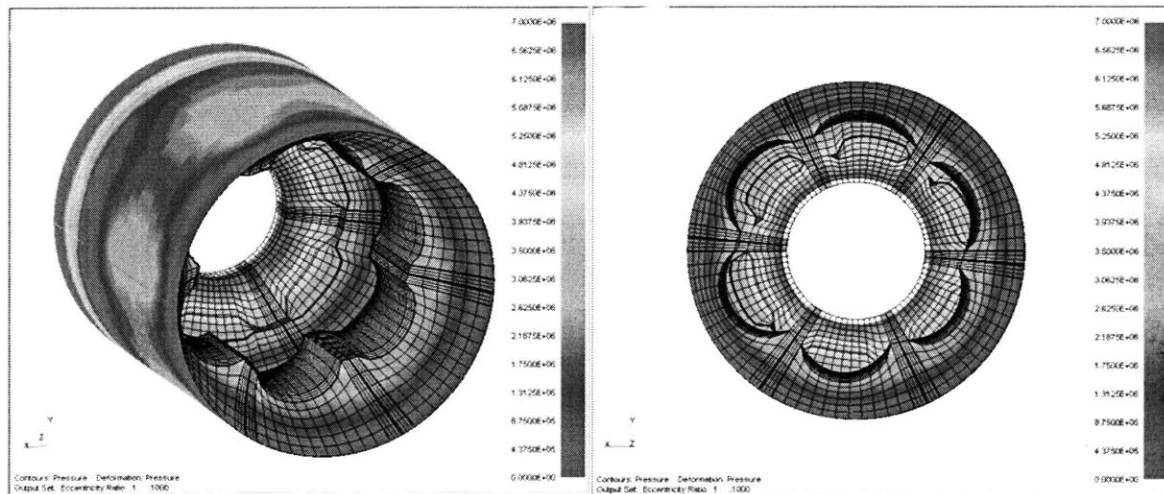


Figure 5.24 Pressure distribution for SC6 small recess design at 100 000 rpm. $\varepsilon = 0.1$

It should be noted that all the results based on the finite difference method are subject to certain possibility of errors. The bearing behavior change when the land flow becomes turbulent is not as sudden in reality as the computational results indicate. These possible errors are explained in more detail in the modeling section.

TABLE 5.10 Summary of the high speed designs (100 000 rpm)

	SC5	SC5 small recess	SC6 small recess
Measure			
Force (N), $\varepsilon = 0.1$	315	180	340
Force Angle ($^{\circ}$)	10	-29	-73
Pumping Power (W)	700	430	350
Shear Power (W)	8470	7480	6440
Pp/Ps @ 0 rpm	0.3	0.3	0.3
Pp/Ps @ 100 000 rpm	0.5	0.55	0.58
Damping (Ns/m)	$\begin{bmatrix} 0.8 & 0 \\ 0 & 0.9 \end{bmatrix} \cdot 10^4$	$\begin{bmatrix} 1.3 & 0 \\ 0 & 1.4 \end{bmatrix} \cdot 10^4$	$\begin{bmatrix} 3.7 & 0 \\ 0 & 3.9 \end{bmatrix} \cdot 10^4$

5.4 Adjustable Clearance and Shape

In some cases it might be desirable to adjust the bearing clearance. One reason is that if the bearing can be adjusted slightly the manufacturing tolerances can be loosened. Also in one special application, namely a steady rest for large lathes and grinding machines a adjustable clearance is necessary. Since the machining operation removes material and therefore makes the diameter of the machined part smaller the bearing clearance has to be adjusted to keep stiffness and flow rate constant or nearly constant.

First, a displacement relations are derived for two concentric cylinders with different internal and external pressure with different material properties. Also the diameters are different. These relations are also useful in determining displacements and stresses for shrink fits, which are often used to hold the bushing in a housing. A convenient starting point for deriving these relations is the Naviers displacement equations of motion [Malvern, 1969]

$$(\lambda + \mu)(\nabla(\nabla \cdot \mathbf{u})) + \mu \nabla^2 \mathbf{u} + \rho \mathbf{b} = \rho \frac{\partial^2}{\partial t^2} \mathbf{u} \quad (5.47)$$

+Boundary Conditions

where λ and μ are the Lamé constants. By assuming plain strain and radial symmetry ($u_\theta = u_z = 0$) and negligible body forces in static case the equation 5.47 simplifies to

$$\frac{d^2 u}{dr^2} + \frac{1}{r} \frac{du}{dr} - \frac{u}{r^2} = 0 \quad (5.48)$$

where $u = u_r$. This relation can also be derived easily from the equilibrium of a infinitesimal radial section. Equation 5.48 has solutions of the form

$$u = C_1 r + \frac{C_2}{r} \quad (5.49)$$

where C_1 and C_2 are constants which can be determined from boundary conditions. The strains are

$$\varepsilon_r = \frac{\partial u}{\partial r} = C_1 - \frac{C_2}{r^2}, \varepsilon_\theta = \frac{u}{r} = C_1 + \frac{C_2}{r^2}, \varepsilon_{r\theta} = 0 \quad (5.50)$$

Hooke's law relates the strains to the stresses. For convenience the general form is represented in tensor notation

$$\sigma_{ij} = \lambda \varepsilon_{kk} \delta_{ij} + 2\mu \varepsilon_{ij} \quad (5.51)$$

In the case of plain strain and in radial co-ordinates the stresses become

$$\begin{aligned}\sigma_r &= 2C_1\lambda + 2GC_1 - \frac{2GC_2}{r^2} \\ \sigma_\theta &= 2C_1\lambda + 2GC_1 + \frac{2GC_2}{r^2} \\ \tau_{r\theta} &= 0, \sigma_z = 4C_1\nu(\lambda + G)\end{aligned}\quad (5.52)$$

First the stresses and displacements are derived for a single cylinder with internal and external pressures. This situation is shown in 5.25

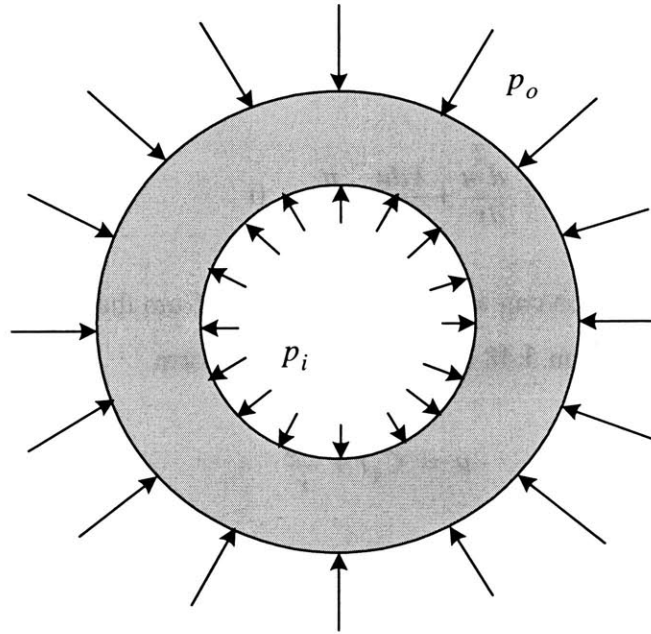


Figure 5.25 Cylinder with internal and external pressure

$$\begin{aligned}\sigma_r(r_i) &= \frac{E}{1-\nu^2} \left(C_1 - \frac{C_2}{r_i^2} + \nu \left(C_1 + \frac{C_2}{r_i^2} \right) \right) = -p_i \\ \sigma_r(r_o) &= \frac{E}{1-\nu^2} \left(C_1 - \frac{C_2}{r_o^2} + \nu \left(C_1 + \frac{C_2}{r_o^2} \right) \right) = -p_o\end{aligned}\quad (5.53)$$

Solving for C_1 and C_2

$$C_1 = \frac{1-\nu}{E} \left(\frac{r_i^2 p_i - r_o^2 p_o}{r_o^2 - r_i^2} \right) \quad (5.54)$$

$$C_2 = \frac{1+\nu}{E} \left(\frac{r_i^2 r_o^2 (p_i - p_o)}{r_o^2 - r_i^2} \right)$$

The displacement is

$$u(r) = \frac{1-\nu}{E} \left(\frac{r_i^2 p_i - r_o^2 p_o}{r_o^2 - r_i^2} \right) r + \frac{1+\nu}{E} \left(\frac{r_i^2 r_o^2 (p_i - p_o)}{r_o^2 - r_i^2} \right) \frac{1}{r} \quad (5.55)$$

and the stresses are

$$\sigma_r = \left(\frac{r_i^2 p_i - r_o^2 p_o}{r_o^2 - r_i^2} \right) - \frac{r_i^2 r_o^2 (p_i - p_o)}{r_o^2 - r_i^2} \frac{1}{r^2} \quad (5.56)$$

$$\sigma_\theta = \left(\frac{r_i^2 p_i - r_o^2 p_o}{r_o^2 - r_i^2} \right) + \frac{r_i^2 r_o^2 (p_i - p_o)}{r_o^2 - r_i^2} \frac{1}{r^2}$$

$$\sigma_z = 2\nu \frac{r_i^2 p_i - r_o^2 p_o}{r_o^2 - r_i^2}; \tau_{r\theta} = 0$$

If the ends of the cylinder are free to move the stresses in longitudinal direction vanish i.e. $\sigma_z = 0$. It is of interest to know what is the maximum possible displacement that can imposed on the internal diameter of the cylinder. This a function of the material properties and the cylinder size and the internal and external pressures. For ductile material the maximum shear stress hypothesis can be used as a failure criteria [Ugural, 1987]. For this case the failure criteria is

$$\tau_{max} = \frac{1}{2}(\sigma_\theta - \sigma_r) < \sigma_{failure} \quad (5.57)$$

The failure will occur at the internal surface, in which case the criteria yields

$$\frac{p_i - p_o}{1 - \left(\frac{r_i}{r_o}\right)^2} = \frac{p_i - p_o}{1 - g^2} < \sigma_{failure} \quad (5.58)$$

where g is the ratio of internal and external diameter. By inserting 5.58 into 5.55 at internal surface the following relation for the displacement is obtained

$$u(r_i) = \frac{\sigma_{failure}}{E} \left[(1 - \nu) \left(\frac{g^2 - P}{1 - P} \right) + (1 + \nu) r_i \right] \quad (5.59)$$

where P is the ratio between external and internal pressure. By letting the internal pressure to approach zero, or by noting that in order to impose displacement to internal surface the difference between internal and external pressure must be large, equation 5.59 becomes

$$u(r_i) = \frac{\sigma_{failure}}{E} [(1 - \nu) + (1 + \nu) r_i] \quad (5.60)$$

For typical materials the yield stress over the Young's modulus is approximately 1/1000 and Poisson's ratio is approximately 0.3. This lead to approximate maximum displacement for typical bearing sizes of

$$u_{max} \approx \frac{0.75}{1000} r_i \quad (5.61)$$

This shows that the clearance can be changed, at maximum, about the order of clearance for typical bearing sizes.

Next the displacements and stresses are derived for the case of locational or shrink fit. First a displacement of internal surface of a cylinder with internal pressure is

$$u_{Ili} = \frac{p^* r_{Ili}}{E_{II}} \left(\frac{r_{Ili}^2 + r_{IIo}^2}{r_{Ili}^2 - r_{IIo}^2} + \nu_{II} \right) \quad (5.62)$$

This is the displacement of the inner surface of the outer cylinder. Next a displacement of the inner cylinder interface surface is

$$u_{I_o} = \frac{-p^* r_{I_i} \left(\frac{r_{I_i}^2 + r_{I_o}^2}{r_{I_i}^2 - r_{I_o}^2} - \nu_I \right)}{E_I} \quad (5.63)$$

where p^* is the interface pressure. The sum of displacements is equal to the interference specified by the type of fit selected

$$|u_{I_o}| + |u_{II_i}| = \delta \quad (5.64)$$

Substituting equations 5.62 and 5.63 into equation 5.64 and solving for p^*

$$p^* = \frac{\delta}{r_{I_o}} \left[\frac{1}{E_I} \left(\frac{r_{I_i}^2 + r_{I_o}^2}{r_{I_i}^2 - r_{I_o}^2} - \nu_I \right) + \frac{1}{E_{II}} \left(\frac{r_{II_i}^2 + r_{II_o}^2}{r_{II_i}^2 - r_{II_o}^2} + \nu_{II} \right) \right]^{-1} \quad (5.65)$$

Once the interface pressure is known the stresses can be solved to make sure that shrink fit does not yield the material. This will not happen if the interference values are obtained from tables provided by ANSI and ISO standards for example in [Oberg, 1996]. What is more of interest is the displacement of the internal surface due to the shrink fit, since this determines how much material has to be removed to obtain the specified internal diameter. In some cases it might be acceptable to machine the bearings before fitting them to housing. In this case the clearance would be smaller than intended by amount of this displacement assuming it was at the intended value before fit. The displacement of the internal surface due to fit is

$$u_{I_i} = -\frac{2p^* r_{I_o} r_{I_i}}{E_I (r_{I_o}^2 - r_{I_i}^2)} \quad (5.66)$$

If the bearing clearance is to be changed this must be done by forcing the outer surface of the bearing assembly. To calculate the displacement of the internal surface the same approach that was used earlier can be used. Namely, having constraint that the interface surfaces must remain in contact and therefore have the same displacements. The interface pressure is taken to be the unknown and solved for. The stresses obtained must be added to the stresses caused by the interference or locational fit.

The above analysis is for idealized case of smooth cylinders under plane strain. It does not take into account stress concentrations caused by the grooves on the bearing surface. These will make the largest possible adjustment possible even smaller. This makes the adjusting unpractical for smaller bearing sizes. In practise, if approximately 0.001" shrink fit is used it will cause stresses in the bearing that in the order of 2-15 ksi for 6-1.25" internal diameters, respectively. Yield strength for typical bearing bronze is in the order of 20-25 ksi. This means that a smaller bearing can not be adjusted basically at all if shrink fit is used to secure the bushing in the bearing housing. A 2 ksi maximum stress is result of approximately 0.0002" change in internal diameter for 6" ID bearing. Taking into account stress concentrations maximum displacement that can be imposed is in the order of 0.0015". If larger displacements than this are desired then the elastic deformation approach is not practical.

5.5 Summary of Design

Here all the first order estimates necessary to estimate the bearing performance are summarized. All the expressions are explained and derived in the previous section. These relations are derived for laminar land flow and for the bearing geometry described earlier.

Load capacity:

$$F = \tilde{F} P_s L D \text{ where } \tilde{F} \cong \frac{1}{3} \quad (5.67)$$

Initial stiffness:

$$K = \tilde{K} \frac{P_s L D}{h} \text{ where } \tilde{K} \cong 0.5 - 1 \quad (5.68)$$

Flow rate:

$$Q = \tilde{Q} P_s \frac{\pi D h^3}{12 \mu L} \text{ where } \tilde{Q} \cong 10 \quad (5.69)$$

Shear power:

$$P_{\tau} = \frac{1}{4}\mu\pi\frac{LD^3\omega^2}{h} \quad (5.70)$$

(for more accurate prediction see equation 5.17)

Pumping power:

$$P_p = P_s Q \quad (5.71)$$

Power ratio:

$$\Pi = \frac{P_{\tau_{tot}}}{P_p} = \frac{3\mu^2\omega^2 DLA^*}{P_s^2 Q \tilde{\pi} h^4} \quad (5.72)$$

where A^* can be found from Figure 5.6-Figure 5.8. The hydrodynamic effects can safely be discarded if this parameter is less than 4. For higher power ratio values are acceptable but bearings should be analyzed more carefully. One way to lessen the hydrodynamic effects is to remove the central bearing lands. This will lessen damping. It should also be noted that the hydrodynamic effects not necessarily detrimental to bearing performance.

Pumping ratio:

$$\psi = \frac{\mu UD}{h^2 P_s} = \frac{\mu \omega D^2}{2h^2 P_s} \quad (5.73)$$

This parameter estimates how severely the fluid is being pumped back toward restrictors by the bearing rotation. If this parameter exceeds the value of 6 great care should be taken when designing the bearing and the bearing should be analyzed carefully. If this parameter has high values it is recommended that the bearing circuitry is removed to the outside surface of the bushing.

Chapter 6

MANUFACTURING

In this chapter alternative methods for manufacturing the bushings are presented. The selected methods are then described in detail. Shrinkage and dimensional variation is determined by measuring dimensions in prototype bearings and then compared with figures obtained from literature. The effect of manufacturing errors to bearing performance will be analyzed using models described in Section 6.4 and statistical methods (Monte-Carlo method).

6.1 Selecting a Manufacturing Method

The fairly complex surface geometry of the bushing makes their manufacturing non-trivial. Also different sizes pose additional constraints on different methods.

The main requirements for various potential manufacturing methods are:

- Cost effectiveness
- Ability to form required geometries
- Flexibility to produce many alternative sizes
- Ability to use selected materials
- Ability to meet required tolerances

In Table 6.1 different methods considered are summarized.

TABLE 6.1 Possible bushing manufacturing methods

Mfg. Method	Cost	Part Size Constraints	Tolerances	Special
Sand Casting	+	ID>2.5"	~0.05"	Core box
Die Casting	0 ^a	ID, Length	~0.01"	Collapsible core
Investment Casting	+	Wall thickness	~0.005"	RP wax model
Injection Molding	(++) ^b	Wall thickness, ID, Length	~0.005"	Collapsible core
Machining	-	ID	~0.001"	90° angle end-mill
EDM	-	Tooling	~0.001"	Tooling

a. Expensive mold. Otherwise similar to sand casting

b. Expensive mold and limited materials

Sand Casting

Sand casting is a flexible manufacturing method in terms of part size and material. Its shortcomings include fairly low accuracy and rough surface finish. In order to produce geometry required for the surface self-compensated bushing a special core box is needed in order to manufacture the internal geometry of the bushing. This special core constraints the internal diameter of the bushing to larger than approximately 2.5".

Sand casting was chosen to manufacture the large 6" prototype bushing. The method, as it is applied in this case, will be described in detail in Section 6.2.

Die Casting

In die casting the molds are expensive to manufacture, but once made can be used multiple times. Material selection is also great and the tolerances are generally better than in sand casting.

In this application the internal surface geometry requires a collapsible core, which is not readily available for metal castings. Also the length of the internal core poses problems for the use of collapsible core. Hence die casting is not considered further as a possible manufacturing method

Investment Casting

Investment casting uses plastic or wax patterns to produce the mold, therefore for every part produced, a wax pattern must be manufactured. Usually this is done with separate molds, but in this case the internal geometry prohibits the use of simple mold. New manufacturing methods called rapid prototyping allows the fast and relatively cost effective way of making wax or plastic patterns of complex geometry. Tolerances produced by investment casting are good, provided the tolerances of the pattern are good. Accordingly investment casting was chosen to manufacture small 1.25" ID bushings and the method, as it is used in this case, is described in detail in Section 6.3.

Injection Molding

Injection molding is very cost effective if a large number of parts is needed. For smaller batches the expensive molds will raise the unit price. The material selection is limited by the high surface pressures in the bearing, which only few plastics can withstand. One possible material is Delrin. Internal geometry of the bushing will require a collapsible core, which are available for injection molding. The use of collapsible core poses constraints on the length and the diameter of the bore. The wall thickness must also be as small as possible to avoid molding problems and to minimize cooling time. In summary, it is possible to use injection molding as a manufacturing method for mass producing smaller size bushings.

Electric Discharge Machining (EDM)

Electric discharge machining can be used to make complex geometries, but it is fairly expensive and slow. EDM can produce very good tolerances and surface finishes. It is not

easily applicable to this case but with specialized tooling and machine it could be used if, for some reason, very accurate surface geometry is needed.

Machining (milling)

Machining can be easily applied to produce the necessary surface geometry if the grooving is made on the rotary part [Wasson, 1996]. If a bushing is produced, a 90° spindle is needed and the internal diameter must be large enough for the tool to operate in. Tolerances of the grooving geometry produced this way would be good, but it is fairly expensive and slow compared to casting the bushings. Trade off between the accuracy and cost are discussed in more detail in Section 6.4.

Some of the alternative designs are also machined easily. The back groove design, where the grooves connecting the restrictor collectors to the pocket region are on the backside of the bushing is machinable. However, this will require a precision shrink fit between the bushing and the bore. If the shrink fit is not strong or accurate enough a leakage flow between the grooves might occur which is detrimental to the bearing performance.

Other Manufacturing Methods

Powder metallurgy and certain rapid prototyping methods could also be used to manufacture the bushings. Powder metallurgy is not economically viable for this application and using it is also problematic due to the surface geometry. There exists rapid prototyping (RP) methods which are able to produce functional metal parts such as 3D-printing a porous aluminum or stainless steel structure and infiltrating it with bronze. These methods are better suited for producing few or a single prototype but are not economically competitive with other methods described above.

6.2 Manufacturing of the 6" Prototype Bushing

Sand Casting was chosen to manufacture the 6" prototype bushings. In order to make the sand core with the internal diameter grooving geometry, a special core box was needed.

The geometry of the grooving is such that the sand cannot be packed in a standard to halves box without breaking the core when opening the box, in other words the geometry does not "draw". The box must be cut into multiple pieces in order to make the sand core with required geometry. The following procedure was developed to make the core box:

- Stereolithography model of the negative of the internal diameter geometry of the bushing, as shown in Figure 6.1, is made
- Epoxy is poured on the model and it is attached to the wooden frame of the core box
- Cut the epoxy and wood into pieces in such way that the packed sand can be removed to form the core for the casting as shown in Figure 6.2

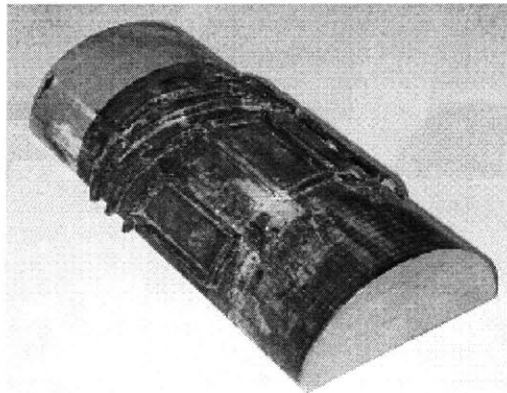


Figure 6.1 Stereolithography negative of grooving geometry

The finished sand core is shown in Figure 6.2 with the rest of the sand mold. After the bearing material is poured and cooled the sand can be broken off and the desired geometry is achieved as shown in Figure 6.3.

After the bushing is cast it must be cleaned and machined into its final dimensions. These machining operations are relatively simple because the grooving can be left as cast, provided that no large residuals have been left into the grooves. For all of the bushings cast (10 pieces), only wire brushing the grooves was enough to clean them. The process was deemed very useful for mass production, should the need ever arise.

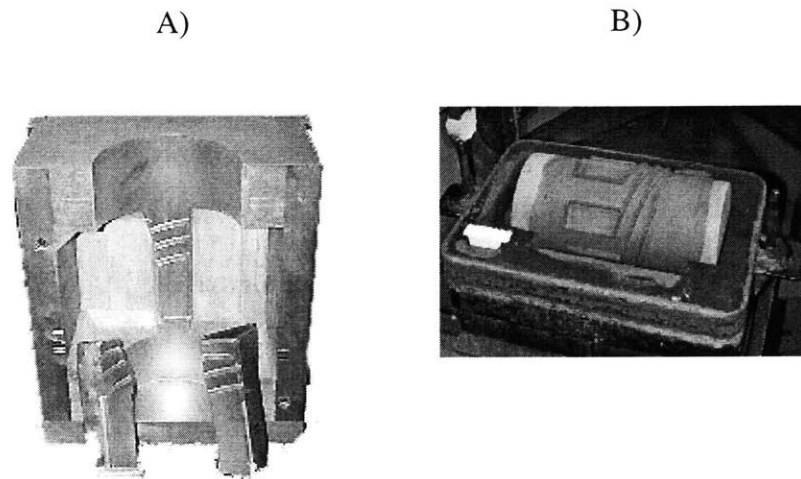


Figure 6.2 A) Core-box, B) Sand core in the mold

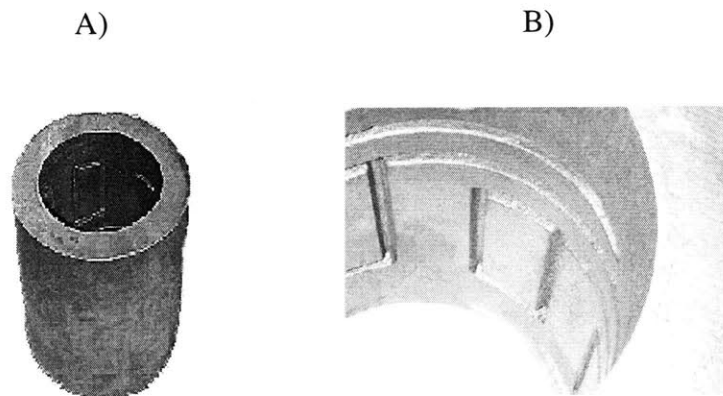


Figure 6.3 A) Cast bushing, B) Groove detail

6.2.1 Shrinkage and Dimensional Variation

In order to determine the dimensional variation and distribution of the prototype castings, several measurements were made. This data was analyzed and then used as input to statistical analysis of the effect of manufacturing errors on the performance of the bearing. Also the actual shrinkage was measured to determine the allowances necessary to make functional bearings. This was necessary due to the many processing steps to make the actual sand core and therefore there are multiple unknown factors involved in the process.

CDA 937 Bronze alloy was chosen as a bearing material. This is a common high pressure bearing material and it contains 80% Cu, 10% Sn and 10% Pb. According to CDA (Copper Development Association) specifications the shrinkage allowance is 1.5% of the dimension and the tolerance, according to manufacturer, are $\pm 0.03''$.

In this case the shrinkage allowance must be correct within a certain envelope. If the bearing shrinks too much, the grooves are not deep enough when the ID is machined to its final dimension. If the bearing does not have sufficient shrinkage and machining allowances, the internal diameter can not be machined to its final dimension and roundness tolerances. This problem becomes more significant as the bearings get smaller. For small bearings, the grooves cannot be made very deep because the molten metal would have trouble flowing around them and might even break them as the metal is poured. As the bearing gets bigger this situation eases and therefore it will not pose a significant problem in 6" bearings once the correct shrinkage factors and machining allowances are determined.

The 6" bearing design was designed to be cast as 5.7" internal diameter to allow 0.15" machining stock. This amount of machining stock is little less than recommended for this size part, but in order to keep the groove depth reasonable it was chosen. The shrinkage factor of 1.5% was added to that to make the internal diameter 5.7855" for the CAD file.

The internal diameter was measured from 3 different bushings and from 3 different locations circumferentially and 6 different locations axially, which makes total of 18 measurements per bushing. Table 6.2 Summarizes diameter measurements of the bushings.

TABLE 6.2 Diameter Measurements of 6" Bushings

	Part 1	Part 2	Part3
Average Diameter	5.768	5.780	5.774
Standard Deviation	0.018	0.020	0.014
Max. Diameter	5.794	5.882	5.807
Min. Diameter	5.735	5.749	5.753
Average Diameter of All Parts		5.744	
Standard deviation of All Parts		0.018	

The shrinkage factor is calculated from

$$\text{shrinkage \%} = \frac{\text{CAD diameter} - \text{Average diameter}}{\text{CAD diameter}} \cdot 100\% = 0.20\% \quad (6.1)$$

This shrinkage is very small compared to CDA provided shrinkage of 1.5%. There are two possible explanations for such a low measured shrinkage. The stereolithography part might have not shrank as much as the manufacturer thought. This is very well possible since the internal geometry of stereolithography part is complex and the parts produced this way are usually used only as visual aids or prototypes, without a need for high dimensional accuracy and therefore the shrinkage factors are not very accurate. The second possibility is that since the sand core is very large, it prevented the bronze from freely shrinking. This would cause internal stresses in the part that might be partly released when the part is machined to its final dimensions, therefore the machining must be done carefully so that the tight dimensional tolerances required can be achieved. The low measured shrinkage is probably due to the both of the above mentioned possibilities. This shows that the dimensional allowances must be carefully selected and be large enough for such large deviations from recommended shrinkage factors.

In addition to measuring the diameter to determine the shrinkage factor, also the error or deviation from desired values of land widths must be determined. This was done by measuring the groove width from multiple locations (70). In Table 6.3 the groove width measurement results are summarized.

TABLE 6.3 Groove Width Measurement Statistics

Statistic	Value
Average	0.206"
Standard deviation	0.008"
Maximum Width	0.227"
Minimum Width	0.186"
Average Error	0.006"
Average Relative Error%	3%

This information will be later used when the effect of manufacturing errors to the bearing performance is analyzed. To effectively use statistical methods, the distribution of the dimensional variation must be determined. The standard distribution that most manufacturing errors are suggested to follow is the normal or Gaussian distribution. Most statistical process control methods assume or invoke normal distribution by central limit theorem. In this case, however, due to the non-standardness of the manufacturing methods, it was necessary to test if the measured data followed normal distribution. This can be done by Chi-Square (χ^2) goodness of fit test. Another test must be performed before Chi-Square test to determine that the variation in the data is random and does not have underlying trends. This can be done by run-test [Bendat, 1971].

6.2.2 Run-Test of Groove Width Measurement Data

The run test is used to determine if measurement data had some underlying trend or in other words is not independent. Non-independents would suggest non-randomness of manufacturing variability and therefore constitute out of control manufacturing accuracy.

If measurements are independent observations of the same random variable, the probability of change from measurement to measurement does not change. This can be tested in the following way:

Let the null hypothesis be that there is no underlying trend in the N observations. By marking all observations with values above median with (+) and values below median with (-) a sequence of (+) and (-) observations is obtained. Every time (+) changes to (-) or vice versa it ends an run. Then the number of runs for N observations will be random variable r with mean and variance as follows [Bendat, 1971]

$$\mu_r = \frac{N}{2} + 1 \quad (6.2)$$

$$\sigma_r^2 = \frac{N(N-2)}{4(N-1)}, \quad (6.3)$$

assuming the number of (+) and (-) observations is equal (which is true since the observations were divided by the median). The sampling distribution has tabulated values in Bendat, 1971. The hypothesis can be tested, to the desired level of significance α , by comparing the observed runs to the interval between $r_{n;1-(\alpha/2)}$ and $r_{n;\alpha/2}$, where $n = N/2$. If the number of observed runs falls within the interval the hypothesis is accepted with α level of significance.

In this case, $n = 35$ and the number of runs equals 31. The acceptance region with $\alpha = 0.05$ level of significance is between 27 and 44 and therefore the null hypothesis that there is no trend and the observations are independent is confirmed.

6.2.3 Chi-Square (χ^2) Test of Groove Width Measurement Data

Chi-Square goodness of fit test is often used to compare measured data to some theoretical probability density function, such as normal distribution [Bendat, 1971]. In other words it can be used to test the hypothesis that some measured data is actually distributed in a certain way. The approximate chi-squared distribution is used as a measure of the discrep-

ancy between an observed probability density function and the theoretical density function.

In this case it is necessary to check if groove widths and therefore the land widths are actually normally distributed. This will be done by grouping the measurements into intervals or bins forming a frequency histogram. Then the frequency of measurements falling into each bin is compared to the expected number of measurements in that bin. Discrepancies between the sampled and expected data are summed over all the bins according to Equation 6.4, where f_i is sampled frequency, F_i expected frequency and K the number of bins.

$$X^2 = \sum_{i=1}^K \frac{(f_i - F_i)^2}{F_i} \quad (6.4)$$

The distribution of X^2 is compared to χ^2 distribution with n degrees of freedom and desired level of significance α . The degrees of freedom are determined by Equation 6.5

$$n = K - 3, \quad (6.5)$$

where the 3 comes from the fact that two different parameters are calculated from measured data in order to determine the theoretical distribution, namely the mean and the variance (or standard deviation) and in addition when the frequencies in the $K-1$ bins are determined the frequency in the last bin is also determined. The hypothesis will be accepted if the Equation 6.6 holds true.

$$X^2 \leq \chi_{n:\alpha}^2 \quad (6.6)$$

The value for the $\chi_{n:\alpha}^2$ can be found from any basic statistics book, for example [Bendat, 1971] or can be calculated with an Excel function.

Chi-square test for this case is summarized in Table 6.4 and the histogram is shown in Figure 6.4

TABLE 6.4 Chi-Square Test for Groove Width Measurement Data

Bin	f	F	$\frac{(f-F)^2}{F}$
1	1	0.41	0.85
2	2	1.76	0.03
3	5	5.71	0.09
4	6	12.31	3.24
5	25	17.62	3.09
6	19	16.74	0.31
7	7	10.55	1.20
8	3	4.41	0.45
9	3	1.22	2.58
X^2		7.29	
$\chi_{6:0.05}^2$		12.59	

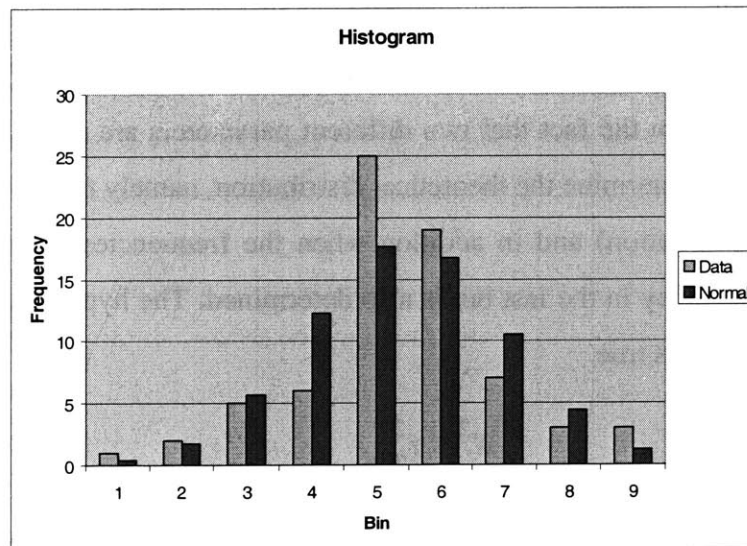


Figure 6.4 The measured and normal distributions for groove width data

The null hypothesis that the groove (and therefore the land widths) are normally distributed is accepted at $\alpha = 0.05$ level of significance. Figure 6.4 also gives strong indication that the measurements are indeed normally distributed.

6.3 Manufacturing of the 1.25" Prototype Bushing

Investment casting was chosen as the manufacturing method for the 1.25" bushings. The sand casting of this size bearing would become very difficult because the core geometry (grooves) are very intricate. The wax patterns needed for the investment casting mold were produced by 3D-Printing, which is a relatively new rapid prototyping technology. Other possibility would have been stereolithography, but this was not chosen for economic reasons, although it would have been able to produce slightly more accurate parts.

In 3D-Printing, the part is formed layer by layer in similar fashion as in stereolithography. The part is formed by spraying binder on a bed covered by powder of cellulose and sugar. After each layer is bind the bed is lowered and next layer is formed. After the part is finished it is cleaned of excess powder and infiltrated with glue or wax. If the part needs to be investment cast afterwards, wax must be used, because the glue can form poisonous gases as the mold is emptied. Infiltration with wax is a manual process. After the waxing, the parts are baked in a oven for few hours to make the wax penetrate all areas of the part and also to remove excess wax and make the part more durable. The finished 3D-Printed part is shown in Figure 6.5.

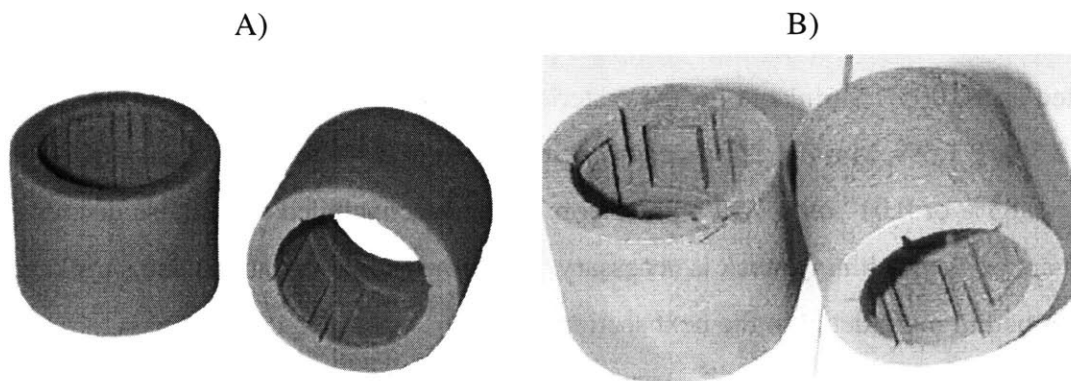


Figure 6.5 A) 3D-Printed wax pattern, B) Investment cast part

The grain size of the 3D-Printing powder is fairly large and therefore the surface finish of the cast part is not very good. The cast prototype bushing is shown in Figure 6.5. The

internal and the external surfaces of the bushings will be machined but the groove surfaces are left as cast. The surface finish of the grooves is not of concern at lower speeds when the flow is laminar (and therefore the surface finish does not affect the flow) and even at high speeds the friction losses generated in the channels represent a small portion of the total losses.

The investment casting of the wax pattern requires nothing unusual. The primary parameters of interest are the formation of the grooves and to make certain that the metal has enough free space to flow around the grooves and fill the spaces in between the grooves. This has to be done before 3D-Printing the part by having the external diameter (OD) to be large enough. The yield with prototype bushings was about 80% which is little less than typical investment casting yield.

6.3.1 Problems with 1.25" Prototype Manufacturing

The bushing ID has to be ground or honed to very close tolerances. With the unknowns associated with the dimensional tolerances of the 3d-printing, relatively large machining stock is needed for the parts. We also have take into account the shrinkage and tolerances of investment casting. These quantities are better known than the ones of 3d-printing but still some uncertainty is associated with them. The casting handbook suggests dimensional tolerances for linear dimensions of 1-2" to be ± 0.013 ", but manufacturers tolerances are stated as ± 0.005 ". Shrinkage for the material in use (Copper alloy C872 Cu 89%, Si 5%, Fe 2.5%, P 1.5%, Mn, Zn, Sn) is according to literature 2.1%, but measured shrinkage was only 0.83% or 0.01" on a 1.17" dimension. It can be concluded from these discrepancies that an ample machining stock is necessary. The dimensional variations and shrinkages are described in more detail in the next section.

This relatively large machining stock requires deep grooves in order for them to remain deep enough after the finish machining. The pressure drop in the groove has to much less than the pressure drops across the lands or the flow in the groove must be much larger than the flow in the land areas. The flow is proportional to h^3 , therefore if the groove is 10

times the clearance, the flow resistance would be approximately 1000 times less. This indicates that the grooves do not have to be very deep but due to the tolerances and inconsistencies in manufacturing process, the 10 times the clearance is good guideline. This is approximately 0.01" groove depth after machining for most bearings.

As the groove depth increases it makes the 3D-Printing of the patterns more difficult. During the wax infiltration process excess wax collects into the bottom of the grooves making them too shallow. After finish machining some or parts of some grooves disappear therefore making the bearing loose its performance partly or in most cases totally (see Figure 6.6).

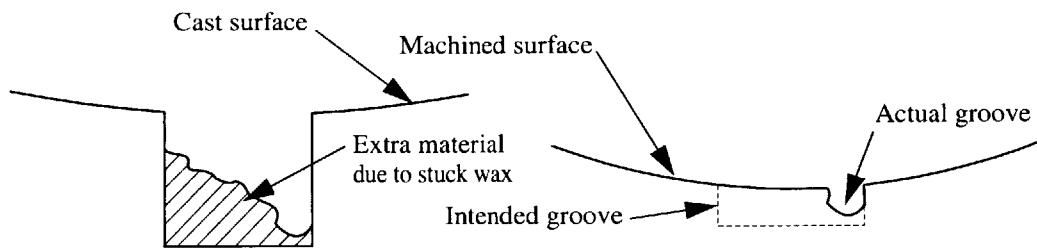


Figure 6.6 Problems with printing deep grooves

One set of prototype castings showed very unusual behavior. The 3D-Printed patterns were measured before they were sent out to outside foundry. The cast parts were measured and they were actually larger than the patterns meaning no shrinkage occurred. This of course can not be true. Something happened to the patterns before they were used in casting. What exactly is almost impossible to tell, but one guess is that the patterns were exposed to moisture and they expanded. Due to the large allowances designed in the prototype stage bearing these bearings were still useful. This further highlights the fact that there are large amount of unknowns in the manufacturing process and a great amount of attention must be paid to the design and manufacturing process.

6.3.2 Solutions to Manufacturing Problems

The obvious solution to the aforementioned problems is making the grooves deeper and adding machining stock. This does not, however, solve the problem with wax stuck in the grooves, but can make it even worse. Deep grooves are also more difficult to cast and therefore reducing casting yield. The problem lies in the 3D-Printing process and therefore the solution must be found in that process.

The excess wax can be taken out by hand, by running a tool through all the grooves. This is very tedious and labor intensive process and is not recommended. It can also alter the geometry by removing some of the material in between the grooves. Better solution was to be very careful when waxing the parts and trying to use a minimum amount of wax. After the waxing, parts must be kept in the oven for an extra long time to drain as much of the wax as possible out of the grooves.

During machining, great care must be taken to make sure the external and internal diameter are as concentric as possible before machining the internal diameter. This ensures the minimum amount of material is removed from the internal surface. The easiest way to do this is to machine the external surface first by holding the part by the internal surface. Then the bushing is placed in a collet and bored.

6.3.3 Shrinkage and Dimensional Variation

Two sets of measurements were taken from the 1.25" prototypes. One set of measurements was taken from the 3D-printed patterns and second set from finished castings. Several different batches were measured in order to determine batch to batch variation and variation within the batches.

The material for the 1.25" prototypes was chosen to be CDA87200 copper alloy (or silicon bronze), containing 89% Cu, 5% Si and 5% Sn. The shrinkage factor for CDA87200 is 2.1% and manufacturers tolerances for the castings are ± 0.005 "/inch. Table 6.5 summarizes the first two sets of measurements from 3D-printed parts.

TABLE 6.5 Measurement statistics of the first two sets of 3D-printed parts

Statistic	Set I	Set II
Average Diameter	1.175	1.16
Standard Deviation	0.007	0.007
Max. Diameter	1.185	1.172
Min. Diameter	1.159	1.148

There is a clear difference between the two sets and both sets have shrunk more than expected. The shrinkage for set I is 2.1% and for set II 3.9%. Both are clearly larger than the manufacturers expected value of approximately 1%. The most probable explanation is that at some point in determining the shrinkage factors and applying it to CAD model some error occurred and the parts were made smaller than intended. For these parts the previously explained problem of too shallow groove becomes critical and the bushings could not be machined to the intended ID.

The next two sets were manufactured and the solution to the problems explained in Section 6.3.2 was applied. The summary of the measurements is presented in Table 6.6.

TABLE 6.6 Measurement statistics of the sets III and IV of 3D-printed parts

Statistic	Set III	Set IV
Average Diameter	1.193	1.197
Standard Deviation	0.007	0.007
Max. Diameter	1.205	1.212
Min. Diameter	1.18	1.187
Shrinkage%	1.1%	0.7%

These sets behave much more as expected, and can be successfully machined to the desired ID.

In the case of the 1.25" bushings there was no groove width measurements due to the small size of the diameter and the groove width itself. When statistical analysis is performed, the diameter measurements are converted to the groove width and scaled statistics

will be used. Measurements followed normal distribution and it will also be used in this case.

6.4 Sensitivity of the Bearing to Manufacturing Errors

In many cases the selection of manufacturing method is based simply on historical knowledge of how different methods will work in a certain case and the decision to use a certain method is either obvious or is made based on experience. In this case where the product itself is novel and historical knowledge has not yet been developed it is justified to spend more time and attempt to perform more rigorous analysis to justify a certain manufacturing method. Also, the surface self-compensated bearing is inherently less sensitive to errors in bearing geometry than any other type of compensation, as explained in the introductory section, but it also has many more geometry features. It is of interest to know how sensitive the bearing is to the errors in its multiple features. It would also be interesting to correlate these sensitivities to different errors introduced by different manufacturing methods. An example of the results this type of analysis would give are the variation of the load capacity at a certain eccentricity or variation or expected value of the rotation center compared to geometrical center.

All this can be conveniently done by statistical methods, namely by the Monte-Carlo method. A Monte-Carlo method is chosen due to fact that any closed form solutions of the variation are very long and extremely tedious to find.

6.4.1 Model

The lumped parameter model is used to perform this analysis. The selected method requires hundreds or thousands of single solutions and therefore the finite difference solution is too time consuming. The model is implemented in spreadsheet format, where each land width and length is represented by one cell. The discretization for single pocket is shown in Figure 6.7.

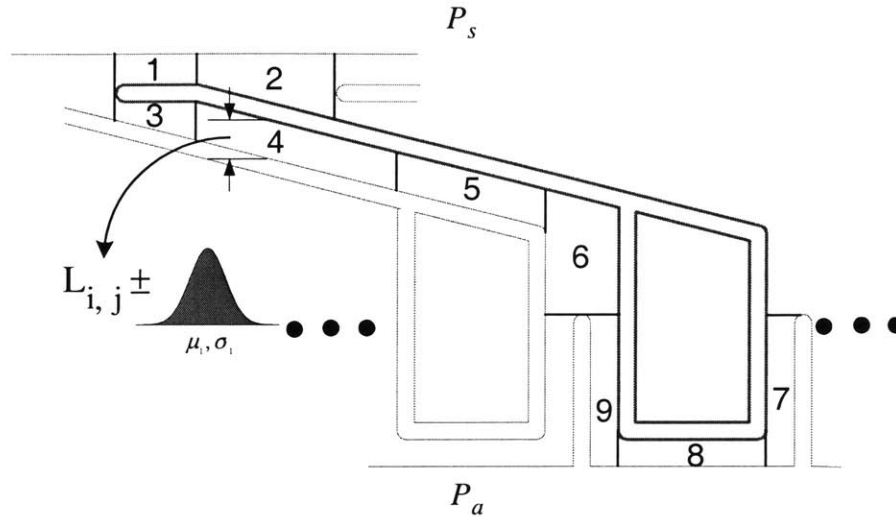


Figure 6.7 Lumped parameter discretization.

This numbering is repeated n times, where n is the number of pockets. The flow in each numbered patch is modeled as a flow between flat plates. Each of these patch dimensions are assigned with probability distribution (probability density function), which represents the manufacturing error. These assigned pdf's are called the assumptions. By assuming that the manufacturing process used is under control, only random errors exist and these errors can be represented with probability distribution. Most of the errors will follow normal distribution as was concluded from the measurement data. However if any other type distribution is expected or reasonable that can also be assigned to represent the manufacturing error. Equation 6.7 defines the normal distribution with mean μ and standard deviation σ being the two parameters defining the distribution [DeVor, 1992].

$$f(x) = \frac{1}{\sigma_x \sqrt{2\pi}} e^{-0.5 \left(\frac{x-\mu}{\sigma_x} \right)^2} \quad (6.7)$$

The mean and the standard deviation can be approximated by the sample mean and standard deviation obtained from the measured parts.

When assigning the manufacturing errors it is best to assign the error in the direction where actual errors could occur. For example, the width of the patch number 4 does not make a difference since this dimension exists only for modeling purposes. Instead the length (direction of the flow) of patch number 4 is a real dimension and the variation should be assigned to it. There are few assumptions one can make how the manufacturing errors form and how they should be assigned. It is reasonable to argue that to certain extent the manufacturing error is due to shrinkage or similar phenomena and is therefore a function of the dimension or some percentage of that dimension value. In other words, the longer the land width the larger the error. However this is not reasonable for all manufacturing methods, for example in EDM only the grooves are machined, which are constant width resulting in constant error (constant mean and standard deviation) no matter what the land width is (due to tool error and positioning error). In the following analysis both methods are used when reasonable. Also a distinction should be made for mean error and deviation. Mean error is an error that is a constant offset from desired value and deviation represents the centered probability distribution around that point. The mean error is implemented as a constant offset in either direction, meaning too wide or too shallow land widths. It is also assumed that the groove width acts as a buffer dimension to keep the bearing geometry consistent with the bearing outside dimensions.

After all the assumptions are defined, the Monte-Carlo method draws random values from the pdf's assigned to that particular cell. The combination of these values are then used to calculate single value of output measure, for example the bearing resultant force. This is then repeated multiple times and each solution is stored in a histogram. This histogram then represents the probability distribution function for the output measure. This output measure is called the forecast.

6.4.2 The Effect of Manufacturing Errors on Load Capacity

In this section the effect of manufacturing error for load capacity at different eccentricities and with different bearing sizes is discussed.

1.25" Bearing

The first analysis presents the variation with zero offset, meaning that the mean value of error distribution is the nominal design value. The standard deviation is set at conservative 10% of the particular land width. All the land widths are drawn from normal distributions. The Monte-Carlo method is used to search for total bearing force distribution at a given eccentricity and the corresponding force angle distribution. Figure 6.8 and Figure 6.9 shows the resulting distributions respectively. The results are overlaid with normal distribution with calculated parameters.

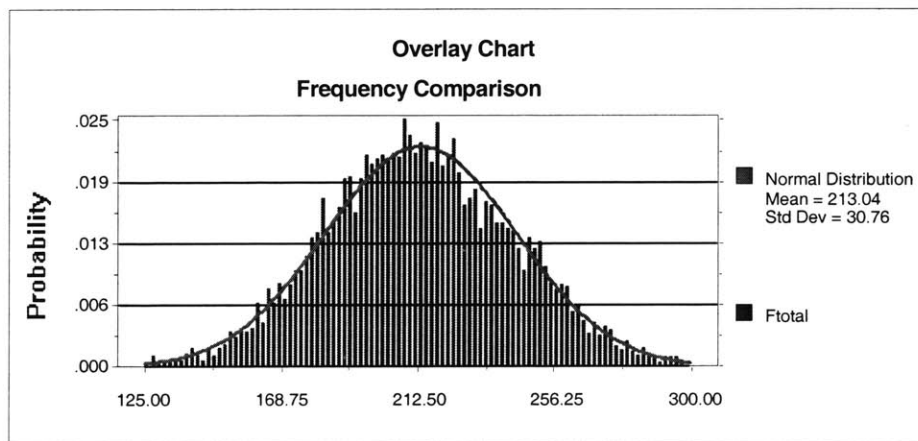


Figure 6.8 Bearing force distribution with $\text{ecc}=0.1$, $\Delta\mu = 0$, $\sigma = 10\%$ of land width

Results with multiple eccentricities are listed in Table 6.7. As can be expected both the force and the angle are centered around the nominal value. The standard deviation of the load is independent of the eccentricity, but the standard deviation of the force angle decreases as eccentricity is increased. The standard deviation in this case is fairly large, but the 10% deviation in land widths is very pessimistic estimate and would indicate minimum of 0.15 mm and maximum of 0.55 mm standard deviations for land widths. More realistic analysis will be represented later in this section. Results scale linearly with assumed land widths, meaning that if assumption standard deviation is 1/10 of the above assumption ($=1\%$) the resulting standard deviation will 1/10 from the listed results ($=3.1$).

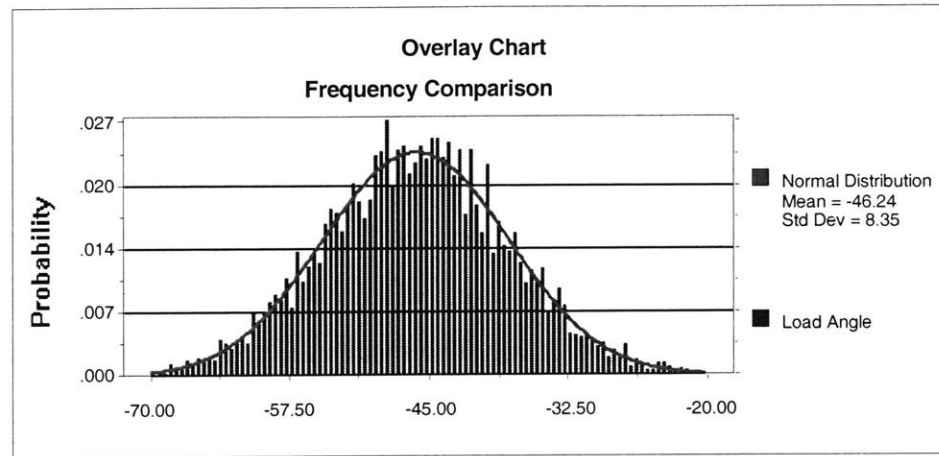


Figure 6.9 Force angle distribution with $\text{ecc}=0.1$, $\Delta\mu = 0$, $\sigma = 10\%$ of the land widths

TABLE 6.7 Summary of the results for $\Delta\mu = 0$, $\sigma = 10\%$ of the land widths case

Eccentricity	$F_{nominal}$	μ_F	σ_F	$\phi_{nominal}$	μ_ϕ	σ_ϕ
0.1	211.4	213.0	30.8	-46.2	-46.2	8.4
0.2	413.2	414	30.6	-46	-45.9	4.3
0.3	597.4	597.4	31.3	-45.7	-45.6	2.9
0.4	759.4	759.6	32.0	-46.4	-45.3	2.3
0.5	895.6	895.9	31.7	-45.2	-45.2	2.0

Another scenario is when the land width standard deviation is assumed to be constant rather than dependent of the land width. The following results are obtained with the land width standard distribution being 10% of the groove width. This again is fairly large value but to get scalable results it will be used. Again the mean offset is zero. Results are listed in Table 6.8. The standard deviation is about half of what it was in the previous case. Again the standard deviation remains constant for the force and decreases for the angle.

TABLE 6.8 Summary of the results for $\Delta\mu = 0, \sigma = 10\%$ of the groove width case

Eccentricity	$F_{nominal}$	μ_F	σ_F	$\phi_{nominal}$	μ_ϕ	σ_ϕ
0.1	211.4	212.1	17.0	-46.2	-46.3	4.5
0.2	413.2	414.0	16.9	-46	-46.0	2.3
0.3	597.4	598.0	17.0	-45.7	-45.7	1.6
0.4	759.4	759.6	16.7	-46.4	-45.4	1.2
0.5	895.6	895.8	16.5	-45.2	-45.3	1.0

In the previous cases the mean shift for the land widths has been zero. Next cases with 5% mean shifts and 5% standard deviations (of the land widths) are presented. In this case only two eccentricities were simulated since the way the results behave as a function of eccentricity are already known, namely that the standard deviation for the force remains approximately constant and decreases for the force angle. Table 6.9 summarizes the results for the case $\sigma = 5\%, \Delta\mu = 5\%$ and Table 6.10 for the case $\sigma = 5\%, \Delta\mu = -5\%$.

TABLE 6.9 Summary of the results for $\Delta\mu = 5, \sigma = 5\%$ of the land widths case

Eccentricity	$F_{nominal}$	μ_F	σ_F	$\phi_{nominal}$	μ_ϕ	σ_ϕ
0.1	211.4	215.2	15.7	-46.2	-46.1	4.2
0.2	413.2	419.7	15.7	-46	-45.6	2.1

TABLE 6.10 Summary of the results for $\Delta\mu = -5, \sigma = 5\%$ of the land widths case

Eccentricity	$F_{nominal}$	μ_F	σ_F	$\phi_{nominal}$	μ_ϕ	σ_ϕ
0.1	211.4	208.8	16.1	-46.2	-46.4	4.4
0.2	413.2	406.9	16.3	-46	-46.3	2.3

It can be noticed that the mean offset of assumption did not change the mean of the forecast considerably, only between 1-1.5%. The standard deviation is what can be expected from the previous simulations.

For the 1.25" bearing, the land width data is not available due to the difficulty of measuring it. Therefore the values from the 6" bushing are used to represent the most likely error

distributions. The values for the mean offset and the standard deviation are $\sigma = 3\%$, $\Delta\mu = 4\%$ of the groove width. This corresponds to approximately 0.1 mm, which is reasonable for the manufacturing method used. Results are summarized in Table 6.11.

TABLE 6.11 Summary of the results for $\Delta\mu = -4$, $\sigma = 3\%$ of the land widths case

Eccentricity	$F_{nominal}$	μ_F	σ_F	$\phi_{nominal}$	μ_ϕ	σ_ϕ
0.1	211.4	208.7	9.2	-46.2	-46.4	2.6
0.2	413.2	408.0	9.6	-46.0	-46.3	1.4
0.3	597.4	589.9	9.5	-45.7	-45.9	0.9
0.4	759.4	749.8	9.7	-46.4	-45.7	0.7
0.5	895.6	884.1	9.8	-45.2	-45.5	0.6

This data will be later used in cost-quality analysis. The bearing resultant force distribution is shown in Figure 6.10 together with normal distribution with the sample mean and standard deviation. The significance of the standard deviation decreases as the eccentricity is increased, because it remains constant. This suggests that for precision applications where only very low eccentricities are desirable the manufacturing accuracy becomes more important. When eccentricity is zero, a perfect bearing would have zero eccentricity. If this is not the case the bearing rotation center is not the geometrical center. This does not matter in the case that the bearing geometry (grooves) are stationary. In the case that the geometry is on the rotating element this will make the shaft center rotate around in the bore. The radius of this circle is fairly small, even at the 3σ limit the radius is less than $0.4\mu\text{m}$.

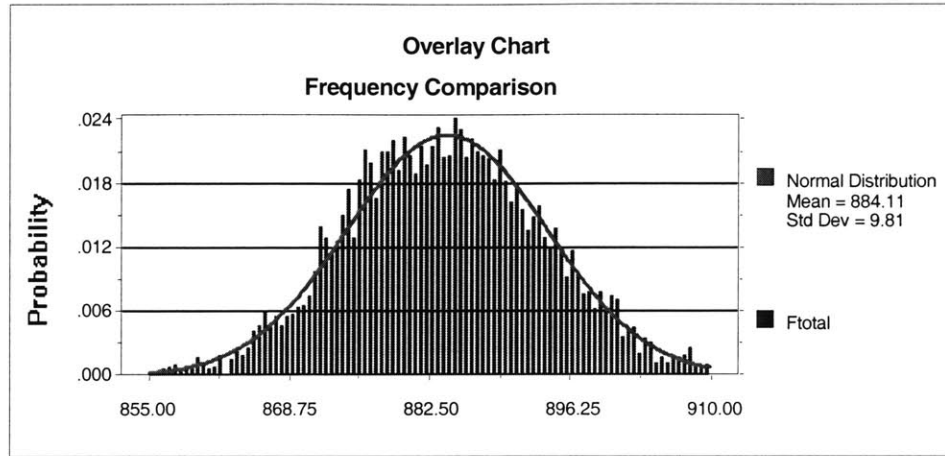


Figure 6.10 Bearing force distribution with $\text{ecc}=0.5$, $\Delta\mu = -4$, $\sigma = 3\%$ of land width

6" Bearing

In the case of the 6" bearing the measured data will be used to perform the same analysis as in the case of the 1.25" bearing. The standard deviation and the mean offset are $\sigma = 3\%$, $\Delta\mu = 4\%$ respectively. These correspond to approximately 0.2mm errors, which is a reasonable number for this size casting. Figure 6.11 shows the distribution at $\text{ecc}=0.1$ together with the overlaid normal distribution with the sample mean and standard deviation summarizes the results at different eccentricities..

TABLE 6.12 Summary of the results for $\Delta\mu = 4$, $\sigma = 3\%$ of the land widths case

Eccentricity	$F_{nominal}$	μ_F	σ_F	$\phi_{nominal}$	μ_ϕ	σ_ϕ
0.1	6832	6843	328	-28.1	-28.1	2.9
0.2	13139	13146	314	-28.2	-28.3	1.4
0.3	18563	18567	288	-28.5	-28.5	1.0
0.4	22966	22974	266	-28.8	-28.8	0.7
0.5	26387	26398	251	-29.1	-29.1	0.6

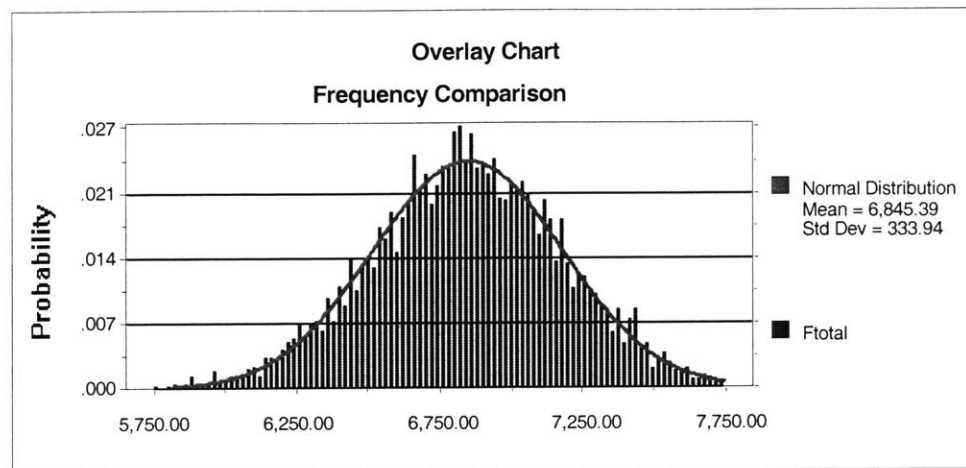


Figure 6.11 Bearing force distribution with $\text{ecc}=0.1$, $\Delta\mu = -4$, $\sigma = 3\%$ of groove width

Again the effect of the assumption mean offset is very small to the forecast mean offset. The standard deviation is of the same order of magnitude as in the previous case or a little less. The only major difference between the small and large designs is that it seems like the standard deviation of the force is decreasing as the eccentricity is increased with the large bearing. Large bearing does not have drainage grooves between the pockets which can be the explanation to this behavior. Also the lack drainage grooves makes the lands between the pockets fairly large. This makes the approximations made in the modeling less accurate. When the cost-quality analysis is performed the maximum value for the standard deviation is used. At $\text{ecc}=0$, the 3σ limit force corresponds to a displacement of approximately $0.4\mu\text{m}$.

It seems that the bearing size does not have a significant effect on the sensitivity of the bearing to manufacturing errors. Although this can be expected if the errors introduced are relative to bearing size (groove or land widths). In the case of absolute errors the larger bearing is naturally less sensitive to errors.

6.4.3 Cost vs. Quality Analysis

In this section an attempt is made to make non-biased comparison between different manufacturing methods. Quality is a very broad term and can be understood very differently in different situations. Quality could be described as fitness for use, the degree to which product satisfies the wants of a specific customer, the degree to which a product conforms to design specifications, providing products and services that meet customer expectations over the life of the product or service at a cost that represents customer value, the characteristics or attributes that distinguishes one item or article from another or conformance to applicable engineering requirements as described in engineering drawings, specifications and related documents [DeVor, 1992]. These criteria are reasonable, but they are qualitative in nature and therefore of little help if a quantitative analysis is desired. These criteria are also easily interpreted as two valued, either the product is good or bad. Instead of using some arbitrary limit telling when the product is good or bad a concept called loss function will be employed here and with the help of loss function the expected value of the total cost of the product will be used as a measure to compare different manufacturing methods. These concepts are borrowed from broad range of quality design methods called Taguchi methods. Taguchi methods focus attention on the engineering design process and has emphasis on minimizing variation and centering the mean on designed target. Taguchi methodology has a much broader perspective on the design process as whole than what some of its concepts are used here for.

The Loss Function Concept

Taguchi argues that it is important to think quality in terms of the loss imparted to society during product use as result of functional variation and harmful effects. Taguchi defines quality as loss due to functional variation and further argues that the loss is minimized (as it should be) when performance is at design nominal and that the cost increases as the performance deviates from the nominal. In many cases a quadratic loss function is appropriate [DeVor, 1992]. Figure 6.12 illustrates the loss function concept. It is not enough to define some arbitrary function to make any meaningful comparisons.

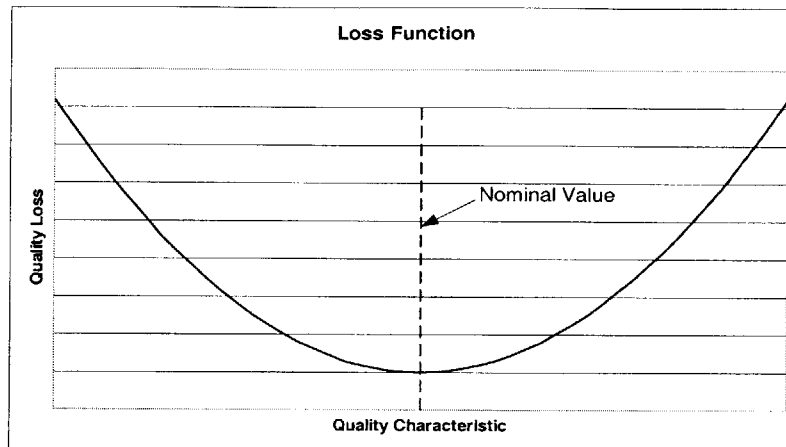


Figure 6.12 Loss function concept

This function has to be somehow consistently related to the performance of the product. One way to do this is to define some acceptable quality level or variation from nominal and associate a cost to the product when this variation is exceeded. This cost can be, for example, scrap cost or some penalty cost at that point. This way the loss function becomes:

$$L(x) = k(x - x_0)^2 \quad (6.8)$$

where x is the quality characteristic, x_0 the intended target value and k the factor used to calibrate the cost function. Alternatively a simple way to define a cost function is to add constant manufacturing cost term in the end of the loss function. It could be argued that in the case of the bearing the loss function should not exist beyond the nominal value, meaning that no loss should be associated with the bearing if it carries more load than intended. This argument makes sense in most cases, but philosophically it could be argued that resources are wasted if the performance is better than nominal. The quadratic function will be used in this case.

$$C(x) = k(x - x_0)^2 + M \quad (6.9)$$

Having the cost in a function form is still not very convenient if comparisons are to be made. In addition the cost function does not in itself take into account the product quality itself. The product quality characteristic or variation in product performance has to be related to the cost function in order to obtain meaningful measure to compare. This can be conveniently done by mathematical expectation which relates the probability density function to the cost function. In the case of a continuous X , the mathematical expectation is defined by [Kreyzig, 1993].

$$E(g(X)) = \int_{-\infty}^{\infty} g(x)p(x)dx \quad (6.10)$$

The Expected Cost

The expected cost is defined as the expected value of the cost function. The probability density function used will be the one simulated in the last section. The quality characteristic will be the bearing force. This way the probable performance of the bearing is related to the cost function. Figure 6.13 shows the cost function and the quality characteristic distribution which, in this case, is the bearing force.

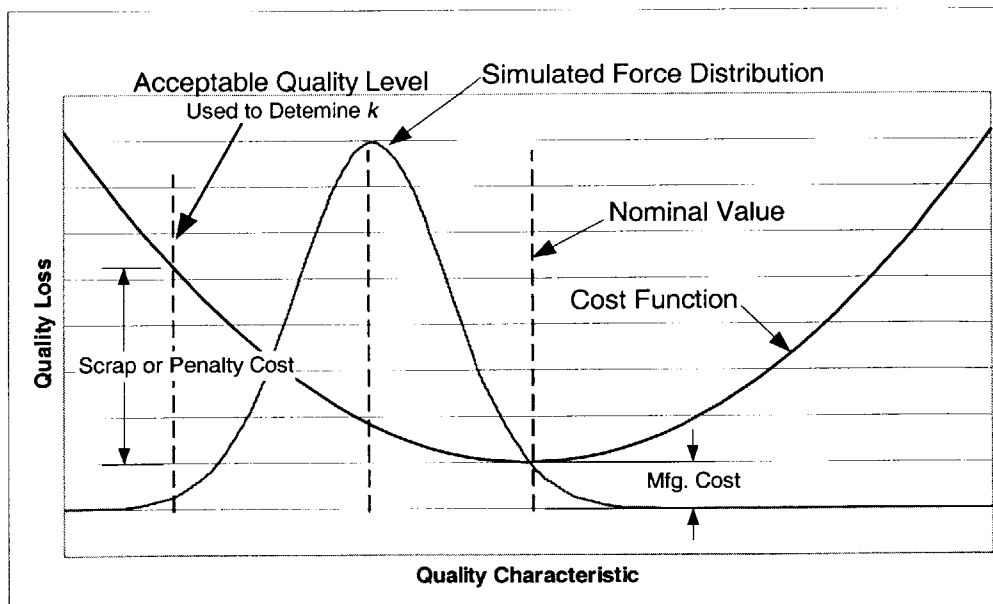


Figure 6.13 The derivation of expected cost

The expected value of the cost becomes

$$E(C(F)) = \int_{-\infty}^{\infty} C(F)p(F)dF = \int_{-\infty}^{\infty} [k(F - F_0)^2 + M] \frac{1}{\sigma\sqrt{2\pi}} e^{-0.5\left(\frac{F-\mu}{\sigma}\right)^2} dF \quad (6.11)$$

where σ and μ are the mean and standard deviation calculated by the simulation in the previous section. By expanding the square and taking into account the following relations

$$\begin{aligned} \int_{-\infty}^{\infty} p(x)dx &= 1 & (6.12) \\ \mu &= \int_{-\infty}^{\infty} xp(x)dx \\ \psi^2 &= \int_{-\infty}^{\infty} x^2p(x)dx = \sigma^2 + \mu^2 \end{aligned}$$

the expected value becomes

$$ETC = E(C(F)) = k(\sigma^2 + (\mu - F_0)^2) + M \quad (6.13)$$

What remains to be defined is the acceptable quality level or the level at which it should be stated that the bearing does not function properly and therefore some cost can be assigned to it. This definition can be somewhat arbitrary and depends on application. A quick survey among machine designers proposed the 10% deviation as acceptable. On the other hand it is hard to believe that such deviation would even be noticeable in most applications. On the other hand it can hardly be said that 50% deviation is acceptable. To be safe the 10% limit will be used. The other question is what cost should associated with this deviation? Should it be the manufacturing cost or some scrap cost with the manufacturing plus some environmental impact cost. In a worse case it could be argued that the cost is the cost of rebuilding the machine component with new better performing bearing or even worse the loss of customer. Here as a primary mean of comparison the 10% limit with the manufacturing cost as a penalty will be used. These assumption can be changed which ever way the reader wants or is reasonable for the specific application. The main thing is

accomplished once the variability is considered in the design. The coefficient k for the cost function becomes

$$k = \frac{M}{0.1^2 F_0^2} = \frac{M}{0.01 F_0^2} \quad (6.14)$$

The most general form of the expected total cost is

$$ETC = \frac{X}{(1 - \vartheta)^2 F_0^2} (\sigma^2 + (\mu - F_0)^2) + M \quad (6.15)$$

where X is the penalty cost (here set equal to manufacturing cost M), ϑ is the fraction of nominal value at which the penalty cost is applied (here $\vartheta = 0.9$), σ is the calculated standard deviation and μ is the calculated mean.

1.25" Bearing

It is clear that the expected total cost (ETC) will depend on which eccentricity the bearing is designed to operate at. The smaller the eccentricity, the larger the ETC . Taking into account that these bearing are used in pairs, but all the analysis in this section is done for a single bearing, eccentricity of 0.1 will correspond to approximately $1\mu m$ displacement. This is small displacement and therefore a conservative point to calculate the ETC . By using the values from Table 6.7 the ETC will become

$$ETC = \frac{M}{0.01 \cdot 211.2^2} (30.8^2 + 1.6^2) + M \approx 3.1M \quad (6.16)$$

This indicates that the actual or expected cost is approximately three times the manufacturing cost. However, if the larger eccentricity can be used the expected cost quickly drops closer to manufacturing cost. At eccentricity = 0.5 the ETC will only 1.1 times the manufacturing cost. For the less pessimistic case from Table 6.8 the ETC becomes $1.65M$ for the 0.1 eccentricity. In the case of more accurate manufacturing methods such as machining or EDM the ETC is very close to the manufacturing cost. This shows the robustness of the design. In Figure 6.14 the normalized cost of the 1.25" bearings as a function of the

quantity they are manufactured is shown. for the different manufacturing methods. The cost is normalized with respect to the *ETC* of the 3D-printing and investment cast method. The only method competitive with the selected method is injection molding at larger quantities. The cross over quantity is approximately 650 bushings, which is 325 bearings when the bushings are used in pairs. This is with $ETC = 1.65M$. If the pessimistic value for the *ETC* is used these values become approximately half of the above. This analysis concludes that unless very significant number of same size bearings are to be produced, the 3D-printing/investment casting is the most cost effective way to make the bearings.

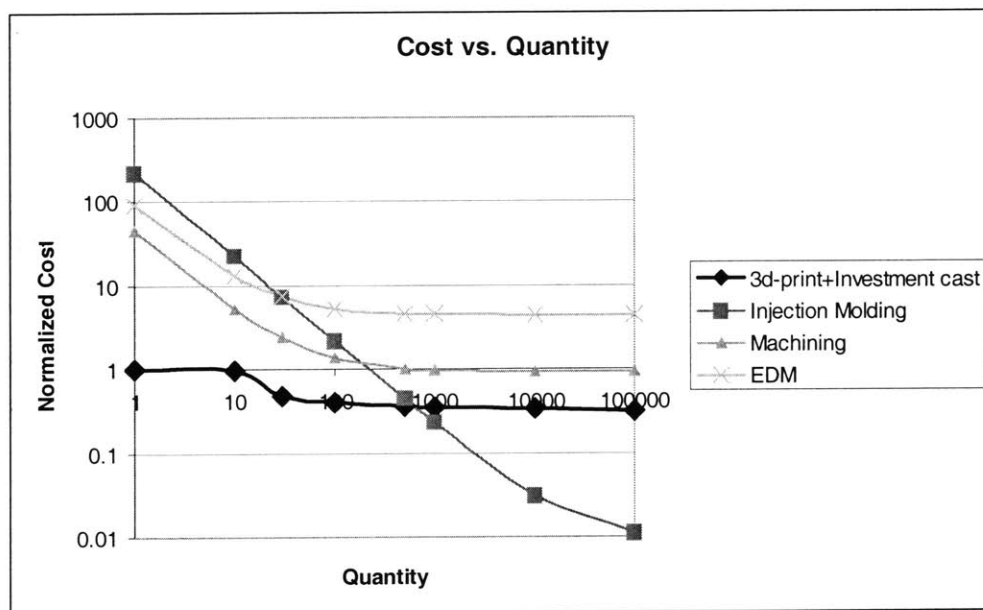


Figure 6.14 Normalized manufacturing cost as function of quantity

6" Bearing

By using the data from Table 6.12 the *ETC* for the sand cast 6" bearing becomes

$$ETC = \frac{M}{0.01 \cdot 6832^2} (328^2 + 11^2) + M \approx 1.23M \quad (6.17)$$

Now the cost or expected cost for the different manufacturing methods can be compared. In Figure 6.15 the manufacturing cost is plotted as function of quantity. In this case the difference in cost is not as significant. All the methods require some special tooling that is fairly expensive, which makes the quantity versus cost graphs similar. The 6" inside diameter is a little too large for the 3D-Printing, but approximately 4" internal diameter bearings could be manufactured with 3D-printing and investment casting..

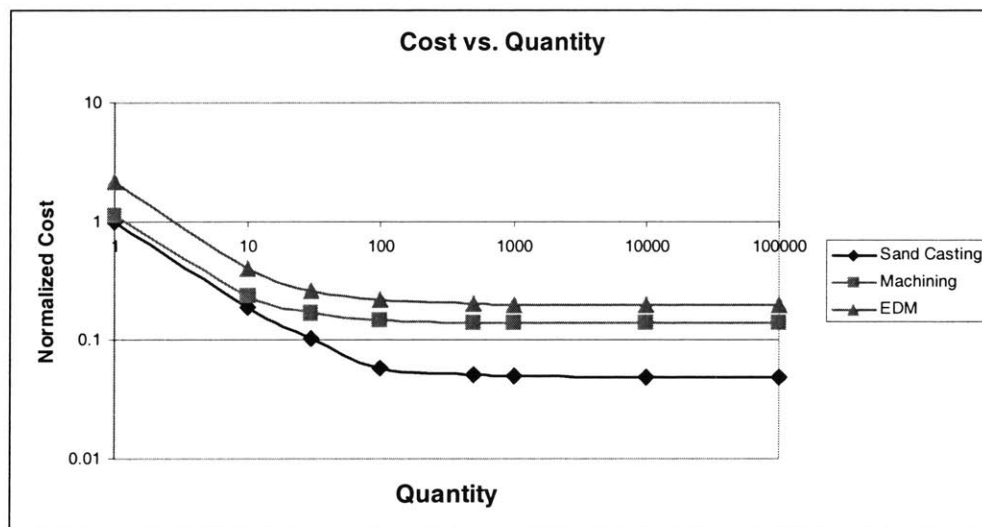


Figure 6.15 Normalized manufacturing cost as function of quantity

Chapter 7

TESTING

In this chapter the testing of different prototypes will be described. In static testing the force-displacement behavior of the bearing is measured. Also the flow rate is measured. These results will then be compared to the theoretical predictions.

The combination of radial and tilt error motion of the bearing is measured by rotating a shaft in the bearing. Error motion is a very important property of the bearing if it is to be used in precision applications.

Dynamic tests are performed to evaluate the stiffness as a function of frequency and to approximately evaluate the damping behavior of the bearing. The dynamic testing is very difficult due to the high stiffness and very high damping of the bearing.

7.1 Static Testing of the 6" Prototype

The purpose of the testing of the 6" prototype was to determine the static behavior and to prove the concept of low cost large hydrostatic surface self-compensating bearing.

When the bearing becomes large the manufacturing and assembly processes pose significant challenges. Since the bearing is used in pairs, the alignment and precise manufacturing becomes a challenge. It was intended to prove that due to the self-compensating bearings robustness against manufacturing errors, no ultra high precision manufacturing

was needed and the bearing would still work. Test results were also compared to the modeled results.

7.1.1 Test Set-up

In order to perform the force-displacement measurements a test rig and bearing assembly was designed and manufactured.

Test-rig

The requirements for the test rig was to be able to carry the bearing loading force which could reach 100 000 N. It was also desired that the bearing could be moved along the shaft while the bearing was loaded. Figure 7.1 shows the general view of the test setup. More detailed drawings of the test stand are shown in Appendix E.

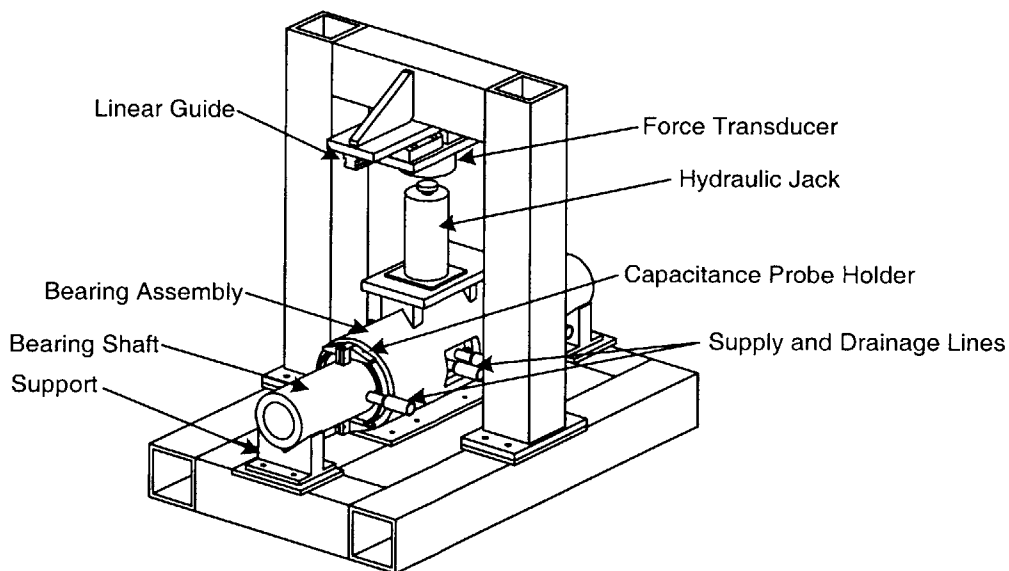


Figure 7.1 General view of the test setup

The test-rig allowed for the bearings or the shaft to be supported during the testing. This was desirable because in order to demonstrate the frictionless behavior of the bearing, the bearing housing had to be supported so that the shaft could float freely. If the shaft was supported,

the hydraulic piping would introduce forces that would constraint the free motion and the frictionless motion would be lost. When actual testing was done, it was better to support the shaft and force the bearing assembly. The motion capability was provided by the linear guide and the two trucks. If this capability was to be used, the shaft had to be supported. This feature was not used due to the equipment failure and the linear guide assembly was replaced by the stationary part.

A 50 ton hydraulic jack was chosen to be the forcing device. The force output was measured by tension-compression "s" load cell with maximum capacity of 5000 lbs or by low profile tension-compression load cell with maximum capacity of 50000 lbs. Table 7.1

TABLE 7.1 Specifications of the load cells

Specification	50k Tranducer	5k Transducer
Output	3.015 mV/V	2.999 mV/V
Accuracy (Full Scale)	NA	0.037%
Linearity FS	±0.1 %	0.03%
Repeatability FS	±0.03 %	0.01%
Zero Balance	±2 %	1%
Thermal Effects	0.002% FS/° F	0.0015% FS/° F
Max. Deflection	0.003"	0.02"

summarizes the specifications of the load cells [Omega, 1992]. The 50k load cell was used less due to its worse noise characteristics and the fact that the full load capacity was not meaningful measurement in this case as explained in the results section. Both load cells were supplied by a 12.15 V DC power supply.

The sensitivity of the of the 50k [lbs] force transducer is 15.027 mV/10V at 25000 lbs. With the above mentioned power supply the conversion formula for the recorded voltages to Newtons is the following:

$$\text{Force [N]} = 1000 \cdot \text{input [V]} \cdot 4.44822 \cdot \frac{25000}{(1.215 \cdot 15.027)} \quad (7.1)$$

The sensitivity of the of the 5k [lbs] force transducer is 2.999 mV/V at 5000 lbs. With the above mentioned power supply the conversion formula for the recorded voltages to Newtons is the following:

$$\text{Force [N]} = 1000 \cdot \text{input [V]} \cdot 4.44822 \cdot \frac{5000}{(12.15 \cdot 2.999)} \quad (7.2)$$

The displacement was measured by four capacitance probes. These probes were held by mounting brackets to the bearing assembly and measured the relative displacement between the bearing assembly and the shaft thus eliminating most of the elastic deflection. Not all the elastic deflection could be eliminated by the placement of the probes and had to be eliminated computationally as explained in more detail in the next section. The probe mounts could be moved around the shaft to measure the displacement in different directions. Figure 7.2 shows the location of the measuring devices.

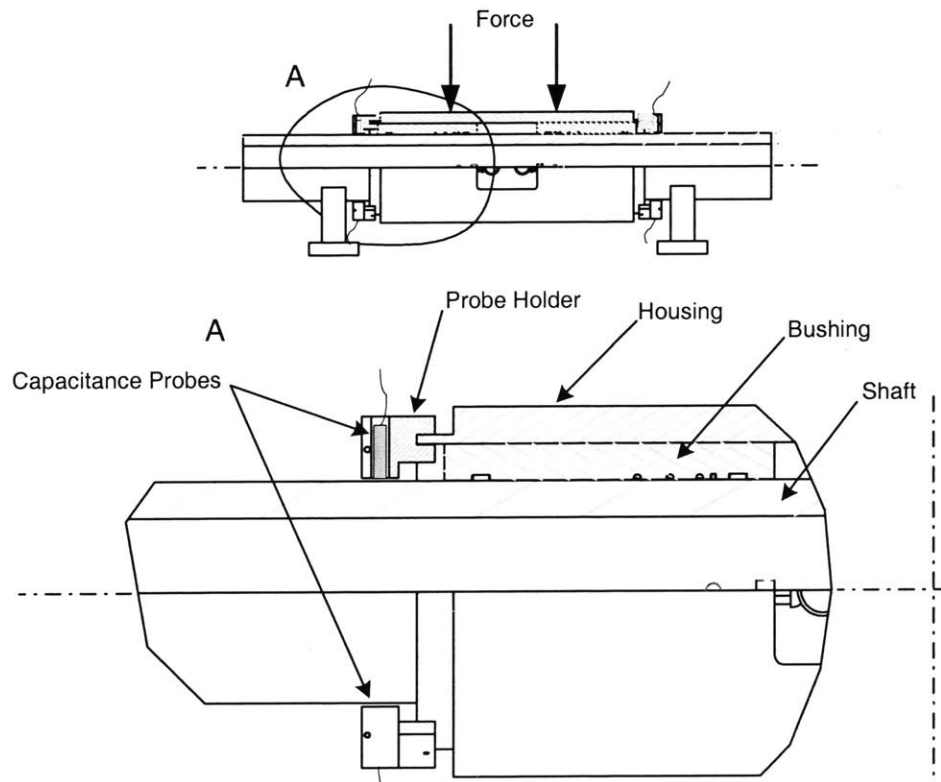


Figure 7.2 Bearing assembly and the location of the capacitance probes

Figure 7.3 shows a photograph of the test setup.

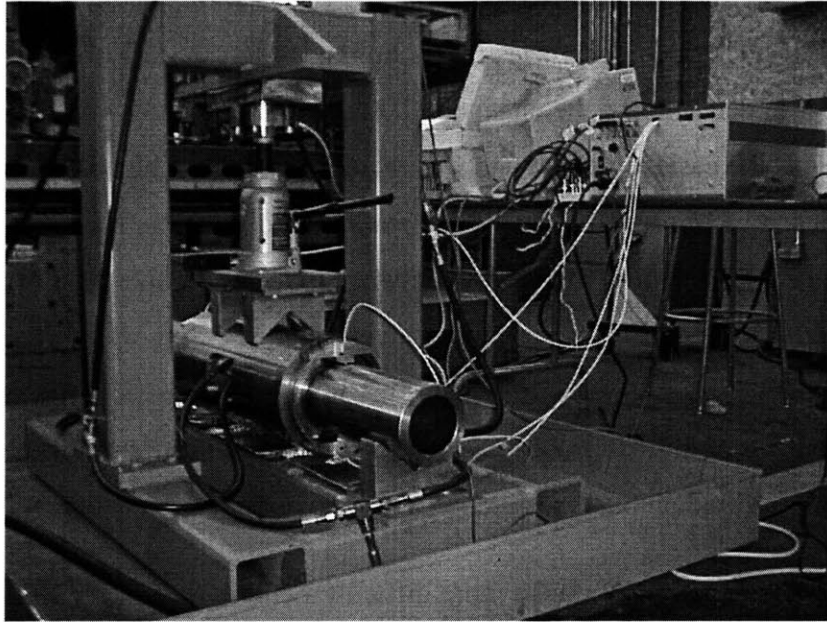


Figure 7.3 Photograph of the test setup

Both the capacitance probes and the force transducer were connected to data acquisition board on PC. The data was collected with LABView software and saved as an ASCII file and then imported to Excel for data analysis.

Bearing Assembly

These bearings have to used in pairs to obtain acceptable moment carrying capability, unless other means are used to provide it. For a certain range of aspect ratios (L/D) the casting of the part is considerably easier to cast with one bearing at a time and then assembling the pair to obtain bearing pair. This also makes the handling and machining of the bearings easier. On the other hand it requires fairly accurate alignment of the two bearing parts or special machining. The two different procedures to make the bearing assembly are as follows:

- Machine the housing

- Determine how much the ID of the bushings will change due to locational fit between them and the housing
- Machine the bushing taking into account the calculated change in ID
- Assemble the bushings and the housing together

This method will stack the inaccuracies in machining the housing ID, the bushing OD and ID and the error in determining the change in ID due to the shrink or locational fit. On the other hand, this is the easiest method and was therefore chosen. The alignment or the geometrical errors can be improved by using replication to align the bushings in the housing. This can be done by machining a small gap between the housing and the bushings and filling that gap with epoxy. While the epoxy is not yet set, the bearing will be turned on and it is allowed to align itself and set into place. This is not recommended unless absolutely necessary, as each bushing itself does not have high moment stiffness this may introduce non-cylindricity (individual bushings are twisted with respect to each other).

An alternative more accurate, but also more difficult method, is:

- Machine the housing
- Machine the OD of the bushing
- Assemble the bushings and the housing
- Line bore the ID of both bushings simultaneously

The difficult part in the second method is the last step. The assembly can be fairly large (in this case over 1m long) and finding a machine that is able to machine the ID to the required tolerances is difficult. If this can be done it will produce the best results since it eliminates any errors in the housing ID and bushing OD.

As mentioned earlier, this assembly consists of three parts, the two bearing halves and the housing (see Figure 7.4) The two bearing halves are first cast then the supply and drainage grooves are machined along with the interface to hydraulic system. They are then machined to required tolerances and assembled into the housing. The hoses are then connected and the bearings cleaned thoroughly. The cleaning is important so that the machining chips and dust do not interfere with the bearing performance. It will also loosen any

particles that might come loose during the operation. After the cleaning, the shaft can be inserted into the bearing assembly.

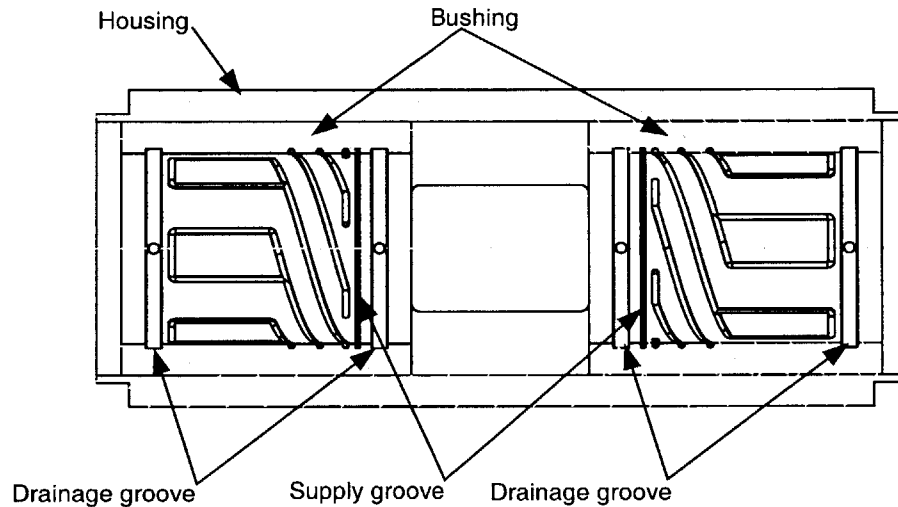


Figure 7.4 Bearing assembly

Normally the two bearing halves would be mirror images of each other, but in this case, in order to save in tooling costs, they were identical. This will have an effect on the bearing performance by introducing a moment around the center of the bearing. This will in turn have an effect on the equilibrium position of the bearing. The bearing will have a reaction force perpendicular to displacement due to the relative location of the collector groove and the pockets. This will cause problems in measurement accuracy since the displacement in the perpendicular direction is not constrained fully, but it is also not entirely free. This will cause a reaction force in the forcing system, which magnitude is unknown due to the side load rejection of the force transducers. However, the bearing design was such that the side component of the force is relatively small ($\frac{1}{\sqrt{3}}$ of the vertical force). Also intention was to prove the functionality of the bearing and verify the theoretical model, this is acceptable.

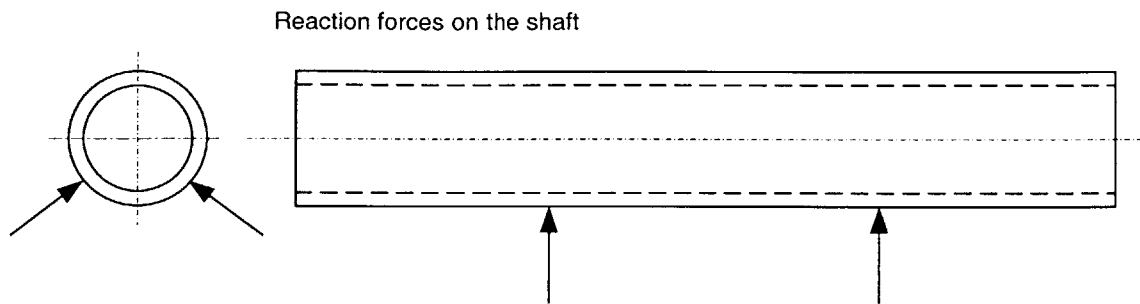


Figure 7.5 Reaction forces on the shaft in the case that both bushings have the same geometry

Hydraulic unit

The bearing fluid supply system consisted of a constant pressure pump, oil cooler and plumbing. The pressure of the pump was adjustable between 200 - 500 psi. The temperature of the oil was 25°C and was cooled to that temperature before returned to bearing.

Oil

The oil used was Shell Pella ISO 5 oil with viscosity of 5 cSt = 4.56×10^{-3} Pa s at 20°C and 4.43 cSt at 40°C. The density at 15°C is 823 kg/m³. Pella A oil is a low viscosity straight mineral oil. It is used as a diluent to adjust viscometric properties of heavy duty metalworking oils, as a cutting fluid in lapidary applications, and as a calibration fluid for adjusting diesel fuel injectors. Pella A is nearly odorless and it has a near transparent color. Pella A oil has been used to grind lenses for eye glasses, as a coolant and lubricant for diamond tipped saws, for cutting stones and ceramics, and in the machining of non-ferrous metals and alloys. The fact that this oil can be used as a coolant makes it attractive bearing fluid, so that the coolant system does not have to be entirely separate from the bearing fluid system in some machine tool applications.

7.1.2 Results

Clearance tests

To get an idea of the actual clearance of the bearings the following test was performed. The displacement measurement was started and after a while the pump was turned on and then after few moments turned off again. In this procedure the bearing will lift itself up from the resting position on the shaft as the pressure is turned on and finds its equilibrium within the bearing bore. This equilibrium position is the geometrical center of the bearing under ideal conditions and is very close to it in the presence of manufacturing errors. The measured displacement is therefore close to the clearance of the bearing. This of course is a certain type of average or effective clearance, since the real clearance changes from point to point and the only way to measure it would be to directly measure the ID of the bearing and the OD of the shaft.

Figure 7.6 Shows typical results of the gap test. The clearance is approximately $23 \mu m$, which very close to the specification clearance of $25.4 \mu m$.

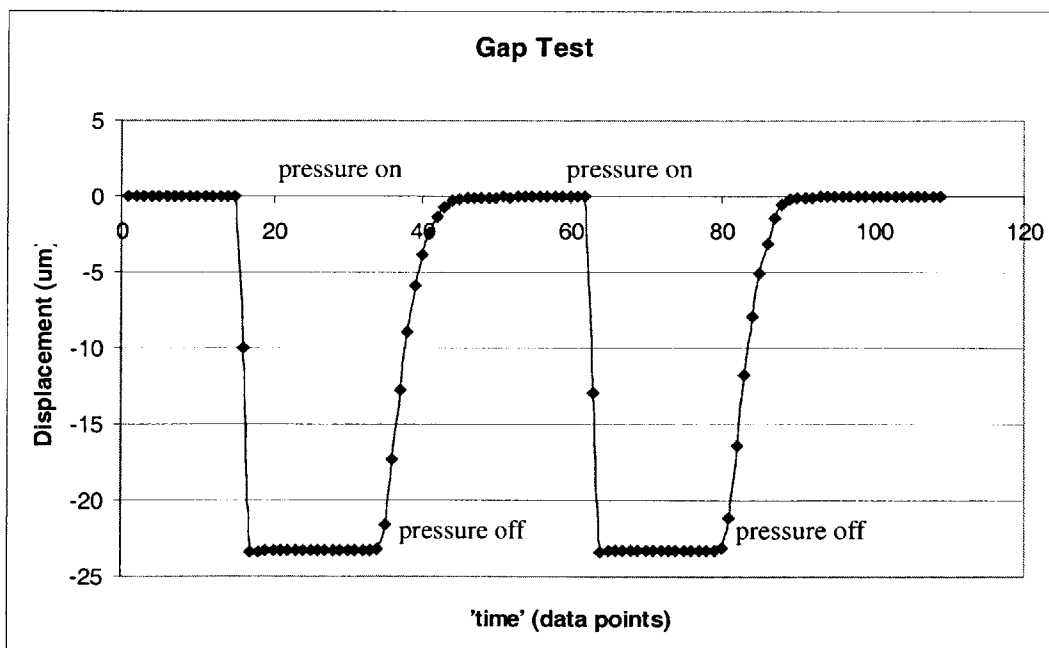


Figure 7.6 Gap test. Pump turned off and on while measuring the displacement.

Uncorrected (for elastic deflection) force-displacement tests

Figure 7.7 shows the uncorrected measurement data at 500 psi and the modeled force-displacement curve. It is clear from the plot that a correction for shaft bending is needed due to the fact that the maximum displacement measured is larger than the gap. The measured data also deviates clearly from the theoretical curve. Dots represent the measured data and the continuous line is the theoretical curve. Each point is an average value of four measured samples.

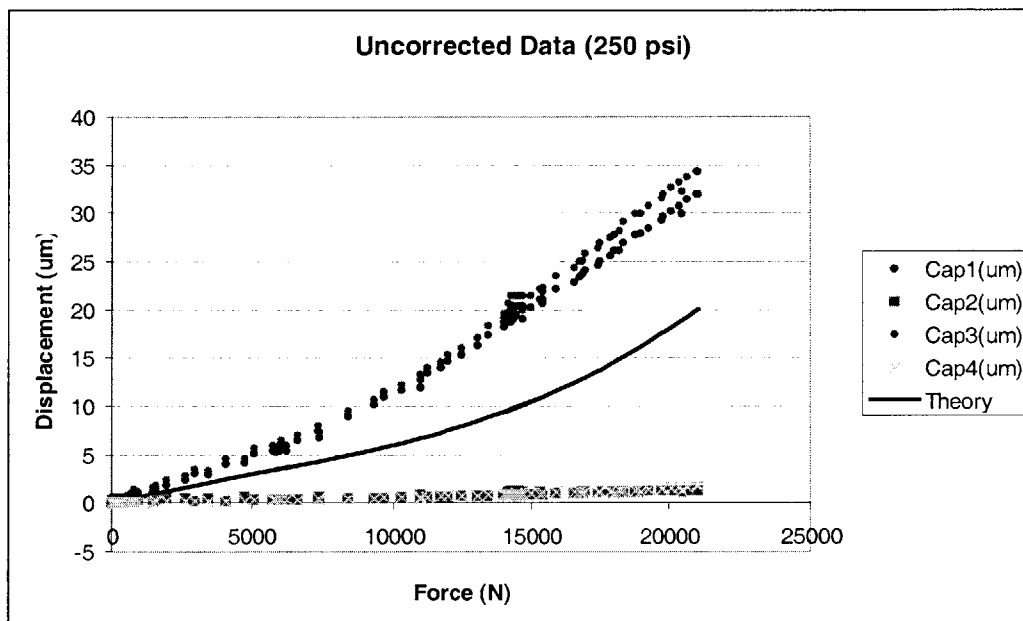


Figure 7.7 Uncorrected force-displacement curves at 250 psi measured with the 50k force transducer

Data also shows that the moment created by the bearing is carried by the test structure. This is shown by the fact that the horizontal displacements are small compared to the vertical (force direction) displacements. If the bearing was free to move in a horizontal direction the displacements in that direction would be of the same order of magnitude. This means the force transducer takes heavy side loading and therefore it is important that it has good side load rejection capabilities. The measurement shown in Figure 7.7 was done with the large (50k) force transducer.

There was also an unsuccessful attempt to do the measurements at 500 psi. The results looked very similar to those of at 250 psi which suggest that either the pressure did not rise or the other more likely possibility is that the gap between the capacitance probe and the shaft surface was filled with oil, thus changing the sensitivity of the probes. The expected change would be about a factor of 2, which agrees with results. These results were disregarded. In general it is easier to measure deflections at lower supply pressures, so that the bearing stiffness is lower and not totally dominant compared to the test structures.

Corrected (for elastic deflection) force-displacement tests

Even though the test set up was such that the effect of the elastic deflections was minimized they still have a significant effect on the results. If the pure performance of the bearing is desired then these deflections must be eliminated. This is fairly straight forward since most of the elastic deflection is due to the bending of the shaft which can be calculated using well known beam theory. The aspect ratio is such that it is necessary to take the shear deflections into account so that the deflection is defined by [Pennala, 1993]

$$\frac{d^2 v}{dx^2} = -\frac{M}{EI} - \zeta \frac{q}{GA}, \text{ where } \quad (7.3)$$

$$\zeta = \frac{A}{Q^2} \int_A \tau^2 dA$$

The last term represent the deflection due to the shear and the ζ is dimensionless constant determined by the geometry of the cross section of the beam. Equation 7.3 is rather tedious to solve for the distributed load and in this case only one solution is required so a finite element solution is sufficient. This one solution representing the case in question can be scaled with load (due to linearity) to represent the different load magnitudes.

In order to check that no unexpected displacements exist, a 3-dimensional finite element elasticity model of the bearing assembly and the shaft was first made. This model was made to resemble the actual situation as closely as possible even with the cost of computational time. Symmetry was used where possible to make the solution as efficient as possi-

ble Figure 7.8 describes the model. The support and the forcing devices were modeled with contact elements. The rest of the system was modeled with 3-dimensional linear elements except the capacitance probe and its holder which were modeled with beam elements. The probe and its holder have no significant effect on the elastic response of the system but the displacement of the probe tip is of utmost interest. The problematic feature to model is the connection between the bearing assembly and the shaft, namely the oil film. The best way to model that is to place a linear spring with stiffness of the bearing at the effective center of the bearing. This introduces point reaction forces on both shaft and the bearing assembly and therefore unrealistically large displacements (and infinite stresses) in the vicinity of the spring. By invoking the St. Venants principle these displacements can safely be ignored and the displacements sufficiently far away from the spring will still be correct. The spring takes the bearings inability to carry moment loads correctly into account while the alternative method of replacing the oil film with material with modified Young's modulus, to achieve the correct effective stiffness, does not. The system was also modeled without the oil film i.e. with direct contact between the bushing and the shaft. .

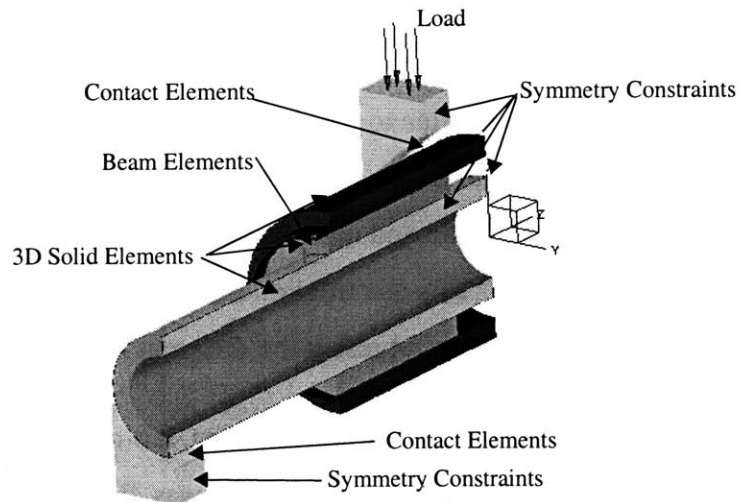


Figure 7.8 3D Finite element model

Figure 7.9 shows the displacements computed by the above described model. Nothing unexpected happens. The displacement field is mainly due to the displacement of the shaft. The displacements of the housing is not significant. This allows us to use much simpler model consisting only of the shaft modeled with beam elements capable of taking the shear deflections into account. The loading of the beam model can be thought of as distributed load around the effective center of the bearing or alternatively as a point load at the effective center of the bearing. .

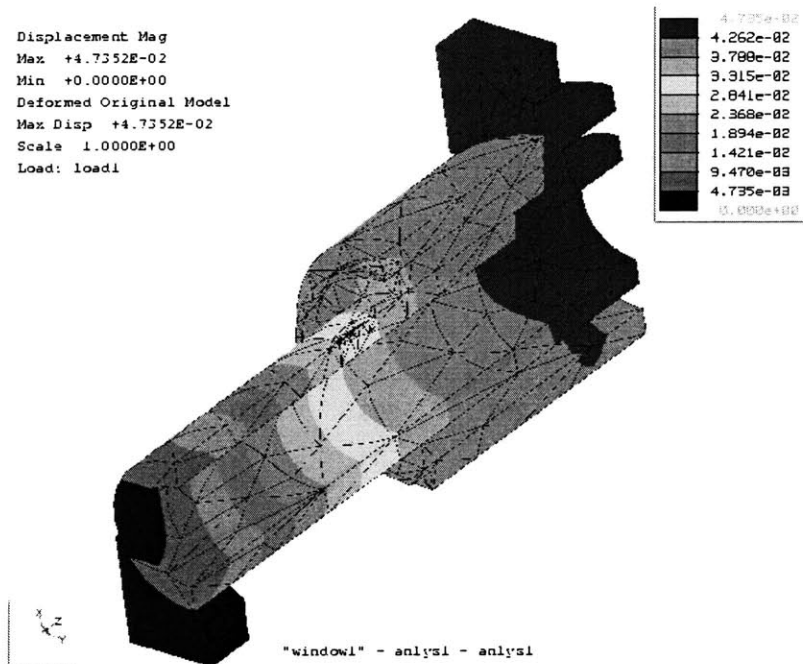


Figure 7.9 Displacement of the test setup with 10 000N load

Figure 7.10 describes the beam model. Only half of the beam (length wise) is modeled due to symmetry. The resulting displacement is shown at Figure 7.11. The x-coordinate represent the distance from the left edge of the shaft. The beam and the solid model agree very well on the displacements (as can be expected).

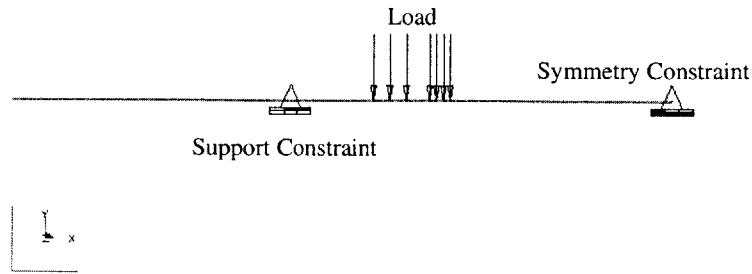


Figure 7.10 The simplified beam model

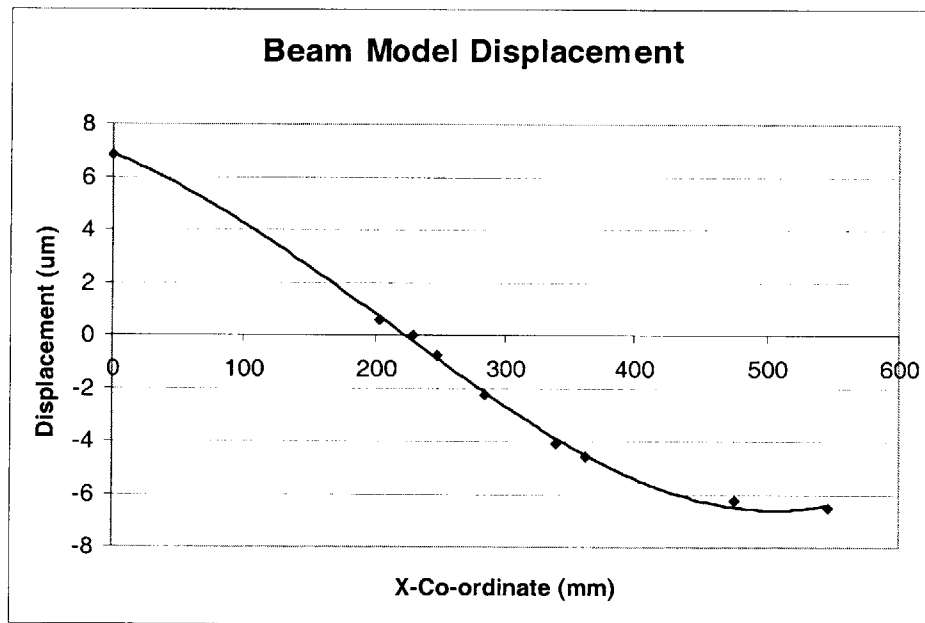


Figure 7.11 Beam model displacement

The correction for the displacement can be calculated many ways. It is reasonable to say that the housing with the capacitance probes moves down by an amount that equals the average between the displacements of the shaft at both ends of the bushing and the amount the clearance closes, or it is equally reasonable to assume that the displacement of the bearing assembly is equal to the displacement of the shaft at the location of the effective center of the bearing and the amount the clearance closes. Both way yield very similar

results. Let this displacement be called the measured displacement. In order to determine the stiffness of the bearing only it is desired to find out only the amount that the bearing clearance closes. The clearance displacement of the bearing is now found by

$$\delta_{cl} = \delta_{measured} - \delta_{correction} , \tag{7.4}$$

where the $\delta_{correction}$ is the difference between the extra housing displacement and the displacement of the shaft at the location of the capacitance probe. The model suggest that the correction is

$$\delta_{correction} = 4.6 \mu\text{m} / 10\,000 \text{ N} \tag{7.5}$$

The corrected force-displacement curve is shown in Figure 7.12.

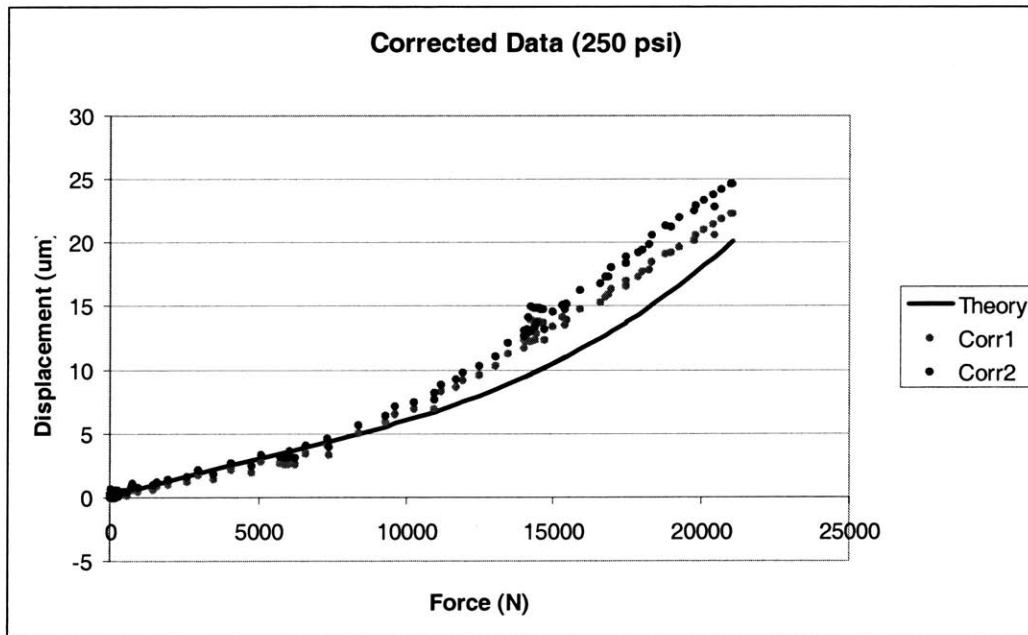


Figure 7.12 Corrected force-displacement curves at 250 psi with 50k force transducer. (Corr1=corrected results of the probe 1, Corr2=corrected results of the probe 3)

It can be seen that the agreement is much better than in the uncorrected case. The agreement is excellent until about 10 000 N. At loads greater than about 10 000 N the theory

predicts the bearing to be stiffer than the measurements indicate. This can be expected due to the model that neglects curvature effects in a bearing gap (this is explained in the modeling section). Also the procedure to predict the correction and the way the theoretical curve is computed is not entirely correct. The bending of the shaft makes the bearing clearance vary along the bearing which in turn has an effect on the bearing pressure distribution which in turn effects the load capacity and therefore the displacement of the bearing and the shaft. This is clearly an iterative problem. In order to solve this problem the bearing model has to be coupled with beam model. When designing a bearing for a certain application this should be taken into account, but due to the inaccuracies of the testing and the parts it does not add any information in this case. In addition usually only the small displacements are of concern.

To get even better idea of the force-displacement behavior this measurement was repeated with the less noisy 5k lbs force transducer for the smaller displacements of interest. Figure 7.13 shows these results. In this case it seems that the forcing device was not quite centered and the bearing assembly tilted slightly. The fact that the other probe shows such excellent agreement with the theory is likely to be partly due to coincidence rather than actual agreement. Agreement is still very good and the probe that deviates more from theory actually shows stiffer bearing than the theory. This also probably partly due to the computational correction made to the displacement.

As can be seen, the bearing behaves very linearly when displacements are small. This justifies the use of single number to describe the stiffness of the bearing. It must be noted, however, that this number is only the initial stiffness and in the case of large displacements the non-linearity of the behavior must be taken into account. Table 7.2 shows the initial stiffness as predicted and measured with 250 psi supply pressure. The measured initial stiffness is taken to be the average of the two measured and plotted in Figure 7.13. The agreement is entirely satisfactory and it can be concluded that the bearing with cast hydrostatic features behaves as would be expected of a bearing with machined hydrostatic features.

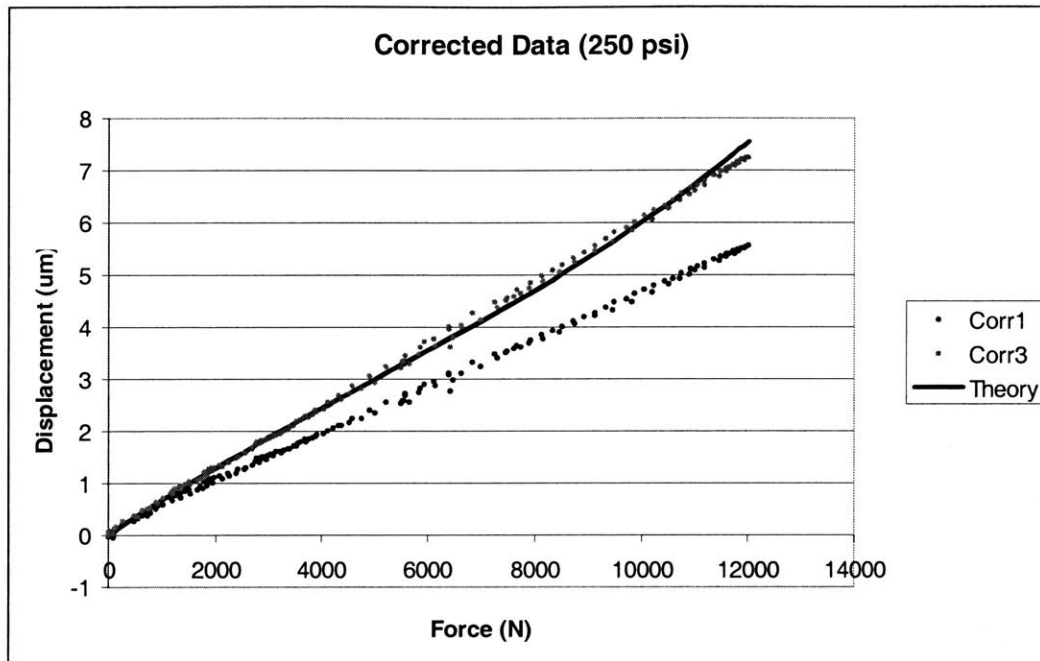


Figure 7.13 Corrected force-displacement curves at 250 psi supply pressure and the 5k force transducer. (Corr1=corrected results from probe 1, Corr3=corrected results from probe 3)

TABLE 7.2 Initial Stiffness at 250 psi

Measure	Value	Unit
Predicted Initial Stiffness	1770	N/ μ m
Measured Initial Stiffness	1915	N/ μ m
Difference	7.6	%

It must be noted that several data sets of these measurements had an problem where the displacements indicated by the probes were about twice the expected, as explained earlier. They were very consistent with each other and therefore it can said with fairly high confidence that these sets have an systematic error and can be discarded. This is further proved by the good agreement in the testing of the small prototype (See Section 7.3).

The other characteristic that was measured was the flow rate. The predicted and the measured flow rate are in Table 7.3.

TABLE 7.3 Flow rate at 500 psi

Measure	Value
Predicted Flow	11.2 l/min
Measured Flow	13.1 l/min
Difference	14.4%

This is in fact excellent agreement, even though the difference is percentage wise relatively high, when the fact that the flow rate varies according to h^3 is taken into account. Even a small errors in the clearance will cause the flow rate to vary considerably. Also the viscosity of the fluid might not be exactly right since it varies with temperature. The measured temperature was at the tank and it is possible that the temperature rises slightly as the oil passes through the pump and the bearing.

7.1.3 Conclusions

6" Diameter cast Bushings were tested for their static properties and compared to predicted values. The very high stiffness caused some problems measuring the actual displacement of the bearing even though the test structure was designed to minimize the effect of the elastic deflections in the measured results. This was corrected by calculating the elastic deflection of the test structure by means of finite element method.

The corrected data was in good agreement with the predicted results. The relative error in the initial stiffness was less than 8% and the error in flowrate prediction was less than 15%..

The most important conclusion is that large cast hydrostatic bearings work, even when the bearing parts are machined separately and then assembled. Also when this technology is

used, no special machining or manufacturing operation is needed which makes the bearing very cost effective when compared to existing systems with similar performance.

The results and the difficulty of measuring them shows that when designing machine structures with these bearings, it is likely that the compliance of the structure dominates over the compliance of the bearings. Therefore much attention must be paid to design of the structure, and if optimum performance is desired the bearing should be optimized together with the structure.

7.2 Dynamic Stiffness Testing of the 6" Prototype

It was attempted to measure the dynamic stiffness of the 6" bearing. This was done with impact hammer testing. Due to the time limitations only few separate points could be measured and therefore the results only yield an very rough idea of the dynamic behavior of the bearing. Also due to the high damping and stiffness it is very hard to separate the structural modes of the bearing from the ones of the test structure and even the floor.

7.2.1 Test Set-up

The same test set-up was used as in static testing. The only difference was, this time the bearing was supported instead of the shaft. Figure 7.14 shows the test-setup, the impact

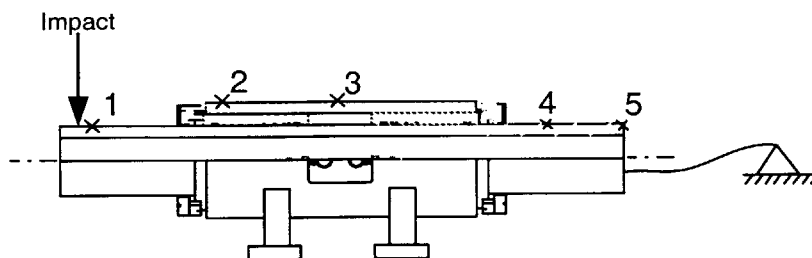


Figure 7.14 Impact and acceleration measurement points

point and the points where the acceleration was measured. The shaft is floating free inside the bearing and had to be constrained with a rope.

The measurement was taken with one Hz resolution for the range 0-400 Hz. The accelerometer had sensitivity of 100mV/g and the force transducer 1mV/lbs. The data was collected and Fourier transformed with signal analyzer and saved as an data file. Each trace was taken with 10 averages and an constant window was applied to time signal before the FFT (fast fourier transform).

The output frequency response function was in the form of inertance or accelerance (acceleration/force). In order to get the dynamic stiffness this has to integrated twice or in frequency domain divided by ω^2 .

7.2.2 Results

The dynamic stiffness and the phase are presented in Figure 7.15. The dynamic stiffness is presented for points 1,2 and 5 of Figure 7.14. The rest of the measured data was corrupted. The frequency response does not show any apparent resonances. Also the level of compliance is much lower than in the case static testing. This means that the response is in large part due to dynamic properties of the test stand and floor rather than the bearing.

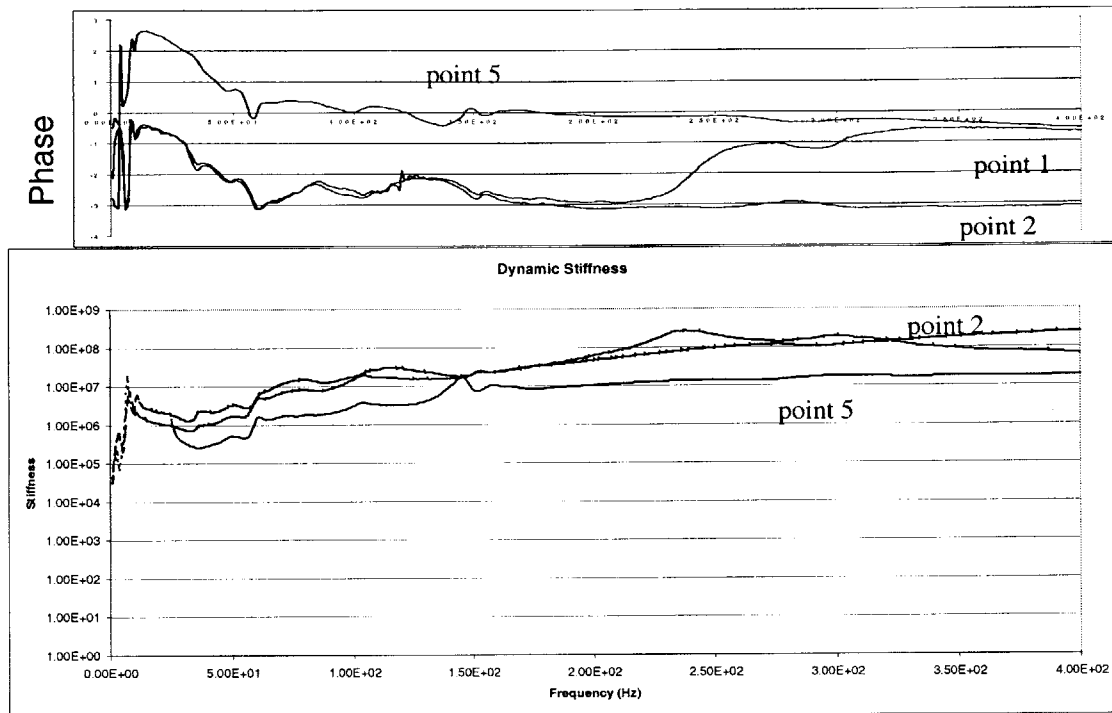


Figure 7.15 The dynamic stiffness and phase traces for the points 1,2 and 5.

The bearing dynamic properties can be checked by simple one degree of freedom model. Figure 7.16 shows the model and the parameter values.

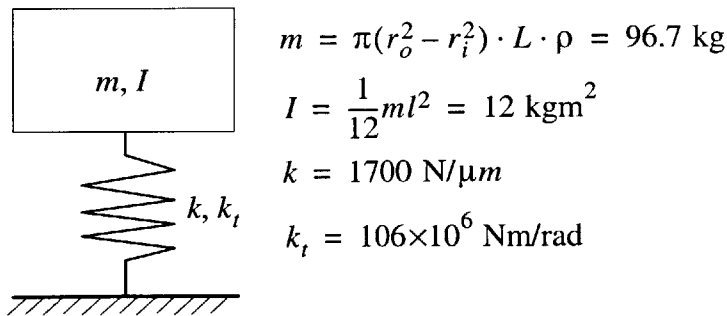


Figure 7.16 Simple single d.o.f system

First linear and rotational undamped natural frequencies are:

$$f_l = \frac{1}{2\pi} \sqrt{\frac{k}{m}} \approx 670 \text{ Hz} \quad . \quad (7.6)$$

$$f_r = \frac{1}{2\pi} \sqrt{\frac{k_t}{I}} \approx 475 \text{ Hz}$$

This simplified model does not take into account the compliance or the stiffness of the shaft. By performing a simple finite element beam analysis, with the bearings represented by spring elements, it is confirmed that there is no undamped natural frequencies below 400 Hz. The critical damping can be approximated by

$$c_c = 2\sqrt{mk} \cong 8 \cdot 10^5 \text{ Ns/m} \quad (7.7)$$

The bearing damping is approximately $1 \cdot 10^8$ Ns/m, which means that the first modes are over damped. This makes the dynamic testing extremely difficult. This will left as future work. There is little uncertainty in the bearing stiffness and damping properties, but the main question is how to best utilize these properties in machine design.

7.3 Static Testing of the 1.25" Prototype

In this section the testing of the 1.25" prototype will be explained and the results compared with the predicted values.

7.3.1 Test Set-up

In order to measure the static behavior of the bearing a test set-up was designed. To minimize the effect of structural deformation the structural loop of the set-up was made as stiff and small as possible. Figure 7.17 describes the test set-up. Figure 7.18 shows a photograph of the test set-up. Other important issues to consider besides the stiffness of the structural loop is the sealing the oil from getting into the gaps between the bearing housing and the capacitance probe. Here this is achieved by placing the capacitance probes above the bearing.

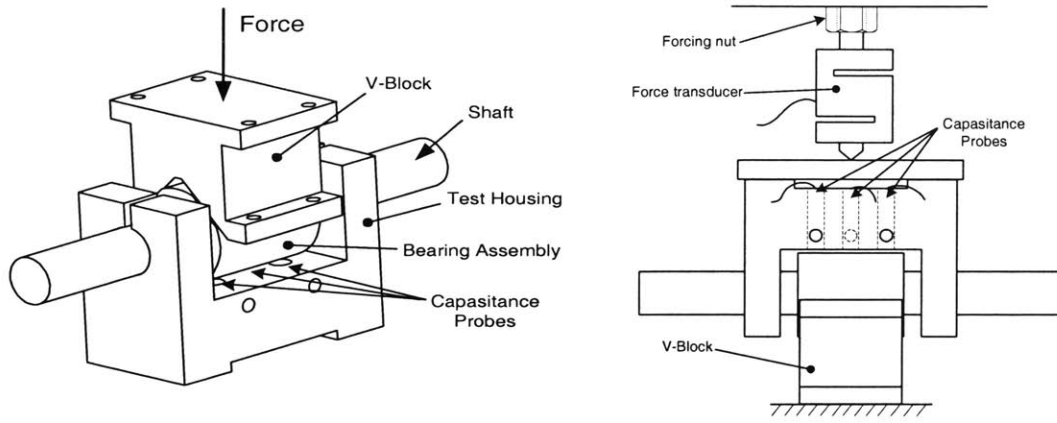


Figure 7.17 General and side view of the test set-up. General view is rotated upside down for clarity.

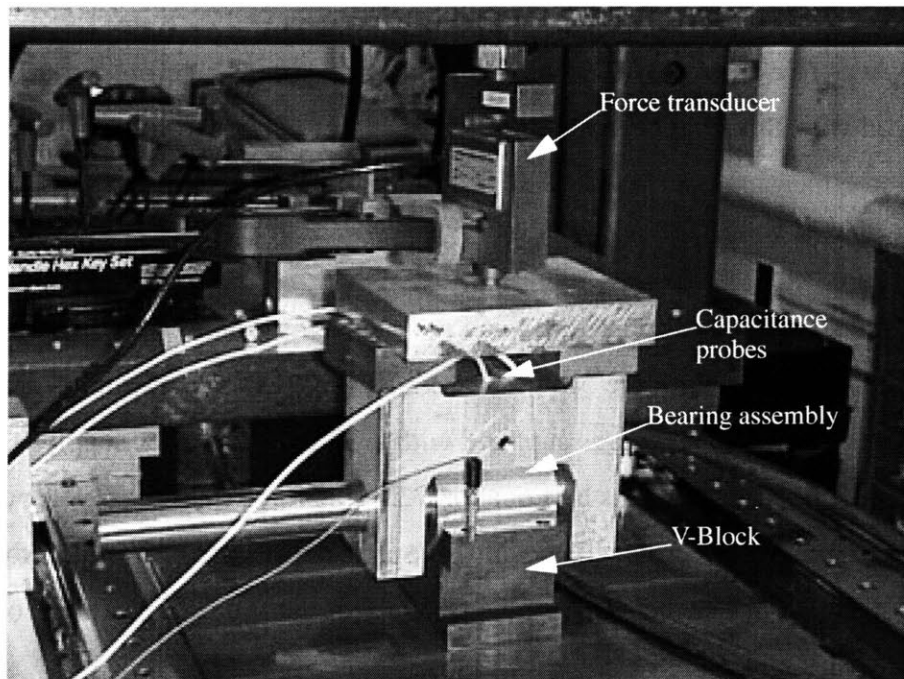


Figure 7.18 Photograph of the test set-up

The bushings were shrunk fit into an aluminum housing. The internal surface was machined after the assembly so that the cylindricity of the internal surface would be as

good as possible. Flats were machined to the housing to accommodate the v-block support and a flat surface for the capacitance probes. Figure 7.19 shows the bearing assembly.

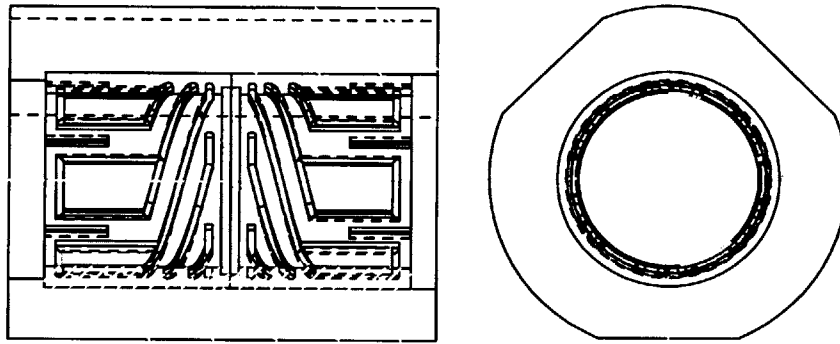


Figure 7.19 Bearing assembly

The bearing was free to move in Θ (or rotational) direction. Therefore the displacement was measured with three capacitance probes which were offset from the bearing centerline. With three measurement points the location of the flat in the housing is known and the tilt or the rotational displacement can be computationally removed from the results.

The bearing was loaded by threaded rod and a nut pushing against beam above the bearing. Force was measured with the 5k 's' force transducer with specifications described in Table 7.1. The force transducer was supplied with a 12.15V dc power supply. The output voltage is transformed to Newtons by Equation 7.2. This force transducer was not optimal for these measurements. The small bearing size and the test set-up limited the load to under 2000 N which is less than 10% of the capacity of the transducer. This is one reason why the results are fairly noisy.

Hydraulic Unit

The hydraulic unit used consisted of a constant pressure pump and a oil cooler and plumping. The oil cooler kept the oil at 25° C. The oil was ISO 60 oil with viscosity of 60 cSt. The viscosity was measured to be 0.061 Pa s [Kane, 1999]. This isa typical machine oil.

7.3.2 Results

The force-displacement curve is shown in Figure 7.20 together with the predicted curve and the curve fit for the measurements. The agreement between the measured and theoretical values is excellent except for the relatively high noise. This noise is due to the too large force transducer and the vibrating forcing structure. The agreement is good enough so that it is not necessary to redo the test with more sensitive force transducer.

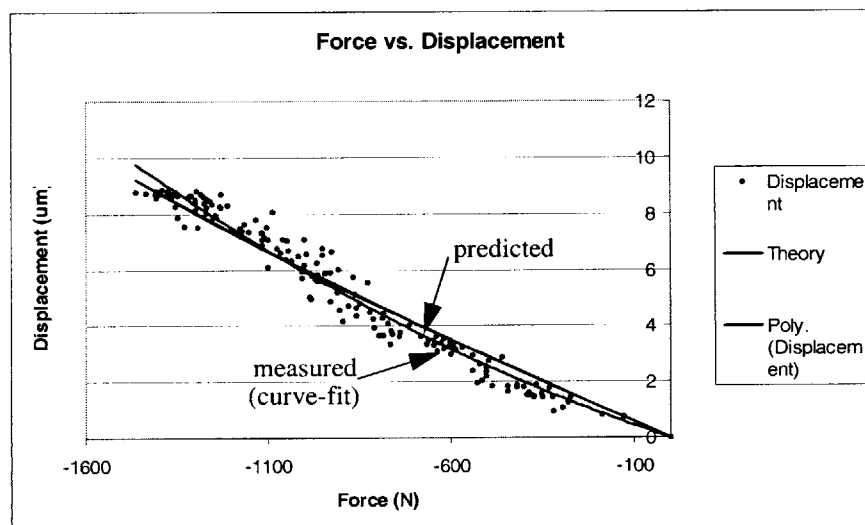


Figure 7.20 Force displacement results at 500 psi.

Here again the displacement was only measured up to approximately 10 μm . This is the most interesting part of the bearing behavior from application point of view. Also the tilting motion resulted in capacitance probes touching the bearing at larger forces.

The initial stiffness (taken as linear fit at 500N) is presented in Table 7.4. The maximum relative error between the curve fit and the predicted data was 24.4% and the average relative error 8.4%. The maximum error occurred at small displacement and the absolute value of the error was only 0.14 μm . These error values are acceptable taking into account the noise and the variation due to the manufacturing errors shown in Section 6.4.

TABLE 7.4 Initial stiffness of the 1.25" prototype

Measure	Value
Predicted Stiffness	170 N/ μ m
Measured Stiffness (curve fit)	185 N/ μ m
Relative Error	8.1%

The flow rate was also measured. The results are summarized in Table 7.5. It seems that at lower pressures the error is greater. This can be due to slight change in viscosity due to temperature or most likely due to small errors in the clearance. At higher pressure the clearance increases slightly thus correcting the flow rate. Overall the agreement is good. I

TABLE 7.5 Measured and predicted flow for the 1.25" bearing

Pressure (psi)	Measured Flow (l/min)	Predicted Flow (l/min)	Difference (%)
200	0.045	0.055	22%
500	0.116	0.139	20%
1000	0.28	0.28	0.4%

7.3.3 Conclusions

1.25" prototype was designed, manufactured and tested. The force-displacement curves agreed well with the predicted values, the average relative error being 8.4%. More sensitive force transducer would have produced less noisy data, but together with the 6" prototypes test results it can be concluded that the lumped parameter model predicts the bearing behavior well. Some problems were encountered due to the rotation of the bearing during the measurements, but this error could be canceled by multiple measuring points up to displacements of $<10 \mu$ m. The agreement in the flow rate was also good.

7.4 Error Motion Measurements

One important characteristic of a bearing is the accuracy of the motion the bearing provides. The bearing described in this thesis allows linear motion, so the only relevant error motion is the radial error motion. The most common way to measure radial error motion is to attach a precisely circular section to the rotating part and measure the radial movement by means of dial indicator. However, this method is not satisfactory if pure eccentricity is desired to be separated from other types of error motions [Tlusty, 1992]. Moreover, the method does not provide any information on the course of the deviation vector during rotation. Therefore a different method was selected as described in the following section.

7.4.1 Testing Method

The method selected is a two gauge method for rotating sensitive direction [ASME, 1985]. In this method two gauges are spaced angularly 90° apart (mutually perpendicular) and measure the motion of a spherical master. The spherical master is offset on purpose from the axis of rotation. This set-up is shown schematically in Figure 7.21. In case of perfect rotation the gauges would measure a x and y-coordinates of a perfect circle. In other words, the offset provides information about the angular position of the rotating member. Any deviation of the measured trace from perfect circle indicate error motions. After the data is collected a circle has to be fitted to the data in order to determine the error motions. This can be done many different ways. The [] describes the following ways:

- minimum radial separation (MRS)
- least squares circle (LSC)
- maximum inscribed circle (MIC)
- minimum circumscribed circle (MCC)

The one most convenient to use in case of computerized measurement is the least squares circle. It is unique and can be defined mathematically (MRS is not unique and defining it requires trial and error method). In addition it is conservative, the error motion values obtained by it are generally 10% larger the values obtained using MRS method [ASME,

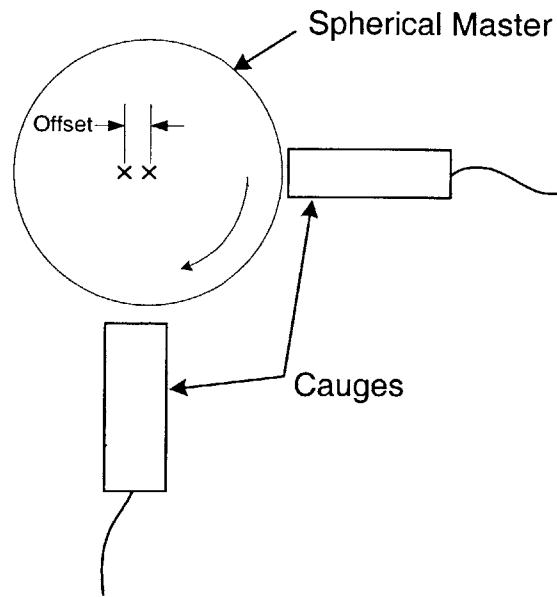


Figure 7.21 Two gauge method with offset spherical master

1985]. The LSC can be found by performing the following unconstrained optimization problem

$$\min \left(\sum_{i=1}^n \{ [(x_i - x_0)^2 + (y_i - y_0)^2]^{1/2} - R \}^2 \right) \quad (7.8)$$

w.r.t x_0, y_0, R

where subscript i refers to a measured point and the optimization variables are the coordinates of the center point and the radius of the LSC. The minimization can be performed by, for example, Nelder-Mead direct search method, which is multidimensional unconstrained nonlinear minimization method used by MATLAB function `fminsearch`. The error motion values are then the maximum and the mean deviation from the LSC. Asynchronous error motion is the variation of the error vector in single direction during multiple revolutions. This can be calculated as the thickness of the error motion trace in radial direc-

tion. Maximum and mean asynchronous error motions are calculated. MATLAB scripts that perform the circle fit and the error motion calculations are shown in Appendix B.

7.4.2 Test Set-up

Some special arrangements had to be made in order to measure this bearing, since it does not have thrust bearing. The test set-up consists of the bearing assembly, V-block, shaft, wobble plate, precision ball and a precision cast iron angle. Whole set-up is assembled on a surface plate which is at very slight angle from horizontal (approximately 0.0005:1). This slight tilt is used to preload the shaft against the cast iron angle. The precision ball contacts the cast iron angle and acts as an thrust bearing. The ball is 1" diameter grade 5 steel ball. Grade 5 means that the spherity of the ball is within 5 microinches or $0.127 \mu\text{m}$. The wobble plate is used to offset the ball from the canter of the rotation. A machining drawing of the wobble plate is shown in Appendix A. The viscous forces due to the fluid flowing in the grooves is enough to rotate the shaft slowly (10-20 s/rev depending on the pressure). Therefore, no external drive is needed to rotate the shaft. The hydraulic unit and the oil are the same as in the static testing of the 1.25" bearing. The motion is measured with two capacitance probes. The data is collected with a National Instruments PMCIA data acquisition card and processed with Labview software and saved into a ASCII file for further analysis. A drawing of the test set-up is shown in Figure 7.22 and a photograph is shown in Figure 7.23. This set-up measures both radial and angular error motions combined without separating them..

Possible error sources in the measurement are the environment noise, the ball spherity errors, probe alignment, friction force caused by the ball touching the cast iron angle and the pump pressure pulsations. The pump pressure pulsations are inherent to a hydrostatic system, but by carefully designing a hydraulic system with sufficient accumulators, this effect can be made smaller.

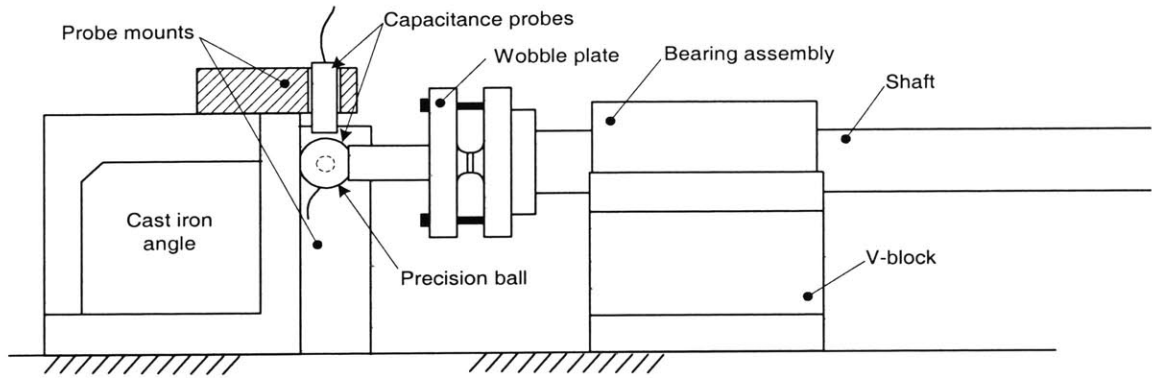


Figure 7.22 The error motion test set-up.

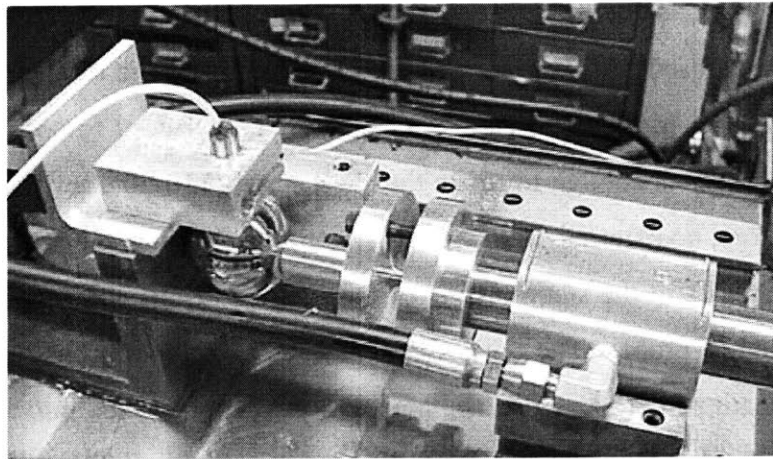


Figure 7.23 Error motion test set-up (2" ball)

7.4.3 Results

In Figure 7.24 the motion trace for single revolution is shown. The maximum deviation from LSC is $0.17 \mu\text{m}$ and the mean deviation $0.055 \mu\text{m}$.

In Figure 7.25 the motion trace for single revolution is shown. The maximum deviation from LSC is $0.20 \mu\text{m}$ and the mean deviation $0.05 \mu\text{m}$. This test was run at 6 rpm and there is 10 revolutions in the error motion trace. By looking at the error motion trace it

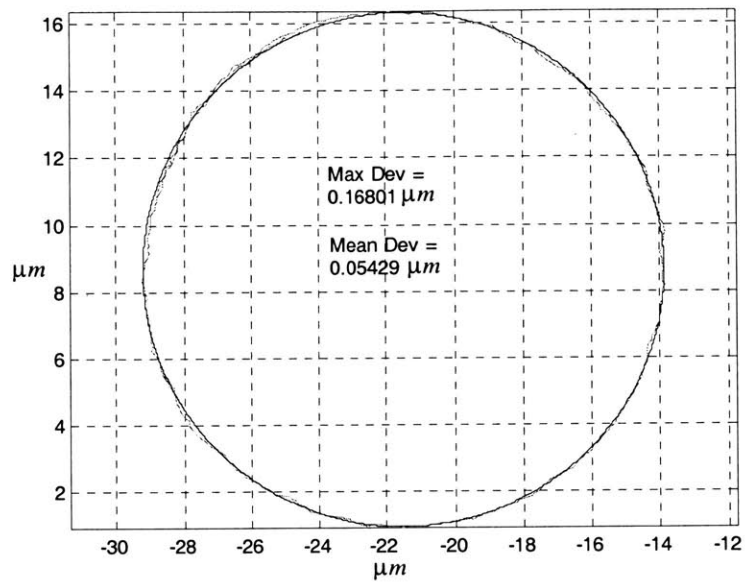


Figure 7.24 Error motion trace for single revolution

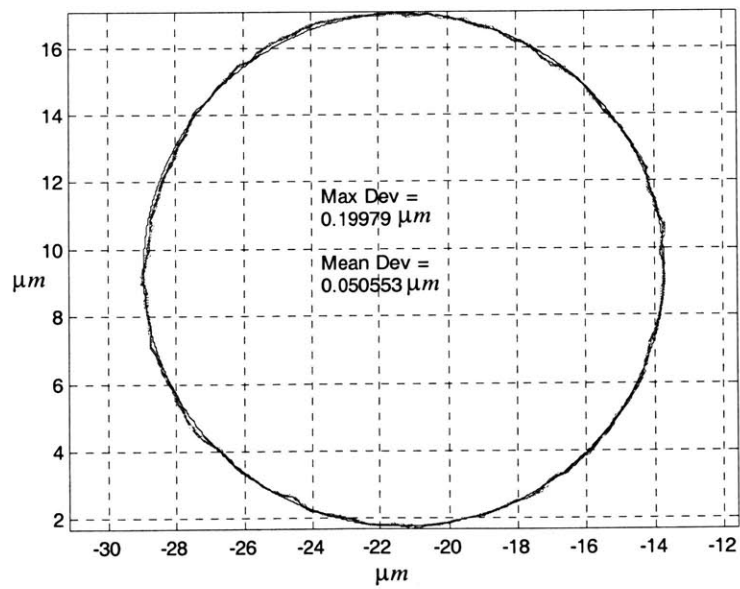


Figure 7.25 Error motion for multiple revolutions

seems that the largest deviations from the LSC are of fairly short wavelength. This would seem to indicate a scratch with burr on its edges in bearing surface or a dimple either in the ball or in the bearing surface. A fairly large surface feature would be necessary in the bearing for it to produce a significant deviation, because of the error averaging effect of the oil film.

The asynchronous error motion for the error motion trace of Figure 7.25 shown in Figure 7.26. The maximum asynchronous error motion is $0.20 \mu\text{m}$ and the mean asynchronous error motion is $0.07 \mu\text{m}$. Spectral analysis of the asynchronous error motion does not reveal any specific frequencies at which the error occurs.

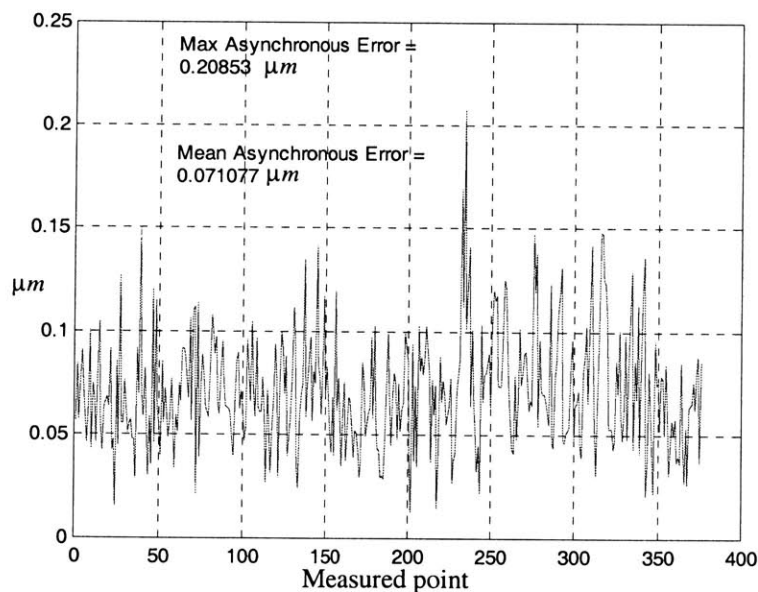


Figure 7.26 Asynchronous error motion

In order to assess the noise level the measurement was run with the bearing rotation enabled with the pump on and off. Figure 7.27 shows the noise measurement with the pump on. The maximum deviation from a straight line is $0.13 \mu\text{m}$ and the mean deviation is $0.024 \mu\text{m}$. Figure 7.28 shows the noise level with the pump turned off. The maximum

deviation from a straight line is $0.49 \mu\text{m}$ and the mean deviation is $0.14 \mu\text{m}$. An interesting phenomenon is observed, the noise level with the pump on is larger than with the pump turned on. This can be explained by the damping properties of the bearing. The bearing actually isolates itself from the environment, thus lowering the noise level when the pump is turned on and the shaft is supported by oil film.

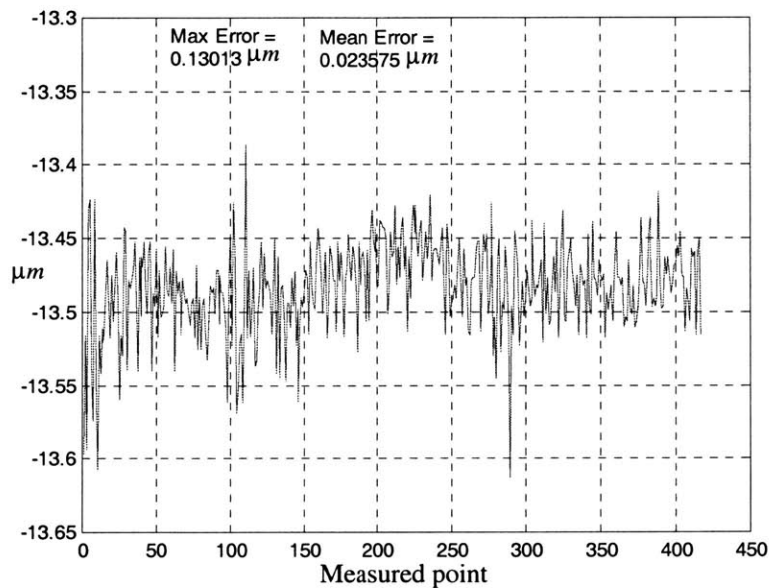


Figure 7.27 Noise level with pump on

The bearing bore and shaft was made to tolerances of $5 \mu\text{m}$. The error motion is less than $0.2 \mu\text{m}$ which means error reduction approximately by a factor of 25.

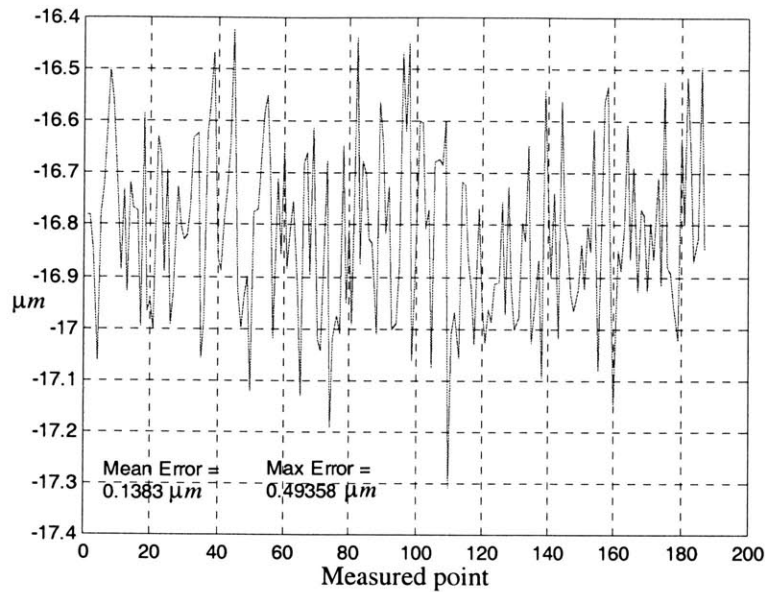


Figure 7.28 Noise without the pump

7.4.4 Conclusions

The bearing error motion is less than $0.2 \mu m$ with manufacturing tolerances of $5 \mu m$. The error motion value of $0.2 \mu m$ is conservative considering all the environmental disturbances. This leads to a error reduction factor of approximately 25. This is very accurate bearing, considering no special precision manufacturing steps were needed to manufacture them. The shaft used can be standard ground shaft and the bearing bore can be ground or honed to desired tolerances by almost any standard machine shop.

Chapter 8

APPLICATIONS

In this chapter a general discussion is presented about suitable applications of this bearing. Then a few specific applications are discussed in a little more detail. The bearing design is discussed in detail in the design chapter, in this chapter the emphasis is on the application itself. Also some general ideas about sealing is presented because it will be encountered in most applications.

8.1 General

In the introduction a typical applications for hydrostatic bearings were listed. They were [Bassani, 1992, Slocum, 1992]

- Telescopes, radio telescopes, large radar antennas. For example the Mount Palomar telescope where hydrostatic bearings support 500 ton mass that makes a one revolution in a day
- Air preheaters for boilers in power plants
- Rotating mills for ores or slags
- Stamping presses
- Machine tool slides and spindles
- Hydrostatic steady rests for large lathes and cylindrical grinders
- Vibration attenuators for measuring instruments
- Dynamometers

The most obvious uses for the bearing introduced by this thesis are naturally the ones where the hydrostatic bearings are already used. This bearing provides, in most cases, more cost efficient and robust hydrostatic bearing which is very easy to install and maintain.

8.2 TurboTool

TurboTool is a very high speed machining spindle driven by turbine instead of a electric motor. This way very large cutting power can be achieved without significant heating problems. This potential application is described in [Slocum, 1997]. The general problem with high speed, high power spindles is, in addition to power source, the high power losses due to bearings. On the other hand the damping properties of fluid film bearings are very desirable in this case, as shown later in this chapter. In case of a fluid film bearing the viscosity of the fluid and the radius of the bearing should be minimized in order to reduce the power losses. For example, a 50 mm diameter water bearing would consume about 60 kW at 50 000 rpm as a 25 mm water bearing would consume about 25 kW at 100 000 rpm. Because the hydrostatic bushing can operate on smooth shaft, the tool shaft may directly be used without a tool holder, thus reducing the diameter of the bearing. The tool is attached to the turbine by shrink fit and is then balanced dynamically. This assembly can then be inserted into a tool head which is part of machine tool and has all the necessary fluid connections. An embodiment of the design is shown in Figure 8.1 [Slocum, 1997].

In the concept shown in Figure 8.1 the bearing geometry is machined into the tool shaft, which is then inserted into a smooth bore. Having the bearing grooves on a bushing offers several advantages. No expensive machining operation is needed. The tool is carbide or some other very hard material which makes the machining process difficult. Also the balancing is easier as the tool without grooves is inherently more balanced. Also in a case of a crash the bushings are very easy to replace and since they are very low cost this can provide large economic benefits.

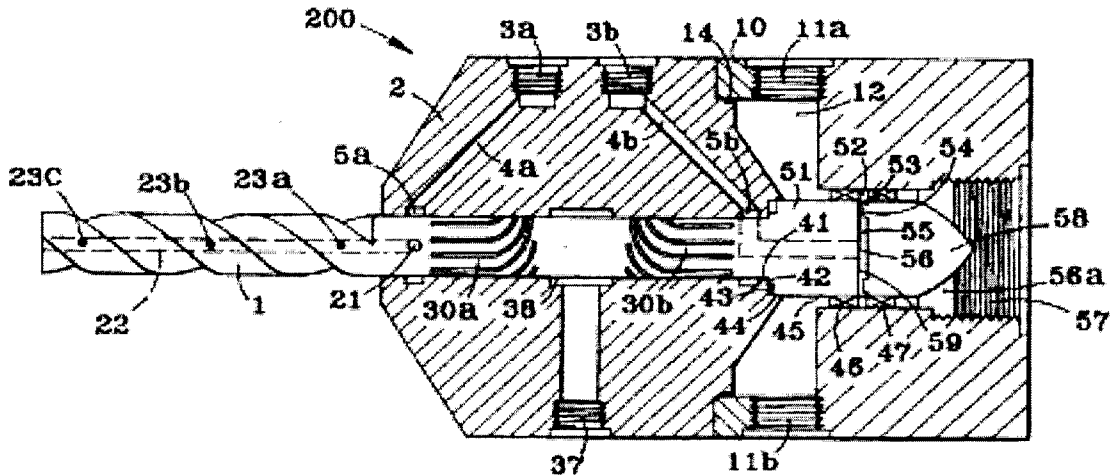


Figure 8.1 Embodiment of a TurboTool concept

8.2.1 Preliminary Analysis of TurboTool Concept

Turbine and Fluid Supply System

First a required pressure drop is calculated for a turbine. Here a inviscid and incompressible flow is assumed and only the first order equations are used to estimate the turbine performance. This analysis is not meant go into detail about turbine design but rather to show feasibility of the concept. The required flow rate and turbine diameter for a given turbine power can be calculated from [Fay, 1994]

$$P = Q\Delta p = \dot{m}\omega^2 R^2 \quad (8.1)$$

$$\Rightarrow Q = \frac{P}{\Delta p}, R = \sqrt{\frac{\Delta p \rho}{\omega^2}}$$

If 120 000 W is required and the pressure drop across the turbine is 7 MPa (1000 psi), the flow rate becomes approximately 1000 l/min and the turbine radius 8 mm. Above equations assume perfect radial turbine. In practise the turbine would be larger in size, approximately 20 mm in radius [Slocum, 1997]. This calculation shows that a very small turbine

can produce the necessary power. There are two options for choosing the fluid supply system, either choosing low pressure high flow rate or high pressure low flow rate system. The high flow rate system is more desirable, because it can be used more easily with the bearing, where maximum allowable pressure is limited. In addition higher flow rate has higher momentum which is important when the rotating tool is pushed into material it is supposed to cut. Also, the high flow rate can be used to remove heat from the system very effectively. The pumping system that can deliver required power is fairly expensive and comparable in price to other spindles that could have similar capabilities. Although rolling element bearings can not reach speeds as high as is required here, magnetic and air bearings could. The major advantage with this system is that the expensive equipment is separated from the actual machining head that is moving at high speed in hazardous environment. The expensive equipment is located away from the machining operation. In case of a crash only the relatively inexpensive tool and in worst case the housing for it is destroyed, not the entire drive. Fluid bearings also provide higher load capacity and damping than magnetic or air bearings.

Rotor System

The rotor system consists of bearings and the tool shaft and the attached turbine. In order to size the bearings first the shaft radius is selected. As mentioned earlier in order to minimize the shear losses the radius should be minimized. The manufacturing methods described in the manufacturing section determine the minimum diameter for the bushing to be approximately 25 mm. Also for sizing the tool and the bearings expected machining forces must be estimated. This can be done simply once the cutting power is determined. The total required power was stated as 120 kW from where 100 kW is the power reserved for the cutting. The force can be calculated from

$$F = \frac{T}{R} = \frac{P}{R\omega} \quad (8.2)$$

For a 25 mm diameter tool this force becomes approximately 765 N. For a 50 mm overhang tool this will lead to a tool tip deflection of approximately without bearing deflections.

$$\delta_{tip} = \frac{Fl^3}{3EI} = 9 \times 10^{-6} m \quad (8.3)$$

This is reasonable for such a high power operation. The high speed bearing from Section 5.3 is used as a bearing. The clearance and the viscosity are chosen in such a way that the land flow remains laminar (see Table 8.1).

TABLE 8.1 Bearing dimensions for TurboTool

Dimension	Value
D	25 mm
L	25 mm
h	15 μ m
P_s	7 MPa
μ	0.0025 Pa s
ρ	995 kg/m ³
N	100 000 rpm

The bearing with central lands in the pocket is chosen due to its better damping properties and slightly higher load capacity and stiffness. A simple finite element model of the rotor system is constructed in order to estimate linearized dynamic behavior in the vicinity of the equilibrium under machining load. This analysis is simplified and does not take into account the gyroscopic effects which will make the natural frequencies dependent on the rotational speed and make the mode shapes complex (rotating). The bearing properties at equilibrium point are summarized in Table 8.2.

TABLE 8.2 Bearing properties at equilibrium point under maximum machining force

Property	Value
Eccentricity at 765 N	0.25
Force Angle	-51°
Pumping Power	90 W
Shear Power	5880 W
Stiffness (N/m)	$\begin{bmatrix} 5.8 & 9.2 \\ -7.4 & 6.5 \end{bmatrix} \cdot 10^7$
Damping (Ns/m)	$\begin{bmatrix} 2.9 & 0 \\ 0 & 3.1 \end{bmatrix} \cdot 10^4$
Critical Mass	8.2 kg

From there the linearized stiffness and damping coefficients in the load direction are: stiffness 65 N/ μ m and damping 31 000 Ns/m per bearing half. The finite element model is shown in Figure 8.2. The spring and the dashpot are located at effective force center of the bearings. A two node, four degree of freedom beam element is chosen to model the system. The mass matrix is consistent, meaning same polynomials are used to formulate the mass and stiffness matrices. The system equations of motion become

$$[M]\{\ddot{x}\} + [C]\{\dot{x}\} + [K]\{x\} = \{F\} \quad (8.4)$$

where M , C and K are the mass, damping and stiffness matrix respectively. This can be transformed to a first order state space system by defining state variable vector

$$\{x\} = \begin{Bmatrix} \{x\} \\ \{\dot{x}\} \end{Bmatrix} \quad (8.5)$$

The first order system of equations is

$$\{\dot{x}\} = [A]\{x\} + [B]\{F\} \quad (8.6)$$

In terms of the mass, damping and stiffness matrices and displacement vector equation 8.6 becomes

$$\begin{Bmatrix} \{\dot{x}\} \\ \{\ddot{x}\} \end{Bmatrix} = \begin{bmatrix} 0 & [I] \\ [M]^{-1}[-K] & [M]^{-1}[-C] \end{bmatrix} \begin{Bmatrix} \{x\} \\ \{\dot{x}\} \end{Bmatrix} + \begin{bmatrix} 0 & 0 \\ 0 & [M]^{-1}[I] \end{bmatrix} \begin{Bmatrix} 0 \\ \{F\} \end{Bmatrix} \quad (8.7)$$

where the vector F is input vector of forces and moments. In this analysis contains only one non-zero element, the cutting force applied at tool tip. The MATLAB program that assembles the finite element system and sets up the state space model and solves it is presented in Appendix D. The desired dynamic response is the dynamic response of the tool tip. Convenient MATLAB function to obtain is the bode-function. In order to use this function the output is formulated the following way

$$\{Y\} = [Cc]\{X\} + [D]\{F\} \quad (8.8)$$

where Cc and D are row vectors. The only non zero component is the component in C which corresponds to the tip displacement and can be set to equal the magnitude of the cutting the force in which case the output corresponds to the actual displacement. The stiffness and damping coefficients of the bearings are added to the associated degrees of freedom in the stiffness and damping matrices. A damping ratio ζ can be set for all modes by setting the damping matrix [O'Sullivan, 1998]

$$C = 2\zeta M^{1/2}(M^{-1/2}KM^{-1/2})^{1/2}M^{1/2} \quad (8.9)$$

The transfer function of the TurboTool is shown in Figure 8.3. Also shown is the same system with bearings having low damping. These results are computed with modal damping of 1% ($\zeta = 0.001$). Figure 8.3 shows clearly the advantageous damping properties of fluid film bearings. All of the resonance peaks almost vanish due to the high damping. Actually some modes become over damped, thus vanishing from the plot. This can be seen by calculating the eigenvalues of the A matrix, which for the most part, are complex. The real part of the eigenvalue indicates the rate at which free oscillations will die out and

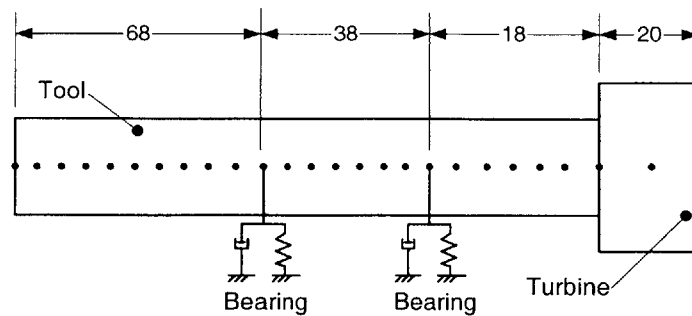


Figure 8.2 Finite element representation of the TurboTool

the imaginary part the frequency of the damped oscillations [Den Hartog, 1985]. Some of the computed eigenvalues are real for the damped case, indicating over damped mode. The only undamped resonant peak that exists below the rotational frequency of 10 470 rad/s (100 000 rpm) is one of the modes that vanish. Only the sixth undamped mode remains approximately the same. This mode does not have large displacements at the bearing locations and therefore the damping of the bearings does not play significant role. The model deceases the effect of damping in this case since it concentrates the damping into a single node although in reality it is distributed along the bearing length. The static displacement of the tool tip is approximately -75 dB which corresponds to 180 μ m. This is also the maximum displacement for the damped case.

According to the linearized analysis the concept seems feasible due to the high damping in the bearings, which highly reduces the risk of chatter. The excitation frequency from cutting depends also on the number of flutes the tool will have. Due to the high damping there is much wider spans where these excitation frequencies can fall without necessarily causing any problems. In another words, the modal density is far less for the damped case.

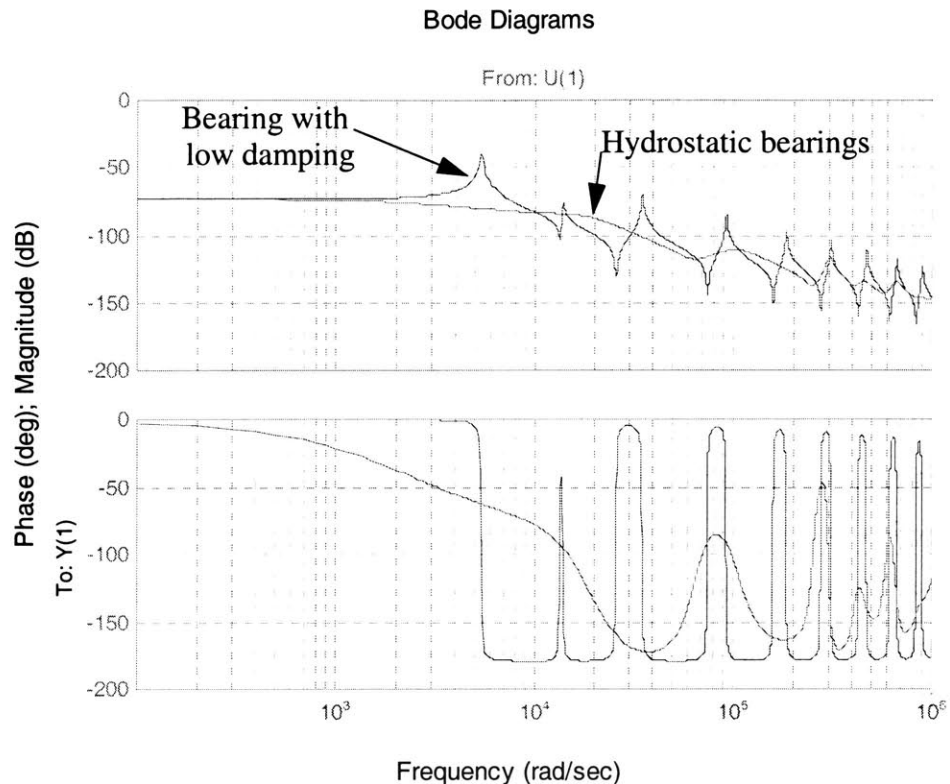


Figure 8.3 Transfer function for the tool tip displacement of the TurboTool

8.3 Conceptual Very Small Machine Tool

Hydrostatic bearings have a special property that a single bearing can provide both rotary and linear motion. This can be used as an advantage when multiple degree of freedom tools are designed. It can reduce the number of stacked axis dramatically. Here a conceptual design of small 5 degree of freedom (5-axis) machine tool is presented as an example of linear-rotary capabilities of the bearing and the new freedom it can provide when designing multiple d.o.f machinery.

8.3.1 Functional Requirements for Small 5-Axis Machine

The first order functional requirements for a small 5-axis machine are (numbers in parenthesis are target assumptions):

- § Accuracy in the order of 10 μm
- § 5-Axis of motion
- § Small workspace (30x30x30mm)
- § Small footprint (400x400x400 mm)
- § Simplicity

Additional requirements for a machine would be the reliability, ease of use and operating ergonomics. Concepts shown here show only the primary component configuration and do not consider the latter requirements. Later in design process these requirements will be given the attention they deserve.

There are literally hundreds of different ways of arranging the machine axis to achieve the required degrees of freedom. However, very few of them are fundamentally different. The most typical 5-axis arrangement is gantry type as shown in Figure 8.4. The machine consists of a bridge and worktable. The bridge, which holds the spindle, has vertical, one horizontal and one rotary degree of freedom. The base, where the workpiece is located, has usually the two remaining degrees of freedom (one horizontal and one rotary). There can be many different permutations of this same basic design. The advantages of this design are that it does not need any special components and it can be made fairly stiff. In addition, the work space to footprint ratio is good when larger machines are concerned. The disadvantages are cantilevered structures, stacked axis and large ABBE errors. ABBE errors are angular errors that are magnified by the distance between the error source and the tool tip. Most significant ones are the result of the offset between the tool tip and the center of stiffness of the bearings carrying the axis in question. In case of the stacked axis the errors add up quickly and can become unacceptably high. The accuracy of this type of machine depends greatly on manufacturing, assembly and component quality. One aspect also of concern, in the most typical arrangement, is that one of the rotary axis is aligned with the rotary axis of the spindle when it is in vertical position. This results in a singularity in the tool motion in the middle of the work space.

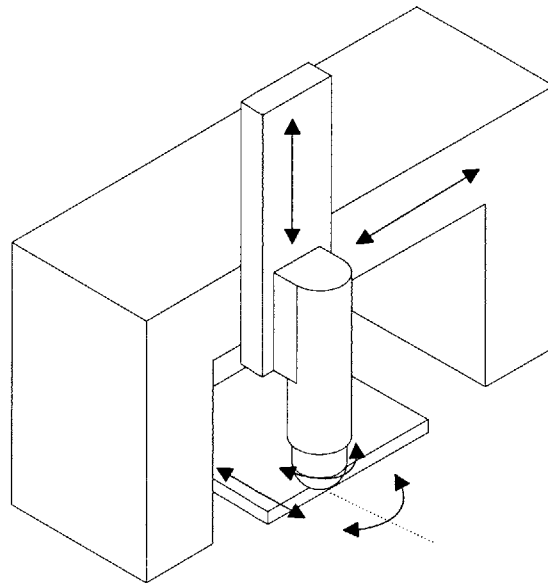


Figure 8.4 Typical gantry type arrangement of axis

The second fundamentally different configuration is the hexapod or Stewart platform. In this type of machine the spindle is moved by changing the angular position and length of the rods that support the spindle (see Figure 8.5). The advantages of this type of machine are the high stiffness (in the middle of the work space) and relatively simple structure. Hexapod also scales well when machine size gets larger. The disadvantages are the highly non-constant stiffness within the work space, ABBE errors and control problems. In addition, most of the components have to be custom made and are very complicated. This type of machine was expected to change the machine tool business, but it has not done so, mainly due to the above mentioned problems. There is also different variations of this type, some of the degrees of freedom can be achieved by linear tables or rotary platforms and only some with moving platform. This type can be called a mix between the hexapod and the traditional type. With true hexapods the goal accuracy of $10\ \mu\text{m}$ will be hard to achieve.

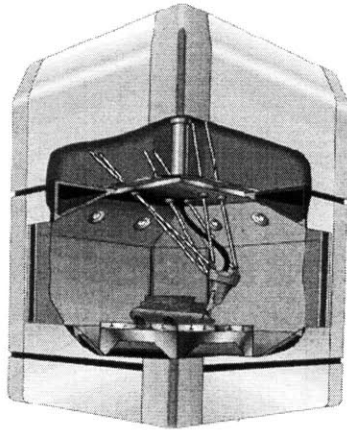


Figure 8.5 Hexapod (Stewart platform)

The third type here is by far the simplest for a small machine. It introduces the idea of having the same physical structure perform both rotary and linear degrees of motion. By combining two of these structures perpendicular to each other and utilizing direct drive technology the total of four degrees of freedom (the rotational and horizontal) can be achieved by just two moving parts, as shown in Figure 8.6. The fifth degree of freedom (vertical) can be achieved either by moving one of the axes up and down as a whole or by moving just the spindle. The former is more attractive in terms of simplicity. The advantages of this design are very high stiffness, high accuracy due to the close proximity of tool point to the center of stiffness of the bearings. This also results to almost zero moments around the bearing axis due to the cutting forces. Another advantage is the simplicity of the structure and the components. Disadvantages are that this type of machine does not scale up well. As the machine is scaled up the footprint grows very rapidly and the inertia of moving parts becomes large. Also linear rotary actuators are not readily available. A separate rotary and linear actuator can be combined to achieve the desired motion, but this will lead to inefficient use of space for larger machines. A work space up to 100x100x100mm can be achieved with a desktop size machine. There are several configurations derivable from this basic idea. For example, by cutting the machine shown in

Figure 8.6 A into half a cantilevered design is achieved as shown in Figure 8.6 B. Having both yokes cantilevered will save footprint but will sacrifice stiffness.

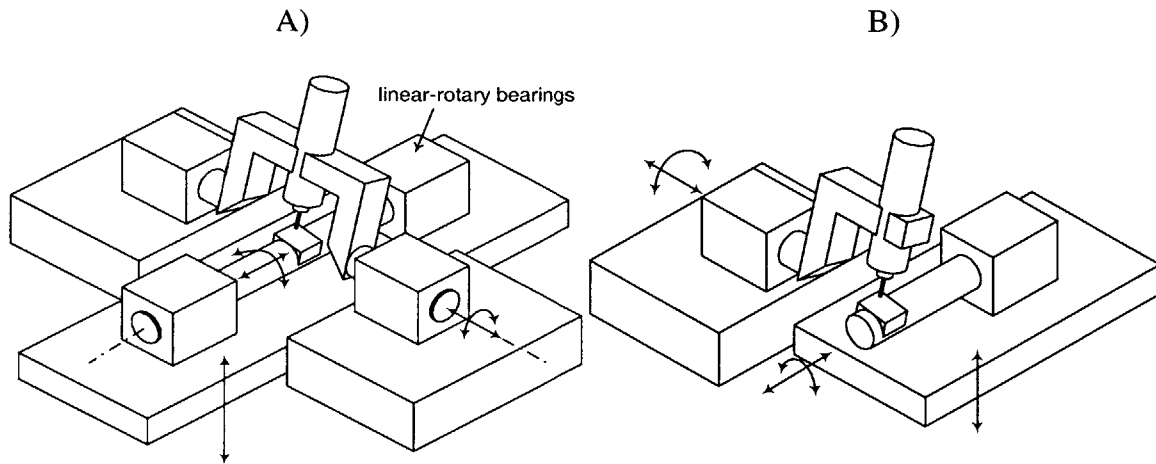


Figure 8.6 Linear-rotary concepts (actuators not shown)

One variation of the double yoke concept is shown in Figure 8.7. This configuration is more complex, but can be made to fit into smaller footprint.

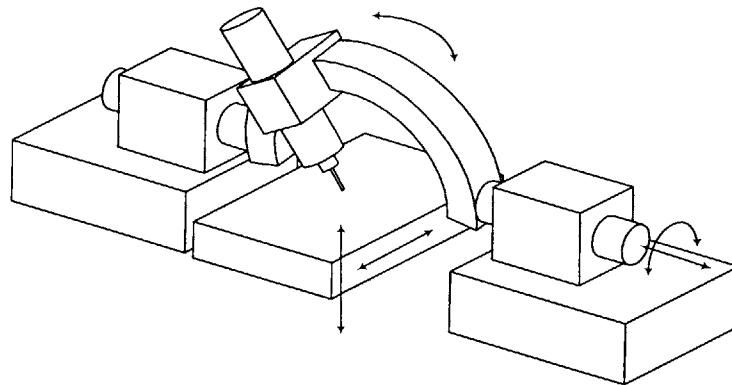


Figure 8.7 Circular concept

8.3.2 Concept Selection

In Table 8.3 different configurations are compared in terms of the functional requirements. This comparison is done at very general level and its intent is to find the configuration with most potential. As the design process goes further more detailed comparisons can be made and the issue revisited. The results can also vary if different requirements are given different weights. The work space to footprint ratio is not very important if footprint is kept under certain limits (desktop size). More thorough comparison can utilize, for example, analytical hierarchy process (AHP) [Slocum, 1992], in which inputs from all the people involved in the project can be utilized.

TABLE 8.3 Concept selection

Functional Requirement	Weight	Gantry	Hexapod	Double yoke	Circular
Accuracy	3	0	-	++	+
Work space/ Footprint	1	+	++	-	0
Simplicity	2	-	--	+	0
Total		-1	-5	7	2

The double yoke and the circular concept seem most promising, according to preliminary studies, and are therefore studied further.

8.3.3 Concept Feasibility

This concept is fundamentally different from other types of axis arrangements in two ways. The tool point is very close to the center line of the rotational axis at all times and the rotary and linear motions are combined into one structural element. This arrangement has several desirable properties, which are explained later.

Kinematics

Singularities. A singularity is defined as the situation when a machine tool passes through a configuration where infinite power of an actuator is needed to satisfy the tool orientation and position. 5-axis machine can not avoid such situations, but the location of the singularities can be designed into less obstructive place. In the concept shown above, the singularity is located at $b=p/2$ (equator), which is rarely visited during the machining operation. Depending on the design the singularity might not be accessible because of the limited range of motion.

Coupling of rotational and translational axis. If the tool tip is not placed on the center line of the rotational axis, the coupling effect exists. When the tool is oriented with angular velocity, the translational axis has to compensate with corresponding velocity.

With this design, the maximum offset between the center line of the rotational axis (a) and the tool point is small (max. half of the z travel = 15mm). The tool tip is always located at the center line of b -axis, if the z -axis moves the whole structure (not just the spindle).

Geometric Error Gains

The geometry is very beneficial when geometric error gains are considered. Again, the close location of the tool tip to the center lines of rotational axis almost eliminates ABBE-errors. Table 1 shows the error gains for different components. The locations of co-ordinate system are at the center of stiffness of different components. Since some of the structural loops are closed, the values of angular errors are worst case estimates, which are obtained by dividing the linear error of the bearing by the distance from the center of stiffness of that component to the tool tip. The error gains are shown in Table 8.4. The subscript s refers to spindle, subscript c to the component in question (or bearings that support that component) and a , d and h are shown in Figure 8.8 and are the dimensions between x -axis, y -axis and z -axis bearing center of stiffness and tool tip, respectively.

TABLE 8.4 Geometric error gains

Component	δ_x	δ_y	δ_z	ϵ_x	ϵ_y
Spindle	$\delta_{xs} + \epsilon_{ys}g$	$\delta_{ys} + \epsilon_{xs}g$	δ_{zs}	ϵ_{xs}	ϵ_{ys}
$x - \beta$ Axis	control	δ_{yc}	δ_{zc}	control	$\frac{2\delta_{zc}}{d}$
$y - \alpha$ Axis	δ_{xc}	control	δ_{zc}	$\frac{2\delta_{zc}}{h}$	control
z Axis	$\epsilon_{yc}a$	$\epsilon_{xc}a$	control	ϵ_{xc}	ϵ_{yc}

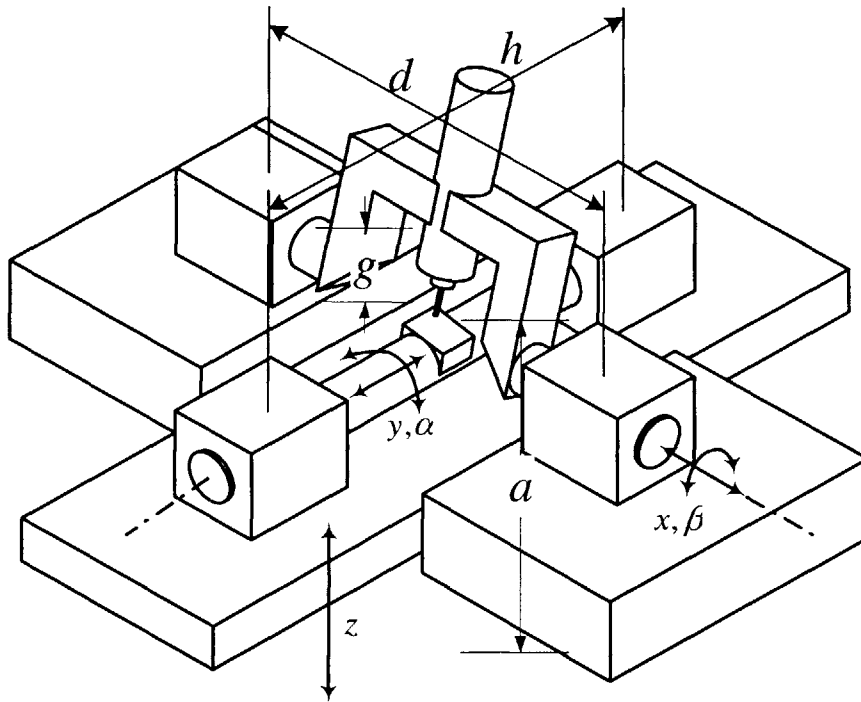


Figure 8.8 Double yoke design

The component error values are substituted into the table and the corresponding tool tip errors can be calculated with the formulas in the cells. The only ABBE-errors that exist are introduced by spindle and z -axis. If all the component errors are expected to be in sub-micron range, that will result in micron range total errors even if the errors are simply added up. Adding up the errors is very conservative method to approximate errors, since it

occurs very rarely, if at all, that all the errors would add rather than partly cancel each other. It can be concluded that the geometric error gains of this arrangement are almost negligible.

Static Stiffness

The static stiffness of the system is a strong function of the diameter of the yokes ($K \propto D^4$) and can therefore be easily increased, and the bearing stiffness, which is the function of supply pressure. Both can be orders of magnitude higher than the actual cutting tool stiffness. The presented results are calculated with following general properties:

- $K_b=350 \text{ N}/\mu\text{m}$ (bearing stiffness @ 1000 psi)
- $D=1.25''$
- Work space $30 \times 30 \times 30 \text{ mm}$
- Total mass 5 kg

The static stiffness properties of the yokes are presented in

TABLE 8.5 Static stiffness of the double yoke concept

Property	Upper yoke	Lower yoke
x stiffness K_x	$160 \text{ N}/\mu\text{m}$	$750 \text{ N}/\mu\text{m}$
y stiffness K_y	$150 \text{ N}/\mu\text{m}$	$130 \text{ N}/\mu\text{m}$
z stiffness K_z	$65 \text{ N}/\mu\text{m}$	$100 \text{ N}/\mu\text{m}$
displacement, $F=50 \text{ N}$ in direction $\{1,1,1\}$	$0.5 \mu\text{m}$	$0.35 \mu\text{m}$

Static stiffness of the structure will not present a problem due to the low cutting forces expected in a small machine. This system is a direct drive system and therefore some of the compliance comes from the control loop. This question is discussed more detailed in next section. Calculated values are based on the assumption that the drive is infinitely rigid and therefore any static compliance of the control loop must be added.

These stiffness coefficients do not take into account the compliance of the cutting tool itself. The compliance of the cutting tool often dominates the total static deflection and therefore the structures static stiffness characteristics are not very critical in small machine tools.

Dynamic Characteristics

The dynamic characteristics become increasingly important as machining speed increase. One of the advantages of a smaller machine is its superior dynamics compared to larger and more compliant machines. Also the moving masses are much smaller, allowing for higher accelerations. The natural frequencies of the yokes will mostly determine the dynamic behavior of the machine. summarizes the first undamped natural frequencies.

TABLE 8.6 First natural frequencies of the yokes

Mode	Upper Yoke	Lower Yoke
1	570 Hz	720 Hz
2	655 Hz	810 Hz
3	710 Hz	2310 Hz
4	770 Hz	3350 Hz

The finite element representation of the lower yoke is shown in Figure 8.9.

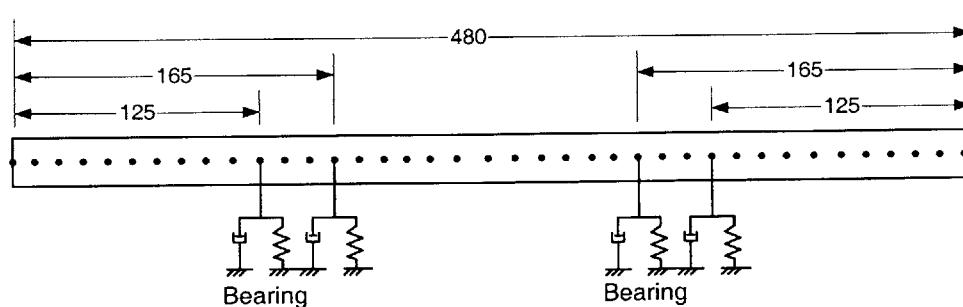


Figure 8.9 Finite element representation of the lower yoke

This length includes the necessary lengths for the actuators outside the bearings. The same state space model is used as in a case of the TurboTool to obtain a transfer function for the lower yoke. This is done in order to estimate the effect of damping on the frequency response of the structure. The transfer function (for 1 N force) is for the center node of the yoke and is shown in Figure 8.10 for the fluid film bearing case and for low damping case. The bearing damping is calculated with oil viscosity of $\mu = 0.06$ Pa s (approximately 60 cSt) and is $3.7 \cdot 10^5$ Ns/m per bearing half.

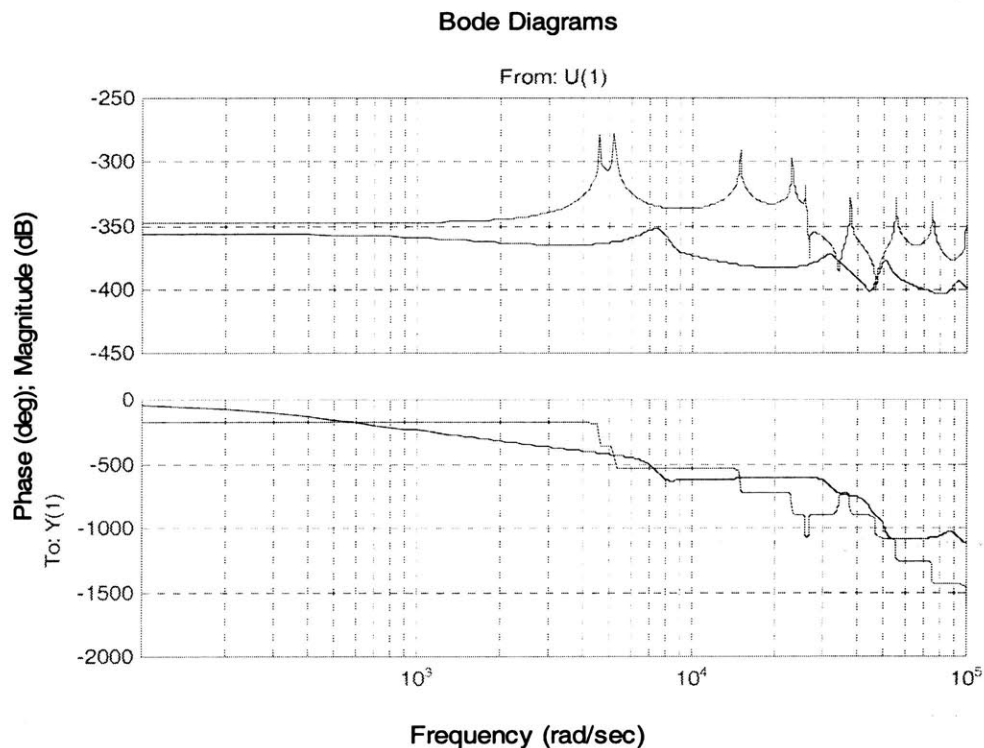


Figure 8.10 Transfer functions for the lower yoke

Again the benefits of high damping are very evident. By looking at the roots of characteristic equation, the two first undamped modes become over damped and vanish. The first damped mode is the third undamped one. The frequency of the first resonant peak moves from 4500 rad/s (720 Hz) to approximately 7500 rad/s (1190 Hz).

Another dynamic characteristic of importance is the damping in the linear and rotary (actuated) directions of the moving axis. These can be approximated to first order by

$$b_l = \frac{F}{U} = \frac{\mu\pi DL}{h} \quad (8.10)$$

for the linear case and for the rotary case

$$b_r = \frac{T}{\dot{\alpha}} = \frac{\mu\pi D^3 L}{4h} \quad (8.11)$$

These relations yield results that are very close to actual for the bearing discussed in laminar design section. Since the surface speed are not likely to reach similar values as in the case of rotary bearings the laminar design with damping lands is recommended for these types of applications.

Another desirable characteristic of hydrostatic bearing in these types of applications is zero static friction, which results in a very possible motion resolution. This is possible because no stick-slip effects occur.

One issue that is not discussed here in detail, but is left as future work, is the motion control of these very light weight direct drive structures. With low mass there is less inertia to eliminate higher frequency disturbances and with direct drive there is no mechanical stops either. This might pose control problems if very high accuracy is desired.

8.4 Sealing

One of the major practical issues of using hydrostatic bearings is the sealing of the bearing and therefore a quick look at the possible sealing methods is provided here. Standard contacting seals such as lip seals can be used, but if the non stick slip conditions are desired a non-contact seal is required. Examples of non-contacting seals are slingers, labyrinth-, screw-, pump seals and air barriers [Heinz, 1998, Warring, 1981]. Slingers are formed by circular rings that centrifugally spray off the liquid on the shaft surface as shown in

Figure 8.11. The rotor diameter is made smaller than actual to better illustrate the seal geometry. This seal can also incorporate a pump seal, which contains the grooves in stator face, which pump the fluid back towards collecting chamber when rotor rotates. Seal exit gap should be larger than 0.5 mm to prevent surface tension driven flow out through the seal (fluid bridging) [Heinz, 1998]. .

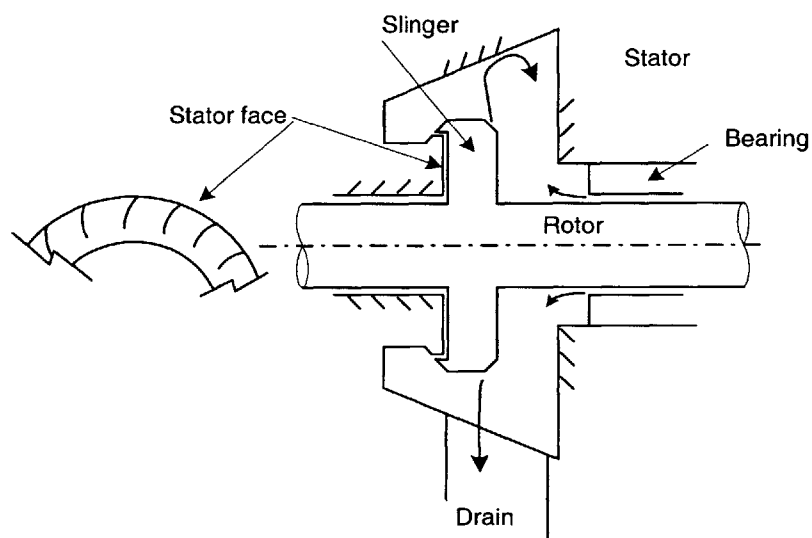


Figure 8.11 Slinger seal

Labyrinth seals are based on passage with higher hydraulic resistance as shown schematically in Figure 8.12. The rotor diameter is made smaller than actual to better illustrate the seal geometry.

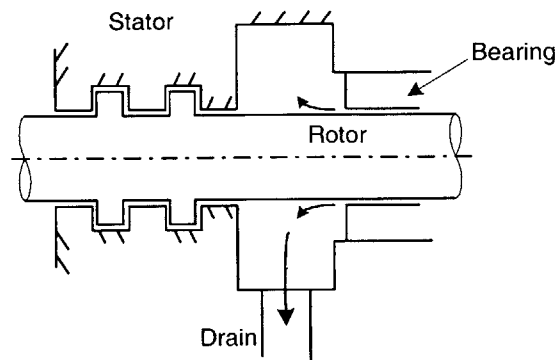


Figure 8.12 Labyrinth seal

Screw and pump seals have grooves on the shaft surface that pump back the fluid as the bearing is rotated, similarly to the pumping back effect discussed in the design chapter. These types of seals are not recommended since they can more easily than slingers or labyrinth seals effect the dynamics of the bearing system. It must be noted that when designing any kind of sealing system attention should be paid to the dynamics of the seal and if possible try to design the seals in such way that they do not have significant effect on the system dynamics.

Air barriers use pressurized air to make sure flow in the sealing area is into desired direction thus preventing flow into opposing direction. These types of seals can be used in combination with contacting lip seals to make them non-contacting. The air pressure can be used to lift off the lip from contacting the surface. A desirable characteristic of this arrangement is that even if the air pressure fails or is turned off the seal will still prevent leakage. This approach was successfully used in [Sihler, 1998]. In this approach it is important that the sealing material and structure is stiff enough that lift off can be ensured along the entire circumference of the seal. The deflection of the lip can be estimated by the following formula [Avallone, 1999]

$$\delta = 0.0025 \frac{pa^4}{Et^3} \quad (8.12)$$

which is for the case shown in Figure 8.13 with R/r of 1.25. This formula is not entirely correct because it assumes Poisson's ratio of 0.3. For rubber like material the actual Poisson's ratio is between 0.4-0.5 The complete formula for the tip is [Roark, 1938]

$$\delta = \frac{3p(m^2 - 1)}{16m^2Et^3} \left[a^4 + 5b^4 - 6a^2b^2 + 8b^4 \log\left(\frac{a}{b}\right) \right. \tag{8.13}$$

$$\left. + \frac{(8b^6(m + 1) - 4a^2b^4(m + 3) + 4a^4b^2(m + 1)) \log\left(\frac{a}{b}\right) - 16a^2b^4(m + 1) \left(\log\left(\frac{a}{b}\right)\right)^2 - 4a^2b^4 + 2a^4b^2(m + 1) - 2b^6(m - 1)}{a^2(m - 1) + b^2(m + 1)} \right]$$

where $m = \frac{1}{\nu}$ (1/Poisson's ratio). E is the Young's modulus which typically for elastomers is 1-20 MPa. This is fairly low value and standard shop air provides more than enough pressure to lift the seal up. Therefore a hard stop should be designed that determines the maximum deformation for the lip seal (as shown in following figures).

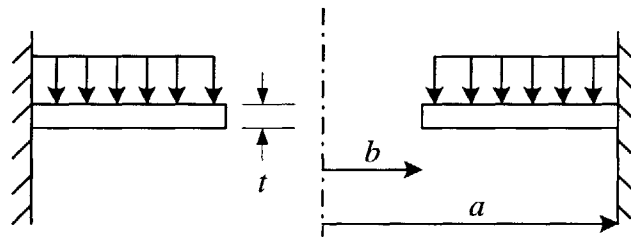


Figure 8.13 Clamped circular flat plate

A one possible seal design combining slinger, lip and air barrier seals is shown in Figure 8.14. The simpler implementation of air barrier lip seal is shown in Figure 8.15 .

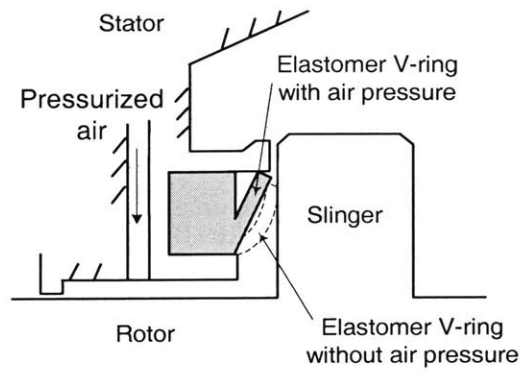


Figure 8.14 Combination of slinger, lip and air barrier seal

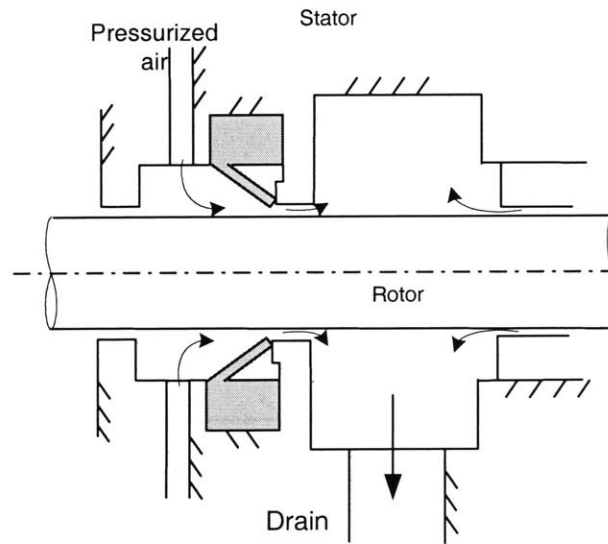


Figure 8.15 Combined air barrier lip seal

Chapter 9

CONCLUSIONS AND FUTURE WORK

In this work surface self-compensating hydrostatic bearing technology was successfully implemented into a bushing. This means very low cost, robust and simple hydrostatic bearings which do not require expensive tuning procedures to be implemented into machines. Finite difference methods were explored to solve the pressure field in a bearing and solutions were obtained and also some limitations to these methods as applied to this type of bearing were discovered. Different hydrostatic bearing designs were compared and it was concluded that they have very similar performance characteristics and therefore the simplest design to implement was chosen as the design manufactured and considered in this work. Next, a simple first order equations were developed that can be used to estimate the performance of the bearing without going into detailed modeling. These types of relations are very useful in iterative design process where time consuming numerical solutions are not usable. These relations also included two non-dimensional parameters, power ratio and pumping ratio, that can be used to predict the significance of hydrodynamic effects on bearing performance. The design problem was stated as a general optimization problem. Finally the first order solutions were compared to numerical solutions and very good agreement was found.

Different manufacturing methods were considered next. In general, the more expensive the method better the tolerances that can be achieved. In order to compare different methods more quantitatively a single metric is derived. This was done by computing the proba-

bility density function for the bearing characteristic as function of the probability density function(s) of the manufacturing error. This was done by using Monte-Carlo method. Then a cost function was assigned to variations from the nominal bearing characteristic value. By calculating the mathematical expectation using the derived probability density function and the cost function a single metric, called estimated total cost is obtained. By using this metric it was shown that the most economical way of producing the bushings is casting (even when taking into account the loss in quality).

Two different prototype sizes, 6' and 1.25" ID, were manufactured. The larger prototype was manufactured by sand casting. In order to make the necessary surface geometry on the internal surface, novel manufacturing steps were introduced. The smaller prototype was manufactured by investment casting. The patterns were produced by 3D-Printing. Both of these methods are very cost effective, especially the 3D-Printing and investment casting procedure.

The prototypes were tested and good agreement with the theory was achieved. The error motion of the smaller prototype was measured. The maximum error motion was smaller than $0.2 \mu m$ and the average error motion less than $0.05 \mu m$. Both of these values were close to the noise and measuring ball tolerance levels. The error motion characteristics are excellent considering the economic manufacturing of the bearing.

As future work, the main question is how to implement these bearings in such way that the excellent characteristics are best utilized. Also the effect of surface roughness in the grooves is of interest. It was concluded that globally they have very little effect in frictional characteristics of the bearing. However, the local effect is of interest, namely the effect of higher friction factors on the hydraulic resistance. This could be done computational with finite element or finite difference codes that allow to modify the friction factors according to surface finish. As first order analysis only the groove could be modeled. Also high speed experimental testing to verify bearing performance at high speeds together with non-linear rotor dynamics. The high speed experimental work should search for

instabilities and the results should indicate what happens instability occurs. High speed testing could also be used to verify the pressure rise along the surface grooves and the search for the limits of power and pumping ratios could be performed. This would help to determine how accurately the finite difference code can predict this phenomena and what is the effect of modeling the grooves with only half of the actual depth. As mentioned before, the final proof of the performance of the bearing is its use in real world applications.

REFERENCES

- [ASME, 1985] ANSI/ASME B89.3.4M 1985, *Axes of Rotation, Methods for specifying and Testing*. ASME New York 1985
- [Avallone, 1999] Avallone, E. *Mark's Standard Handbook for Mechanical Engineers (CD-ROM)*, McGraw-Hill, New York 1999
- [Bassani, 1992] Bassani, R., *Hydrostatic Lubrication*, Elsevier Press, Amsterdam, 1992.
- [Bendat, 1971] HBendat, J., Piersol A., *Random Data: Analysis and Measurement Procedures*, John Wiley & Sons, Inc., New York, 1971.
- [Booker, 1965] Booker, J. F., *A Table of the Journal Bearing Integrals*. Trans. ASME Journal of Basic Engineering, vol 87, #3, pp. 533-535, 1965.
- [Brzeski, 1979] Brzeski, L., Kazimierski Z., *High Stiffness Bearing*, ASME Trans., J. of Lubrication Technology, 101 (1979) p. 520-525.
- [Constantinescu, 1968] Constantinescu, V., *Lubrication in Turbulent Regime*, U.S. Atomic Energy Commission/Division of Technical Information, Available as AEC-tr-6959 from Clearinhouse for Federal, Scientific and Technical Information, National Bureau of Standards, U.S. Department of Commerce, Virginia 1968.
- [Den Hartog, 1985] Den Hartog, J., *Mechanical Vibrations*, Dover Publications Inc. New York, 1985. Reprint Originally published as: 4th Ed. McGraw-Hill, New York 1956.
- [DeVor, 1992] DeVor, R. Chang, T. Sutherland, J., *Statistical Quality Design and Control*, Prentice Hall, New Jersey 1992.
- [Dowson, 1967] Dowson, D., Taylor, C., *Elastohydrostatics of Circular Plate Thrust Bearing*, ASME Trans., J. of Lubrication Technology, 89 (1967) p. 237-262.
- [Elrod, 1967] Elrod, H., Ng, C., *A Theory for Turbulent Fluid Films and Its Application to Bearings*, Trans. ASME, Journal of Lubrication Technology, Vol. 89, Series F, No. 3, July 1967, p. 346-362
- [El Telbany, 1982] El Telbany, M., Reynolds, A., *The Structure of Turbulent Plane Couette Flow*, Journal of Fluids Engineering, Volume 104, 1982, pp. 367-372
- [Fay, 1994] Fay, J., *Introduction to Fluid Mechanics*, MIT Press, Cambridge MA, 1994.

- [Geary, 1962] Geary, P., *Fluid Film Bearings, A Survey of Their Design, Construction, and Use*, B.S.I.R.A, Kent 1962.
- [Frene, 1990] Frene, J. et Al., *Hydrodynamic Lubrication Bearings and Thrust Bearings*, Elsevier Press, Amsterdam 1997.
- [Heinz, 1998] Heinz, M. *Fluid Sealing Technology*. Marcel and Dekker Inc. New York 1998.
- [Hirs, 1973] Hirs, G. *A Bulk Flow Theory for Turbulent Lubrication Films*, ASME Journal of Lubrication Technology, April 1973, p. 137-146
- [Kane, 1999] Kane, N., *Surface Self-Compensated Hydrostatic Bearings*. MIT Ph.D. Thesis in Mechanical Engineering, Massachusetts Institute of Technology, Cambridge, 1999.
- [Kivioja, 1996] Kivioja, S., *Voitelun Perusteet*. Helsinki University of Technology, Faculty of Mechanical Engineering, Laboratory of Machine Design, Otaniemi 1996
- [Kreuzig, 1993] Kreuzig, E. *Advanced Engineering Mathematics 7th Ed.*, John Wiley & Sons, Singapore, 1993.
- [Kurtin, 1993] Kurtin, A., Childs, D., San Adres, L., Hale, K. *Experimental Versus Theoretical Characteristics of a High-Speed Hybrid (Combination Hydrostatic and Hydrodynamic) Bearing*, Journal of Tribology, January 1993 Vol. 155 p. 160-167.
- [Lund, 1978] Lund, J., Thomsen, K. *A Calculation Method and Data for the Dynamic Coefficients of Oil-Lubricated Journal Bearings in Topics in Fluid Film Bearings and Rotor Bearing System Design and Optimization*, ASME New York 1978.
- [Malvern, 1969] Malvern, L. *Introduction to the Mechanics of Continuous Medium*, Prentice-Hall Inc. New Jersey 1969.
- [Miyasaki, 1974] Miyasaki, Y. *Static Fluid Pressure Bearings*, U.S. Patent #3,785,708, January 15, 1974.
- [Oberg, 1996] Oberg, E. *Machinery's Handbook*, Industrial Press Inc. New York 1996
- [Omega, 1992] *The pressure, strain and force handbook, Vol 28.*, Omega Engineering Inc, 1992.
- [O'Sullivan, 1998] O'Sullivan, D. *Aircraft Interior Structural-Acoustic Control Design*, M.I.T M.Sc Thesis in Aeronautics and Astronautics. Massachusetts Institute of Technology, Cambridge, 1998
- [Pennala, 1993] Pennala, E. *Lujuusopin Perusteet*, Otatiecto, Hämeenlinna, 1993.

-
- [Pinkus, 1961] Pinkus, O., Sternlicht, B. *Theory of Hydrodynamic Lubrication*, McGraw-Hill, New York, 1961.
- [Roark, 1938] Roark, R. *Formulas for Stress and Strain*. McGraw-Hill, New York 1938
- [Shah, 1978] Shah, R., *A Correlation for Laminar Hydrodynamic Entry Length Solutions for Circular and Noncircular Ducts*, Journal of Fluids Engineering, 1978, Vol 100 p. 177-179.
- [Sihler, 1998] Sihler, J., *Design, Manufacturing and Test of a Self-Compensating Hydrostatic Rotary Bearing for Rotary Machine Axes*. MIT M.Sc Thesis in Mechanical Engineering, Cambridge, 1998.
- [Slocum, 1992] Slocum, A. *Precision Machine Design*, Elsevier Press, New Jersey, 1992
- [Slocum 2, 1992] Slocum, A. *Self Compensating Hydrostatic Linear Bearing*, U.S. Patent #5,104,237, April 14, 1992.
- [Slocum, 1994] Slocum, A. *Self-Compensating Hydrostatic Bearings for Supporting Shafts and Spindles and the Like for Rotary and Translational Motion and Methods Therefor*, U.S. Patent #5,281,032, January 25, 1994.
- [Slocum, 1997] Slocum, A. *Tooling System and Method with Integral Hydrostatic Bearings and Turbine Power Source*, U.S. Patent #5,674,032, October 7, 1997
- [Stansfield, 1970] Stansfield, F., *Hydrostatic Bearings for Machine Tool and Similar Applications*, The Machinery Publishing Co. London, England 1970.
- [Taguchi, 1989] Taguchi, G., Elsayed, A., Hsiang, T., *Quality Engineering in Production Systems*, McGraw-Hill, New York, 1989.
- [Tlusty, 1992] Tlusty, J. *System and Methods of Testing Machine Tools*, in *Tutorial on Axis of Rotation* by Bryan, J. Annual Meeting of ASPE, 1992
- [Tully, 1977] Tully, N., *Static and Dynamic Performance of an Infinite Stiffness Hydrostatic Bearing*, ASME Trans., J. of Lubrication Technology, 99 (1977) p. 106-112.
- [Ugural, 1987] Ugural A., *Advanced Strength and Applied Elasticity*, Elsevier Science Publishing Co. New York 1987.
- [Warring, 1981] Warring, R. *Seals and Sealing Handbook 1 Ed.*, Gulf Publishing Company, Houston 1981
- [Wasson, 1997] Wasson, K. *Integrated Shaft Self-Compensating Hydrostatic Bearing*. U.S. Patent #5,700,092, December 23, 1997.

- [Wasson, 1996] Wasson, K., *Hydrostatic Machine Tool Spindles*, MIT Ph.D. Thesis in Mechanical Engineering, Cambridge, 1996.
- [Wasson, 1994] Wasson, K., *Hydrostatic Radial Bearings for High Speed Precision Machine Tool Applications*, MIT M.Sc. Thesis in Mechanical Engineering, Cambridge, 1994.
- [Zirkelback, 1998] Zirkelback, N. San Andres, L., *Finite Element Analysis of Herringbone Groove Journal Bearings: A Parametric Study*, Journal of Tribology, Trans. of ASME, Vol. 120 (1998) p.235-240.

Appendix A

AUTOMATIC GEOMETRY GENERATION

This MATLAB script generates the geometry for the SC10 Bearing

```
clear all;
%Automatic Bearing Geometry Creation for RBTS

%*****
%*****
%INPUT
%*****
%*****
%System of Units
units=1; %0=english, 1=SI (actually mm in linear dimensions)

%General Dimensions
D=2.35*25.4; %Diameter
L=2.2*25.4; %Total lenght (from end to the symmetry plane)
CL=0.015; %bearing clearance 0.0012*25.4
np=6; %number of pockets
GW=0.08*25.4; %Groove widht
GD=-CL*13; %Groove depth (give negative value (a bug :))

%drainage grooves
drains=1; %drains (0=false, 1=true)
dgl=0.96*25.4; %drainage groove lenght 0.96*25.4
```

```

divgw=30; %determines how close the points are to the grooves (GW/
divgw)

%Circumferential dimensions
cpc1=0.74*25.4; %1st dimension (pocket width)
cpc2=0.985*25.4; %2nd dimension (0 to first drainage groove)
cpc3=3.089*25.4; %3rd dimension (0 to beginning of restrictor groove)
rgl=0.51*25.4; %restrictor groove length

%Axial dimensions
cpa1=0.15*25.4; %1st dimension (exit land width)
cpa2=1.955*25.4; %2nd dimension (end to the restrictor groove (first
edge from end)
cpa3=2.1*25.4; %3rd dimension (from end to the supply)
dl=1.271*25.4; %0 to end of first pocket groove (defines the snake
line)

%pockets
deepock=1; %if land is removed deepock=1 if not deepock=0;

%*****
%*****
%CONVERT DIMENSIONS INTO DEGREES
%*****
%*****
GWD=GW*360/(pi*D);
cpc1=cpc1*360/(pi*D);
cpc2=cpc2*360/(pi*D);
cpc3=cpc3*360/(pi*D);
rgl=rgl*360/(pi*D);

%*****
%*****
%GENERATE GRID LOCATION VECTORS
%*****
%*****
CRG=[];
AXG=[];
cld=GW*360/(divgw*pi*D); %the dimension of how close the "close"

```

```

points are to the groove edges (degrees)
cl=GW/divgw;           %same in axial units

%Circumferential locations (in
degrees)*****
****

if drains==1          %locations if drains exists
    %locations of the given points
    CRG=[0 cld GWD-cld GWD GWD+cld cpc1-cld cpc1 cpc1+cld cpc1+GWD-cld
cpc1+GWD cpc1+GWD+cld ...
        cpc2-cld cpc2 cpc2+cld cpc2+GWD-cld cpc2+GWD cpc2+GWD+cld 360/
np-cld];

    %add 2 points into the grooves
    gs=(GWD-2*cld)/3; %step lenght (dimension between grid points)
    CRG=[CRG cld+gs cld+2*gs cpc1+cld+gs cpc1+cld+2*gs cpc2+cld+gs
cpc2+cld+2*gs];

    %add 14 points into the pocket
    pos=(cpc1-GWD-2*cld)/15; %step lenght inside pocket
    i=1;
    for i=1:14
        CRG=[CRG GWD+cld+i*pos];
    end

    %add 10 points between the pocket and drainage grooves
    ros=(cpc2-cld-(cpc1+GWD+cld))/11; %step lenght between pockets
    i=1;
    for i=1:10
        CRG=[CRG cpc1+GWD+cld+i*ros cpc2+GWD+cld+i*ros];
    end

else                  %locations if drains do not exists

    %locations of the given points
    CRG=[0 cld GWD-cld GWD GWD+cld cpc1-cld cpc1 cpc1+cld cpc1+GWD-cld
cpc1+GWD cpc1+GWD-cld 360/np-cld];

```

```

%add 2 points into the grooves
gs=(GWD-2*cld)/3; %step length (dimension between grid points)
CRG=[CRG cld+gs cld+2*gs cpc1+cld+gs cpc1+cld+2*gs];

%add 14 points into the pocket
pos=(cpc1-GWD-2*cld)/15; %step length inside pocket
i=1;
for i=1:14
    CRG=[CRG GWD+cld+i*pos];
end

%add 20 points between the pockets
ros=(360/np-(cpc1+GWD+cld)-cld)/21; %step length between pockets
i=1;
for i=1:20
    CRG=[CRG cpc1+GWD+cld+i*ros];
end

end %end making first set of circumferential points

%Arrange points in ascending order
CRG=sort(CRG);

%make the rest of the points

CRG=[CRG CRG+360/np CRG+2*360/np CRG+3*360/np CRG+4*360/np CRG+5*360/
np];

%Axial loca-
tions*****
*****

%Given locations
AXG=[0 c1 cpa1-c1 cpa1 cpa1+c1 cpa1+GW-c1 cpa1+GW cpa1+GW+c1 ...
    cpa2-c1 cpa2-2*c1 cpa2 cpa2+c1 cpa2+GW-c1 cpa2+GW cpa2+GW+c1 ...
    cpa3-c1 cpa3 cpa3+c1 (L-cpa3-c1)/2+cpa3+c1 L-c1 L];

%add 2 points into the grooves

```

```

gsa=(GW-2*c1)/3; %step length
AXG=[AXG cpa1+c1+gsa cpa1+c1+2*gsa cpa2+c1+gsa cpa2+c1+2*gsa];

%add 7 points into drainage land and compensator land
dls=(cpa1-2*c1)/8; %drainage land step size
cls=(cpa3-c1-(cpa2+GW+c1))/8; %compensator land step size
i=1;
for i=1:7
    AXG=[AXG c1+i*dls cpa2+GW+c1+i*cls];
end

%add 60 points to the rest of the bearing

step=(cpa2-cpa1-2*c1-GW)/61;
i=1;
for i=1:60
    AXG=[AXG cpa1+GW+c1+i*step];
end

%Arrange points into ascending order
AXG=sort(AXG);

%end making point locations

%Start making the deformation
matrix*****
*****

GDM=[];

%make the snake grooves
%calculate the dimensions that locate the groove

k=(d1-cpa2)/(GWD-cpc3); %slope of the snake z=k*theta+b
b=d1-k*GWD;

k2=(d1-cpa2)/(GWD-cpc3); %second snake line (defines the end of the

```

```

groove in axial direction)
b2=(d1+GW)-k2*GWD;

for circumindex=1:size(CRG,2)/6
    z1=k*CRG(circumindex)+b; %calculate the starting locations of the
grooves
    z2=k*(CRG(circumindex)+360/np)+b;
    z3=k*(CRG(circumindex)+2*360/np)+b;

    z1e=k2*CRG(circumindex)+b2; %calculate the ending location of the
groove (axially)
    z2e=k2*(CRG(circumindex)+360/np)+b2;
    z3e=k2*(CRG(circumindex)+2*360/np)+b2;

    diff2=AXG-z1;
    diff3=AXG-z2;
    diff4=AXG-z3;

    diff2e=AXG-z1e;
    diff3e=AXG-z2e;
    diff4e=AXG-z3e;

    [value2,index2]=min(abs(diff2)); %get the index of the closest axial
point to the starting point
    [value3,index3]=min(abs(diff3));
    [value4,index4]=min(abs(diff4));

    [value2e,index2e]=min(abs(diff2e)); %get the index of the closest
axial point to the ending point
    [value3e,index3e]=min(abs(diff3e));
    [value4e,index4e]=min(abs(diff4e));

    for axialindex=1:size(AXG,2)-14 %make the 3d matrix of deformations
for the snakegrooves
        if axialindex>=index2&axialindex<=index2e
            GDM(circumindex,axialindex)=GD;
        elseif axialindex>=index3&axialindex<=index3e
            GDM(circumindex,axialindex)=GD;

```

```
elseif value4<=cpa2

    if axialindex>=index4&axialindex<=index4e
        GDM(circumindex,axialindex)=GD;
    else
        end
    else
        GDM(circumindex,axialindex)=0;
    end
end
end
end

%make the first pocket groove

if deeppeock==1 %make deep pockets if desired
    varcirc=22;
else
    varcirc=6;
end

for circumindex=1:varcirc
    z6=k*CRG(circumindex)+b;
    diff6=AXG-z6;
    [value6,index6]=min(abs(diff6));
    for axialindex=11:index6
        GDM(circumindex,axialindex)=GD;
    end
end

%make the second pocket groove

for circumindex=23:28
    z7=k*CRG(circumindex)+b;
    diff7=AXG-z7;
    [value7,index7]=min(abs(diff7));

    for axialindex=11:index7
```

```
        GDM(circumindex,axialindex)=GD;
    end
end

%make the drainage groove

if drains==1
    diff5=AXG-dgl;
    [value5,index5]=min(abs(diff5));

    for circumindex=41:46
        for axialindex=1:index5
            GDM(circumindex,axialindex)=GD;
        end
    end
else
end

%make the circumferential pocket groove

for circumindex=7:22
    for axialindex=11:16
        GDM(circumindex,axialindex)=GD;
    end
end

%make the restrictor collecting groove

diff8=CRG-cpc3;
diff9=CRG-(cpc3+rgl);

[value8,index8]=min(abs(diff8));
[value9,index9]=min(abs(diff9));

if cpc3>=120    %if collector if more than 2 pockets away
    cpc3reg=cpc3-2*360/np;
```

```
diff8=CRG-cpc3reg;
diff9=CRG-(cpc3reg+rg1);
[value8,index8]=min(abs(diff8));
[value9,index9]=min(abs(diff9));

for circumindex=index8:index9
    for axialindex=80:85
        GDM(circumindex,axialindex)=GD;
    end
end
else %collector one pocket away
    cpc3reg=cpc3-360/np;

    diff8=CRG-cpc3reg;
    diff9=CRG-(cpc3reg+rg1);
    [value8,index8]=min(abs(diff8));
    [value9,index9]=min(abs(diff9));

    for circumindex=index8:index9
        for axialindex=80:85
            GDM(circumindex,axialindex)=GD;
        end
    end
end

%Make the restrictor lands
for circumindex=1:size(CRG,2)/6
    for axialindex=86:94
        GDM(circumindex,axialindex)=0;
    end
    for axialindex=95:99 %make center groove
        GDM(circumindex,axialindex)=GD;
    end
end

%GDM2=[GDM;GDM;GDM;GDM;GDM;GDM];
%CRG2=CRG(15:15+size(GDM,1)-1);
%CRG2=[CRG2 CRG2+360/np CRG2+2*360/np CRG2+3*360/np CRG2+4*360/np
CRG2+5*360/np];
```

```

%GDM=GDM2(15:15+size(GDM,1)-1,:);
%end making GDM
*****
*****

CRGx=CRG(1:58);
surf(AXG,CRGx,GDM)

```

This script writes the geometry generated by the previous script into a .inp file, which can be used by the finite difference code

```

%THIS PROGRAM GENERATES THE JOURNB.INP FILE THAT IS NEEDED BY THE RBTS
PROGRAM
%RUN FIRST THE GEOMETRY_GEN.M PROGRAM BEFORE USING THIS
%*****
*****
%INPUT*****
*****
L=2.2*25.4; %total length of the bearing (NOT from end to the symmetry
plane)

necc=1; %number of eccentricities considered in this run
niter=1; %number of iterations to solve for load angle convergence (if
niter=1 displacement will along -y axis
        % and the Fx and Fy are calculated) if >1 the displacement angle
will be calculated
npiter=15; %# of iterations to solve for recess pressure (only with ori-
fice restrictors)
nreces=0; %# of recesses in the bearing
npump=0; %# of pumps in the bearing

nfastp=0; %axial grid point # of the FIRST axial location of circumfer-
ential step or beginning of pocket
nsastp=0; %axial grid point # of the SECOND axial location of circum-
ferential step or beginning of pocket
ncstp=0; %circumferential grid point # of circumferential step or
pocket

```

```
vargrd='T';
taperb='F';
symtr='F';
dambrg='F';
condns='F';
struct='T';
nondim='F';
```

```
padang=360;
flmang=0;
ortang=0;
```

```
prelod=0;
stepht=0;
angecc=270;
anglod=270;
SPEED=10000; %RPM !!!!
```

```
cavp=0;
grovep=0;
sidelp=0;
side2p=3447500;
```

```
amisx=0;
amisy=0;
rens=0.0011; %lubricant viscosity (lbf*sec/in^2 or PA*sec)
densty=995; %lubricant density (lb/in^3 or kg/m^3)
```

```
dx=0.5; %if 0 automatically set by the program
dy=-0.5;
dxdot=0;
dydot=0;
trunc=0;
```

```
%eccentricities (type in wanted ecc) See that the variable necc corresponds
to #ecc typed in the vector ECC
ECC=[0];
```

```
Psupply=3500000; %psi or Pa
```

```
%generate
```

```
file*****  
*****
```

```
fid=fopen('C:\temp\oldcomputer\bearing\jurnbr.inp','wt');
```

```
fprintf(fid,'%d',units); %system of units (0=english, 1=si)  
fprintf(fid,'\t');  
fprintf(fid,'V5.0G1 \n'); %version
```

```
fprintf(fid,'Heading \n');  
fprintf(fid,'Heading \n');  
fprintf(fid,'Heading \n');
```

```
fprintf(fid,'%d\t',size(AXG,2)); %start line 5  
fprintf(fid,'%d\t',size(CRG,2)+1);  
fprintf(fid,'%d\t',1);  
fprintf(fid,'%d\t',necc);  
fprintf(fid,'%d\t',0); %if sidepressure is not used this should read  
4*size(CRG,2)  
fprintf(fid,'%d\t',niter);  
fprintf(fid,'%d\t',npiter);  
fprintf(fid,'%d\t',nrecs);  
fprintf(fid,'%d',npump);  
fprintf(fid,'\n');
```

```
fprintf(fid,'%d\t',nfastp); %start line 6  
fprintf(fid,'%d\t',nsastp);  
fprintf(fid,'%d',ncstp);  
fprintf(fid,'\n');
```

```
fprintf(fid,'%s\t',vargrd); %start line 7  
fprintf(fid,'%s\t',taperb);  
fprintf(fid,'%s\t',symtr);  
fprintf(fid,'%s\t',dambrg);  
fprintf(fid,'%s\t',condns);  
fprintf(fid,'%s\t',struct);
```



```
fprintf(fid, '%s', nondim);
fprintf(fid, '\n');

fprintf(fid, '%d\t', D); %start line 8
fprintf(fid, '%d\t', L);
fprintf(fid, '%d\t', pandang);
fprintf(fid, '%d\t', flmang);
fprintf(fid, '%d', ortang);
fprintf(fid, '\n');

fprintf(fid, '%d\t', CL); %start line 9
fprintf(fid, '%d\t', prelod);
fprintf(fid, '%d\t', stepht);
fprintf(fid, '%d\t', angecc);
fprintf(fid, '%d\t', anglod);
fprintf(fid, '%d', SPEED);
fprintf(fid, '\n');

fprintf(fid, '%d\t', cavp); %start line 10
fprintf(fid, '%d\t', grovep);
fprintf(fid, '%d\t', side1p);
fprintf(fid, '%d', side2p);
fprintf(fid, '\n');

fprintf(fid, '%d\t', amisx); %start line 11
fprintf(fid, '%d\t', amisy);
fprintf(fid, '%d\t', rens);
fprintf(fid, '%d', densty);
fprintf(fid, '\n');

fprintf(fid, '%d\t', dx); %start line 12
fprintf(fid, '%d\t', dy);
fprintf(fid, '%d\t', dxdot);
fprintf(fid, '%d\t', dydot);
fprintf(fid, '%d', trunc);
fprintf(fid, '\n');

fprintf(fid, '%12.3f %12.3f %12.3f %12.3f %12.3f %12.3f\n', ECC(:));
%line 13
```

```

fprintf(fid, '\n');

%generate the given pressures in format (axialpoint circumpoint value)
%for j=1:size(CRG,2)
    %for i=96:size(AXG,2)
        % fprintf(fid, '%12.0f %12.0f %12.0f\n', i, j, Psupply);
        %fprintf(fid, '\n');
    % end
%end

%generate grid intervals in circumferential direction (degrees)
ANGINC=[];
for i=2:size(CRG,2)
    ANGINC=[ANGINC CRG(i)-CRG(i-1)];
end

ANGINC=[ANGINC 360-CRG(size(CRG,2))];
fprintf(fid, '%12.8f %12.8f %12.8f %12.8f %12.8f %12.8f\n', ANGINC(:));
fprintf(fid, '\n');

%generate grid intervals in axial direction
AXLINC=[];
for i=2:size(AXG,2)
    AXLINC=[AXLINC AXG(i)-AXG(i-1)];
end
fprintf(fid, '%12.8f %12.8f %12.8f %12.8f %12.8f %12.8f\n', AXLINC(:));
fprintf(fid, '\n');

%print number of POINTS in format (AXIAL CIRCUM) (NOTICE! CIRCUM=CIRCUM-
GRID+3)
fprintf(fid, '%d\t', size(AXG,2));
fprintf(fid, '%d\t', size(CRG,2)+3);
fprintf(fid, '\n');

%print the locations of points in circumferential direction
fprintf(fid, '%12.8f %12.8f %12.8f %12.8f %12.8f
%12.8f\n', CRG(size(CRG,2))-360, CRG(:), 360, 360+CRG(2)-CRG(1));
fprintf(fid, '\n');

```

```
%print the locations of points in axial direction
fprintf(fid,'%12.8f %12.8f %12.8f %12.8f %12.8f %12.8f\n',AXG(:));
fprintf(fid,'\n');

%print the structural deformation values

fprintf(fid,'%12.8f %12.8f %12.8f %12.8f %12.8f
%12.8f\n',GDM(size(CRG,2)/6,:)); %print the first theta value
fprintf(fid,'\n');

for j=1:np
    i=1;
    for i=1:size(CRG,2)/6
        fprintf(fid,'%12.8f %12.8f %12.8f %12.8f %12.8f
%12.8f\n',GDM(i,:));
        fprintf(fid,'\n');
    end
end

fprintf(fid,'%12.8f %12.8f %12.8f %12.8f %12.8f %12.8f\n',GDM(1,:));
%print the theta=360 value
fprintf(fid,'\n');
fprintf(fid,'%12.8f %12.8f %12.8f %12.8f %12.8f %12.8f\n',GDM(2,:));
%print the last theta value

fclose(fid);
```

This MATLAB script generates the geometry and calculates the equivalent capillaries for the backgroove SC5-6 designs

```
clear all;
%Automatic Bearing Geometry Creation for RBTS

%Backgroove designs
```

```

%*****
*****
%INPUT
*****
*****
%System of Units
units=1; %0=english, 1=SI (actually mm in linear dimensions)

%General Dimensions
D=25; %Diameter
L=27; %Total length (from end to the symmetry plane)
CL=0.00075*25.4; %bearing clearance
np=6; %number of pockets
GW=1; %Groove width
GD=-CL*13; %Groove depth (give negative value (a bug :) )
ecc=0.1; %eccentricity
Ps=7000000; %supply pressure

%drainage grooves
drains=1; %drains (0=false, 1=true)
dgl=20; %drainage groove length
divgw=30; %determines how close the points are to the grooves (GW/
divgw)

%Circumferential dimensions
cpc1=7.1; %1st dimension (pocket width)
cpc2=10.1; %2nd dimension (0 to first drainage groove)
%cpc3=31.794; %3rd dimension (0 to beginning of restrictor groove)
rgl=7; %restrictor groove length
ANG=180; %wraparound angle in degrees

%Axial dimensions
cpa1=3; %1st dimension (exit land width)
cpa2=17; %2nd dimension (0 to end of pocket)
cpa3=20; %3rd dimension (from end to the separation groove)
cpa4=25
dl=0.7; %restrictor land width

%pockets
deepock=1; %if land is removed deepock=1 if not deepock=0;

```

```

%*****
*****
%CONVERT DIMENSIONS INTO DEGREES
*****

GWD=GW*360/(pi*D);
cpc1=cpc1*360/(pi*D);
cpc2=cpc2*360/(pi*D);
%cpc3=cpc3*360/(pi*D);
rgl=rgl*360/(pi*D);

%*****
*****
%GENERATE GRID LOCATION VECTORS
*****

CRG=[];
AXG=[];
cld=GW*360/(divgw*pi*D); %the dimension of how close the "close"
points are to the groove edges (degrees)
cl=GW/divgw; %same in axial units

%Circumferential locations (in
degrees)*****

if drains==1 %locations if drains exists
%locations of the given points
CRG=[0 cld GWD-cld GWD GWD+cld cpc1-cld cpc1 cpc1+cld cpc1+GWD-cld
cpc1+GWD cpc1+GWD+cld ...
cpc2-cld cpc2 cpc2+cld cpc2+GWD-cld cpc2+GWD cpc2+GWD+cld 360/
np-cld];

%add 2 points into the grooves
gs=(GWD-2*cld)/3; %step lenght (dimension between grid points)
CRG=[CRG cld+gs cld+2*gs cpc1+cld+gs cpc1+cld+2*gs cpc2+cld+gs
cpc2+cld+2*gs];

%add 7 points into the pocket
pos=(cpc1-GWD-2*cld)/8; %step lenght inside pocket
i=1;

```

```

for i=1:7
    CRG=[CRG GWD+cld+i*pos];
end

%add 5 points between the pocket and drainage grooves
ros=(cpc2-cld-(cpc1+GWD+cld))/6; %step length between pockets
i=1;
for i=1:5
    CRG=[CRG cpc1+GWD+cld+i*ros cpc2+GWD+cld+i*ros];
end

else %locations if drains do not exists

    %locations of the given points
    CRG=[0 cld GWD-cld GWD GWD+cld cpc1-cld cpc1 cpc1+cld cpc1+GWD-cld
cpc1+GWD 360/np-cld];

    %add 2 points into the grooves
    gs=(GWD-2*cld)/3; %step length (dimension between grid points)
    CRG=[CRG cld+gs cld+2*gs cpc1+cld+gs cpc1+cld+2*gs];

    %add 7 points into the pocket
    pos=(cpc1-GWD-2*cld)/8; %step length inside pocket
    i=1;
    for i=1:7
        CRG=[CRG GWD+cld+i*pos];
    end

    %add 10 points between the pockets
    ros=(360/np-(cpc1+GWD+cld)-cld)/11; %step length between pockets
    i=1;
    for i=1:10
        CRG=[CRG cpc1+GWD+cld+i*ros];
    end

end %end making first set of circumferential points

%Arrange points in ascending order
CRG=sort(CRG);

```

```

%make the rest of the points

CRG=[CRG CRG+360/np CRG+2*360/np CRG+3*360/np CRG+4*360/np CRG+5*360/
np];

%Axial loca-
tions*****
*****

%Given locations
AXG=[0 cl cpa1-cl cpa1 cpa1+cl cpa1+GW-cl cpa1+GW cpa1+GW+cl ...
      cpa2-cl cpa2 cpa2+cl cpa2-GW-cl cpa2-GW cpa2-GW+cl ...
      cpa3-cl cpa3 cpa3+cl cpa3+GW-cl cpa3+GW cpa3+GW+cl cpa4-d1-GW ...
      cpa4-d1-GW-cl cpa4-d1-GW+cl cpa4-d1-cl cpa4-d1+cl cpa4 cpa4-cl
cpa4+cl L-(L-cpa4)/3 L-2*(L-cpa4)/3 L]; %cpa4+cl L-(L-cpa4)/3 L-2*(L-
cpa4)/3 L

%add 2 points into the grooves
gsa=(GW-2*cl)/3; %step length
AXG=[AXG cpa1+cl+gsa cpa1+cl+2*gsa cpa2-GW+cl+gsa cpa2-GW+cl+2*gsa
cpa3+cl+gsa cpa3+cl+2*gsa ...
      cpa4-d1-GW+cl+gsa cpa4-d1-GW+cl+2*gsa];

%add 5 points into drainage land and compensator land
dls1=(cpa1-2*cl)/6; %drainage1 land step size
dls2=(cpa3-cpa2-2*cl)/6;
cls=(d1-2*cl)/6; %compensator land step size
i=1;
for i=1:5
    AXG=[AXG cl+i*dls1 cpa2+cl+i*dls2 cpa4-cl-i*cls cpa4-d1-GW-cl-i*cls];
end

%add 20 points into the pocket

step=(cpa2-cpa1-2*cl-2*GW)/21;
i=1;

```

```
for i=1:20
    AXG=[AXG cpa1+GW+c1+i*step];
end

%Arrange points into ascending order
AXG=sort(AXG);

%end making point locations

%Start making the deformation
matrix*****

GDM=[];
%find all the indeces for looping
diff1=CRG-(180-ANG);
diff2=CRG-(180-ANG+rg1);
diff4=AXG-cpa4;
diff5=AXG-(cpa4-d1-GW);
diff6=AXG-(cpa4-d1);
diff7=AXG-cpa1;
diff8=AXG-cpa2;
diff9=AXG-cpa3;
diff10=AXG-(cpa3+GW);

[value1,index1]=min(abs(diff1));
[value2,index2]=min(abs(diff2));
[value4,index4]=min(abs(diff4));
[value5,index5]=min(abs(diff5));
[value6,index6]=min(abs(diff6));
[value7,index7]=min(abs(diff7));
[value8,index8]=min(abs(diff8));
[value9,index9]=min(abs(diff9));
[value10,index10]=min(abs(diff10));

%make the first pocket groove
```



```
if deeppock==1 %make deep pockets if desired
    varcirc=15;
else
    varcirc=6;
end

for circumindex=1:varcirc
    for axialindex=index7:index8
        GDM(circumindex,axialindex)=GD;
    end
end

%make the second pocket groove

for circumindex=16:20
    for axialindex=index7:index8
        GDM(circumindex,axialindex)=GD;
    end
end

%make the drainage groove

if drains==1
    diff5d=AXG-dg1;
    [value5d,index5d]=min(abs(diff5d));

    for circumindex=29:34
        for axialindex=1:index5d
            GDM(circumindex,axialindex)=GD;
        end
    end
else
end

%make the circumferential pocket groove

for circumindex=7:15
    for axialindex=9:14
```

```

        GDM(circumindex,axialindex)=GD;
    end
end

%make the 2nd circumferential pocket groove

for circumindex=7:15
    for axialindex=index8-4:index8
        GDM(circumindex,axialindex)=GD;
    end
end

%make the separation groove

GDM(1:size(CRG,2)/np,index9+1:index10)=GD;

%make the restrictor collecting groove

GDM(index1:index2,index5:index6)=GD;

%make the supply groove

GDM(1:size(CRG,2)/np,index4:size(AXG,2))=GD;

%end making GDM
*****

%determine the recess loca-
tions*****
NAGL1=(index8-6)/2+6;      %NW axial
NAGL2=(index8-6)/2+8;      %SE axial

NCGL1=[10]; %[3 17]
for i=1:np-1
    NCGL1=[NCGL1 NCGL1(1)+i*size(CRG,2)/np]; %NW circum
    NCGL1(2)+i*size(CRG,2)/np
end

```

```

NCGL2=NCGL1+2; %SE circum

%determine the restrictor recess loca-
tions*****
NAGL1r=index5      %NW axial
NAGL2r=index6      %SE axial

NCGL1r=index1+4;
NCGL2r=index2-2;
for i=1:np-1
    NCGL1r=[NCGL1r NCGL1r(1)+i*size(CRG,2)/np];%NW circum
    NCGL2r=[NCGL2r NCGL2r(1)+i*size(CRG,2)/np];
end

%determine the equivalent capillary dimen-
sions*****
Lc=30; %equivalent capillary lenght
Ncap=1; %# of capillaries per pocket
Lz=rgl*(pi*D/360); %restrictor length
fi=(ANG-0.5*rgl)*pi/180; %angle from x-axis to first restrictor groove

i=0:5;
hr=CL*(1+ecc*sin(fi+i*2*pi/np));

Dc=((3.395.*Lc.*Lz.*hr.^3)/(Ncap*d1)).^(1/4);
Dc2=[];
for i=1:size(Dc,2)
    Dc2=[Dc2 Dc(i)];
end

%determine the equivalent capillary dimensions for restric-
tors*****
Lcr=5; %equivalent capillary lenght= thickness of the part
Lzr=rgl*(pi*D/360); %restrictor length

Dcr=sqrt(4*GW*Lzr/pi);
Dcr(1:6)=Dcr;

%Create "pumps" for the restrictors

```

```
Prets=[0.5*Ps 0.5*Ps 0.5*Ps 0.5*Ps 0.5*Ps 0.5*Ps]; %initial guess values
for the pumps
```

```
axpi=index5+(index6-index5)/2;
i=0:5;
circpi=[(index2-index1)/2+i*(size(CRG,2)/np)];
```

```
% *****
*****
CRGx=CRG(1:size(CRG,2)/np);
surf(AXG,CRGx,GDM)

view(2)
```

This MATLAB script writes the input file for the finite difference code for the backroove designs SC5-6

```
%THIS PROGRAM GENERATES THE JOURNB.INP FILE THAT IS NEEDED BY THE RBTS
PROGRAM
%RUN FIRST THE GEOMETRY_GEN.M PROGRAM BEFORE USING THIS
% *****
*****
%INPUT*****
*****
L=27; %total length of the bearing (NOT from end to the symmetry plane)

necc=1; %number of eccentricities considered in this run
niter=1; %number of iterations to solve for load angle convergence (if
niter=1 displacement will along -y axis
        % and the Fx and Fy are calculated) if >1 the displacement angle
will be calculated
npiter=15; %# of iterations to solve for recess pressure (only with ori-
fice restrictors)
nreces=2*np; %# of recesses in the bearing
npump=12; %# of pumps in the bearing

nfastp=0; %axial grid point # of the FIRST axial location of circumfer-
ential step or beginning of pocket
```

```
nsastp=0;    %axial grid point # of the SECOND axial location of circum-
ferential step or beginning of pocket
ncstp=0;    %circumferential grid point # of circumferential step or
pocket

vargrd='T';
taperb='F';
symtr='F';
dambrg='F';
condns='F';
struct='T';
nondim='F';

padang=360;
flmang=0;
ortang=0;

prelod=0;
stepht=0;
angecc=270;
anglod=270;
SPEED=100000;  %RPM !!!!

cavp=0;
grovep=0;
side1p=0;
side2p=7000000;

amisx=0;
amisy=0;
rens=0.0009;    %lubricant viscosity (lbf*sec/in^2 or PA*sec)
densty=995; %lubricant density (lb/in^3 or kg/m^3)

dx=0; %if 0 automatically set by the program
dy=0;
dxdot=0;
dydot=0;
trunc=0;
```

%eccentricities (type in wanted ecc) See that the variable necc corresponds to #ecc typed in the vector ECC

```
ECC=[ecc];
```

```
Psupply=3500000; %psi or Pa
```

```
%generate
```

```
file*****
*****
```

```
fid=fopen('C:\temp\oldcomputer\bearing\jurnbr.inp','wt');
```

```
fprintf(fid,'%d',units); %system of units (0=english, 1=si)
```

```
fprintf(fid,'\t');
```

```
fprintf(fid,'V5.1G2 \n'); %version
```

```
fprintf(fid,'TurboTool REV 4 \n');
```

```
fprintf(fid,'100000 rpm backgrooves \n');
```

```
fprintf(fid,'11/4/99 \n');
```

```
fprintf(fid,'%d\t',size(AXG,2)); %start line 5
```

```
fprintf(fid,'%d\t',size(CRG,2)+1);
```

```
fprintf(fid,'%d\t',1);
```

```
fprintf(fid,'%d\t',necc);
```

```
fprintf(fid,'%d\t',2); %if sidepressure is not used this should read
4*size(CRG,2) #number of point pressure is specified
```

```
fprintf(fid,'%d\t',niter);
```

```
fprintf(fid,'%d\t',npiter);
```

```
fprintf(fid,'%d\t',nreces);
```

```
fprintf(fid,'%d',npump);
```

```
fprintf(fid,'\n');
```

```
fprintf(fid,'%d\t',nfastp); %start line 6
```

```
fprintf(fid,'%d\t',nsastp);
```

```
fprintf(fid,'%d',ncstp);
```

```
fprintf(fid,'\n');
```

```
fprintf(fid,'%s\t',vargrd); %start line 7
```

```
fprintf(fid,'%s\t',taperb);
```

```
fprintf(fid, '%s\t', symtr);
fprintf(fid, '%s\t', dambrg);
fprintf(fid, '%s\t', condns);
fprintf(fid, '%s\t', struct);
fprintf(fid, '%s', nondim);
fprintf(fid, '\n');

fprintf(fid, '%d\t', D); %start line 8
fprintf(fid, '%d\t', L);
fprintf(fid, '%d\t', padang);
fprintf(fid, '%d\t', flmang);
fprintf(fid, '%d', ortang);
fprintf(fid, '\n');

fprintf(fid, '%d\t', CL); %start line 9
fprintf(fid, '%d\t', prelod);
fprintf(fid, '%d\t', stepht);
fprintf(fid, '%d\t', angecc);
fprintf(fid, '%d\t', anglod);
fprintf(fid, '%d', SPEED);
fprintf(fid, '\n');

fprintf(fid, '%d\t', cavp); %start line 10
fprintf(fid, '%d\t', grovep);
fprintf(fid, '%d\t', sidelp);
fprintf(fid, '%d', side2p);
fprintf(fid, '\n');

fprintf(fid, '%d\t', amisx); %start line 11
fprintf(fid, '%d\t', amisy);
fprintf(fid, '%d\t', rens);
fprintf(fid, '%d', densty);
fprintf(fid, '\n');

fprintf(fid, '%d\t', dx); %start line 12
fprintf(fid, '%d\t', dy);
fprintf(fid, '%d\t', dxdot);
fprintf(fid, '%d\t', dydot);
fprintf(fid, '%d', trunc);
```

```
fprintf(fid, '\n');

fprintf(fid, '%12.3f %12.3f %12.3f %12.3f %12.3f %12.3f\n', ECC(:));
%line 13
fprintf(fid, '\n');

%generate the given pressures in format (axialpoint circumpoint value)
%for j=1:size(CRG,2)
%for i=96:size(AXG,2)
%for i=1:np
    fprintf(fid, '%12.0f %12.0f %12.0f\n', axpi, circpi(i), Pri(i));
%end

fprintf(fid, '%12.0f %12.0f %12.0f\n', index9+1, 5, 0);
fprintf(fid, '%12.0f %12.0f %12.0f\n', index9+1, 120, 0);
    % end
%end

%generate grid intervals in circumferential direction (degrees)
ANGINC=[];
for i=2:size(CRG,2)
    ANGINC=[ANGINC CRG(i)-CRG(i-1)];
end

ANGINC=[ANGINC 360-CRG(size(CRG,2))];
fprintf(fid, '%12.8f %12.8f %12.8f %12.8f %12.8f %12.8f\n', ANGINC(:));
%fprintf(fid, '\n');

%generate grid intervals in axial direction
AXLINC=[];
for i=2:size(AXG,2)
    AXLINC=[AXLINC AXG(i)-AXG(i-1)];
end
fprintf(fid, '%12.8f %12.8f %12.8f %12.8f %12.8f %12.8f\n', AXLINC(:));
%fprintf(fid, '\n');

%generate recess and capillaries
for i=1:6
fprintf(fid, '%3.0f %3.0f %3.0f %3.0f %3.0f %3.0f %3.0f %3.0f %12.8f
```



```

%5.3f %5.6f\n',1,i,i,3,NAGL1,NCGL1(i),NAGL2,NCGL2(i),Dc2(i),Lc,rens);
end
%fprintf(fid,'\n');
%restrictor recesses
for i=1:6
    fprintf(fid,'%3.0f %3.0f %3.0f %3.0f %3.0f %3.0f %3.0f %3.0f %12.8f
%5.3f
%5.6f\n',1,i+6,i+6,3,NAGL1r,NCGL1r(i),NAGL2r,NCGL2r(i),Dcr(i),Lcr,rens);
end

%generate pumps
%fprintf(fid,'\n');
for i=1:6
    fprintf(fid,'%3.0f %3.0f %3.0f %5.3f\n',i,2,0,side2p); %supply pump
end
for i=1:6
    fprintf(fid,'%3.0f %3.0f %3.0f %5.3f\n',i+6,2,0,side2p/2);%initial
pressure guess for fake pumps
end
%fprintf(fid,'\n');
%print number of POINTS in format (AXIAL CIRCUM) (NOTICE! CIRCUM=CIRCUM-
GRID+3)
fprintf(fid,'%d\t',size(AXG,2));
fprintf(fid,'%d\t',size(CRG,2)+3);
fprintf(fid,'\n');

%print the locations of points in circumferential direction
fprintf(fid,'%12.8f %12.8f %12.8f %12.8f %12.8f
%12.8f\n',CRG(size(CRG,2))-360,CRG(:),360,360+CRG(2)-CRG(1));
fprintf(fid,'\n');

%print the locations of points in axial direction
fprintf(fid,'%12.8f %12.8f %12.8f %12.8f %12.8f %12.8f\n',AXG(:));
fprintf(fid,'\n');

%print the structural deformation values

fprintf(fid,'%12.8f %12.8f %12.8f %12.8f %12.8f
%12.8f\n',GDM(size(CRG,2)/6,:)); %print the first theta value

```

```
fprintf(fid, '\n');

for j=1:np
    i=1;
    for i=1:size(CRG,2)/6
        fprintf(fid, '%12.8f %12.8f %12.8f %12.8f %12.8f %12.8f
%12.8f\n', GDM(i, :));
        fprintf(fid, '\n');
    end
end

fprintf(fid, '%12.8f %12.8f %12.8f %12.8f %12.8f %12.8f\n', GDM(1, :));
%print the theta=360 value
fprintf(fid, '\n');
fprintf(fid, '%12.8f %12.8f %12.8f %12.8f %12.8f %12.8f\n', GDM(2, :));
%print the last theta value

fclose(fid);
```

Appendix B

DATA ANALYSIS FOR ERROR MOTION MEASUREMENTS

This script performs least squares circle fit for measured error motion data

```
clear all;
close all;
%read in data
[A,B]=textread('Z:\Hydrobushing\testing\small bushing tests\errormo-
tion\test144.txt','%f %f');
%Initial Guess for x0,y0,R
D=[-47;31;35];
%Valuate error function with initial guess
C=feval('qfunction',D)
%set tolerances for terminating optimisation routine
OPTIONS=OPTIMSET('TolFun',1e-7,'TolX',1e-8);
%minimize Q
[Param,val]=fminsearch('qfunction',D,OPTIONS)

%Plot Data and Fitted Curve
plot(A,B,'r.')
hold on
Theta=linspace(0,2*pi,1000);
X=Param(3)*cos(Theta)+Param(1);
Y=Param(3)*sin(Theta)+Param(2);
plot(X,Y,'k')
grid on;
axis equal;
%Calculate maximum and mean deviation from best fit
Rm=sqrt((A-Param(1)).^2+(B-Param(2)).^2);
```

```

%mean deviation
Meandeviation=sum(abs(Rm-Param(3)))/(length(Rm))
%maximum deviation
Maxdeviation=max(abs(Rm-Param(3)))
%place calculated deviations on graph
gtext({'Max Dev =',num2str(Maxdeviation)})
gtext({'Mean Dev =',num2str(Meandeviation)})

```

Following is the qfunction called by the previous script

```

%minimized function to fit circle in to data
%q=sum of squares of deviation from fitted circle
function q=qfunction(x0);
[A,B]=textread('Z:\Hydrobushing\testing\small bushing tests\errormo-
tion\test144.txt','%f %f');
d=sqrt((A-x0(1)).^2+(B-x0(2)).^2);
q=sum((d-x0(3)).^2);

```

Following script calculates the asynchronous error motions from the measured data

```

%find asynchronous error motion
zerovector=[];
indeces=[];
threshold=0.1; %value which the point can deviate from zero
                %to be still picked into zerovector
AA=A-Param(1);
BB=B-Param(2);
%find when the curve crosses x=0 axis
for i=1:length(AA);
    if abs(AA(i))<=threshold
        zerovector=[zerovector AA(i)];
        indeces=[indeces i];
    end
end
%Throw out double points
indeces2=[];
for i=1:length(indeces)-1
    if indeces(i+1)-indeces(i)<50
        indeces2=[indeces2];
    else
        indeces2=[indeces2 indeces(i)];
    end
end

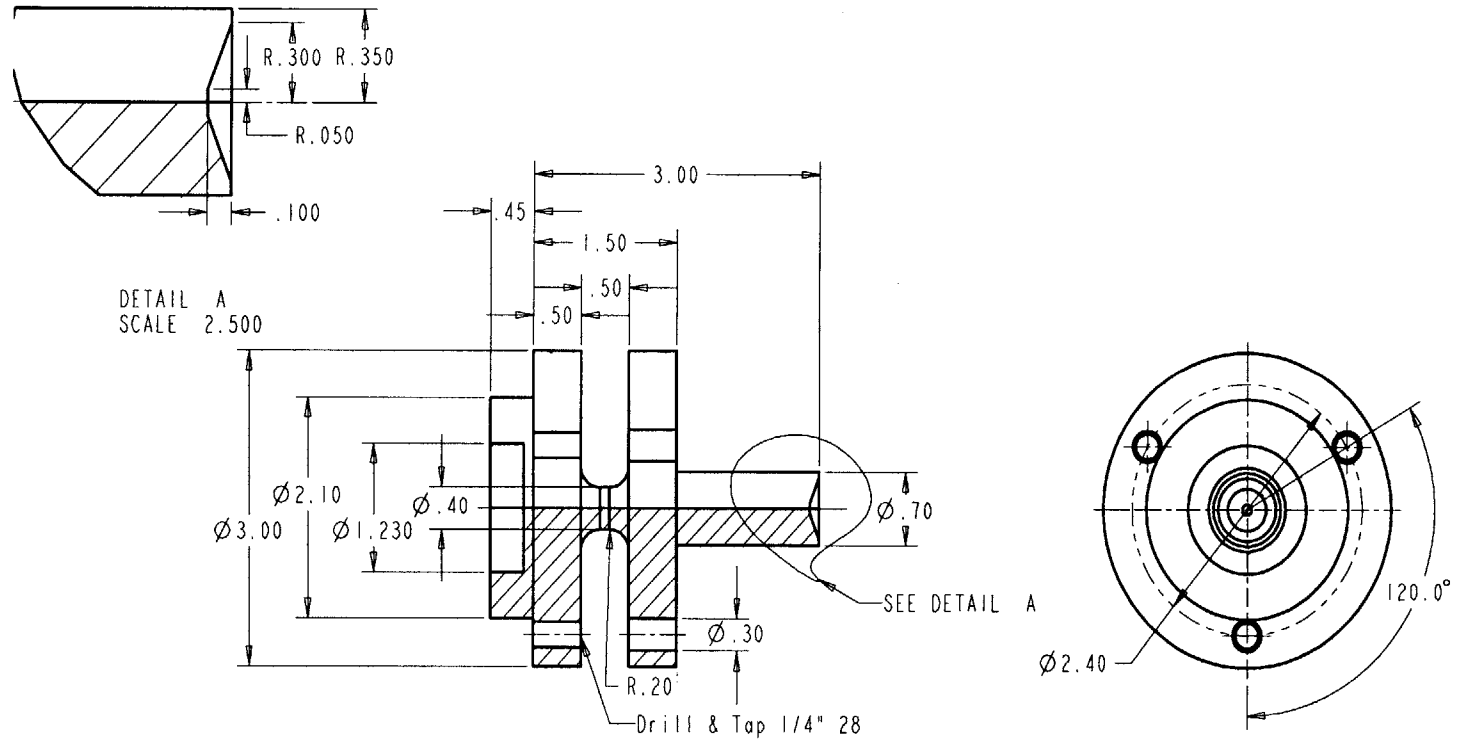
```

```
end
end
%pick out points that form full circle
indec3=[];
Astar=[];
for i=1:(length(indec2)+1)/2
    indec3=[indec3 indec2(2*i-1)];
end
%calculate how many points approximately form a single circle
npoints=[];
j=1:length(indec3)-1;
npoints=[indec3(j+1)-indec3(j)];
npoints=min(npoints);
%make a matrix containing one revolution per row
for i=1:length(indec3)-1;
    Astar(i,:)=[AA(indec3(i):indec3(i)+npoints)'];
    Bstar(i,:)=[BB(indec3(i):indec3(i)+npoints)'];
end
%calculate the radius for each point
Rstar=(Astar.^2+Bstar.^2).^0.5;
Async=max(Rstar)-min(Rstar);
figure
plot(Async);
grid on;
Max_Asyncronous_Error=max(Async)
Mean_Asyncronous_Error=mean(Async)
gtext({'Max Asyncronous Error =',num2str(Max_Asyncronous_Error)})
gtext({'Mean Asyncronous Error =',num2str(Mean_Asyncronous_Error)})
figure
spectrum(Async)
```


Appendix C

WOBBLE PLATE

Following is the drawing of the wobble plate used in the error motion measurements.



Material: Aluminum

Appendix D

FINITE ELEMENT PROGRAM TO SOLVE LINEARIZED DYNAMIC RESPONSE OF THE TURBOTool

This MATLAB program solves the linearized dynamic response of the TurboTool to the cutting forces.

```
clear;
%SIMPLE BEAM FEA TO GET FREQUENCY RESPONSE
%WITH BEARING AND DAMPING

%PARAMETERS
L=0.144;      %length of the entire beam
x0=0.02;     %length of the turbine
x1=0.038;    %x coordinate of the first bearing spring dashpot
x2=0.078;    %x coordinate of the second bearing spring and dashpot

N0=2; %number of elements to represent the turbine
N1=10; %number of elements before x1
N2=10; %number of elements after x2
N3=10; %number of elements between x1 and x2

%beam x-sectional parameters
E1=206e9;    %Youngs Modulus
Izz=1.917e-8; %x-sections 2nd moment of inertia
A=4.91e-4;   %x-sectional area
```

```

rho=7850;    %density

%turbine x-sectional parameters
Izz0=7.36e-8;
A0=9.62e-4;

%bearing parameters
stiff=65e6;    %bearing stiffness (per half)
damp=3e1;      %bearing damping (per half)
ksi=0.01 % proportional modal (material) damping

%calculate element lengths
length0=x0/N0;
length1=(x1-x0)/N1;
length2=(L-x2)/N2;
length3=(x2-x1)/N3;

%calculate element stiffness and mass matrices
[ke0,me0]=febeam1(E1,Izz0,length0,A0,rho,1);
[ke1,me1]=febeam1(E1,Izz,length1,A,rho,1); %last number=1 for consistent
mass matrix, number=2 for lumped
[ke2,me2]=febeam1(E1,Izz,length2,A,rho,1);
[ke3,me3]=febeam1(E1,Izz,length3,A,rho,1);

%Assemble element matrices into global matrices
Kg(1:2*(N0+N1+N2+N3+1),1:2*(N0+N1+N2+N3+1))=0;
Mg(1:2*(N0+N1+N2+N3+1),1:2*(N0+N1+N2+N3+1))=0;
index=[-1 0 1 2];
k=1;
for k=1:N0
    index=index+2;
    Kg=feasmb11(Kg,ke0,index);
    Mg=feasmb11(Mg,me0,index);
end
k=1;
for k=1:N1
    index=index+2;
    Kg=feasmb11(Kg,ke1,index);
    Mg=feasmb11(Mg,me1,index);

```

```

end
k=1;
for k=1:N3
    index=index+2;
    Kg=feasmb11(Kg,ke3,index);
    Mg=feasmb11(Mg,me3,index);
end
k=1;
for k=1:N2
    index=index+2;
    Kg=feasmb11(Kg,ke2,index);
    Mg=feasmb11(Mg,me2,index);
end

%THIS PORTION IS TO CHECK DEFLECTIONS AND FIRST 5 NATURAL FREQUENCIES
AGAINST ANALYTICAL SOLUTIONS
%constrain the dofs
constraints=[1 2];
[Kgt,Mgt]=feaplycs(Kg,Mg,constraints);
%deflection test
Ft(1,1:(N0+N1+N2+N3+1)*2)=0;
Ft((N0+N1+N2+N3+1)*2-1)=100;
def=inv(Kg(3:size(Kgt,2),3:size(Kgt,2)))*Ft(3:size(Ft,2))';
check=100*L^3/(3*E1*Izz);
Errorstatic=def(size(def,1)-1)-check
%calculate natural frequencies
F=[];
[Omegat, Phit, ModF]=femodal(Mgt,Kgt,F);
%Check natural frequencies
acoeff=[3.52 22 61.7 121 200];
omegaanalyt=acoeff.*sqrt(E1*Izz/(rho*A*L^4));
errormod=omegaanalyt'-Omegat(3:7)
errormodrel=100.*(errormod)./omegaanalyt'

%REAL RESPONSE CALCULATION STARTS FROM HERE AGAIN
%add bearing springs
Kg(2*N1+1,2*N1+1)=Kg(2*N1+1,2*N1+1)+stiff;
Kg(2*(N3+N1)+1,2*(N3+N1)+1)=Kg(2*(N3+N1)+1,2*(N3+N1)+1)+stiff;

```

```

%make damping matrix
%proportional damping
C=2*ksi*sqrtm(Mg)*sqrtm((inv(sqrtm(Mg))*Kg*inv(sqrtm(Mg))))*sqrtm(Mg);
%add dashpots
C(2*N1+1,2*N1+1)=C(2*N1+1,2*N1+1)+damp;
C(2*(N3+N1)+1,2*(N3+N1)+1)=C(2*(N3+N1)+1,2*(N3+N1)+1)+damp;

%apply boundary condition
constraints=[]; %first d.o.f is constrained
%[Kg,Mg]=feaplycs(Kg,Mg,constraints);
Kg=Kg(2:size(Kg,2),2:size(Kg,2));
Mg=Mg(2:size(Mg,2),2:size(Mg,2));
C=C(2:size(C,2),2:size(C,2));
%another test
Ft(1,1:(N1+N2+N3+1)*2)=0;
Ft((N1+N2+N3+1)*2-1)=800;
def=inv(Kg)*Ft(2:size(Ft,2))'

%set up state-space model
Aa=[zeros(size(Mg,2)) diag(ones(1,size(Mg,2)),0);inv(Mg)*(-Kg)
inv(Mg)*(-C)];
Bb=[zeros(size(Mg,2)) zeros(size(Mg,2));zeros(size(Mg,2))
inv(Mg)*diag(ones(1,size(Mg,2)),0)];
Cc=zeros(1,2*size(Mg,2));
Dd=zeros(1,2*size(Mg,2));

Cc((size(Mg,2))-1)=800;

%calculate natural frequencies
F=[];
[Omega, Phi, ModF]=femodal(Mg,Kg,F);
%plot the modes
Ndisp=size(Phi,1);
j=1;
for j=1:Ndisp
    i=1;
    for i=1:(Ndisp-1)/2
        Phi2(i,j)=Phi(2*i,j);
    end
end

```

```
end
```

```
OM=linspace(0,1000000,10000);
```

```
bode(Aa,Bb,Cc,Dd,2*size(Mg,2)-1,OM)
```

Next the function called by the main program are presented.

```
function [k,m]=febeam1(el,xi,leng,area,rho,ipt)
```

```
%-----
% Purpose:
%   Stiffness and mass matrices for Hermitian beam element
%   nodal dof {v_1 theta_1 v_2 theta_2}
%
% Synopsis:
%   [k,m]=febeam1(el,xi,leng,area,rho,ipt)
%
% Variable Description:
%   k - element stiffness matrix (size of 4x4)
%   m - element mass matrix (size of 4x4)
%   el - elastic modulus
%   xi - second moment of inertia of cross-section
%   leng - element length
%   area - area of beam cross-section
%   rho - mass density (mass per unit volume)
%   ipt = 1: consistent mass matrix
%         2: lumped mass matrix
%         otherwise: diagonal mass matrix
%-----
```

```
% stiffness matrix
```

```
c=el*xi/(leng^3);
```

```
k=c*[12      6*leng  -12      6*leng;...
     6*leng  4*leng^2 -6*leng  2*leng^2;...
     -12     -6*leng   12      -6*leng;...
     6*leng  2*leng^2 -6*leng  4*leng^2];
```

```
% consistent mass matrix
```

```

if ipt==1

    mm=rho*area*leng/420;
    m=mm*[156      22*leng   54      -13*leng;...
          22*leng  4*leng^2  13*leng -3*leng^2;...
          54      13*leng   156      -22*leng;...
          -13*leng -3*leng^2 -22*leng  4*leng^2];

% lumped mass matrix

elseif ipt==2

    m=zeros(4,4);
    mass=rho*area*leng;
    m=diag([mass/2  0  mass/2  0]);

% diagonal mass matrix

else

    m=zeros(4,4);
    mass=rho*area*leng;
    m=mass*diag([1/2  leng^2/78  1/2  leng^2/78]);

end

function [kk]=feasmb11(kk,k,index)
%-----
% Purpose:
%   Assembly of element matrices into the system matrix
%
% Synopsis:
%   [kk]=feasmb11(kk,k,index)
%
% Variable Description:
%   kk - system matrix

```



```

%      k - element matri
%      index - d.o.f. vector associated with an element
%-----

edof = length(index);
for i=1:edof
    ii=index(i);
    for j=1:edof
        jj=index(j);
        kk(ii,jj)=kk(ii,jj)+k(i,j);
    end
end

function [kk,mm]=feaplycs(kk,mm,bcdof)

%-----
% Purpose:
%      Apply constraints to eigenvalue matrix equation
%      [kk]{x}=lamda[mm]{x}
%
% Synopsis:
%      [kk,mm]=feaplycs(kk,mm,bcdof)
%
% Variable Description:
%      kk - system stiffness matrix before applying constraints
%      mm - system mass matrix before applying constraints
%      bcdof - a vector containging constrained d.o.f
%-----

n=length(bcdof);
sdof=size(kk);

for i=1:n
    c=bcdof(i);
    for j=1:sdof
        kk(c,j)=0;
    end
end

```

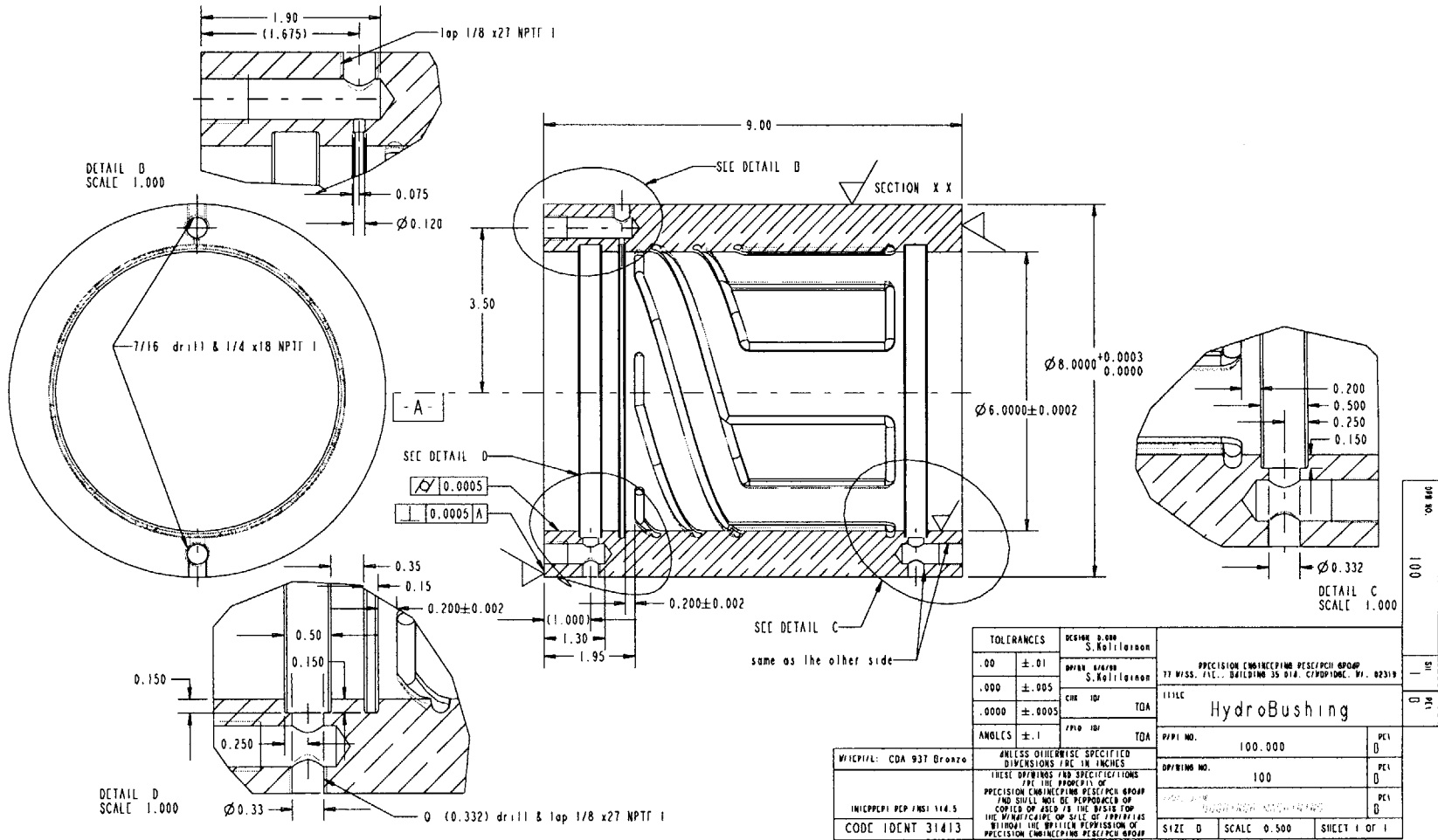
```
    kk(j,c)=0;  
    mm(c,j)=0;  
    mm(j,c)=0;  
end
```

```
mm(c,c)=1;  
end
```

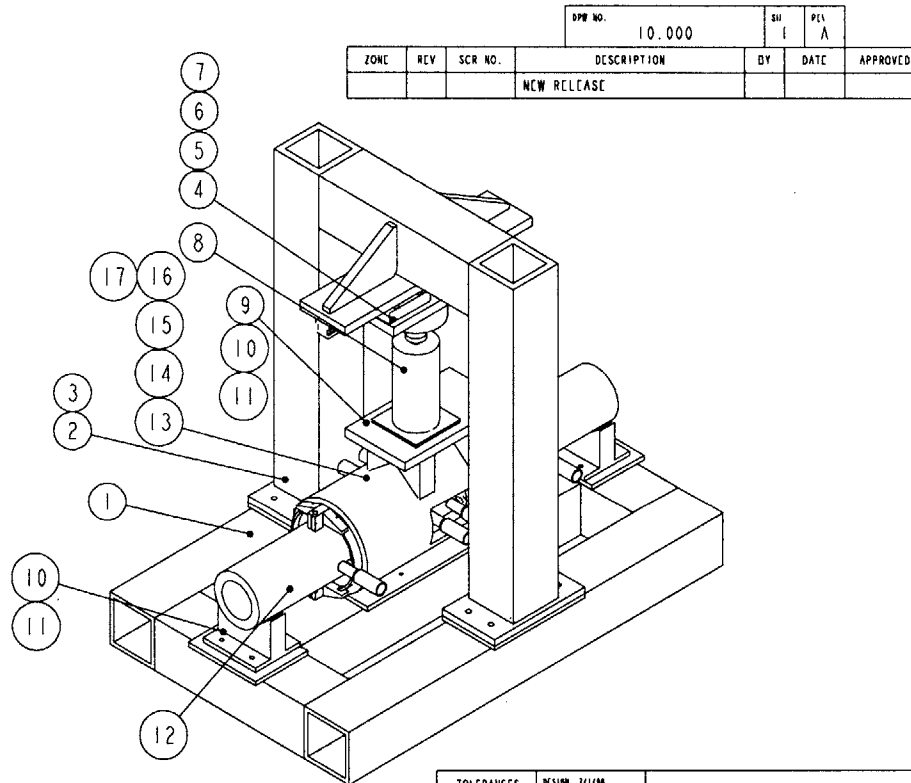
Appendix E

DETAILED DRAWINGS OF THE 6" BEARING TEST STAND

This appendix shown the machine drawings of the 6" prototype and the static test stand.



#	DRW #	Name	Special	Qty
		Hydraulic connectors + hoses		
17			(.125") UNRC	8
16		Cap Screw size 5	(.125") UNRF	4
15	104	Probe Holder		4
14	100	HydroBushing		2
13	103	Test Pipe		1
12	101	Shaft		1
11		Bolt 1/4" UNC	ANSI 18.2.1	16
10	400	V Holder		4
9	800	Force Plate		1
8		Hydraulic jack	20 Ton cap.	1
7	700	Truck Holder		1
6		Cap Screw M12	ANSI B18.3.1M	14
5		AccuGlide 45 rail	length 24"	1
4		AccuGlide 45 truck	standard	2
3		Bolt 1/2" UNC	ANSI 18.2.1	8
2	60	Gantry		1
1	50	Base Frame		1
#	DRW #	Name	Special	Qty



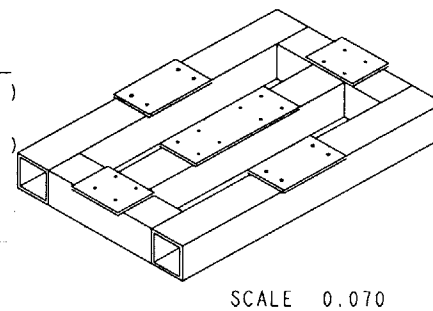
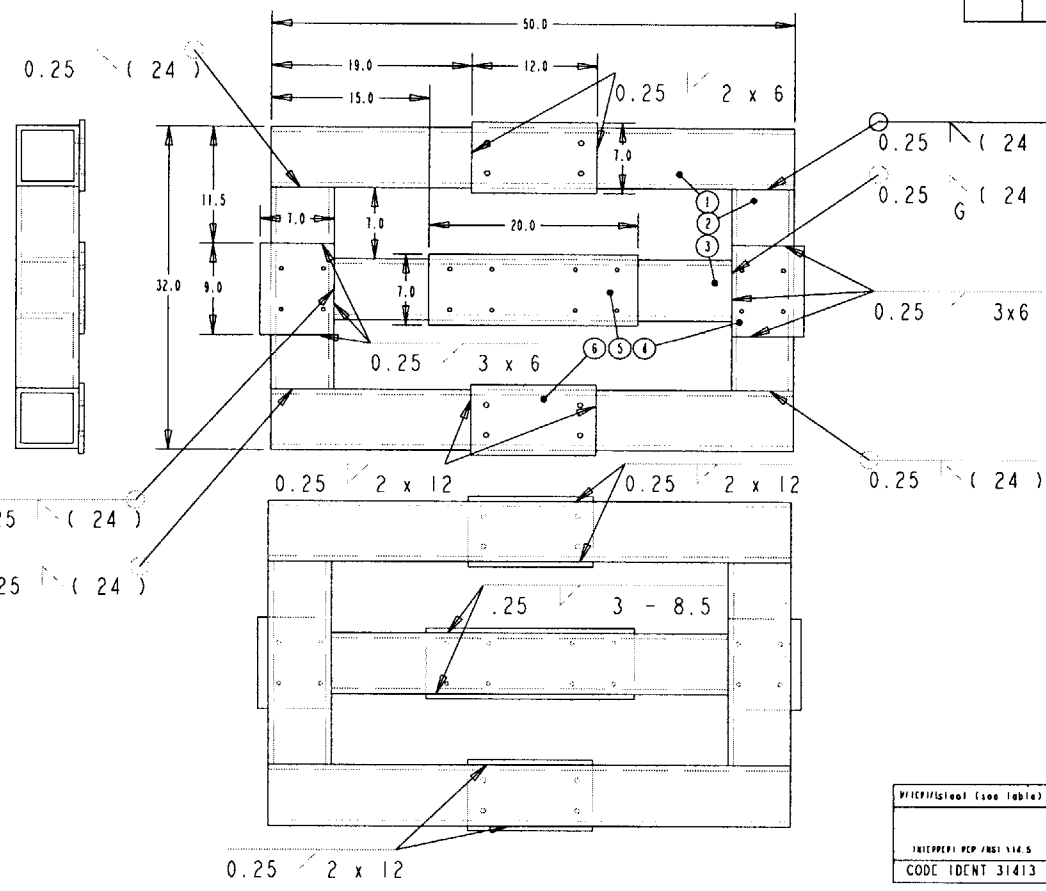
DPR NO.		10.000		SH	PEL	
ZONE	REV	SCR NO.	DESCRIPTION	BY	DATE	APPROVED
			NEW RELEASE			

TOLERANCES		DESIGN 2/100	PRECISION ENGINEERING RESEARCH GROUP 77 WISS. BLDG., DUBLIN 35 014, CROMFORD, W. 02310	SH 1	PEL A
.00	± .01	S. Ratiolairan			
.000	± .005	2/100 S. Ratiolairan			
.0000	± .0005	EN			
ANGLES ± .1		FIN	FALSE	TITLE Test Bed Assembly	
UNLESS OTHERWISE SPECIFIED DIMENSIONS ARE IN INCHES		PRECISION ENGINEERING RESEARCH GROUP AND SHALL NOT BE REPRODUCED OR COPIED OR ADDED TO THE DISK TOP THE WINDUP/DATE OF SALE OF 1/19/77/AS WITHOUT THE WRITTEN PERMISSION OF PRECISION ENGINEERING RESEARCH GROUP		PIPE NO. 10.000	
INTEPERT PEP ANSI 314.5		CODE IDENT 31413		DRAWING NO. 10.000	
				SCALE 0.100	
				SHEET 1 OF 1	

DRW NO. 10.000
SH 1
PEL A

ZONE		REV	SCR NO.	DESCRIPTION	BY	DATE	APPROVED
				NEW RELEASE			

SPR NO.	50.000	SR	PEL
			B

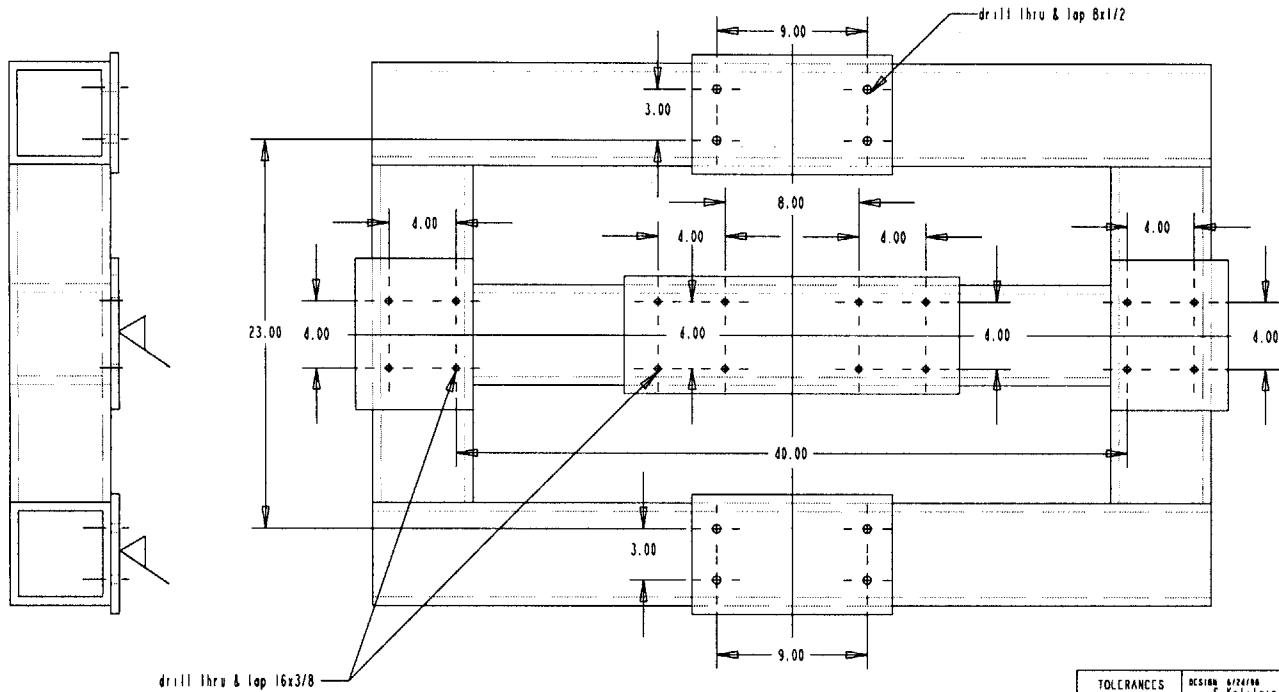


#	Dimensions	Material	Special	Qty
6	12x7x1/2	Steel AISI 1018 (or similar)		2
5	20x7x1/2	Steel AISI 1018 (or similar)		1
4	9x7x1/2	Steel AISI 1018 (or similar)		2
3	38x6x1/2	Steel ASTM500 (or similar)		1
2	20x6x1/2	Steel ASTM500 (or similar)		2
1	50x6x1/2	Steel ASTM500 (or similar)		2

TOLERANCES	DESIGN DIMENSIONS S. A. 11.1-11.2	PRECISION ENGINEERING PEE/PECH GROUP 11 WISS. AVE., DAYTON OH 45424 TITLE Base Frame (welding)
.00	±.01	
.000	±.005	
.0000	±.0005	
ANGLES	±.1	DATE 5/20/88

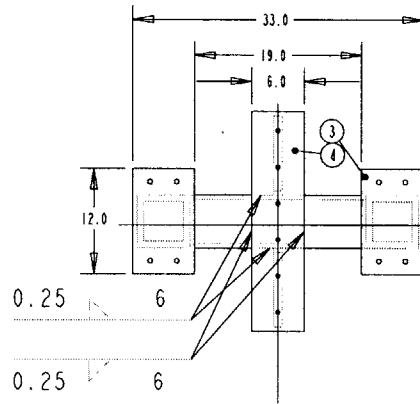
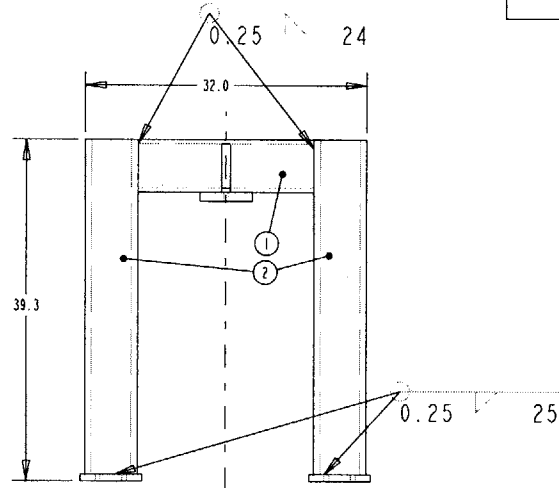
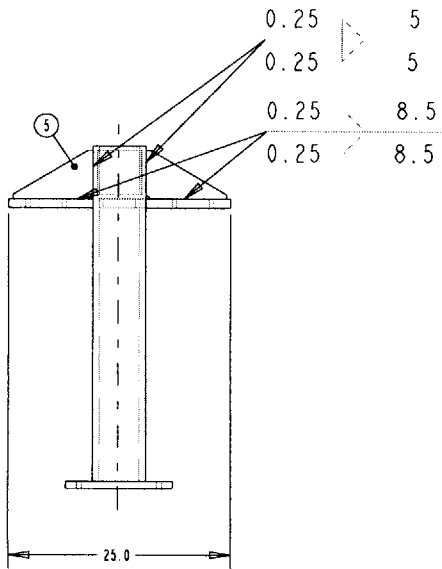
PRECISION ENGINEERING PEE/PECH GROUP	SPR NO.	50.000	PEL
PRECISION ENGINEERING PEE/PECH GROUP	SPR NO.	50.000	PEL
PRECISION ENGINEERING PEE/PECH GROUP	SPR NO.	50.000	PEL
CODE IDENT 31413	SIZE	0	SCALE 0.100 SHEET 1 OF 2

D/W NO.		50.000	SUP	2	PEL	8
ZONE	REV	SCR NO.	DESCRIPTION	DY	DATE	APPROVED
	0		Changed tolerancing	SK	8/19/98	

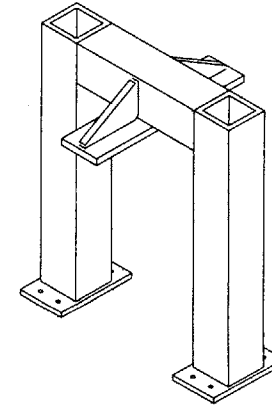


D/W NO.	50.000
SHT	2
PL	B

TOLERANCES	DECIMAL 0/24/98 S. Kollman	PRECISION ENGINEERING RESEARCH GROUP 77 W/SS. P.L.C., BUILDING 35 014, CHADDISDORF, VI. 02318	
.00 ±.01	0/24/98 S. Kollman	TITLE Base Frame machining	
.000 ±.005	CH	D/P/1 NO.	50.000
.0000 ±.0005	P/10	D/P/10 NO.	50.000
ANGLES ±.1		DATE LAM. IN.	BASE FRAME
INTERFERENCE (see table)	UNLESS OTHERWISE SPECIFIED DIMENSIONS ARE IN INCHES	SIZE	0
INTEGRITY PER ANSI Y14.5	THESE DIMENSIONS AND SPECIFICATIONS ARE THE PROPERTY OF PRECISION ENGINEERING RESEARCH GROUP AND SHALL NOT BE REPRODUCED OR COPIED OR USED AS THE BASIS FOR THE FABRICATION OF SILE OF PARTS WITHOUT THE WRITTEN PERMISSION OF PRECISION ENGINEERING RESEARCH GROUP	SCALE	0.150
CODE IDENT 31413		SHEET	2 OF 2



DWP NO.		60.000		SU	1	PEL	A
ZONE	REV	SCR NO.	DESCRIPTION	BY	DATE	APPROVED	
			NEW RELEASE				



SCALE 0.075

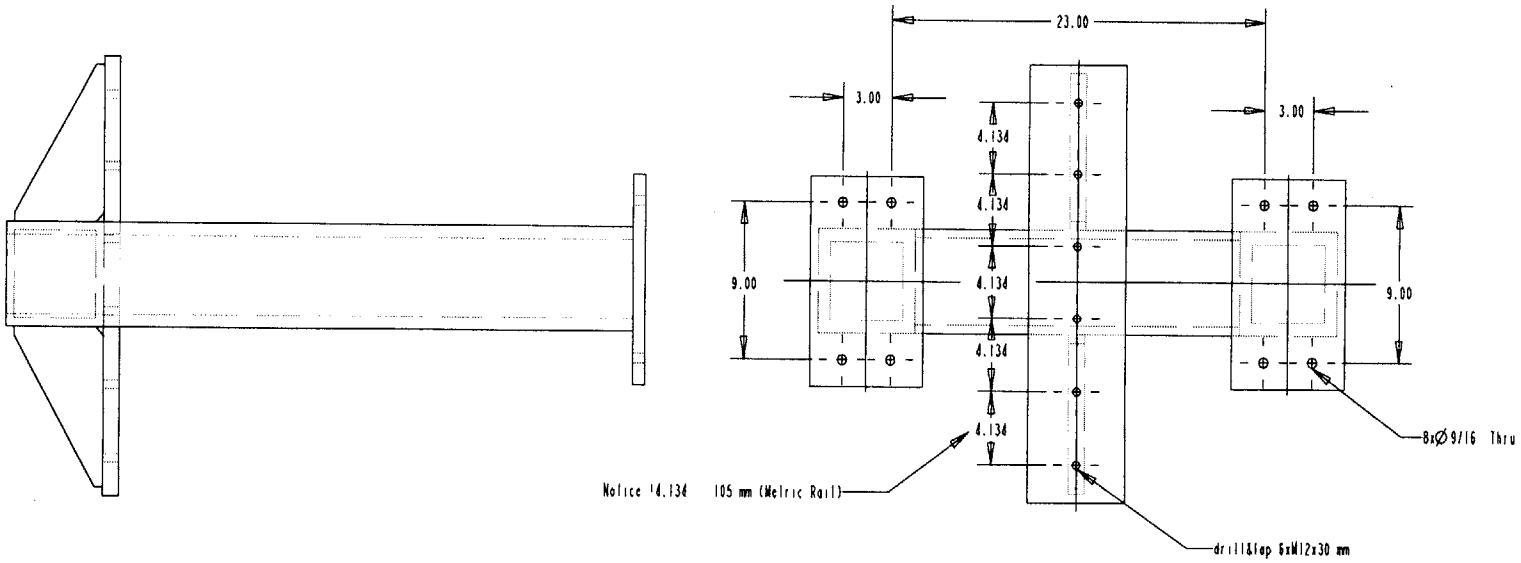
#	Dimensions	Material	Drawing #	Qty
5		Steel AISI 1018 (or similar)	600	2
4	25x6x1	Steel AISI 1018 (or similar)		1
3	12x7x3/4	Steel AISI 1018 (or similar)		2
2	38.5x6x6x1/2	Steel ASTM500 (or similar)		2
1	20x6x6x1/2	Steel ASTM500 (or similar)		1

60.000
 ON FILE
 V 115

TOLERANCES	SECTION 6/29/90 S. Kollmann	PRECISION ENGINEERING RESEARCH GROUP 77 WISS. BLDG. BUILDING 35 DIA. CAMPUS DR., 02319
.00 ± .01	SECTION 4/29/90 S. Kollmann	TITLE
.000 ± .005	CUR	Gantry
.0000 ± .0005	FINISH	Welding
ANGLES ± .1	FINISH	DRAWING NO.
		60.000
		PEL
		PEL
		PEL

UNLESS OTHERWISE SPECIFIED DIMENSIONS ARE IN INCHES	UNLESS OTHERWISE SPECIFIED DIMENSIONS ARE IN INCHES	SIZE	SCALE	SHEET
INHERENT PER ANSI 114.5	INHERENT PER ANSI 114.5	D	0.080	1 OF 2
CODE IDENT 31413	CODE IDENT 31413			

DPP NO.		60.000		SR	2	PC1	A
ZONE	REV	SCR NO.	DESCRIPTION	BY	DATE	APPROVED	
			NEW RELEASE				



Notice 4.134 105 mm (Metric Rail)

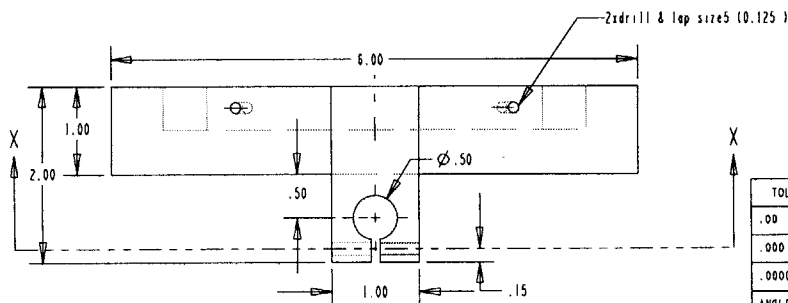
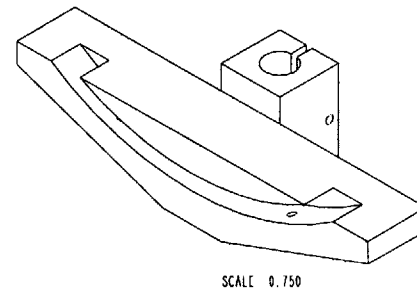
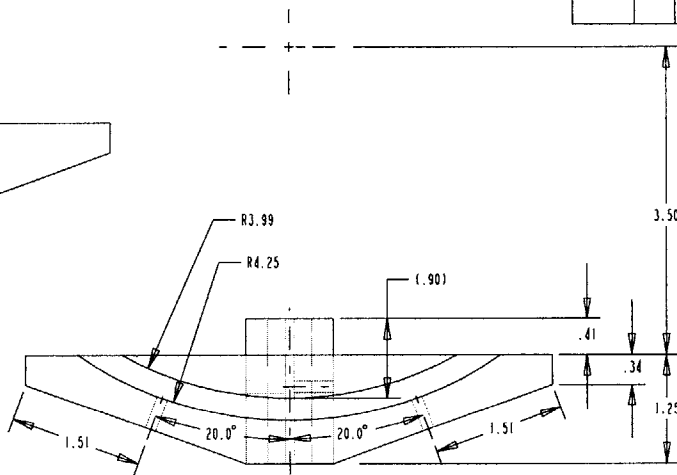
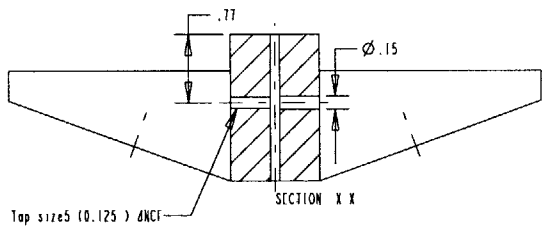
8xØ 9/16 Thru

drill & tap 6xM12x30 mm

DPP NO.	60.000
SR	2
PC1	A

TOLERANCES	DESIGN 6/25MM S. Kolliforner	PRECISION ENGINEERING PESE/PCII GROUP 77 WASS. FLE.. GARDING 35 DICK. C/RODINGE. W. 02319	
.00	± .01	DPP/NO.	60.000
.000	± .005	PC1	A
.0000	± .0005	TITLE Gantry Welding	
ANGLES	± .1	DPP/NO.	60.000
		PC1	A
W/ICP/1/1001 (see table)	UNLESS OTHERWISE SPECIFIED DIMENSIONS ARE IN INCHES	PROJECT DRAW TITLE	GANTRY
	THESE DIMENSIONS AND SPECIFICATIONS ARE THE PROPERTY OF PRECISION ENGINEERING PESE/PCII GROUP AND SHALL NOT BE REPRODUCED OR COPIED OR USED AS THE BASIS FOR THE MANUFACTURE OR SALE OF PRODUCTS WITHOUT THE WRITTEN PERMISSION OF PRECISION ENGINEERING PESE/PCII GROUP	SIZE	D SCALE 0.150 SHEET 2 OF 2
INICP/PEI REP /NSI 114.5			
CODE IDENT 31413			

ZONE		REV	SCR NO.	DESCRIPTION	BY	DATE	APPROVED
				NEW RELEASE			



TOLERANCES	DESIGN 721/FIN S. Kollidomin	PRECISION ENGINEERING RESEARCH GROUP	104.000	SH 1	PEL A
.00 ± .01	DRAW 721/FIN S. Kollidomin	77 WISS. BLDG. BUILDING 35 014. C/PO/PODC W. 02319	TITLE	104.000	SH 1
.000 ± .005	CHE		Probe Holder	104	PEL A
.0000 ± .0005	ANGLES ± .1		DRWING NO.	104.000	PEL A
			SIZE 0	SCALE 0.800	SHEET 1 OF 1

UNLESS OTHERWISE SPECIFIED DIMENSIONS ARE IN INCHES
 THESE DIMENSIONS AND SPECIFICATIONS ARE THE PROPERTY OF PRECISION ENGINEERING RESEARCH GROUP AND SHALL NOT BE REPRODUCED OR COPIED OR USED AS THE BASIS FOR THE FABRICATION OF SCALE DRAWINGS WITHOUT THE WRITTEN PERMISSION OF PRECISION ENGINEERING RESEARCH GROUP

INTEGRITY REP / NSI 114.5
 CODE IDENT 31413

104.000
 SH 1
 PEL A